HEAT PARTITION IN ELASTOHYDRODYNAMIC SLIDING CONTACTS UNDER FULL FILM LUBRICATION CONDITIONS

Alastair Clarke

Thesis submitted in candidature

for the degree of Doctor of Philosophy

at Cardiff University

Tribology Group

Institute of Theoretical, Applied and Computational Mechanics

Cardiff School of Engineering

Cardiff University

February 2009

ProQuest LLC
789 East Eisenhower Parkway
P.O. Box 1346
Ann Arbor, MI 48106-1346

Summary

The principal aim of the work within this thesis was to investigate the fundamental problem of how the frictional heat generated by lubricant shearing at a rolling/sliding elastohydrodynamic contact is divided between the contacting bodies. In elastohydrodynamic lubrication (EHL), a knowledge of the temperatures of the contacting bodies is important due to the effects of temperature on lubricant viscosity in the inlet zone and hence on film thickness.

A two-disc test rig previously used to study scuffing was subject to extensive modifications to allow the measurement of disk temperatures at six sub-surface locations in each disk using carefully calibrated embedded thermocouples. A series of experiments using a synthetic gas turbine engine oil was conducted at a range of sliding speeds from 10 ms^{-1} to 20 ms^{-1} and loads equivalent to maximum Hertzian contact pressures between 1.0 GPa and 1.6 GPa. In each experiment, the speed was fixed and the load applied. Once the temperatures had reached steady-state conditions, the load was removed and the disks separated. The disks were run whilst they cooled until they returned to ambient temperatures. The data recorded during these experiments were analysed using a transient two-dimensional conduction model of the outer region of the disks, which attempted to obtain an optimal agreement between calculated and measured temperatures. This was achieved by adjusting the partition of heat between the disks and the level of forced convection from the disk surface until the temperatures during the loaded phase of the test (governed by heat partition and cooling) and the cooling phase of the test (governed by the disk surface convection only) were in closest agreement with experimental measurements.

Whilst the data recorded from the slow disk was found to be repeatable, there were some errors and lack of repeatability noted with the fast disk data. However, using the slow disk data, it was found that approximately 40% of the frictional heat flows into the slow disk, with the remaining 60% flowing into the fast disk.

A series of thermal EHL analyses was performed, using a range of viscosity and rheological models. It was found that the heat partition predicted by the thermal EHL analysis only approached that measured during experiment when the majority of the heat was dissipated by slip at or near to the fast surface. These conditions only occurred when using a limiting shear stress rheological model in conjunction with the Barus viscosity model.

The thesis also contains details of finite-element modelling carried out to study elastic-plastic deformation of asperities during the running-in process. It was found that the residual deformation following loading beyond the elastic regime always followed the same shape, with characteristic "piling up" of material around the boundary of the contact. A series of non-dimensional relations for the shape and magnitude of the residual deformation were developed, and their potential for use in an EHL rough surface solver in order to take into account plastic deformation was noted.

Acknowledgements

It has been a pleasure to carry out this work under the supervision and guidance of Professor Pwt Evans and Professor Ray Snidle. Both have been a constant source of encouragement, wise words and helpful suggestions throughout the course of my studies. I must also thank them for, at times, turning a blind eye to the indulgence of my passion for motorsport with the School of Engineering's Formula Student team. I am also grateful to the School of Engineering and its Head, Professor H.R. Thomas, for making both funding and facilities available to me. In addition, funding was made available from EPSRC and Shell Global Solutions. I must also record my thanks to Dr. Kayri Sharif for his friendship and help over the past four years, particularly with all things point-solver related! Dr. Chris Davies and Dr. Ajay Dhulipalla were most helpful in introducing me to the experimental facilities of the Tribology Group. I must also thank Dr. Dan White, David Morgridge, Dr. Max Qiao, Ben Wright, Giovanni Pugliese, Matteo Carli and Dr. Mark Holmes (for introducing me to the delights of Tecplot) who have all been colleagues within the Tribology Group at one point or another of my studies. In addition thanks are due to the technical staff of the School for their assistance and to Mr. Alan Griffiths for granting me access to workshop facilities during the test rig development work.

I must also thank Professor Karen Holford and Dr Carl Byrne for their guidance and support during my time at Cardiff. In matters of teaching and research, their advice has been invaluable.

I must also record my indebtedness to my parents, who have supported and encouraged me at all times during this work, which must have seemed sometimes like a never-ending process. In addition, I wish to thank my friends – especially Dave, Ifan, Rhys, Mark, Ben, Lys, Katie and members past and present of the Cardiff Formula Student team – for keeping me sane over the past few years!

Contents

Nomenclature

Symbol	Definition	Units
a,b	Hertzian contact dimensions	m
c	specific heat capacity	$Jkg^{-1}K^{-1}$
E'	effective elastic modulus	Pa
h	film thickness	m
h_0	minimum film thickness	m
h_c	central film thickness	m
h_t	disk running track heat transfer coefficient	$Wm^{-2}K^{-1}$
H_v	Vickers' Hardness	$kgf\ mm^{-2}$
L	Peclet number	-
p	pressure	Pa
p_0	maximum Hertzian contact pressure	Nm^{-2}
q	heat flux	Wm^{-2}
q_f	fast surface heat flux	Wm^{-2}
q_s	slow surface heat flux	Wm^{-2}
r	radial co-ordinate in conduction equation	m
R	radius of relative curvature	m
R_x	radius of relative curvature in x direction	m
R_y	radius of relative curvature in y direction	m
T	temperature	°C, K
t	time	s
T_f	fast surface temperature	°C
T_m	mid-film oil temperature	°C
T_{max}	maximum oil film temperature	°C
T_s	slow surface temperature	°C
$\hat{u}$	mean entraining velocity	ms^{-1}
u,v	velocities in x and y directions	ms^{-1}
u_s	sliding speed	ms^{-1}
w'	load per unit length	Nm^{-1}
x,y	co-ordinates in contact plane	m
z	axial co-ordinate in conduction equation	m
z	co-ordinate normal to contact plane (EHL)	m
α	thermal diffusivity	m^2s^{-1}
α	pressure viscosity coefficient	Pa^{-1}
β	heat partition parameter	-
$\dot{\gamma}$	shear strain rate	s^{-1}
ε	thermal expansion coefficient	$°C^{-1}$
η	viscosity	Pa.s
η_0	ambient viscosity	Pa.s
λ	thermal conductivity	$Wm^{-1}K^{-1}$
θ	angular co-ordinate in conduction equation	rad
θ	temperature in energy equation	K
θ_b	inlet boundary temperature	K
θ_s	surface temperature	K
ρ	density	kgm^{-3}

σ_x, σ_y	non-Newtonian flow factors in axis directions	m.s
τ	shear stress	Pa
τ_L	limiting shear stress	Pa
τ_0	Eyring shear stress	Pa
ω	angular velocity	s^{-1}

All other terms or alternative nomenclature are defined as they are introduced in the thesis

Introduction and Review of Relevant Work

1.1 Introduction

The thesis is concerned with a combined experimental and theoretical approach to studying the partition of heat between contacting surfaces in elastohydrodynamic contacts. This chapter gives a brief introduction to the field of tribology and elastohydrodynamic lubrication (EHL). The relevant literature in the field concerned with heat partition in both dry and lubricated contacts is then discussed in detail, followed by an outline of the thesis aims.

1.2 Tribology and elastohydrodynamic lubrication

The use of the word tribology (derived from the Greek *Tribos* – to rub) as an engineering term dates from a Department of Education and Science report (1966) which defined it thus:

"The science and technology of interacting surfaces in relative motion and the practices related thereto."

But in practice tribology existed long before its definition in 1966. For example, Dowson (1979) in his fascinating "History of Tribology" tells of stone carvings found in a tomb at Saqqara, Egypt, which date from around 2400 B.C. These carvings show a statue being transported on a sled pulled by men with ropes. In front of the sled an

early tribologist can clearly be seen pouring liquid from a jar to lubricate the sled tracks.

Many concepts which are now classed as tribological systems also have their origins in the ancient world. For example, bearings were first used in the early Neolithic period in mechanisms such as simple door hinges. In addition, lubrication was first evident on potter's wheels as early as 3250 B.C. As in the modern world where much research is conducted into extending the service life of tribological components through wear reduction, cart wheels dating back to 2750 B.C. have been discovered fitted with metal rims to reduce wear. Systems such as gears developed much later. Archimedes first proposed the concept in 250 B.C.. The earliest evidence for the use of gears is found in the Antikythera mechanism, dating from around 100 B.C., which was discovered during archaeological investigations of a sunken ship in 1900. The mechanism was a Greek astronomical calculator, and contained complex epicyclic differential gearing (Freeth *et.al.* 2006). The remains of the mechanism may be seen in Figure 1.1.

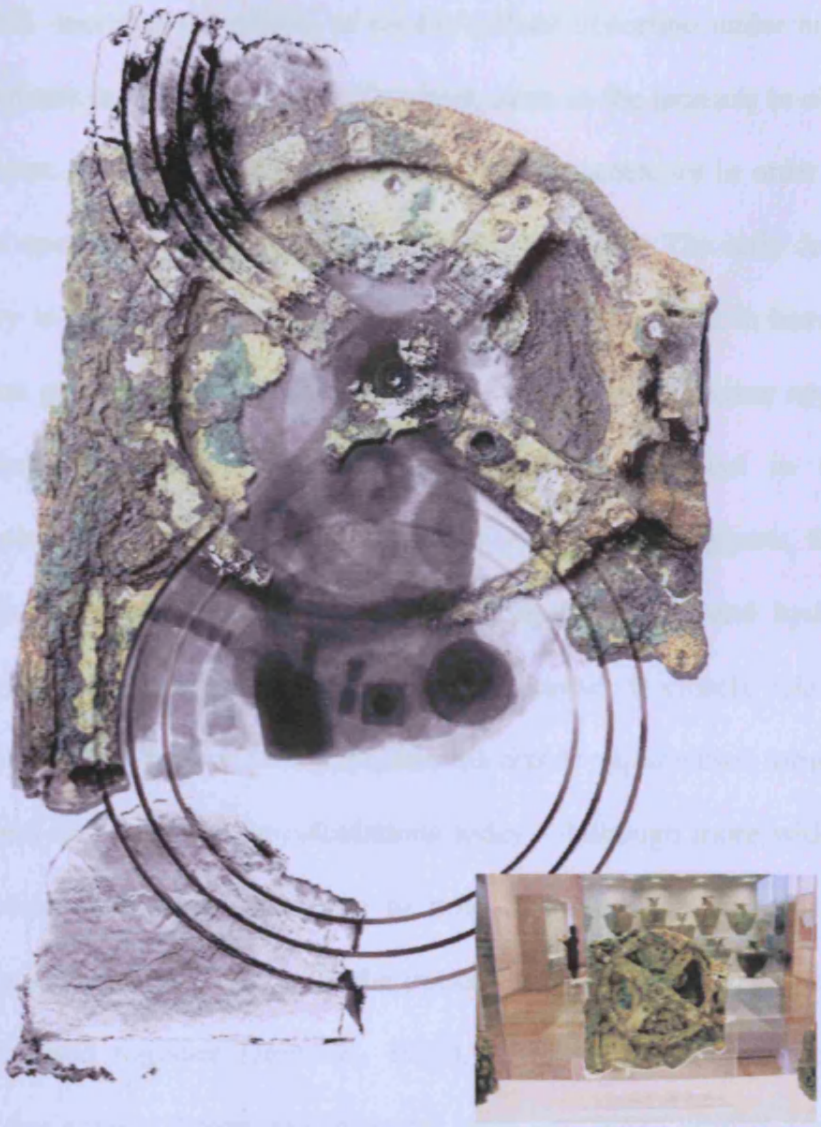

Figure 1.1: The remains of the Antikythera mechanism

The study of elastohydrodynamic lubrication (EHL) has developed during the twentieth century, and is concerned with the carrying of large loads by small, non-conformal lubricated contacts. As Gohar (2001) explains, the concept of EHL appeared rather more by accident than design when engineers noted the very low levels of wear between lubricated gear teeth. Some attributed this to the presence of a relatively thick oil film between the gear teeth, whilst others disputed this since classical rigid-surface, isoviscous hydrodynamic theory predicted a fluid film far thinner than the typical composite surface roughness present on gear teeth. The

concept of EHL includes the effects of elastic surface distortion under high contact pressures, lubricant hydrodynamics and rheology, such as the increase in oil viscosity at high pressures. Consideration of all these aspects is necessary in order to explain the successful operation of heavily loaded, lubricated contacts. The early development of EHL theory is now discussed. Typical examples of EHL occur in heavily-loaded large reduction gear boxes (such as those used in gas turbine engine applications), heavily loaded ball bearings, between cams and tappets, and in the power transmission elements of toroidal traction drives. As its name suggests, the roots of EHL theory can be found in the two fields of elastic theory and hydrodynamic lubrication. The pressure distribution in an EHL contact is closely related to that found in a dry contact. Hertz (1881) published his classic paper which forms the basis of contact stress and deformation calculations today. Although more widely known for his electrical work it is interesting to note that Hertz developed his contact mechanics theory due to an interest in the optical patterns observed when two glass spheres are pressed together (Johnson, 1985). Around the same time as Hertz produced his dry contact theory, experimental work was being carried out in Britain by Beauchamp Tower (1882, 1885) who discovered that substantial pressures were formed in the oil films of journal bearings. Following on from Tower's work, Reynolds (1886) published his theory of lubrication and the differential equation which bears his name and forms the basis of fluid film analysis. Although Reynolds' work was aimed at predicting the behaviour of journal bearings in which relatively thick oil films are generated (>10 μm) his equation has been widely used in the analysis of the EHL problem in which much thinner films occur (<1 μm).

Martin (1916) gave the earliest solution to the problem of a cylinder loaded against a plane as a simplified model of gear tooth lubrication. However, his solution, which considered rigid surfaces and an incompressible isoviscous lubricant, predicted the oil film thickness to be significantly less than the roughness of the best-made gear teeth – which was contrary to in-service observations which showed machining marks on gear teeth to remain after many hours of operation, suggesting full-film lubrication conditions.

Grubin (1949) was the first to consider the combined effects of elastic deflection and the effect of pressure on viscosity. He analysed a heavily loaded EHL "line" contact between cylindrical rollers, assuming that the surfaces were separated by a parallel film, with elastic deflection according to Hertzian theory. His analysis involved a solution of the Reynolds equation in the inlet region of the film only. He developed the following expression for the film thickness in the flattened part of the contact:

$$\frac{h_0}{R} = 1.95 \frac{(\eta_0 \bar{u} \alpha)^{\frac{8}{11}} (E')^{\frac{1}{11}}}{R^{\frac{7}{11}} (w')^{\frac{1}{11}}}$$

The very small dependence of film thickness on load and elastic modulus may be noted. Grubin's work predicted films over an order of magnitude thicker than those predicted by Martin. Petrusevich (1951) subsequently produced three complete solutions, showing more details of the pressure and film profiles, which confirmed the essential features of Grubin's solution for heavily loaded conditions (i.e. an almost parallel film and a pressure distribution close to Hertzian).

By introducing an inverse solution of the Reynolds equation Dowson and Higginson (1959, 1966) obtained a full numerical solution to the EHL line contact problem in

1959 and published a well-known book on EHL later in 1966. Their solutions give detailed results of the pressure and film thickness in the contact over a range of loads and speeds. At heavy loads, their solutions were similar to Grubin's – a parallel film with a pressure distribution close to the Hertzian result. Dowson and Higginson's work introduced two characteristic features not previously seen in EHL solutions – the film constriction and the pressure spike at the exit of the contact.

Subsequent development of EHL solutions has seen the use of more advanced numerical methods such as the Multi-grid method of Venner and Lubrecht (1994), and the theory extended to "point" contacts (such as those occurring between spheres and in ball bearings), thermal effects (Cheng, 1965, Sadeghi & Sui, 1990), non-Newtonian rheology (Sharif *et al.*, 2001, Kim & Sadeghi, 1991) and rough surfaces (Holmes *et al.*, 2003).

1.3 Surface temperatures and heat partition

In practical machinery, where there is relative sliding between the two surfaces the resulting frictionally-generated temperatures are of importance in considerations of wear and damage. The structure and properties of the contacting materials themselves, together with the formation and nature of tribo-chemical films on the surfaces are strongly dependent on temperature. In EHL contacts, the surface temperature has a large influence on the viscosity of the lubricant in the inlet region, and hence the oil film thickness generated. In other areas of study, the effect of surface temperatures at sliding contacts is also of interest. For example, in metal

cutting processes the temperature is of importance in order to estimate both the local strength of the material being cut and the resulting tool wear.

Thus, a means of calculating the surface temperatures at sliding contacts is required in the study of a wide range of tribological processes. The published literature on the subject provides extensive coverage of surface temperature calculations for dry sliding contacts. These are reviewed, and their applicability to lubricated contacts is also discussed. Some work has been published on temperatures at lubricated contacts and this is also reviewed.

1.3.1 Dry sliding contacts

It could be argued that one of the earliest studies of frictional heating of contacts was carried out by early man, using the friction generated between a wooden stick and a stone to light a fire. However, it is not known that early man published any of his findings! Early work, carried out by Blok (1937), Jaeger (1942) and Archard (1959), was based on consideration of the surface temperature rise under a moving source of heat. Blok (1937) considered the case of a semi-infinite body subjected to a concentrated moving heat source, and determined the maximum surface temperature rise at both low and high Peclet numbers. The Peclet number is a dimensionless group which represents the ratio of the speed of the surface to the rate of diffusion of heat into the solid. Thus, for high Peclet numbers the heat will only diffuse a short distance into the solid in the time taken for the surface to move through the contact,

whereas at low Peclet numbers the temperature distribution tends towards the symmetrical, steady-state, result obtained for a stationary source of heat.

Of great importance was the realisation that the temperature rise in the solid surfaces could be considered to consist of two components – a steady-state component and a "flash" or transient component associated with the passage of the surface through the contact. This is illustrated in Figure 1.2.

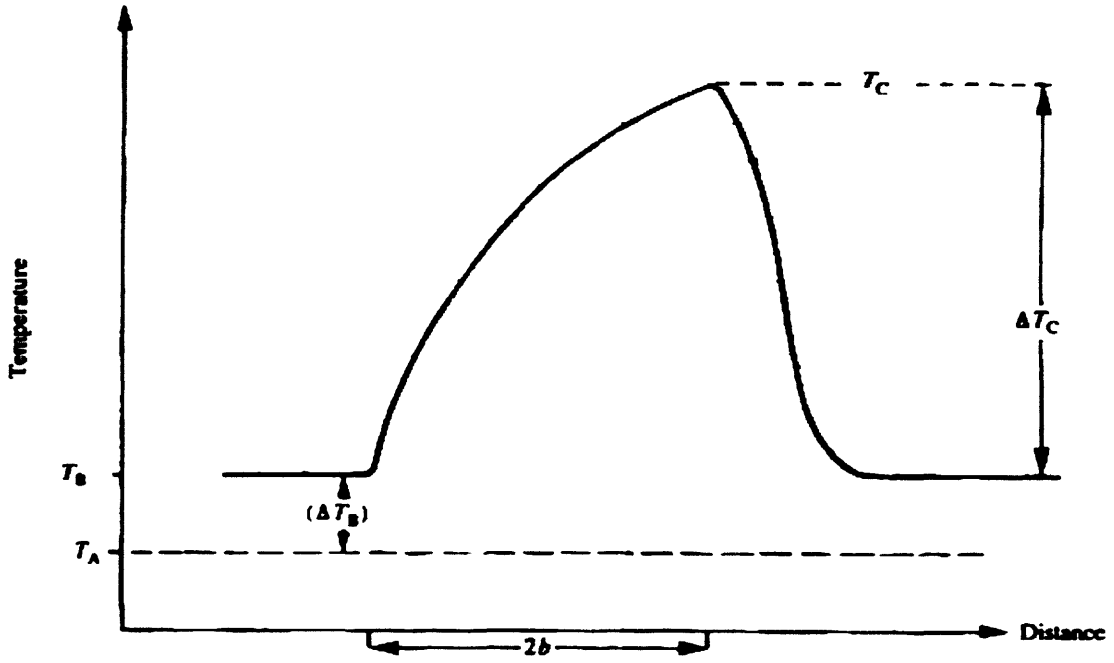

Figure 1.2: Thermal model of a surface within a frictional contact showing the transient temperature rise during the passage of a heat source of width $2b$ (adapted from Olver, 1991)

Thus, the maximum temperature within the contact (T_C) is the sum of a steady-state bulk temperature (T_B) and the flash temperature rise (ΔT_C). The bulk temperature may be estimated using steady-state heat transfer theory, and the flash temperature can be estimated using analytical methods such as the work of Jaeger (1942) on moving sources of heat.

Jaeger (1942) carried out an extensive study of surface temperature rise at sliding contacts using the Blok model. He developed analytical expressions for the flash temperature at both high and low Peclet numbers. In addition, he expressed graphically solutions for the intermediate Peclet number region.

The calculation methods of Blok and Jaeger today form the basis of most methods used to estimate gear contact temperatures (Olver, 1991). In these methods, consideration must be given to the way in which the total frictional heat is partitioned between the two contacting surfaces. On the basis that in a dry contact the two surfaces must be in intimate contact Blok (1937) partitioned heat between the two surfaces such that the maximum contact temperatures on each surface (calculated independently) were equal, whereas Jaeger (1942) considered the *average* temperatures within the contact to be equal, and divided the frictional heat between the two surfaces in order to achieve these equal average temperatures.

Archard (1959) introduced a model for flash temperatures which simplified some of the mathematical complexities and concentrated on physical considerations. In his work, Archard used Blok's maximum temperature method of determining the heat partition. In addition, he introduced the "harmonic mean" method which is based on electrical analogy and stems directly from the assumption of equal maximum temperatures within the contact. This method calculates the average temperature rise at the contact as follows:

$$\frac{1}{\theta_M} = \frac{1}{\theta_A} + \frac{1}{\theta_B}$$

where θ_M is the average interfacial temperature rise; θ_A the temperature rise assuming that all of the frictional heat is supplied to body A; and θ_B the temperature rise assuming all heat is supplied to body B. From this average temperature calculation the required partition of heat between the surfaces may be determined.

In an effort to improve the agreement with experimental results, Greenwood (1991) proposed a method to determine the contact temperature and heat partition, based on the mean of the square of the temperatures:

$$\frac{1}{\theta_M{}^2} = \frac{1}{\theta_A{}^2} + \frac{1}{\theta_B{}^2}$$

This method did not claim to have a physical basis, but Greenwood found that it gave better agreement with experimental results.

A further set of analytical expressions was derived by Kuhlmann-Wilsdorf (1987a) who followed a similar approach to that of Jaeger, and calculated flash temperatures by assuming the average contact temperature within the contact on each surface to be equal. Kuhlmann-Wilsdorf considered a range of speed conditions, including one surface stationary and high and low speed sliding with two moving surfaces. Blok (1969) later returned to his work on contact temperatures in sliding systems. His previous work had considered the flash temperature rise as the surfaces pass through the contact zone and assumed that the bulk temperature was known or could be estimated, and that the bulk temperatures of the two surfaces were equal. Blok extended his earlier theory to allow an estimation of the bulk temperatures using thermal network theory applied to a gearbox or other mechanical system under consideration. He modified his flash temperature theory to remove the restriction that

the bulk temperatures of the two surfaces must be equal. He concluded that his modified theory was more suitable for the analysis of gear teeth and rolling element bearings, where the assumption of equal bulk temperatures may be invalid.

Tian and Kennedy (1993) investigated the contact surface temperature in bodies of finite thickness. They also considered the contact temperature to be made up of a steady-state and a transient (flash) component, and solved the one-dimensional conduction equation to calculate the steady-state bulk temperature. They combined this with a Blok-type approach to calculate the flash temperature, again matching the maximum contact temperatures on each surface in order to determine the heat partition. Further work by Tian and Kennedy (1994) used a Green's function method to calculate both the maximum and average flash temperatures in sliding contacts. They considered a wide range of Peclet numbers, for cases of square, uniform circular and parabolic heat flux distributions. They again used Blok's postulate for the heat partition between the two surfaces, and extended their work to include contact between asperities with plastic deformation taking place.

The commonly used Blok method of determining the heat partition only matches the maximum temperatures within the contact, and therefore the condition that the temperatures at all points on two physically contacting surfaces should be equal is not met, since the peak temperatures occur at different positions within the contact on each surface due to the speed difference.

Bos and Moes (1995) developed a multigrid numerical algorithm which calculates the flash temperature distribution and heat partition by matching the surface temperatures

of the two contacting solids at all points within the contact area, a condition that requires the solution of a singular integral equation. They considered circular, elliptical and arbitrarily shaped contacts. For uniform and semi-elliptical heat flux distributions, they developed functional fits to their numerical results that give flash temperatures as a function of the Peclet numbers of the contacting solids, the conductivity ratio of the two materials and the aspect ratio of the contact. These functional fits showed good agreement (to within 5%) with their numerical results.

Komanduri and Hou (2001) also developed a method which attempted to closely match temperatures at all points within the contact zone. They considered the case of a sleeve bearing as an application for their method, where a rotating shaft is supported by a stationary sleeve bearing. In order to match the temperatures at all points within the contact, they found that a variable rather than a constant partition of the heat had to be adopted. Their analytical method was found to give broad agreement with previously published finite element modelling of the same configuration.

A number of workers have subsequently extended the analytical approaches outlined above to a range of practical applications. Yevtushenko *et.al.* (1996) considered the case of a rotating disk sliding against a stationary pin, which is a common configuration in wear testing machines. They solved the steady-state conduction equation for the pin and disk – simplifying the equation to a one-dimensional axial conduction problem for the pin, and a two dimensional problem for the disk by neglecting variation of temperature through the thickness of the disk. They again used the heat partition criteria so that the average temperatures within the contact on the pin and disk were equal. Their solution used infinite series. Figure 1.3 shows

their calculated disk surface temperatures for a range of Peclet numbers in the form of a dimensionless temperature rise, T*, which is defined as

$$T^* = \frac{KT}{qR}$$

where K is the material thermal conductivity, T is the temperature rise, q is the heat flux and R is the disk radius.

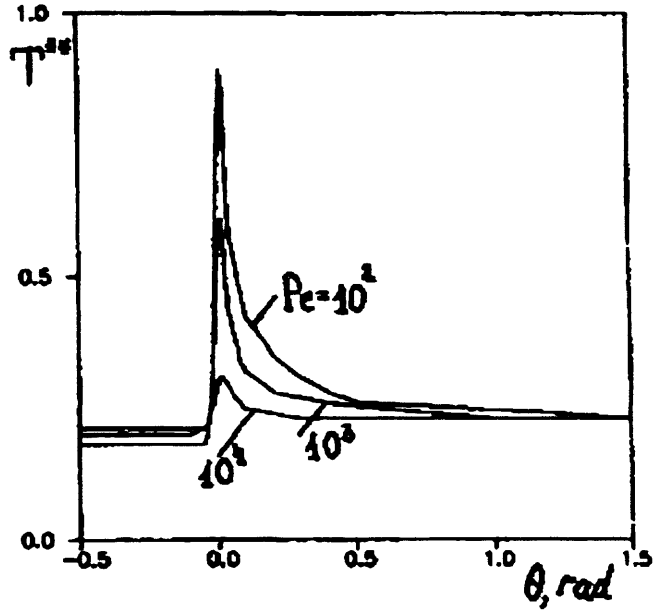

Figure 1.3: Dimensionless disk surface temperature variation around disk for various Peclet numbers (from Yevtuskenko *et.al.*, 1996)

From Figure 1.3, it can be seen that for higher Peclet numbers, the maximum contact temperature decreases as the disk spends less time passing through the contact (and hence spends less time being heated).

Further work on the pin/disk problem was carried out by He and Ovaert (2008) who compared the models of Challen and Dowson (1978) and Harpavat (1974) for the interfacial temperature in a pin on disk test machine. Both models were found to give

good estimates when compared with experimental results, and the relative limitations and validity of the models was discussed.

Lingard (1984) extended the approach of Jaeger and Archard by including additional terms in the equations to take account of junction growth and cold work in the case of sliding asperities where plastic deformation takes place. Results were presented for a wide range of Peclet numbers, and found to be in good agreement with experimentally measured contact temperatures. Figure 1.4 shows the variation of flash temperature with load which Lingard calculated for two different sliding speeds, compared with his experimental temperatures measured under the same conditions using the thermo-electric effect. His experimental work measured the thermo-electric voltage between an aluminium disk and a steel disk in a disk machine.

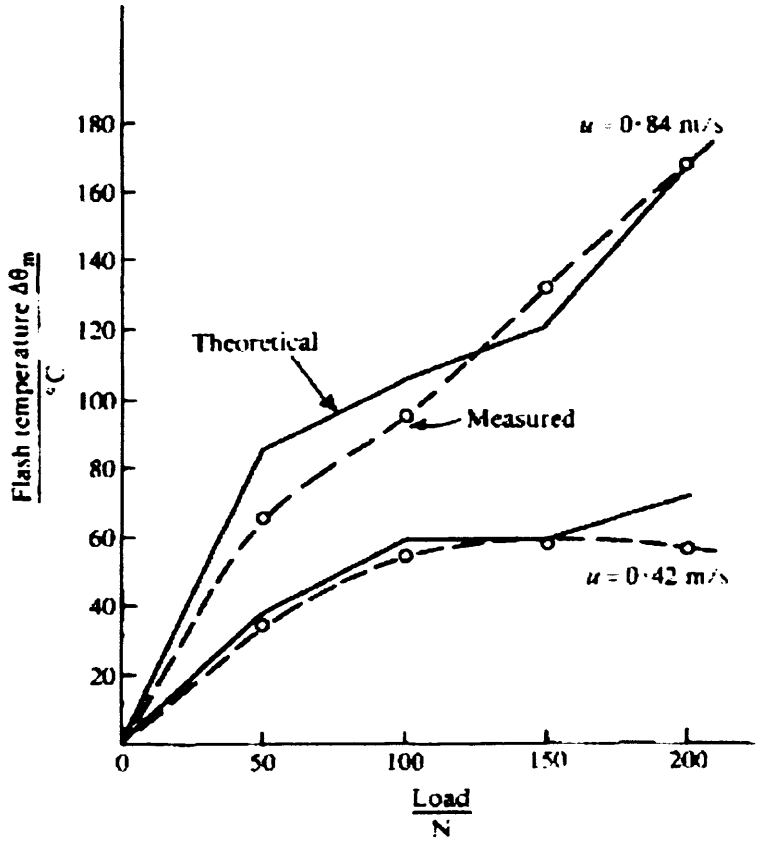

Figure 1.4: Flash temperatures for aluminium sliding on steel (from Lingard, 1984)

Kuhlmann-Wilsdorf (1987b) also considered the flash temperatures at interfacial contact spots subject to plastic deformation, in an extension of her earlier work based on that of Jaeger.

Olver (1991) considered the estimation of bulk and flash temperatures in his work on contact temperatures in various designs of disk machines used for lubricant testing, in order to investigate apparently contradictory results of lubricant tests on different types of disk machine. He considered a variety of disk and shaft geometries, shown in Figure 1.5.

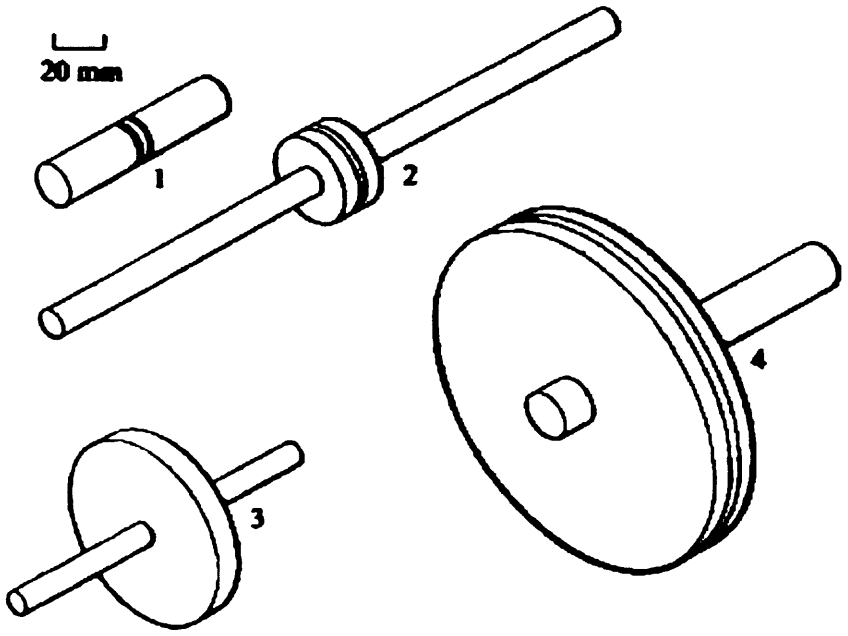

Figure 1.5: Geometry of disks analysed by Olver (1991)

Olver considered the contact temperature to be made up of two components – the bulk and the flash components. His analysis allowed the bulk temperatures of the two disks to be different, and calculated the heat partition by taking the *average* contact

temperatures to be equal. Many of the solutions previously developed for contact temperatures assume the contacting bodies to be insulated at all points outside the contact, whereas Olver's work takes account of convective cooling from the disk and shaft surfaces. He developed analytical expressions for the bulk temperatures for simplified cases where the disk was thin in relation to its diameter, which gives predominantly radial conduction of heat from the running track, and the case of small diameter disks mounted on large shafts, which gives a predominantly axial flow of heat. Olver then carried out finite element studies of the various disk and shaft geometries shown in Figure 4, and compared bulk temperatures calculated using this method with those from the analytical expressions. He found the results to be in good agreement in cases where the geometry approached the idealised cases which his analytical solutions considered. Olver believed his method to offer a useful approximate calculation of contact temperature, but noted that his use of a heat partition method which assumes equal average surface temperatures within the contact may not be appropriate in the case of lubricated contacts with thick films, where a temperature gradient is likely to exist across the oil film. Thermal solutions of the EHL problem which include calculations of the contact temperatures are discussed later in this review.

Many workers have considered the case of sliding contacts with rough surfaces, where actual contact takes place over many small asperities within the nominal region of contact, rather than at all points within the contact region. An early investigation by Barber (1967) developed an analytical expression for the heat conduction in a single asperity interaction, and then extended this solution to cover a case of a contact with multiple asperity interactions of a known number and size distribution. The paper

gives an example calculation based on an assumed exponential distribution of asperity contact size.

Vick and Furey (2001) investigated the temperature rise due to sliding contact between surfaces with multiple, interacting asperities. They developed a solution based on the Green's function method for the basic problem of two half-space regions in sliding contact with an arbitrary arrangement of rectangular asperities. The model partitions heat between the surfaces by ensuring that the surface temperatures are the same on both surfaces at points in contact. They then used their model to study the effect of the number, size, spacing and orientation of the contacts. They found the contact temperatures to be highly sensitive to the number and spacing of the asperities, such that the subdivision of a nominal contact into small, separated asperity contacts significantly reduced the contact temperatures. However, it should be noted that their separated asperities model has the same total area as the original contact, which is unlike the normal physical situation where the area of asperity contact is much smaller than the nominal contact area. This situation would be expected to lead to higher temperatures developing in the asperity contact areas. Their results for two asperity contacts, one downstream of the other, may be seen in Figure 1.6, where the downstream asperity can be seen to reach a higher temperature.

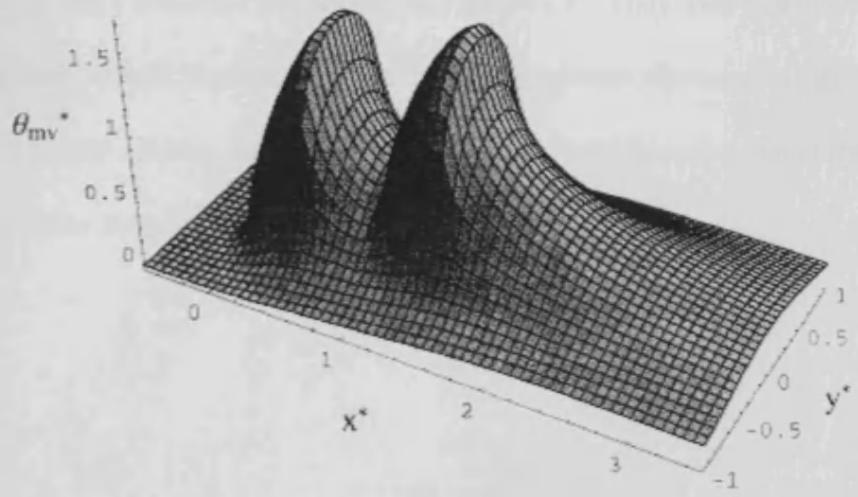

Figure 1.6: Surface temperature rise for a system with two asperities (from Vick and Furey, 2001)

Salti and Laraqi (1999) developed a model for a similar array of rectangular asperities in steady-state sliding against a smooth surface. They solved the conduction equation numerically in an iterative scheme, and also solved the heat partition problem by matching temperatures on both surfaces at points in contact. Their model was compared to an analytical solution for an array of rectangular heat sources on a semi-infinite body, and found to give good agreement.

Gao *et.al.* (2000) modelled the flash temperatures at the contact between a sphere with real roughness and a smooth flat. They used an FFT-based model, which was based on the solution developed by Carslaw and Jaeger (1959) for the temperature rise of a body due to a moving point heat source. The model partitioned heat between the two surfaces in order to ensure that points in contact were at equal temperatures. Their model was validated by comparing results obtained for smooth surfaces from their model with those of Carslaw and Jaeger. Typical steady-state dimensionless temperature rises from their model for the case of a transversely rough surface (where the predominant direction of the roughness is perpendicular to the sliding direction)

with sliding in the x direction are shown in Figure 1.7. They also considered the case of longitudinally rough surfaces, where the predominant direction of the roughness was parallel to the sliding direction, and found the temperatures developed in these cases to be higher than those for transverse roughness.

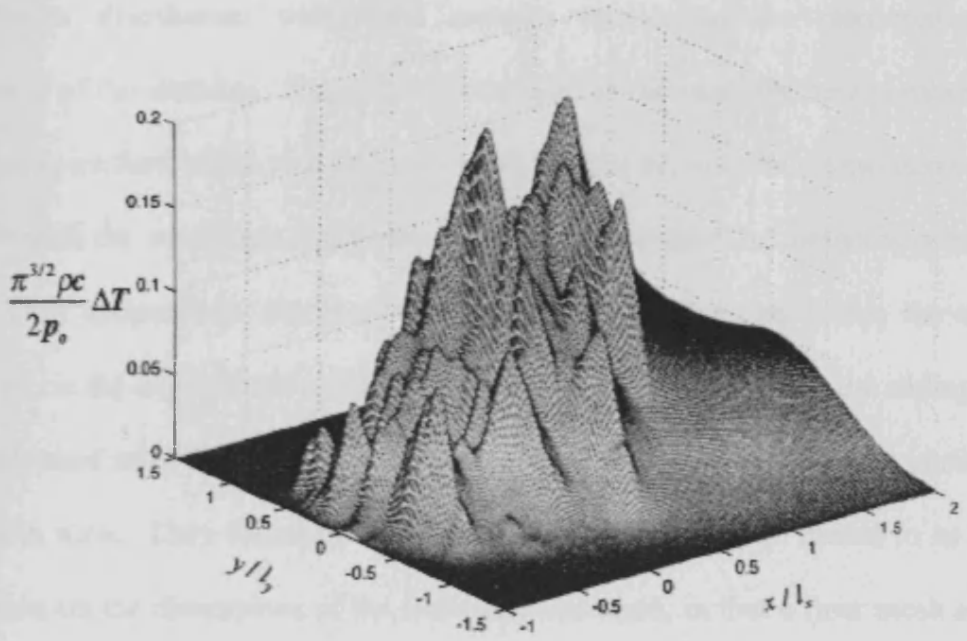

Figure 1.7: Flash temperature for a transversely rough surface (from Gao *et.al.*, 2000)

Similar models of sliding surfaces using real roughness have been presented by Varadi *et.al.* (1998) who developed a transient finite element thermal model to calculate contact temperatures between a rough steel surface and carbon fibre/PEEK composite surfaces. Their model included elastic-plastic deformation of the composite surface, and included the necessary anisotropic material and thermal conductivity treatments. Their model partitioned the frictional heat flux between the bodies as necessary to maintain equal temperatures at points in contact.

Lestyan *et.al.* (2007) performed a multi-scale finite element thermal analysis of a dry-sliding test rig in which the friction and wear properties of an alumina-steel friction pair were being investigated. They developed a macro-scale model of the test rig components which enabled them to calculate the bulk and average contact temperatures. A further contact-scale model was used to investigate the detailed temperature distribution within the contact, considering the measured surface roughness of the surfaces. Their model was used to calculate the heat partition using an iterative method which repeated the calculations at an individual time-step until the difference in the maximum temperatures of the two surfaces in contact was less than 1°C. They assumed the heat partition to be equal at all points within the contact. However, in the experiment which their model was used to simulate, the sliding speed was increased over the course of the test, and so they allowed the heat partition to vary with time. They found the results from their contact-scale model to be highly dependent on the dimensions of the finite element mesh, in that a finer mesh allowed a more accurate discretization of the surface roughness and hence gave a more detailed temperature distribution.

Aside from the consideration of rough surfaces, numerical methods have been applied to the thermal modelling of sliding contact in a number of other cases. For example, Kennedy (1981) used the finite element method to study temperatures in a range of sliding systems – *viz.* dry bronze bearings, plastic sleeve bearings, and rubbing labyrinth seals. Kennedy's model had a number of advantages. Most significantly, the artificial partitioning of heat was not necessary, as heat generated at the contact nodes due to friction was allowed to flow naturally into the adjacent elements on either side of the contact interface. In addition, more complex geometry and material

configurations could be modelled with more accuracy than the analytical solutions which contain inherent simplifications. Kennedy found that his model gave good agreement with experimental results in the cases he investigated.

A further application of finite element modelling was reported by Abukhshim *et.al.* (2005) who used a commercial finite element code to model the thermal response of a cutting tool used in a high speed lathe. The model was subject to convective cooling over the body of the tool, with a frictional heat source applied at the cutting tip. The total frictional heat was obtained from torque measurements made on a suitably instrumented lathe. In addition, temperature measurements were made adjacent to the cutting edge of the tool. The heat flux applied to the cutting tip was adjusted until the calculated temperatures in the cutting tool matched those recorded experimentally. In this way the partition of heat between the work-piece and the cutting tool was determined by direct reference to experimental measurements.

A further area of investigation in which flash temperatures are important is concerned with the wheel/rail interface in the railway industry, since excessive temperatures generated during a wheel slide can lead to a phase transformation to brittle martensite within the wheel or rail material, leading to cracking and failure. Knothe and Liebelt (1995) considered a wheel sliding along a rail. Their model used a Green's function method to solve the conduction equation for the rail. They considered cases of both uniform pressure distribution within the wheel/rail contact, and elliptical Hertzian pressure distribution. Their model assumed the frictional heat to be proportional to the pressure distribution, with a fixed coefficient of friction. They found that temperatures on the rail surface did not exceed 500°C, even when the model was

modified to include the effects of surface roughness. However, their model arbitrarily partitioned heat between the wheel and rail such that all of the heat generated at the sliding contact was conducted into the rail. They argued that this was realistic since the rail was a much colder body than the wheel and that un-heated rail material was constantly arriving at the inlet to the contact.

Kennedy *et.al.* (2006) published finite-element based results which were broadly in agreement with the assumption of Knothe and Liebelt (1995) that all of the frictional heat flowed into the rail. They used a commercial finite element code (ABAQUS) to model a wheel sliding along a rail, with frictional heat generated at the contact between the two bodies. Their model did not have any inherent assumptions regarding the partition of heat between the two bodies, but allowed heat to flow from the contact into the two bodies according to the physics of the problem. They found that, after a very short time from the start of the wheel slide, the heat partition coefficient (defined as the amount of heat passing into the rail) was above 0.9 for all points within the contact. Their results predicted that temperatures were generated above the Martensite transition temperature (approximately 750°C) for the sliding conditions which they analysed, leading to concern that cracking and spalling could result.

Further finite element-based thermal modelling of the wheel/rail contact problem was carried out by Linck *et.al.* (2006) who investigated the effect of dynamic instabilities on the sliding of a wheel on a rail. Their finite-element model used an elasto-plastic material model for the rail, and evaluated the resulting stick-slip behaviour of the wheel sliding along the rail. Their model was used to obtain the transient

temperatures which developed at the contact region under these conditions, and dealt with the partition of frictional heat in a similar manner to the work of Kennedy (2006). They found that the effect of the stick-slip behaviour was to increase the calculated maximum contact temperature rise by about one-third compared to that calculated without such behaviour under steady-state sliding conditions.

Tudor and Khonsari (2006) considered an analytical solution for the case of a wheel under steady-state braking, which was subject to heat inputs due to sliding contact between brake shoes and the wheel, and due to the rolling contact between the wheel and rail. They considered three heat partition coefficients, for each of the contacts between the wheel, the rail and the two brake shoes. The heat generated at each of these contacts was partitioned in order to match average temperatures at each of the surfaces within the contact region. Their results showed that, as expected, the amount of frictional heat partitioned into the wheel increased as the convective cooling from the wheel surface was increased, allowing more heat to be dissipated from its surface.

1.3.2 Lubricated sliding contacts

The majority of the solutions outlined above deal with the division of frictional heat between the surfaces in contact by assuming that either the *maximum* or *average* temperatures on the surfaces are equal or, in the numerical solutions, by matching temperatures on the surfaces at all points in contact. This may be a plausible way in which to proceed in the case of dry contacts, but the presence of an oil film in

lubricated contacts places this assumption of the equality of temperatures at each surface in some doubt, as recognised by Olver (1991).

Fluid film lubrication of heavily loaded concentrated contacts is achieved by means of the EHL mechanism where the pressures developed in the lubricant lead to a significant increase in viscosity together with elastic deflection of the surfaces. When sliding of the surfaces occurs, heat is generated within the film by shearing and compressive heating of the lubricant. The dominant heat transfer mechanism is that of conduction perpendicular to the film. If heat is generated throughout the thickness of the film, the highest temperatures are developed within the film itself, and the temperature gradient necessary to transport the heat by conduction to the surfaces ensures that the surfaces are at lower and generally different temperatures. Thus, the lubricant film must be considered in any study of thermal behaviour of lubricated contacts. In this section, the work of various authors who have considered the oil film in more detail is discussed.

An early analytical analysis which considered the oil film and removed the restriction of equal surface temperatures was published by Merritt (1962). His work was based on that of Blok, but he included the partition of heat between the two surfaces as a variable, which could be adjusted to vary the surface temperatures of the two surfaces. He then used this theory to analyse the results of some disk-machine experiments. He found that more of the heat (around 60%) flowed into the faster disk. In addition, both measured temperatures and his calculations showed that the faster disk achieved a higher surface temperature than the slower disk. Merritt went on to consider conceptually the heat generation and temperature gradients within the oil film, and

found that he could not reconcile the measured and calculated heat partition and surface temperatures with his assumption that the rate of heat generation was uniform across the film thickness. He concluded that there must exist some asymmetry in the mechanism of heat generation within the oil film.

An early attempt to consider the thermal EHL problem was reported by Manton *et.al.* (1967) who developed a numerical thermal model for heavily loaded line contacts. Their model solved the energy equation, and included the variation of viscosity with pressure and temperature. However, in order to simplify the analysis, they considered a parallel film with a film thickness given by the Dowson, Higginson and Whitaker formula (1962) and a semi-elliptical (Hertzian) pressure distribution. They considered these simplifications, which were made to greatly simplify the numerical work, to be justified as previous work had reported that under the heavily loaded conditions which they considered the film thickness was relatively constant except for the exit constriction, and the pressure distribution only differed significantly from the Hertzian form in the corresponding exit pressure spike and in the inlet sweep. Their model used the surface bulk temperatures as inlet boundary conditions, and then calculated oil film and surface temperatures (and hence heat partition). A typical temperature distribution through the contact is reproduced in Figure 1.8.

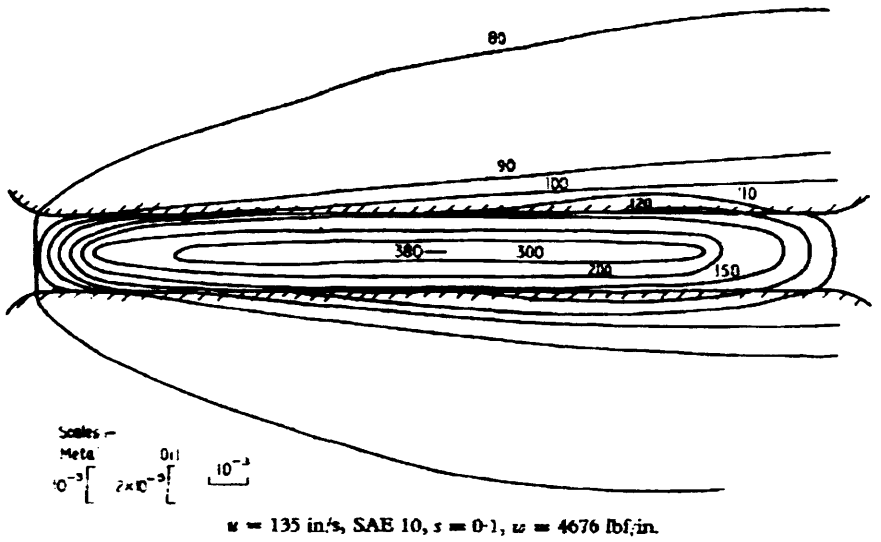

Figure 1.8: Typical temperature distribution in a contact (from Manton *et.al.*, 1967) – N.B. temperature contours given in °F

They initially produced results using equal inlet (bulk) surface temperatures, and investigated the effects of viscosity on the temperatures and heat partition. They found that, for equal inlet temperatures, more heat passed into the slower surface. However, they then used their model to investigate the experimental results of Merritt, where the bulk temperatures were not equal. Figure 1.9 shows the calculated oil film temperature profiles at the contact centre-line when the bulk temperature of the faster surface is increased above that of the slower surface. In Figure 1.9, metal 2 is the slower surface and metal 1 is the faster surface. In profile 1, the inlet temperatures are equal (both 80°F) and the oil film peak temperature is nearer the slower surface, resulting in more heat flowing into the slower surface. In profile 2, the inlet temperature of the faster surface (metal 1) is increased to 90°F, with the result that the temperature peak shifts towards the faster surface. The inlet temperature of the faster surface was then increased again to 100°F, with the cross-film temperature profile shown at profile 3 in Figure 1.9. The peak temperature is clearly shifted towards the faster surface, with a resulting higher surface temperature. The temperature gradient

(and hence heat flow) towards the faster surface is much steeper than that of the slower surface.

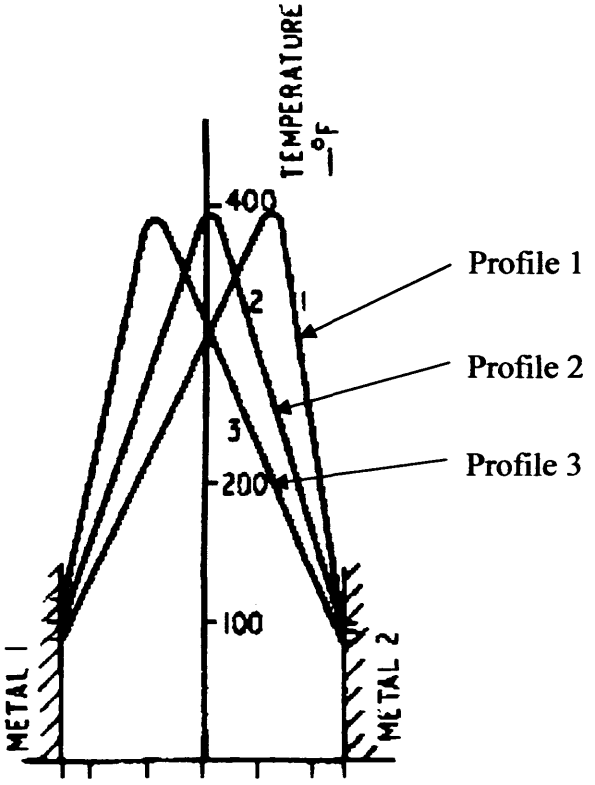

Figure 1.9: Variation of oil film temperature profile with inlet temperature of faster surface (from Manton *et.al.*, 1967)

The heat partition results calculated from the temperature profiles are shown in Figure 1.10. It can clearly be seen that, as the inlet temperature of the faster surface is increased compared to that of the slower surface, more heat flows into the faster surface. This is in accordance with the experimental results reported by Merritt (1962).

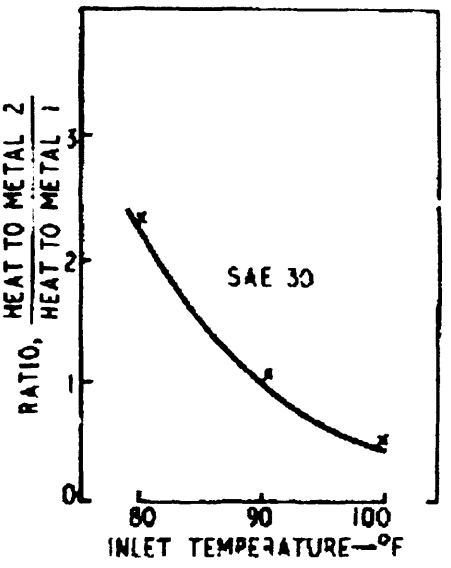

Figure 1.10: Variation of heat partition with faster surface inlet temperature (from Manton *et.al.*, 1967)

Olver (1994) presented a model for film thickness and traction in disk machines and gearboxes, which used the Dowson and Higginson formula and empirically-derived relations for the variation of viscosity and density with temperature and for traction in sliding contacts, in conjunction with his earlier work on temperatures in disk machines (Olver, 1991) to calculate the film thickness in a range of disk machines and gear contacts. He investigated the effect of load and speed variations on the calculated temperatures. However, his work still partitioned the frictional heat based on the assumption that the average contact temperatures were equal for the two surfaces.

In more recent work, Olver and Spikes (1998) developed a simplified non-Newtonian EHL model to calculate the mean traction coefficient in EHL contacts. Their model used an approximate analytical solution (using an Eyring-type rheological model) to calculate the mean shear stress in the oil film, and evaluated the rheological properties

of the lubricant at the mean contact pressure and oil film temperature. The temperatures were calculated by assuming that all of the heat was generated by shearing at the centre of the lubricant film (i.e. along the mid-film plane), and using thermal network theory to model the film and solid bodies as a series of thermal resistances, as shown in Figure 1.11. This leads to an iterative solution for the traction coefficient and oil temperatures. However, their assumption of mid-film shearing led to approximately equal division of heat between the surfaces under the conditions of relatively low sliding which they considered.

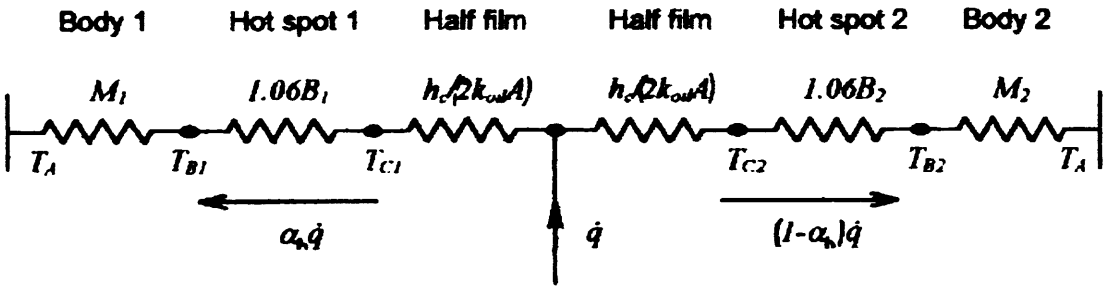

Figure 1.11: Thermal network model of oil film and surfaces (from Olver and Spikes, 1998)

Although the simplified models of Manton *et.al.* and Olver and Spikes offer some insight into the thermal behaviour of the oil film, in order to obtain a more complete picture a full thermal EHL analysis is required. Such an analysis solves the elastic deflection, Reynolds and energy equations for the oil film and contacting solids, and includes the effects of temperature on lubricant viscosity and density. This approach removes the need for the simplifying assumptions, such as those of parallel film thickness and Hertzian pressure distribution, used by Manton *et.al.*

Cheng (1965) was one of the first researchers to produce a numerical solution to the thermal EHL problem. However, the loads considered in this work were extremely low and hence the influence of thermal effects on both film shape and thickness were

insignificant. Later, Wang and Zhang (1987) presented a simplified thermal non-Newtonian model for line contacts, in which cross-film variations of viscosity and density were neglected, and only the mean temperature profile was calculated.

Sadeghi and Dow (1987) developed a thermal line contact EHL model, using Newtonian rheology. They used surface temperature profiles measured using a thin-film temperature transducer in a disk machine as boundary conditions in their finite-difference numerical solution of the energy equation for the oil film. They studied conditions of both pure rolling and around 5% sliding, and found that in the sliding case significant temperature rises were calculated in the oil film due to shearing of the lubricant, whereas in the pure rolling case, the temperature rises were due to compressive heating of the lubricant and were less severe.

Subsequent work by Sadeghi and Sui (1990) further developed the line contact model, removing the need to use measured surface temperatures as boundary conditions for the energy equation. They used a one-dimensional conduction model for the heat-flow into the solids, allowing the calculation of surface temperatures. Their model initially calculated the isothermal pressure and film thickness, using the Newton-Raphson technique to solve the Reynolds and elasticity equations simultaneously. These values were then used to solve the energy equation using the control volume finite element method to give the temperature field within the lubricant film and on the solid surfaces. The effect of the calculated lubricant temperatures on the viscosity and density was then introduced, and the calculation of film thickness and pressure repeated. This process continued iteratively until the film thickness, pressure and temperatures converged. Sadeghi and Sui used their model to study heavily loaded

line contacts at various kinematic conditions from pure rolling to 30% sliding. They found that, as sliding was increased, the thermal effects led to a slight decrease (of the order of 10% or less) in the film thickness. This was expected, since the film thickness is largely governed by the viscosity of the oil in the inlet region. However, the effect of sliding on maximum oil film temperature rise was found to be significant, with (for the conditions they considered) a temperature rise of around 10°C under pure rolling conditions, whereas 30% sliding gave a calculated temperature rise of around 100°C. This significant temperature rise was essentially due to frictional heat generated by shearing of the lubricant. Sui and Sadeghi (1991) later extended their model to include non-Newtonian rheology, using an Eyring-type rheological model.

Wolff *et.al.* (1992) developed a line contact model which was very similar to that of Sui and Sadeghi (1990) in both its formulation and solution method. They used the model to investigate the effect of various pressure/temperature/viscosity relations, and discussed the relative merits of the various models in reproducing experimental results.

Sharif *et al.* (2001, 2004) developed a thermal non-Newtonian EHL model. Their formulation of the energy equation considered both shear heating and compressive heating or cooling, as well as convective heat transfer within the oil film. They used their model to investigate the lubrication of worm gears (Sharif *et al.*, 2001), and in a later formulation, where the elastic deflection equation is expressed in differential form to reduce the computational overheads, to investigate traction in a toroidal-type transmission (Sharif *et al.*, 2004).

Recent work has seen thermal EHL models extended to consider the rolling/sliding contact of rough surfaces. Chang (1992) incorporated rough surfaces (both sinusoidal and measured roughness) into a micro-EHL line-contact solver. Zhu and Hu (2001) and Deolalikar *et al.* (2008) considered point contacts with real roughness, and presented results for surface temperature rise due to both heating from the lubricant and due to frictional contact between asperities.

Whilst numerical solutions of the thermal EHL problem have been widely applied to a range of problems, very little work appears to have been carried out using these models on the partition of heat between surfaces when a lubricant film is present. Some previous work in this area was carried out by the author (Clarke *et al.*, 2006), and is outlined here in detail as it provides a relevant background to the work reported in this thesis.

The work involved the development of numerical heat conduction models to calculate the bulk and total contact temperatures in disk machine experiments carried out by Patching *et al.* (1995) in an investigation of scuffing. Patching's experimental work used a special high-speed power recirculating two-disk machine using crowned disks in order to eliminate edge effects. The disk machine was subsequently developed for the work reported in this thesis and thus the reader is directed to Chapter 3 for a full description. Each disk was fitted with an embedded thermocouple, 3.2mm below the running track on the disk centre-line, and temperature was continuously recorded during an experiment. In addition, friction force at the contact was measured using a torque transducer fitted in the slow disk drive shaft. Typical recorded data from a test are shown in Figure 1.12. In the experimental procedure the load applied between the

disks was increased in steps corresponding to 0.1 GPa increases in maximum Hertzian pressure at three minute intervals. The resulting friction force also increases as a result of the load changes. The corresponding increase in the disk bulk temperatures can also be seen, as can the friction (and temperature) spike when scuffing occurs.

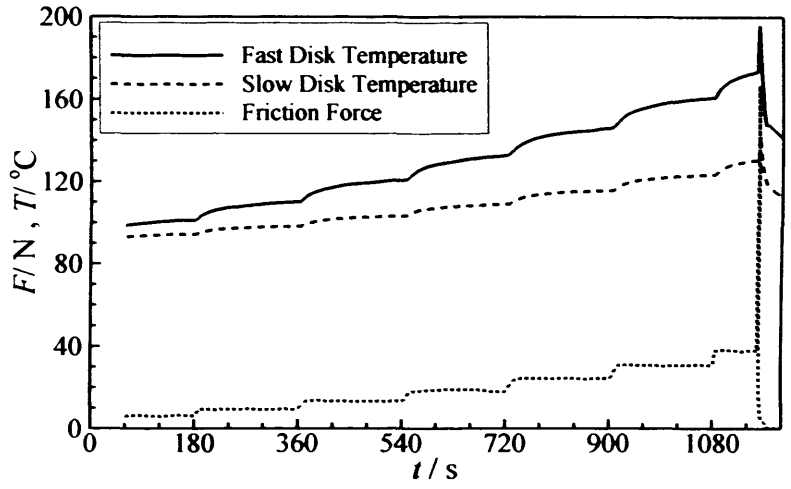

Figure 1.12: Chart record of experiment 2-2 showing measured temperatures and friction force (from Clarke *et al.*, 2006)

The author developed a heat conduction model for the disk and shaft of the test machine, by solving the conduction equation for the disk/shaft combinations, which are illustrated in Figure 1.13, with suitable boundary conditions. The problem was simplified to the form indicated by the broken lines in Figure 1.13. These simplified shafts are symmetrical and have the same thermal mass as the shafts being modelled.

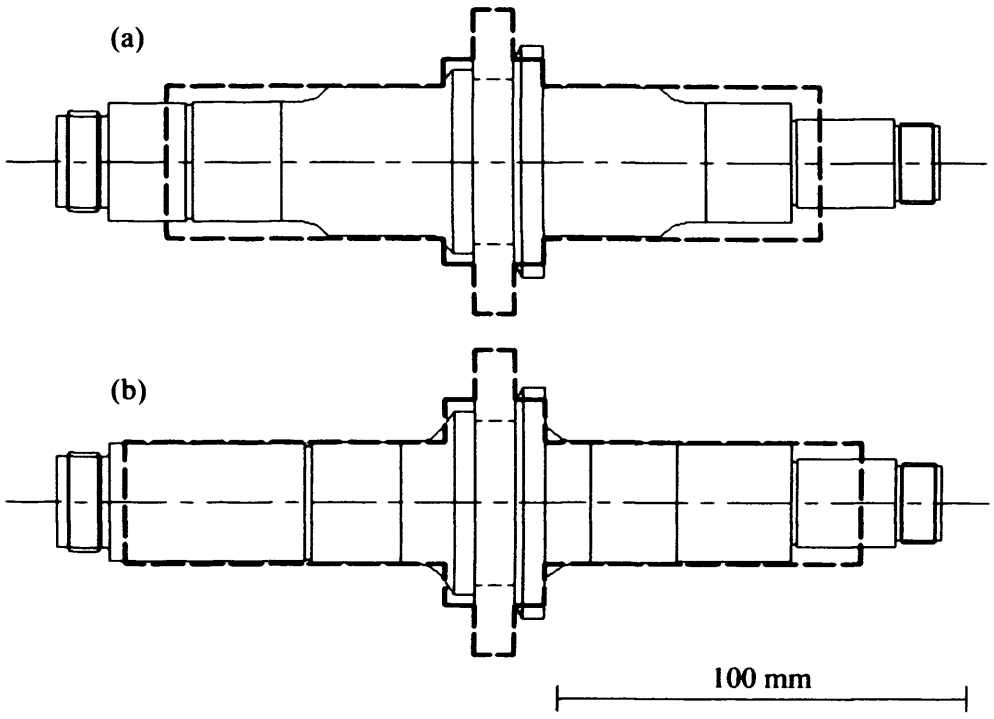

Figure 1.13: Disk machine disks and shafts: (a) Faster shaft and disk (b) Slower shaft and disk. Also shown outlines in broken lines is the simplified geometry modelled (from Clarke *et al.*, 2006)

The temperature developed within the disk and shaft satisfies the differential equation of heat conduction in polar co-ordinates:

$$\frac{\partial T}{\partial t} = \alpha\left[\frac{1}{r}\frac{\partial T}{\partial r} + \frac{\partial^2 T}{\partial r^2} + \frac{\partial^2 T}{\partial z^2} + \frac{1}{r^2}\frac{\partial^2 T}{\partial \theta^2}\right] + \omega\frac{\partial T}{\partial \theta} \tag{1.1}$$

where the axes are fixed in space, and ω is the angular velocity of the disk about its rotational axis which coincides with the z axis. The equation was simplified in two ways for the modelling work. Firstly, in order to calculate the average (over each rotation) transient temperatures in the disk/shaft cross section the frictional heat was assumed to be applied uniformly around the disk's running track. This disregarded the temperature variation around the disk's circumference. Thus, equation (1.1) was simplified to:

$$\frac{\partial T}{\partial t} = \alpha\left[\frac{1}{r}\frac{\partial T}{\partial r} + \frac{\partial^2 T}{\partial r^2} + \frac{\partial^2 T}{\partial z^2}\right] \tag{1.2}$$

The author solved this equation using a finite-difference method for both the fast and slow shafts. The total heat generated at the contact between the disks was known from the experimental friction measurements, but the question of how the heat was partitioned between the two disks had to be addressed. It was assumed that all of the heat passed into one or other of the disks, and a heat partition coefficient, β, was defined which represented the fraction of the total frictional heat which passed into the faster disk. The partition of heat between the disks was varied by adjustment of parameter β at each load stage. The value of β was taken as constant for each load stage and set so as to match the calculated temperatures at the thermocouple positions to those recorded in the experimental work at the end of the three minute load stage. Both disks were analyzed separately, but the total heat supplied to them corresponded to the measured frictional heating with proportions β and $1-\beta$ applied to the fast and slow disks, respectively. Thus, a series of β values was determined for each of the nine experiments considered.

The calculated temperatures at the thermocouple positions and at the centre-line of the running track are shown in Figure 1.14, where the good agreement with the measured temperatures may be seen by comparison with Figure 1.12. The tests referred to in this work (such as test 2-2 shown in Figures 1.14 and 1.12) are numbered to be consistent with those of Patching, on whose results the modelling was based.

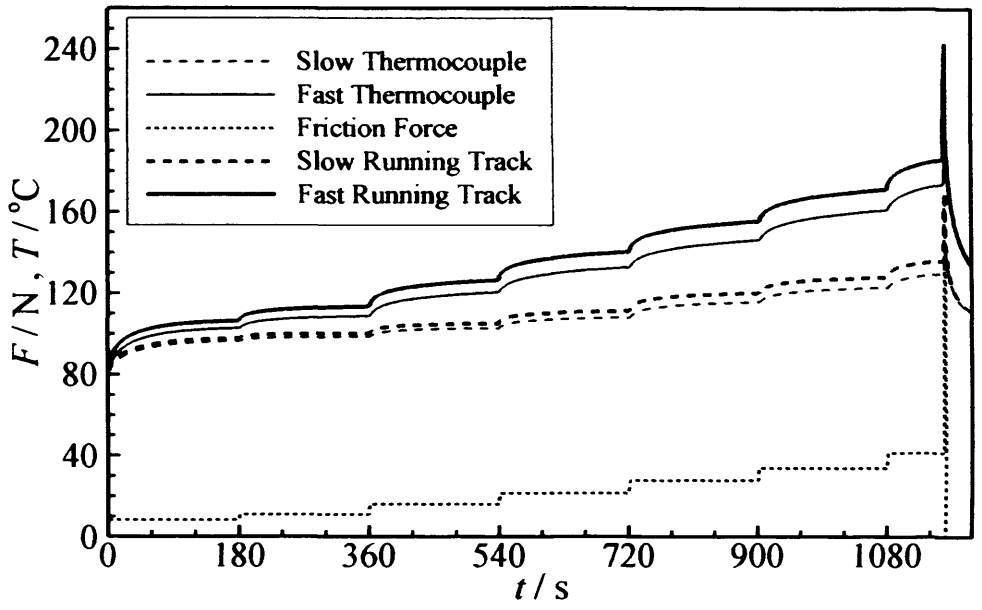

Figure 1.14: Results of Clarke *et al.*'s transient analysis of test 2-2 showing the calculated running track and thermocouple position temperatures for the disks and the assumed friction force taken from Fig. 1.12, adjusted for bearing friction

The calculated temperature distributions in both disk/shafts is reproduced in Figure 1.15, for the end of the last complete load stage prior to scuffing in Test 2-2, at t = 1080 seconds. Note that, due to the symmetry of the simplified shafts only one-quarter of the each disk/shaft cross section was modelled. It can clearly be seen that the average temperatures in the faster disk/shaft are higher than those in the slower disk/shaft. Given the higher rotational speed (and therefore greater convective cooling) of the faster shaft and its higher thermal mass, it is clear that more heat must flow into the faster disk to generate the temperatures shown.

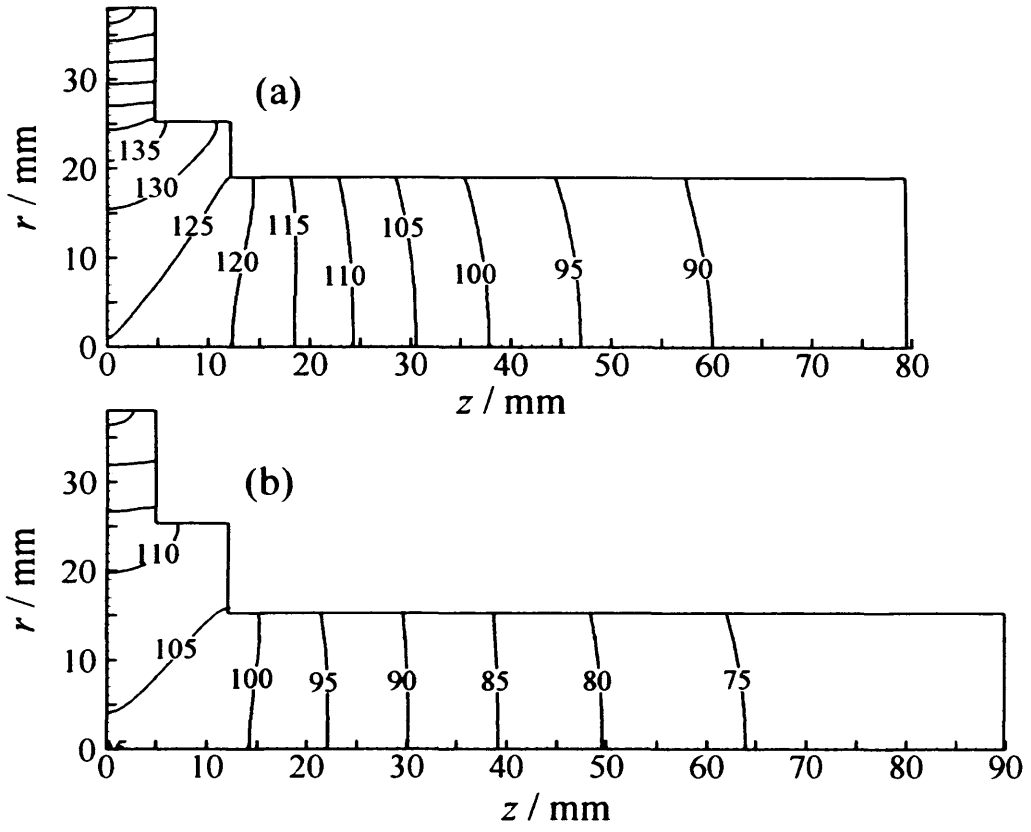

Figure 1.15: Calculated temperature distributions in (a) faster and (b) slower disk/shaft from Clarke *et al.* (2006)

The author investigated the relationship between their calculated heat partition parameter and a range of variables, such as Hertzian contact pressure, load, frictional power, and surface temperature difference between disks. The strongest relationship was found to be with the product of surface temperature difference between the disks and the sliding velocity ($\Delta T.u_s$) where the 62 values of β obtained fell on or close to a single curve, as reproduced in Fig. 1.16. It was suggested that the significance of the term ΔT is that it gives a measure of the temperature gradient across the film for a given film thickness and is thus related to heat conduction across the film. The sliding velocity u_s is proportional to the frictional power dissipated in the contact for fixed values of load and coefficient of friction.

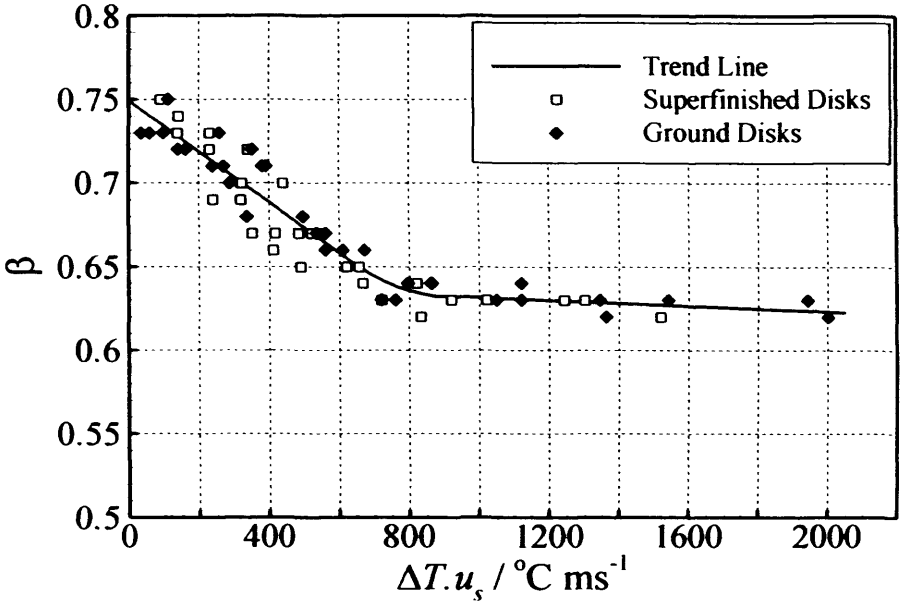

Figure 1.16: Heat partition calculated by Clarke *et al.* (2006)

Figure 1.16 shows that the heat partition required to match the modelled and experimentally measured temperatures was generally found to vary between $\beta \approx 0.75$ (a 75%/25% split between the fast and slow disks, respectively) at the beginning of the experiments and $\beta \approx 0.6$ at the end. In all of the load cases and experiments modelled, the heat partition was found to favour the faster disk.

A further model was then developed, which only considered an outer annular layer of the disk in order to examine the circumferential variation of temperature during one rotation of the disk. Due to the high speed conditions of Patching's experiments, the circumferential variation in disk temperature was confined to a shallow layer of disk close to the running track. Equation (1.1) was simplified by neglecting the variation of temperature with time to become

$$\left[\frac{1}{r}\frac{\partial T}{\partial r}+\frac{\partial^2 T}{\partial r^2}+\frac{\partial^2 T}{\partial z^2}+\frac{1}{r^2}\frac{\partial^2 T}{\partial \theta^2}\right]+\frac{\omega}{\alpha}\frac{\partial T}{\partial \theta}=0 \qquad (1.3)$$

This analysis was applied only to times during the experiment where the temperatures reached steady or near-steady state conditions at the end of each load stage. Boundary conditions for this equation were obtained from the results of the two-dimensional average temperature model, and the heat partition (which was already known from the earlier results) with the heat flux being assumed to follow a semi-elliptical distribution. The circumferential running track centre-line temperature profiles for t = 1080 seconds are shown in Figure 1.17:

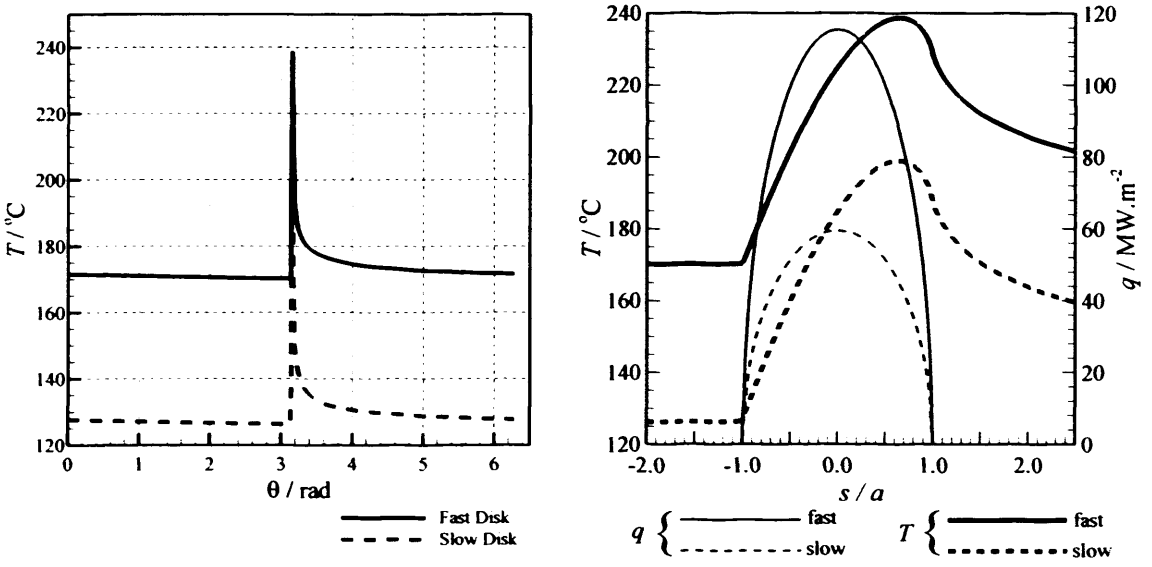

Figure 1.17: Circumferential variation of disk surface temperature for (left) whole disk and (right) the contact region (from Clarke *et al.*, 2006)

It may be seen in Figure 1.17 that the surface temperatures of the contacting solids calculated by consideration of conduction within the solids are not equal – in apparent contradiction of the theory of Blok. However, the work contains some uncertainty with regard to the convective cooling coefficients assumed for the surfaces of the disk and shaft. These coefficients were estimated based on published results, but remain a source of uncertainty in the results. However, the author concluded that the

combination of a suitably instrumented disk machine with conduction modelling of the solids could offer a useful means of studying the rheological and traction behaviour of lubricants, and it is this conclusion which this thesis aims to investigate.

Thermal Elastohydrodynamic modelling of heat partition in rolling/sliding contacts

2.1 Introduction

This chapter describes the steady-state thermal EHL model developed by the Cardiff Tribology Group and used by the author to model the experiments of Patching. The model was used to analyse the partition of heat between the contacting surfaces in order to develop the author's previous work, which concluded that the majority of the frictional heat flows into the faster disk, and investigate the rheological mechanisms by which this division of heat may be achieved. Further details of the work of Clarke *et.al.* (2006) may be found in the review of relevant literature in Chapter 1. A description of the operation of the numerical solver is given, together with details of the various rheological and viscosity models which were investigated.

2.2 Point Contact Thermal EHL Model

The model used is effectively that developed by Sharif *et.al* (2001, 2004) which includes both shear heating and compressive heating/cooling in its formulation, together with convective heat transfer within the oil film. The governing equations are now examined in turn.

2.2.1 Reynolds equation

The Reynolds equation describes the hydrodynamic aspects of the steady-state EHL mechanism. In the case of the disk machine used by Patching, entrainment occurs in the circumferential direction, so the Reynolds equation may be simplified as follows by considering sliding and entrainment to only take place in the x direction:

$$\frac{\partial}{\partial x}\left\{\sigma_x \frac{\partial p}{\partial x}\right\}+\frac{\partial}{\partial y}\left\{\sigma_y \frac{\partial p}{\partial y}\right\}=\frac{\partial}{\partial x}(\rho \hat{u} h) \tag{2.1}$$

The flow factors, σ_x and σ_y are obtained from the appropriate non-Newtonian rheological model, as described in section 2.2.8.

2.2.2 Elastic deflection equation

The surface elastic deflection is given based on the usual assumption that the bodies are semi-infinite. The film thickness is then given by equation (2.2)

$$h(x,y)=h_0+\frac{x^2}{2R_x}+\frac{y^2}{2R_y}+\frac{2}{\pi E'}\iint_A \frac{p(x',y')}{\sqrt{(x'-x)^2+(y'-y)^2}}dx'dy' \tag{2.2}$$

where A is the area over which the pressure acts on the surfaces. In the solution scheme the deflection equation takes the differential form developed by Holmes *et al.* (2003) and the equation is discretized as:

$$\frac{\partial^2 h(x_i, y_j)}{\partial x^2} + \frac{\partial^2 h(x_i, y_j)}{\partial y^2} = \frac{1}{R_x} + \frac{1}{R_y} + \frac{2}{\pi E'} \sum_{\text{all k,l}} f_{k-i,l-j} p_{k,l} \tag{2.3}$$

where $f_{i,j}$ are weighting functions for the influence of pressure on the deflection Laplacian, and are evaluated as described by Evans and Hughes (2000). These weighting functions decay rapidly with increasing index, thus allowing equations (2.1) and (2.3) to be solved as a coupled pair as described by Holmes *et.al.* (2003).

2.2.3 Energy Equation

The energy equation for the fluid is given by

$$\frac{\partial}{\partial x}\left(k\frac{\partial \theta}{\partial x}\right) + \frac{\partial}{\partial y}\left(k\frac{\partial \theta}{\partial y}\right) + k\left(\frac{\partial^2 \theta}{\partial z^2}\right) - \rho c\left(u\frac{\partial \theta}{\partial x} + v\frac{\partial \theta}{\partial y}\right) + \varepsilon\theta\left(u\frac{\partial p}{\partial x} + v\frac{\partial p}{\partial y}\right) = -\left(\tau_x\frac{\partial u}{\partial z} + \tau_y\frac{\partial v}{\partial z}\right) \tag{2.4}$$

and surface temperatures of the contacting solids, which form the boundary conditions for equation (2.4), are obtained using a one-dimensional ("linear heat flow") conduction model, of the form

$$\theta_s = \theta_B + \frac{1}{\sqrt{\pi k \rho c}} \int_0^t \frac{q\,d\lambda}{\sqrt{t-\lambda}} \tag{2.5}$$

Here $\theta_s(x,y)$ is the surface temperature of the solid and θ_B is its value at the inlet boundary. The integration in equation (2.5) is over the time that has elapsed since the point (x,y) of the surface under consideration crossed this inlet boundary. For the steady-state problem considered here, the time integration becomes a spatial integration along the path taken by the surface through the contact. The slowest disc surface speed in the experiments modelled in this chapter is 3.09 m/s (for the slow disc). At the lowest load which was modelled (620 N), the contact semi-dimension, b, in the direction of sliding, is 0.29 mm which gives a Peclet number for this surface of $L = 35.6$. Johnson (1985) states that, for $L > 5$, heat will only diffuse a short distance into the solid in the time taken for it to travel through the contact, and hence the heat flow will be approximately perpendicular to the surface. Thus, the assumption of a one-dimensional ("linear") conduction model is valid for the conditions considered in this work. This argument is further supported by a study carried out by Sharif (2008) which compared the results obtained using the method described here with those from a more exact model which includes a full conduction / convection model of the two surfaces.

2.2.4 Solution Method

Figure 2.1 shows a flow diagram of the solution procedure. The innermost loop of the EHL solver consists of the simultaneous solution of equations (2.1) and (2.3). The way in which the elastic equation has been formulated in differential form, together with the rapid decay of the weighting functions $f_{i,j}$ as the indices increase from zero, allows the equations to be solved simultaneously using a simple iterative method .

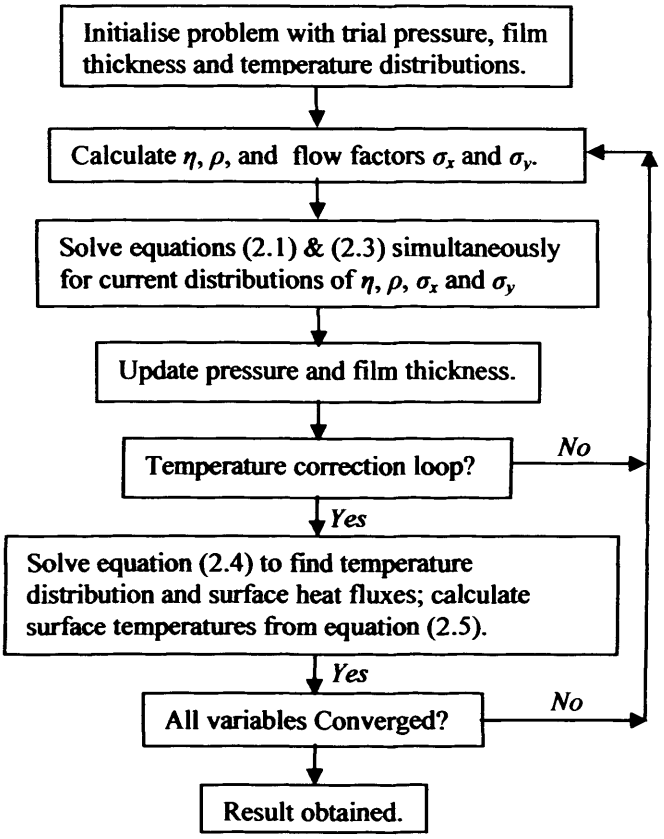

Figure 2.1: Thermal EHL solver flow-chart

For this study equations (2.1) and (2.3) are discretized using a central difference method to give equations relating the pressure and film thickness at a node with the values at the surrounding neighbouring nodes. Equations (2.1) and (2.3) for the (i,j) node are written as

$$\sum_{k=0}^{n_c} A_k p_k + \sum_{k=0}^{n_c} B_k h_k = R_{i,j} \qquad \sum_{k=0}^{n_c} C_k p_k + \sum_{k=0}^{n_c} D_k h_k = E_{i,j} \qquad (2.6)$$

where suffix k represents the nodes contributing to the equation at node (i,j) and $k = 0$ denotes that node. A_k and B_k are the pressure and film variable coefficients for the

Reynolds equation and are non-linear functions of pressure and temperature, and n_c denotes the number of neighbouring nodes involved in the formulation. C_k and D_k are the pressure and film variable coefficients for the differential deflection equation. In the elastic equation, $E_{i,j}$ contains the pressure summation $\sum_{\text{all k,l}} f_{k-i,l-j}\, p_{k,l}$ for all pressure contributions except those included in the first term on the left hand side of the equation.

The summation contributing to $E_{i,j}$ is split into two parts – the "close" and "far" regions. The close region is a band of mesh points surrounding the near region, and the far region makes up the remainder of the summation. The near region contains the points involved in the deflection Laplacian itself. The differential deflection technique results in pressure weighting coefficients whose magnitudes rapidly fall to zero as their indices increase, allowing the close and far contributions to $E_{i,j}$ to be evaluated for the current pressure distribution and regarded as functions of position, such that the coupled equations to be solved are shown in equation (2.6). The coupled equations (2.6) are re-formed to:

$$A_0 p_0 + B_0 h_0 = R_{i,j} - \sum_{k=1}^{n_c} A_k p_k - \sum_{k=1}^{n_c} B_k h_k = \hat{R}_{i,j}$$

$$C_0 p_0 + D_0 h_0 = E_{i,j} - \sum_{k=1}^{n_c} C_k p_k - \sum_{k=1}^{n_c} D_k h_k = \hat{E}_{i,j}$$

These equations are solved simultaneously for the updated values of the pressure and film thickness at node (i,j) – p_0 and h_0. The new iterative values at the node are given by:

$$\left.\begin{aligned} p_{i,j}^{new} &= \frac{\hat{R}_{i,j} D_0 - \hat{E}_{i,j} B_0}{A_0 D_0 - B_0 C_0} \\ h_{i,j}^{new} &= \frac{\hat{E}_{i,j} A_0 - \hat{R}_{i,j} C_0}{A_0 D_0 - B_0 C_0} \end{aligned}\right\} \tag{2.7}$$

Simple iteration using this pair of expressions solves the coupled equations rapidly. The coefficients A_k and B_k, together with the close contribution to $E_{i,j}$, are re-calculated at the end of each iterative solution of equations (2.1) and (2.3). Evaluation of the far contribution is the most time consuming aspect of the procedure and it is updated periodically as required.

The solution to the thermal problem is achieved by solving equations (2.4) and (2.5) periodically during the overall EHL solution procedure. This is carried out in cycles of the main loop of the solver which are specified as thermal correction cycles. Their frequency is varied so that the temperature distribution within the film becomes established as the EHL solution to equations (2.1) and (2.3) is obtained. Thus, the temperature dependence of viscosity is taken into account in determining the flow factors, σ_x and σ_y. In solving equation (2.4) numerically, the film is divided into n_f cross-film node points. The right hand side, and the velocity and pressure gradient dependent terms in θ and its derivates, are evaluated at each cross-film node point using the outer loop values of these parameters. Second order central difference expressions are used for the conductive derivative terms, whilst the appropriate backwards or forwards difference expression is used for the convective terms depending on the sign of the fluid velocity components at each mesh point and cross-

film level to achieve first order upwind differencing. The current values of the surface temperatures are regarded as boundary conditions, and the remaining n_f - 2 cross film temperature values are obtained from the resulting tri-diagonal system, using current temperature values at other (x,y) positions. The boundary conditions used for equation (2.4) for the oil film are that where the lubricant is flowing out of the solution area, the temperature gradient normal to the boundary is zero. Where the lubricant is flowing into the solution area it does so at the mean surface temperature.

The temperature gradient at each of the solid/liquid interfaces is then evaluated, to give the surface heat flux, q, so that equation (2.5) may be used to re-calculate the surface temperatures. For each point on the surface, the integral of equation (2.5) is evaluated by transforming the time integral into a spatial integral by taking note of the locus of the surface point in reaching its current position. It remains necessary to specify the surface temperature at the inlet to the EHL calculation region, θ_B. This value is the mean value of the surface temperatures upstream of the contact obtained from the test disk and shaft heat transfer analysis described by Clarke *et al.* (2006) and is treated as the best estimate for the surface temperatures of the disk upstream of the contact area.

The thermal calculations are carried out once for each cycle of the EHL convergence process. The interface temperature gradients and cross film temperature field are found to converge reliably and stabilize rapidly. The converged thermal EHL solution is obtained when the pressure, film thickness and temperature fields converge, with the constant h_0 in equation (2.2) adjusted to obtain the correct load.

2.2.5 Lubricant Density

Lubricant density will, according to Larsson *et.al.* (2000), increase by some 30 to 40% as the pressure is increased to around 2 GPa. However, as the temperature increases the lubricant density will fall. Thus, a realistic model of the density/pressure and density/temperature behaviour of the lubricant is necessary in a thermal EHL solution.

For the Mobil-Jet 2 lubricant used in Patching's experiments, the modified Dowson-Higginson density formula given by Larsson *et.al.* (2000) was used. It describes both the pressure and temperature dependence of the lubricant density as follows:

$$\rho(p,T) = \rho_0\left(1+\frac{D_1 p}{1+D_2 p}\right)\left[1-\varepsilon(T-T_0)\right] \tag{2.8}$$

where the constants D_1 and D_2 were, in the absence of specific measurements for Mobil Jet 2, taken as typical values given by Larsson *et.al.* for a synthetic lubricant, namely 0.67 GPa^{-1} and 2.68 GPa^{-1} respectively. ρ_0 is the reference density measured at temperature T_0 and atmospheric pressure. Equation (2.9) for ρ_0 is a best-fit line to data published by Mobil (1979).

$$\rho_0 = 1013.8 - 0.7574T_0 \tag{2.9}$$

2.2.6 Lubricant thermal conductivity

Larsson and Andersson (2000) have reported transient hot-wire measurements of thermal conductivity which show a doubling of the conductivity values over the range of pressures of interest in EHL modelling, as shown in Figure 2.2 for a range of lubricants.

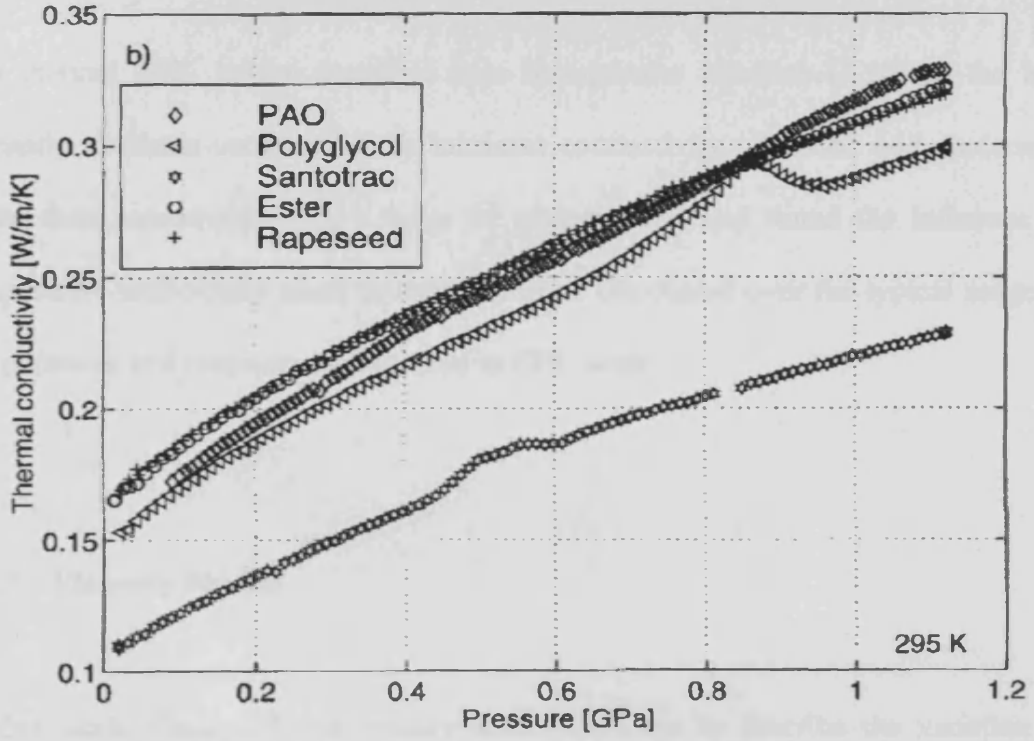

Figure 2.2: Thermal conductivity versus pressure for a variety of oils (from Larsson and Andersson, 2000)

As can be seen in Figure 2.2, the thermal conductivity approximately doubles as a result of a 1 GPa pressure increase. Since the work reported in this thesis is concerned with the generation of frictional heat within the EHL film and its subsequent conduction through the film to the two solid bodies, it was felt important

to take into account this strong dependence of thermal conductivity on pressure. Larsson and Andersson tested a range of lubricants, including a tri-methol-propynol ester (which is reasonably similar to Mobil Jet 2, which has an ester base) and proposed equation (2.10) as a model for the pressure dependence of thermal conductivity for the ester:

$$k = 0.162\left(1+\frac{1.44p}{1+0.56p}\right) \tag{2.10}$$

The thermal EHL solver described here incorporates equation (2.10) as the best currently available estimate of the lubricant conductivity. Larsson and Andersson made their measurements at a range of temperatures, and found the influence of temperature sufficiently small to enable it to be discounted over the typical range of temperatures and pressures encountered in EHL work.

2.2.7 Viscosity Models

In this work, three different models have been used to describe the variation of lubricant viscosity with pressure and temperature. These three models, proposed by Roelands (1966), Barus, and Bair (2001), are now described and compared.

The Roelands expression used is shown in equation (2.11)

$$\eta = \eta_0 \exp\left\{\ln\left(\frac{\eta_0}{\kappa}\right)\left[(1+\chi p)^Z\left(\frac{T+135}{T_0+135}\right)^{-S_0}-1\right]\right\} \qquad (2.11)$$

where κ = 63.15 x 10^{-6} Pa s and χ = 5.1 GPa^{-1}. Published data (Mobil, 1979) were used to define the viscosity at ambient pressure as

$$\eta_0 = 12.30 T_0^{-1.713}$$

and the pressure-viscosity coefficient, α, as

$$\alpha_0 = 60.36 T_0^{-0.3683}$$

The Roelands parameter, Z, was then obtained from the pressure-viscosity coefficient as:

$$Z = \frac{\alpha_0}{\chi \ln\left(\eta_0 / \kappa\right)}$$

The second Roelands parameter, S_0, was obtained from the published oil data (Mobil, 1979) as 1.108.

The Barus model takes the well-known exponential form:

$$\eta(p) = \eta_0 e^{\alpha p} \qquad (2.12)$$

where α is the pressure-viscosity coefficient, and η_0 is the viscosity at ambient pressure. These parameters vary both for different oils and at different temperatures. Power-law fits to data published by the oil manufacturers (Mobil, 1979) allow this temperature dependence to be included in equation (2.12) to give:

$$\eta(p,T) = 12.30T^{-1.713}\, e^{60.36\times10^{-9}T^{-0.3683}p} \tag{2.13}$$

The model proposed by Bair (2001) for a lubricant to the US Mil-specification L23599 (to which Mobil Jet 2 conforms) was based on laboratory data obtained from a high-pressure viscometer and fitted to the model introduced by Yasutomi *et.al.* (1984), shown in equation (2.14).

$$\eta = \eta_g \exp\left[\frac{-2.3C_1(T-T_g)F}{C_2+(T-T_g)F}\right] \tag{2.14}$$

where the glass transition temperature, T_g, is given by

$$T_g = T_{g0} + A_1 \ln(1 + A_2 p)$$

and the relative free volume expansivity is

$$F = 1 - B_1 \ln(1 + B_2 p)$$

The parameters determined by Bair for the lubricant to L23599 specification are: η_g = 10^{12} Pa s; T_{g0} = -87°C; A_1 = 158°C; A_2 = 0.4476 GPa^{-1}; B_1 = 0.194 GPa^{-1}; B_2 = 18.8 GPa^{-1}; C_1 = 16.03°C; C_2 = 22.52°C.

It is informative to compare the three models for Mobil Jet 2 at three temperatures typical of those experienced in the Patching tests – 100°C, 150°C, and 200°C, as shown in Figures 2.3, 2.4 and 2.5 respectively.

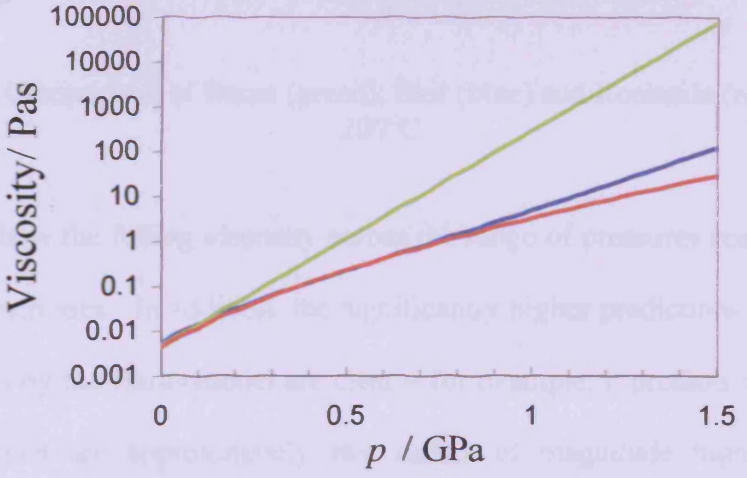

Figure 2.3: Comparison of Barus (green), Bair (blue) and Roelands (red) models at 100°C

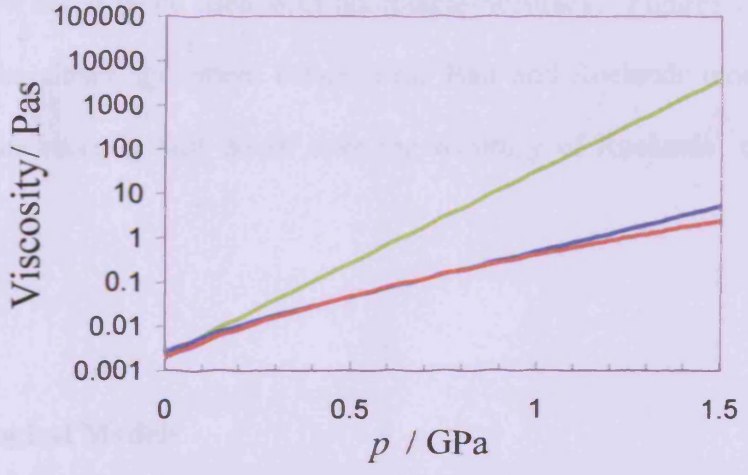

Figure 2.4: Comparison of Barus (green), Bair (blue) and Roelands (red) models at 150°C

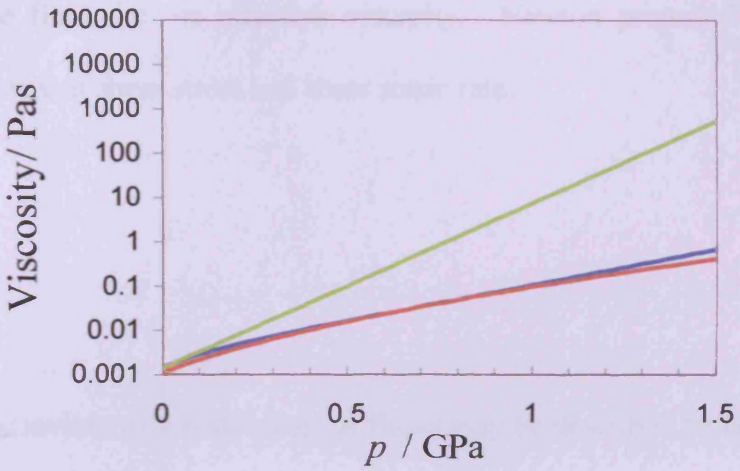

Figure 2.5: Comparison of Barus (green), Bair (blue) and Roelands (red) models at 200°C

The figures show the falling viscosity across the range of pressures considered as the temperature increases. In addition, the significantly higher predictions of viscosity at high pressures by the Barus model are clear – for example, it predicts viscosities at p = 1 GPa which are approximately two orders of magnitude higher than those predicted by Bair and Roelands. However, the Barus formula has been widely used to predict film thicknesses as pressures in the inlet region (where the film is formed) are sufficiently low for it to be used with acceptable accuracy. Figures 2.3 to 2.5 also demonstrate the closer agreement between the Bair and Roelands models, although Bair (2004) has recently cast doubt over the accuracy of Roelands' model at high pressures.

2.2.8 Rheological Models

The friction (or traction) force generated when two surfaces slide past each other separated by a full EHL film (i.e. no asperity contact) is solely due to the internal friction of the fluid, i.e. its effective viscosity. Newton proposed the following relationship between shear stress and shear strain rate:

$$\dot{\gamma} = \frac{\tau}{\eta} \tag{2.15}$$

The viscous behaviour of a wide range of fluids may be described by equation (2.15), and these fluids are referred to as *Newtonian* fluids. However, the lubricant in EHL contacts experiences extremely large and rapid pressure variations, a rapid transit time, large temperature changes and (in sliding contacts) high shear rates. In addition, experimental observations of traction have called into question the applicability of the Newtonian lubricant model since traction measurements are usually significantly lower than those predicted by a Newtonian EHL solution. Thus, various non-Newtonian rheological models have been developed, in which the lubricant shear strain rate is taken as a non-linear function of shear stress. The general form of non-Newtonian model used in this work links shear stress to strain rate according to:

$$\dot{\gamma}_x = \frac{\partial u}{\partial z} = \frac{\tau_x}{\tau_e} F(\tau_e) \qquad \dot{\gamma}_y = \frac{\partial v}{\partial z} = \frac{\tau_y}{\tau_e} F(\tau_e) \quad \text{where} \quad \tau_e = \sqrt{\tau_x^2 + \tau_y^2} \tag{2.16}$$

Two rheological models, for the function $F(\tau_e)$, are used in this work, namely the Eyring-type shear thinning model as proposed by Johnson and Tevaarwerk (1977), and the limiting shear stress model proposed by Bair and Winer (1979a).

For the Eyring-type model, the non-Newtonian function takes the form

$$F(\tau)=\frac{\tau_0}{\eta}\sinh\left(\frac{\tau}{\tau_0}\right) \tag{2.17}$$

The Johnson and Tevaarwerk model is based upon the analysis of the results of EHL traction experiments using a disk machine. In this arrangement, the shear rate within the contact varies with the film thickness, and the viscosity varies very significantly due to pressure and temperature variations within the contact region. Consequently, the authors made some assumptions about the pressure, film thickness and temperature distributions in the experiments in order to determine the non-Newtonian parameters. Their experimental apparatus employed a form of differential heating of the disks in order to minimise temperature variation at different sliding speeds. However, by their very nature, disk machine experiments are limited to determining the average shear stress over the contact area (from the measured traction force) and hence cannot reveal the fundamental details of lubricant behaviour.

The parameter τ_0, known as the Eyring shear stress, is taken as the stress at which the fluid begins to exhibit significant non-Newtonian behaviour. This can be thought of as analogous to the yield stress of a ductile material as determined from a stress-strain plot when the material deviates from Hooke's law. An alternative non-Newtonian model was proposed by Bair and Winer (1979a) which takes the form:

$$F(\tau) = -\frac{\tau_L}{\eta}\ln(1-\tau/\tau_L) \qquad (2.18)$$

Their work used special apparatus where a fluid could be placed under controlled shear rates at constant high pressures and temperatures without using an EHL contact. They observed that, at a given pressure and temperature, there is a critical shear stress above which the lubricant will shear as a plastic solid with no further increase in the shear stress as the strain rate increases. This observed behaviour is embodied in their model as the limiting shear stress, τ_L, which is the maximum shear stress which can develop within the lubricant in the contact.

The characteristic shear stress – strain rate behaviour of the Newtonian, shear thinning and limiting shear stress models may be seen in Figure 2.6. The limiting shear stress of the Bair and Winer model can clearly be seen, as can the Eyring-type model which, whilst it deviates from Newtonian behaviour, does not reach a shear stress limit.

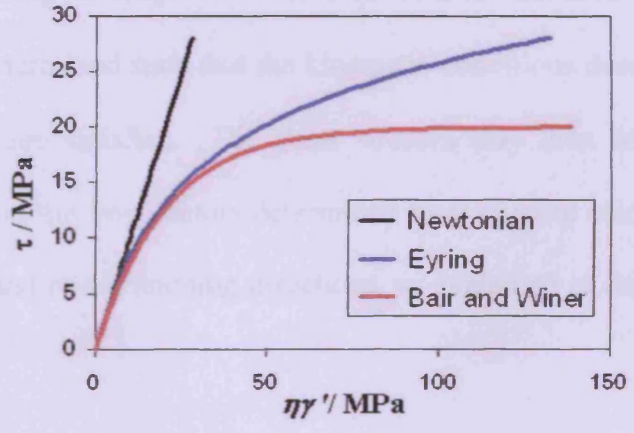

Figure 2.6: Comparison of Newtonian, Eyring-type and limiting shear stress rheological models

A basic consideration of the balance of forces on a fluid element ensures that the shear stress components vary linearly across the film such that:

$$\tau_x(z) = \tau_{xm} + z\frac{\partial p}{\partial x} \qquad \tau_y(z) = \tau_{ym} + z\frac{\partial p}{\partial y} \tag{2.19}$$

Equation (2.16) may be integrated across the lubricant film, to give the difference in the velocity components at the solid/liquid interfaces. Thus the kinematic conditions to be satisfied by the lubricant at each point within the contact are, in the sliding and non-sliding directions respectively,

$$u_s = \int_{-\frac{h}{2}}^{\frac{h}{2}} \frac{\tau_x}{\tau_e} F(\tau_e) dz \tag{2.20}$$

$$0 = \int_{-\frac{h}{2}}^{\frac{h}{2}} \frac{\tau_y}{\tau_e} F(\tau_e) dz \tag{2.21}$$

where u_s is the sliding velocity. The values of the mid-film shear stress components, τ_{xm} and τ_{ym}, are determined such that the kinematic conditions described by equations (2.20) and (2.21) are satisfied. The shear stresses may then be determined using equation (2.19), and the flow factors determined by numerical calculation of the flow in the entraining and non-entraining directions, as explained in detail by Sharif *et.al.* (2001).

2.2.9 Shear limit and slip

When a limiting shear stress rheological model, such as that given in equation (2.18) is used, the maximum shear stress which can develop in the film is constrained to not exceed the value of τ_L, and thus, unless the pressure gradient is zero, there is a maximum amount of sliding which the oil can provide, u_{Smax}. Equations (2.19) ensure that the largest value of τ_e occurs at one or other of the fluid boundaries. When this occurs the fluid experiences the largest possible amount of sliding that the limiting shear stress model can accommodate. The value of u_{Smax} is given by equation (2.20) for these circumstances. If u_S is greater than u_{Smax}, then the lubricant must compensate for this in some way. The oil is thus considered to slip, with slip velocity $u_{slip} = u_S - u_{Smax}$, along a slip plane which, in this study, has been taken to be at the point of highest temperature within the film. This is based on the observation that limiting shear stress levels generally fall with increasing temperature (Bair and Winer, 1979b). The power dissipated at the slip plane is $\tau_x.u_{slip}$ and within the solution of the energy equation this is added to the right hand side of equation (2.4) at the cross film node position corresponding to the slip plane.

When slip occurs in this way the Couette component of the fluid flow is modified. This has the result that the entrainment velocity will vary between the surface velocities u_1 and u_2 according to the position of the slip plane. When slip occurs at the faster moving surface the entrainment velocity is locally reduced towards that of the slower moving surface which has the effect of locally increasing film thickness to

maintain continuity. This is the case for the analyses carried out in this study for most of the area where slip is found to occur. In the exit to the contact where the pressure gradients are positive and extremely high the highest shear stress occurs on the slower moving surface. The pressure gradients within the model can be such that $\frac{z}{2}\sqrt{\frac{\partial p}{\partial x}^2 + \frac{\partial p}{\partial y}^2}$ is greater than the limiting shear stress. In these circumstances the model used is that suggested by Ståhl and Jacobson (2003) with slip at the slower surface, and it is found that this procedure leads to converged solutions where $\frac{z}{2}\sqrt{\frac{\partial p}{\partial x}^2 + \frac{\partial p}{\partial y}^2}$ is below or equal to the limiting shear stress value. For the current work the limiting shear stress is taken to be a function of pressure only.

2.3 Results

In the experiments of Patching *et al.* (1995) and the subsequent heat conduction modelling of Clarke *et al.* (2006), four experiments were reported which used super-finished disks. The work of Clarke *et al.* used a separate value of the heat partition parameter, β, at each load stage, and thus for each experiment modelled a β value was obtained for each load stage, as shown by the open symbols in Figure 1.15. In this thesis, the steady-state thermal EHL model described was applied to conditions at the end of each load stage, where friction and temperatures had reached approximately steady conditions. Details of the four experiments are shown in Table 2.1.

Table 2.1: Summary of scuffing tests

Test	2-2	2-5	2-11	2-13
Fast surface velocity (m/s)	13.09	20.95	26.18	30.10
Slow surface velocity (m/s)	3.09	4.95	6.17	7.10
Mean entraining velocity (m/s)	8.09	12.95	16.18	18.60
Sliding velocity (m/s)	10.00	16.00	20.00	23.00
Scuffing load (N)	3452	4150	3460	4160
Maximum Hertzian contact pressure at scuffing (GPa)	1.6	1.7	1.6	1.7

In order to investigate the influence of lubricant rheology on the partition of frictional heat, six different combinations of the previously discussed viscosity and non-Newtonian models were used, as shown in Table 2.2.

Table 2.2: Models used in thermal EHL analysis (numbers refer to the relevant equations)

Model	**Rheology**	**Viscosity**
A	Johnson and Tevaarwerk (2.17)	Yasutomi (2.14)
B		Roelands (2.11)
C		Barus (2.13)
D	Bair and Winer (2.18)	Yasutomi (2.14)
E		Roelands (2.11)
F		Barus (2.13)

In order to match the calculated friction force to that recorded by Patching in the experimental work, the non-Newtonian parameter was adjusted until the calculated friction force matched that measured in the experiments. Data for these parameters at the range of temperatures and shear rates present in the experiments is not known – it is however clearly necessary that the calculated friction should match that measured in the experiment.

For the Johnson and Tevaarwerk model the value of the Eyring shear stress (τ_0) was assumed to be constant and for each case analysed the value of τ_0 was adjusted until the final converged thermal EHL result gave the measured friction for that stage of the scuffing experiment as illustrated in Figure 1.13. For the Bair and Winer limiting shear stress model, τ_L was assumed to vary linearly with pressure, such that

$$\tau_L = \gamma\, p \tag{2.22}$$

For each case analysed, the value of the constant of proportionality, γ, in equation (2.22) was adjusted to achieve the correct friction force in the final converged result.

Once the model had converged, the heat flux into each solid body was integrated over the surface area of each solid in order to calculate the value of the heat partition parameter, β. This is defined as the proportion of the total heat dissipated passing into the faster body so that

$$\beta = \frac{Q_{fast}}{Q_{fast} + Q_{slow}} \tag{2.23}$$

where Q_{fast} and Q_{slow} are the total heat flowing into the fast and slow surfaces, respectively.

As an example of the results obtained, the final load stage prior to scuffing of experiment 2-13 is now examined in some detail. In this case, the maximum Hertzian

contact pressure was equal to 1.6 GPa. The results obtained with each of the six combinations of viscosity and rheological model are now discussed.

2.3.1 Model A

With this model, which used the Eyring rheological model together with the Yasutomi viscosity model, the correct friction force was obtained with the Eyring shear stress τ_0 = 40 MPa. The maximum value of the shear stress τ_e developed within the oil film was 15.7 MPa, and hence the value of τ_0 ensures that the fluid behaves essentially in a Newtonian manner. This is because the Bair viscosity data used in the Yasutomi model leads, in this case, to the correct friction force as measured by Patching.

The centre-line distributions of surface temperatures, mid-film temperature, and the two surface heat fluxes are shown in Figure 2.7.

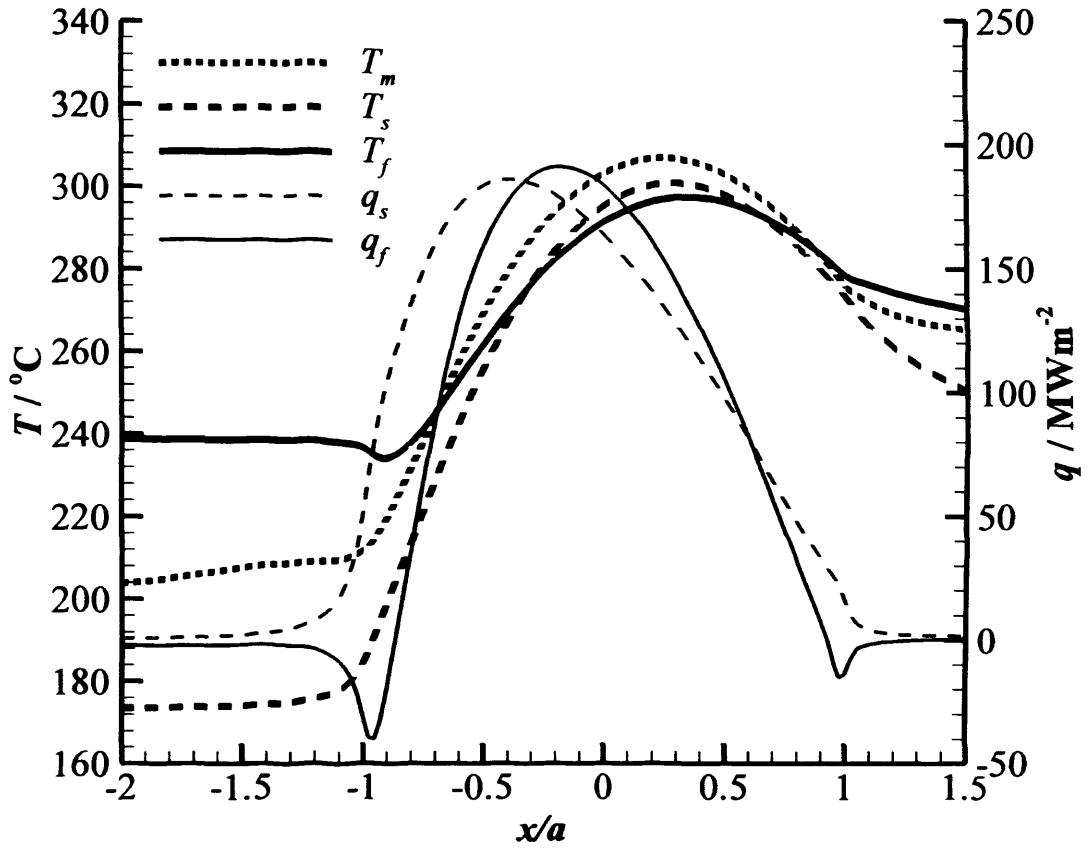

Figure 2.7: Centre-line mid-oil film and surface temperatures and surface heat fluxes using model A.

It can be seen that both maximum surface temperatures are below the maximum mid-film oil temperature. Both surfaces attain similar maximum temperatures as they near the exit of the contact, yet the slow surface enters the contact at a temperature some 65°C lower than the fast surface. The Newtonian behaviour in this EHL analysis leads to the shear heating being developed reasonably uniformly across the oil film.

The surface heat fluxes can be integrated over the contact area, allowing the heat partition parameter, β, to be calculated. For this case, $\beta = 0.33$, showing that the majority of the heat passes into the slower surface. This contrasts markedly with the value of β calculated from the experimental data by the two-dimensional heat transfer modelling, where a value of $\beta = 0.62$ was determined. Contour plots of the surface

heat fluxes within the contact may be seen in Figure 2.8. The Hertzian contact region is illustrated by the broken ellipses.

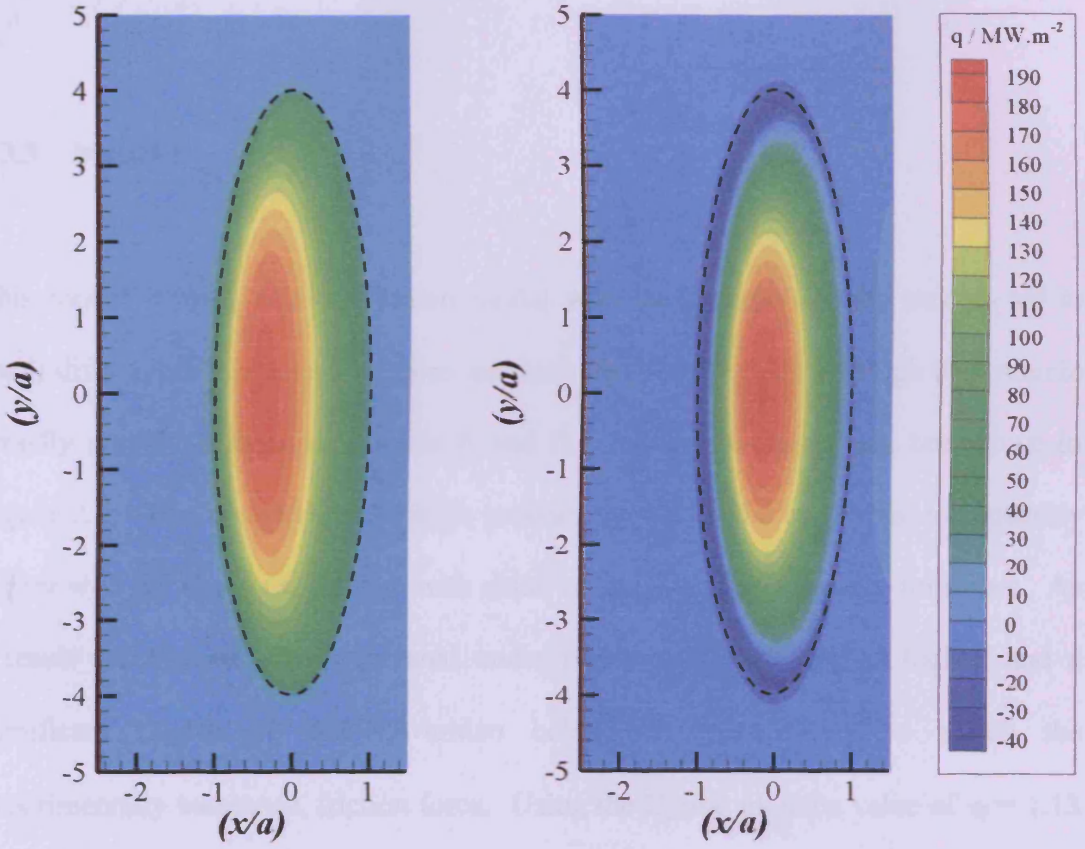

Figure 2.8: Surface heat fluxes using model A, for slow surface (left) and fast surface (right)

2.3.2 Model B

This model used the Eyring rheology with the Roelands viscosity model. Here, τ_0 = 6.5 MPa was required to match the predicted friction with the value recorded in the test. The value of τ_e obtained in the results reaches a level of 14.8 MPa indicating that the non-Newtonian effects are active in the case considered. However, the results for

this analysis showed little difference from those shown in Figure 2.7. β was found to be 0.383, again favouring the slow surface.

2.3.3 Model C

This model (Eyring non-Newtonian model with the Barus viscosity model) led to small differences in the temperatures and heat flux distributions although they remain broadly similar to those of Models A and B. The centre-line results are shown in Figure 2.9. The viscosity in the high pressure region of the contact is considerably higher with the Barus model than with either of the other two viscosity formulas. As a result the friction force generated under Newtonian conditions is higher, and a significant degree of non-Newtonian behaviour is necessary to match the experimentally measured, friction force. Using the Eyring model a value of $\tau_0 = 1.13$ MPa was found to give the measured friction. Again, the heat dissipated in this model was relatively uniformly distributed across the film, with $\beta = 0.371$.

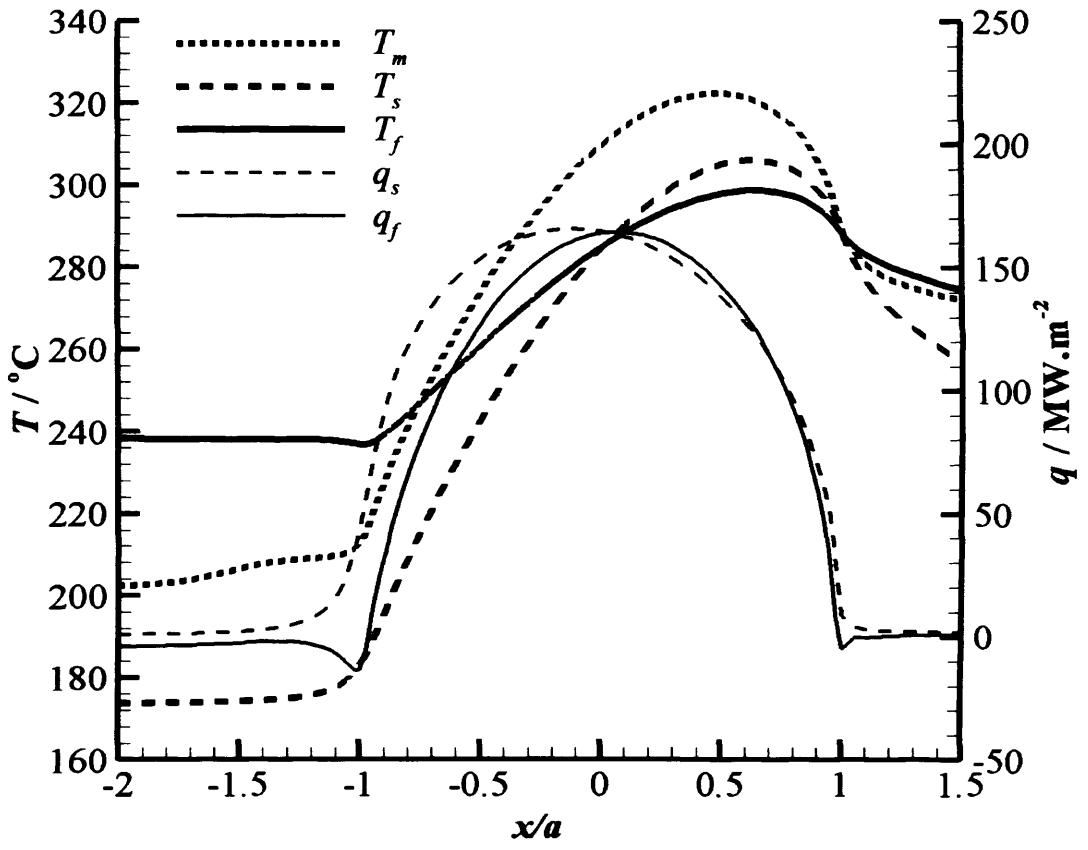

Figure 2.9: Centre-line mid-oil film and surface temperatures and surface heat fluxes using model C.

2.3.4 Model D

The results of Model D, which uses the limiting shear stress rheology with the Yasutomi viscosity model are shown in Figure 2.10 and are very similar to those of Figure 2.7. As in the case of model A the friction force as measured in the experiment was obtained with essentially Newtonian behaviour as the τ_L value required was $0.10p$, with no slip occurring. Again, the slow surface experienced a larger temperature rise in the contact and the surface heat fluxes were of similar magnitude. This model gave a heat partition of $\beta = 0.340$.

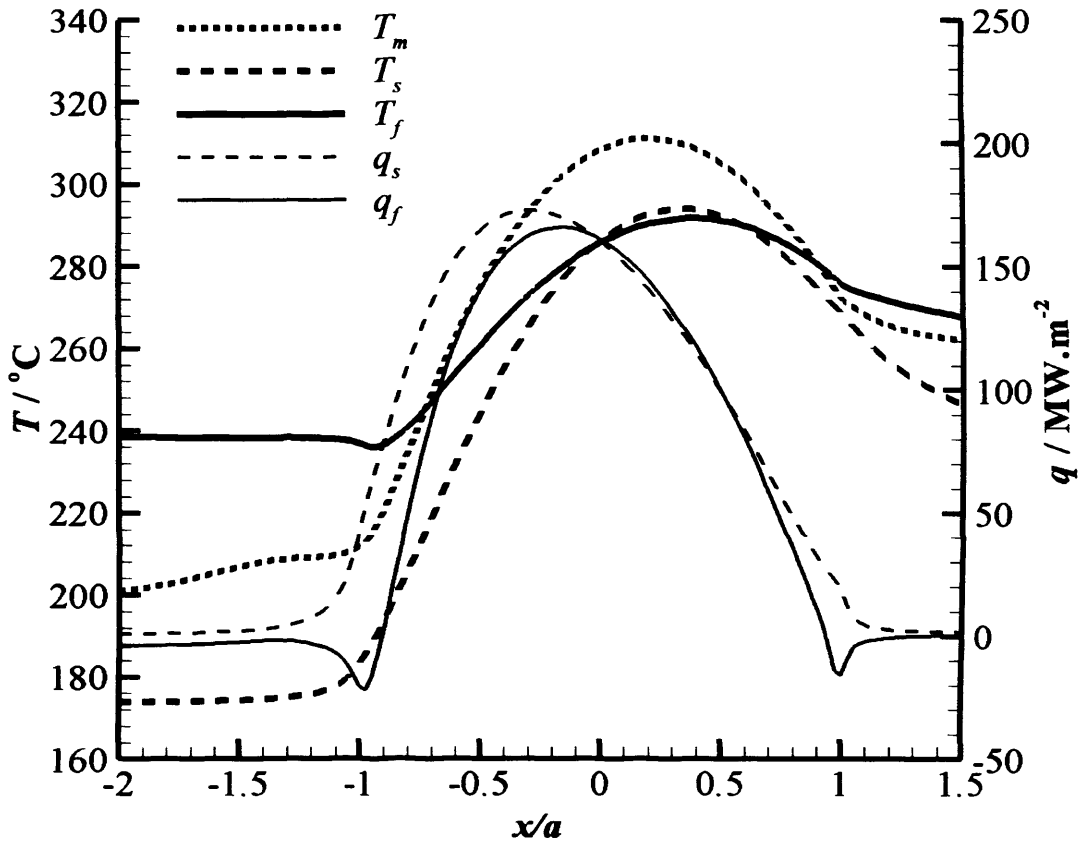

Figure 2.10: Centre-line mid-oil film and surface temperatures and surface heat fluxes using model D.

2.3.5 Model E

The results of Model E, using the limiting shear stress rheology but with the Roelands viscosity model, were again very similar to Model D, with $\beta = 0.371$. However, non-Newtonian behaviour, with $\tau_L = 0.0168p$ was necessary to achieve the correct friction force. In this analysis, no slip took place.

2.3.6 Model F

The final model considered used the limiting shear stress non-Newtonian model with the Barus viscosity. The sliding demand made of the oil at this load was such that u_s exceeded u_{Smax} over most of the Hertzian area. Hence slip occurred within the fluid and was taken to occur where the temperature was highest across the film, as explained in Section 2.2.9. This was found to be at, or near to, the faster surface. The thermal analysis uses 21 cross-film mesh points at each tangent plane mesh position. The energy dissipated at the slip plane was added to the lubricant at a single mesh point. Since there were 20 finite-difference mesh spacings across the film this means that the slip energy was dissipated over 5% of the film thickness (2.5% if the slip occurs at a surface). The results of this calculation can be seen in Figure 2.11. The faster surface remains at a higher temperature than the slower surface throughout the contact. The maximum temperature within the film is also shown in Figure 2.11 – this occurs at or close to the faster surface and exceeds the faster surface temperature by no more than 9°C for the case presented here.

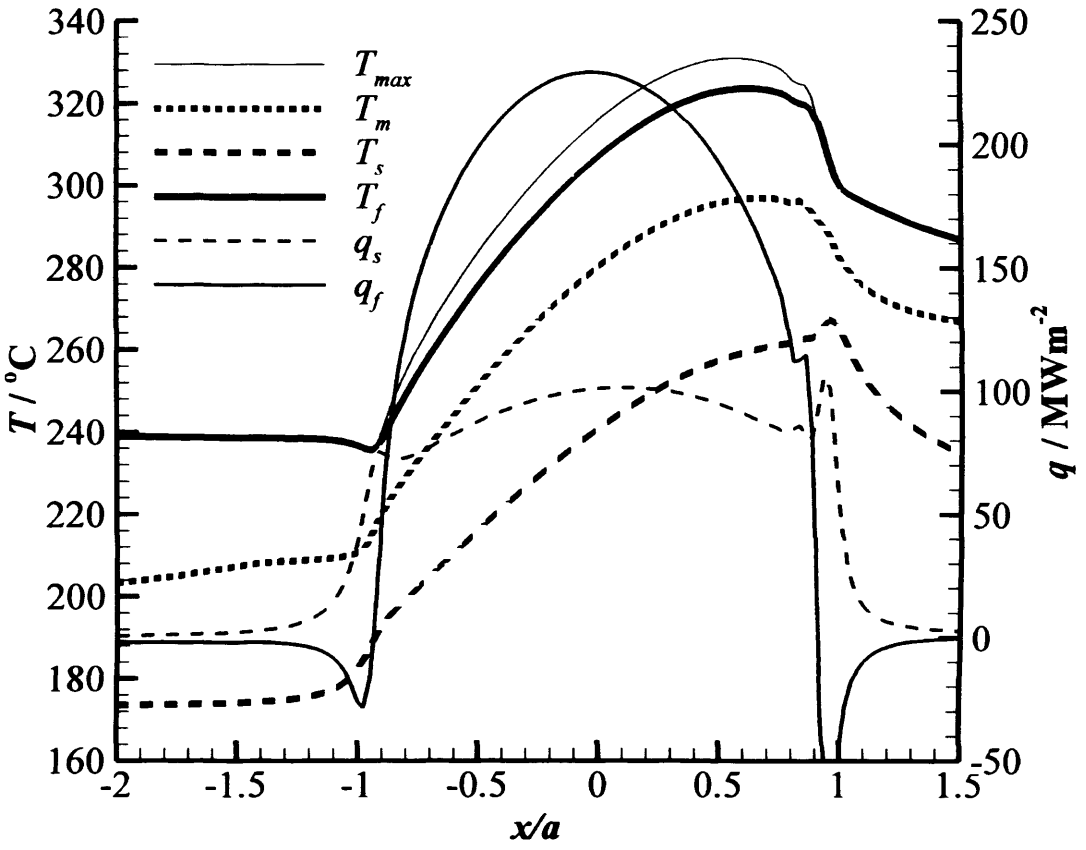

Figure 2.11: Centre-line mid-oil film and surface temperatures and surface heat fluxes using model F.

About 93% of the shear energy is dissipated at the slip surface. Thus, the heat generated within the contact is concentrated near to the fast surface, and the heat which reaches the slow surface has to be transmitted by conduction across the oil film. This leads to the heat partition favouring the faster surface, with $\beta = 0.571$, which is much closer to the value $\beta = 0.62$ obtained previously from the heat transfer analysis. The surface temperature behaviour is markedly different in this case. The difference between the surface temperatures is more or less maintained with the faster surface temperature being at least 60^0C higher than the slower surface throughout. This is in agreement with the flash temperature modelling carried out by the author previously (see figure 1.17) which also predicts that the temperature difference between the surfaces is maintained as they pass through the contact. The oil mid plane

temperature is seen to be intermediate which is to be expected as the oil is now primarily conducting heat across the film from the high temperature surface to the low temperature surface and its energy dissipation role is much reduced.

The different thermal behaviour of the six models is highlighted in Table 2.3, which gives maximum oil, fast surface and slow surface temperatures, together with maximum fast and slow surface fluxes.

Table 2.3: Comparison of maximum temperature, maximum heat flux and heat partition values obtained in analysing the test case (Test 2-13, p_0 = 1.6 GPa) with models A to F.

Model	T_{om} /°C	T_{fm} /°C	T_{sm} /°C	q_{fm} / MWm^{-2}	q_{sm} / MWm^{-2}	β
A	307	297	300	191	186	0.330
B	314	296	300	162	170	0.383
C	311	300	305	170	162	0.371
D	308	298	302	194	188	0.340
E	312	303	307	196	184	0.371
F	297	324	262	229	102	0.571

Table 2.3 clearly demonstrates that, in the case of models A to E, where the shear is fairly evenly distributed across the film thickness, the oil and surface temperatures are of similar magnitude. The largest difference between the maximum surface temperatures occurs in the case of model C, and is only 5°C. Again, the maximum fluxes on each surface are similar, with no more than a 6% difference in maximum flux between the fast and slow surfaces. However, when Model F is considered, where the frictional heating is concentrated at the slip plane near to the fast surface, the surface temperatures and heat fluxes are significantly different – the maximum fast surface heat flux is around twice the maximum slow surface heat flux.

The different behaviour of Model F is also shown in the calculated heat partition β values, also shown in Table 2.3. Models A to E, where the shear is relatively evenly distributed across the film thickness, have β values of between 0.330 and 0.383, with the majority of the heat flowing into the slower surface. This contrasts with the value of 0.62 determined by the earlier conduction modelling of the author. The results of Model F, however, have a β value of 0.571 which is in far closer agreement with the earlier work of the author.

2.3.7 Cross-film temperature distributions

Further illustration of the different shear behaviour of model F is shown in Figure 2.12, which shows cross film centre-line temperature distributions for models A and F.

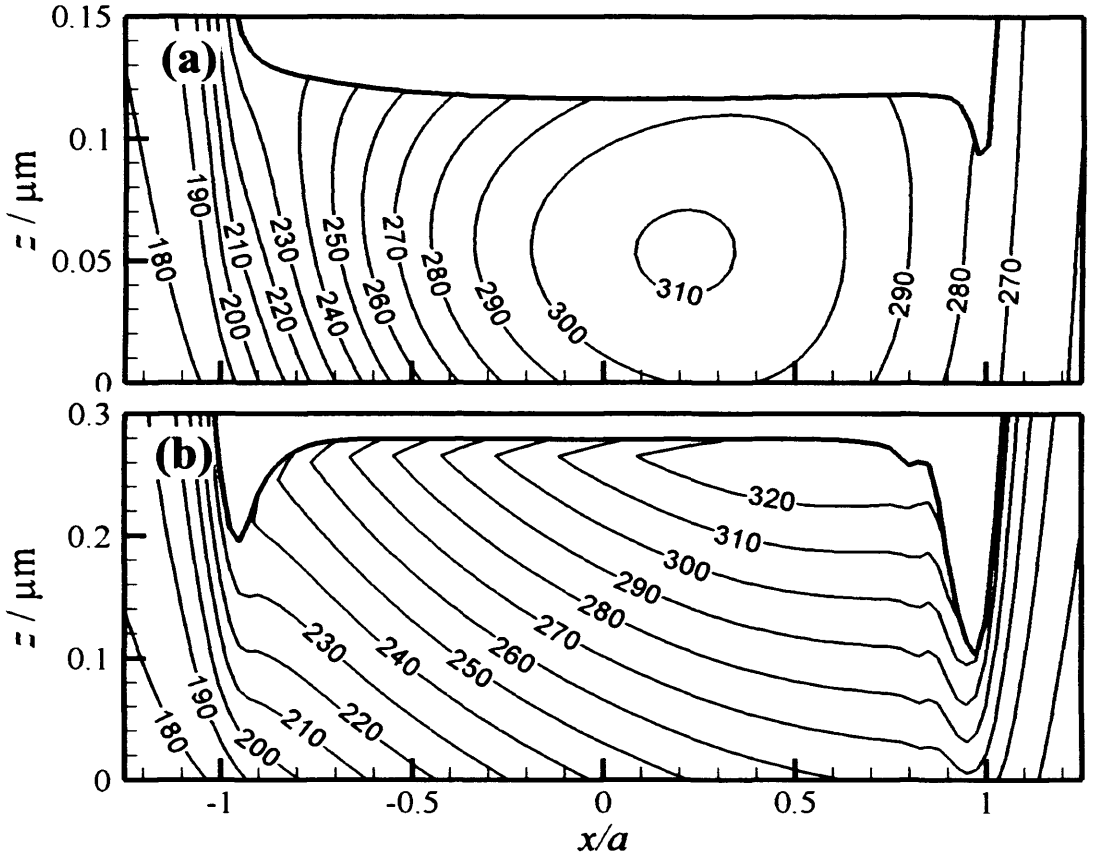

Figure 2.12: Cross-film oil temperature profiles at the plane $y = 0$ for (a) Model A and (b) Model F

The temperature contours in Figure 2.12 (a) are typical of the results of models A-E, where shear heating is reasonably evenly distributed across the film. This leads to the maximum temperature being developed approximately at the mid-film position, at $x = 0.2a$, with temperatures decreasing towards both surfaces. Figure 2.12 (b), however, shows a significantly different temperature distribution, as shear is concentrated near the fast surface. The maximum temperature occurs very near to the faster surface at

the slip plane, and the temperature decreases towards the slow surface, as heat is conducted from the slip plane across the film. The effect of slip at the faster surface in reducing the entrainment velocity is seen in the changed film thickness developed over the slip region from around 0.12μm for Model A to 0.28μm for Model F. This increase in film thickness increases the thermal resistance of the oil film, hence reducing the amount of heat conducted from the slip plane across the film to the slow surface.

2.3.8 Heat Partition Results

The six different models (A to F) were applied to each load stage of the four experiments, and the heat partition results obtained are shown in Table 2.4. It can clearly be seen that, for all the load stages modelled, only Model F which used the limiting shear stress rheology together with the Barus viscosity model gave heat partition (β) values which approach those obtained by Clarke (2006) from heat conduction modelling of the solid bodies.

Table 2.4: Summary of β values

Test No.	p_0 / GPa	β values from 2-d Conduction model of Clarke (2006)	Value of heat partition parameter, β, calculated from thermal EHL model					
			Model A	Model B	Model C	Model D	Model E	Model F
2-2	1.0	0.740	0.509	0.510	0.514	0.510	0.512	0.716
	1.1	0.720	0.488	0.487	0.487	0.486	0.486	0.664
	1.2	0.700	0.470	0.467	0.456	0.458	0.458	0.662
	1.3	0.670	0.445	0.445	0.433	0.436	0.435	0.615
	1.4	0.660	0.423	0.431	0.440	0.436	0.442	0.587
	1.5	0.650	0.401	0.414	0.420	0.424	0.434	0.557
2-5	1.1	0.690	0.488	0.487	0.494	0.498	0.494	0.739
	1.2	0.690	0.476	0.474	0.479	0.477	0.478	0.713
	1.3	0.670	0.467	0.465	0.468	0.469	0.468	0.685
	1.4	0.670	0.449	0.442	0.445	0.450	0.450	0.646
	1.5	0.650	0.440	0.438	0.441	0.443	0.443	0.627
	1.6	0.630	0.429	0.436	0.439	0.437	0.442	0.608
	1.7	0.620	0.402	0.423	0.429	0.410	0.432	0.579
2-11	0.9	0.790	0.487	0.487	0.509	0.490	0.490	0.653
	1.0	0.720	0.481	0.482	0.494	0.484	0.485	0.765
	1.1	0.700	0.472	0.474	0.480	0.478	0.477	0.743
	1.2	0.670	0.463	0.469	0.472	0.468	0.472	0.722
	1.3	0.650	0.455	0.466	0.468	0.460	0.466	0.700
	1.4	0.640	0.430	0.444	0.445	0.437	0.450	0.659
	1.5	0.630	0.397	0.423	0.426	0.404	0.432	0.621
	1.6	0.630	0.339	0.391	0.396	0.348	0.403	0.572
2-13	0.9	0.730	0.526	0.515	0.546	0.565	0.561	0.712
	1.0	0.730	0.504	0.493	0.532	0.563	0.552	0.751
	1.1	0.700	0.480	0.477	0.503	0.498	0.531	0.729
	1.2	0.670	0.462	0.462	0.460	0.470	0.470	0.707
	1.3	0.640	0.453	0.454	0.450	0.453	0.454	0.691
	1.4	0.630	0.429	0.433	0.425	0.428	0.427	0.659
	1.5	0.630	0.385	0.405	0.392	0.388	0.394	0.609
	1.6	0.620	0.330	0.383	0.371	0.340	0.371	0.571

The results are further illustrated by figures 2.13 to 2.18, which show the heat partition results for the four experiments investigated using Models A to F, respectively. In each figure the solid line is the trend-line for the beta values determined by Clarke *et al.* (2006) using a conduction model of the solid bodies.

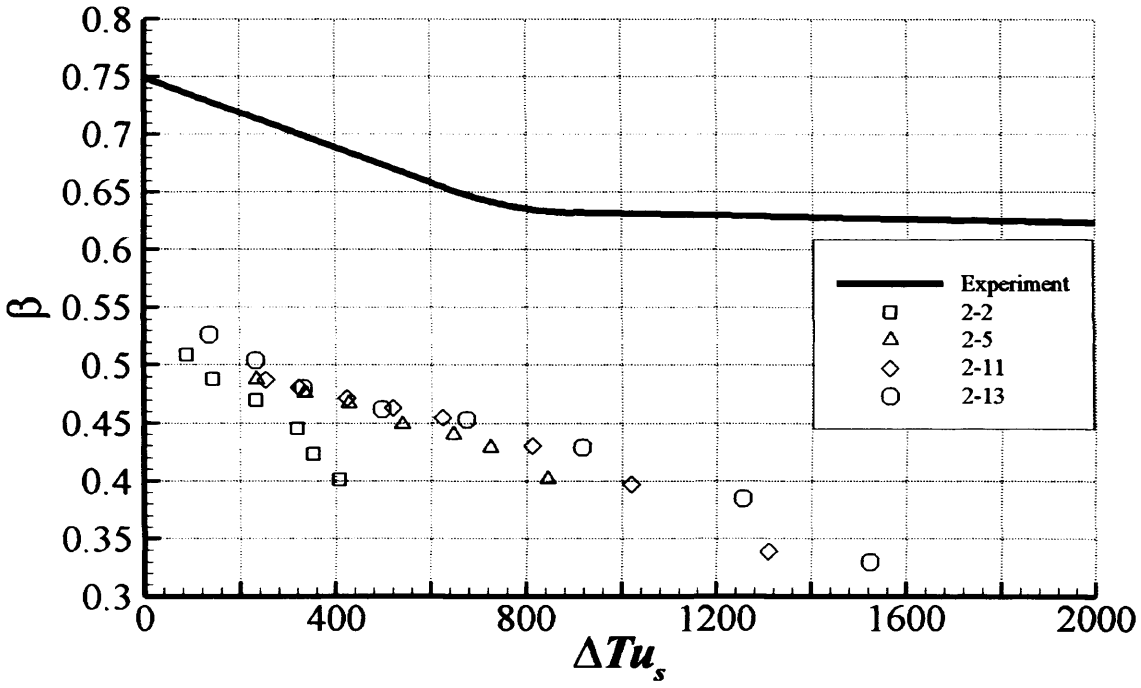

Figure 2.13: Comparison of heat partition parameter, β, calculated by EHL analysis (data points) using Model A with β values calculated from experimental data (solid line) by Clarke *et al.* (2006)

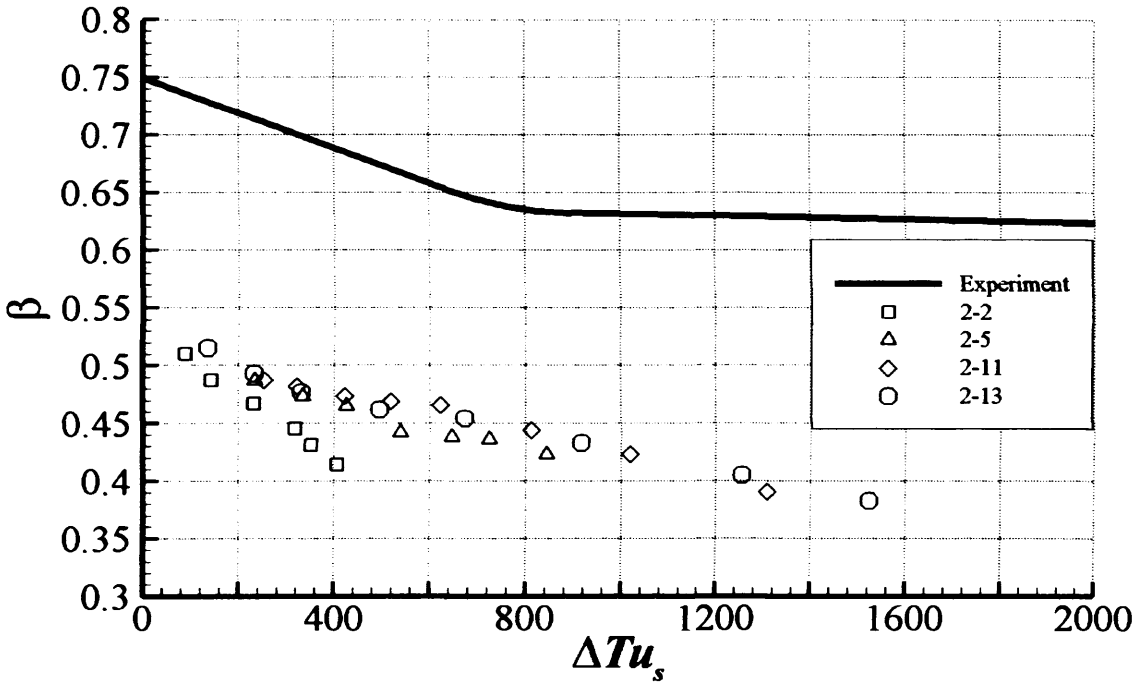

Figure 2.14: Comparison of heat partition parameter, β, calculated by EHL analysis (data points) using Model B with β values calculated from experimental data (solid line) by Clarke *et al.* (2006)

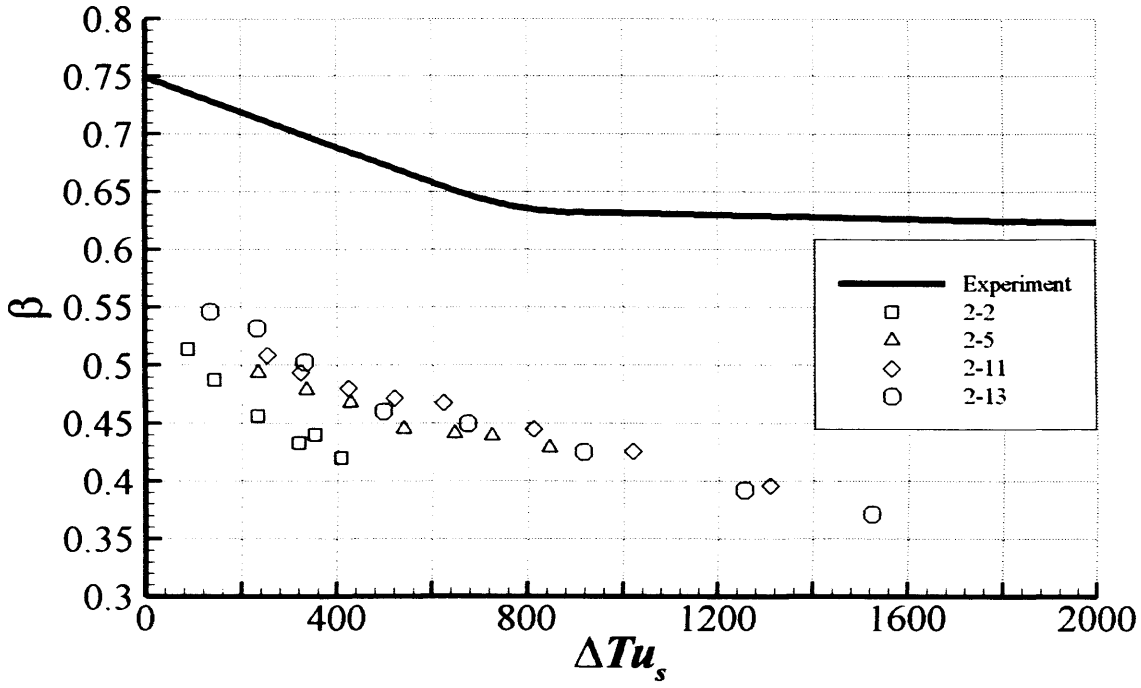

Figure 2.15: Comparison of heat partition parameter, β, calculated by EHL analysis (data points) using Model C with β values calculated from experimental data (solid line) by Clarke *et al.* (2006)

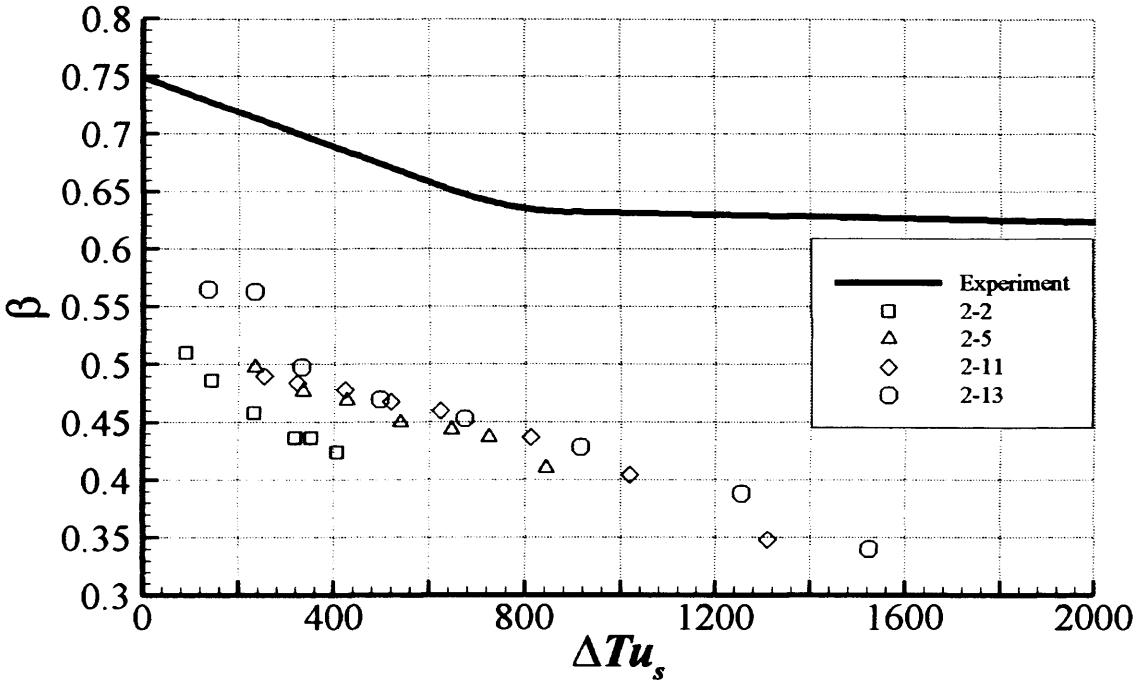

Figure 2.16: Comparison of heat partition parameter, β, calculated by EHL analysis (data points) using Model D with β values calculated from experimental data (solid line) by Clarke *et al.* (2006)

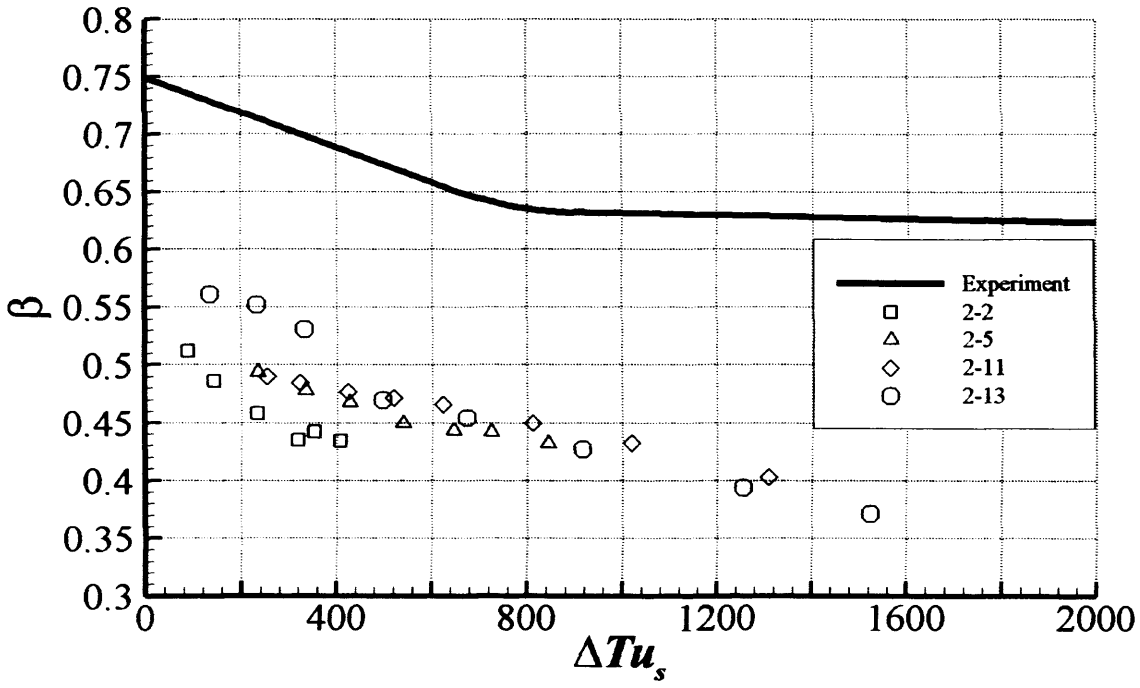

Figure 2.17: Comparison of heat partition parameter, β, calculated by EHL analysis (data points) using Model E with β values calculated from experimental data (solid line) by Clarke *et al.* (2006)

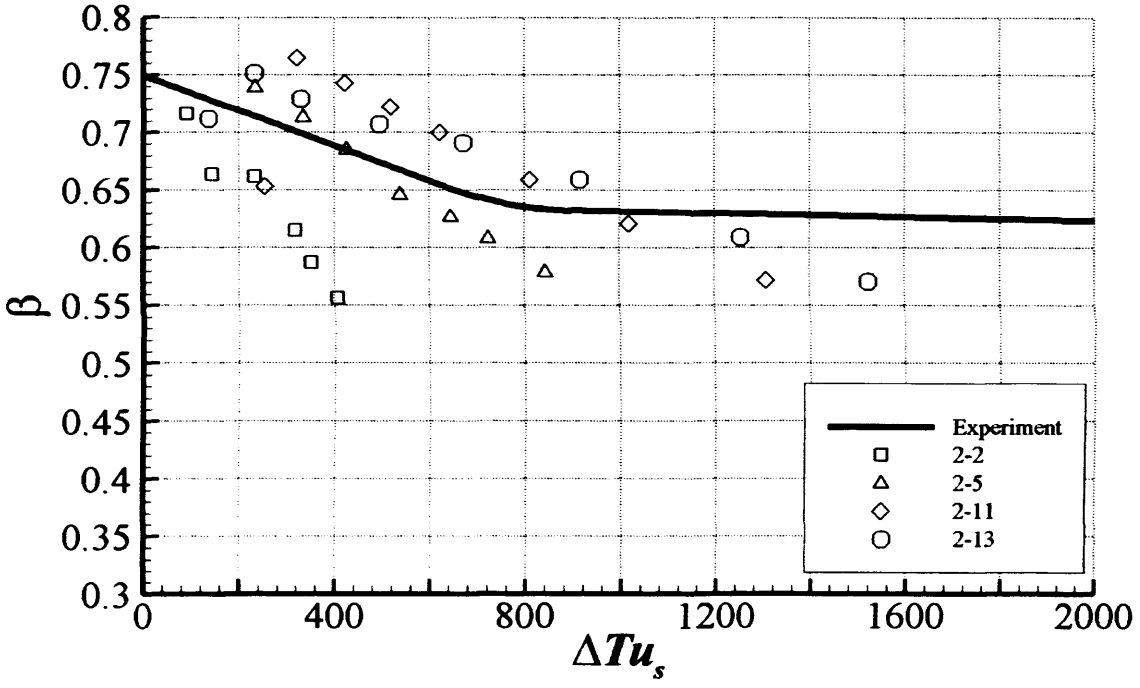

Figure 2.18: Comparison of heat partition parameter, β, calculated by EHL analysis (data points) using Model F with β values calculated from experimental data (solid line) by Clarke *et al.* (2006)

Considering the "distributed shear" results, shown in Figures 2.13 to 2.17, it may be seen that, whilst there are some differences between the results calculated by each of the models, they are in general agreement. They predict that a maximum of around 56% of the frictional heat passes into the fast disk during the early load stages (i.e. when $\Delta T.u_s$ is low) with the proportion falling to a minimum of 33% for higher values of $\Delta T.u_s$. These are in apparent contradiction with the results of Clarke *et al.* (2006) as shown in the solid trend-line in the figures, which ranges between $\beta = 75\%$ and $\beta = 63\%$.

The results shown in Figure 2.18 are those obtained with model F, and all showed slip at or near the faster fluid-solid boundary, with typically some 90% or more of the heat being dissipated at the slip-plane. At the lowest load stage of test 2-13, a smaller level of slip took place with some 58% of the heat dissipated at the slip plane. For the other cases over 90% of the heat was dissipated at the slip plane. This explains why the β value for this test does not follow the trend of the remaining points from that test. Thus model F is much more successful in predicting the experimentally measured heat partition behaviour.

The results do not follow the experimental trend exactly, but are at the correct level with differences in detail. This is in marked contrast to Figures 2.13 to 2.17 which show results which are consistent with each other but in significant conflict with the experimentally determined β value. It is clear that only when the limiting shear stress rheology is used with the Barus viscosity law are heat partition results obtained which approach those determined through heat transfer modelling of the disk machine experiments.

2.3.9 Film thickness

As explained in section 2.8.1, when slip occurs, the effective entrainment velocity is reduced and hence, in order to maintain flow continuity, the film thickness is locally increased. This may be seen in Figures 2.19 to 2.22, which show the central film thickness obtained which each of the EHL models, for tests 2-2, 2-5, 2-11 and 2-13 respectively.

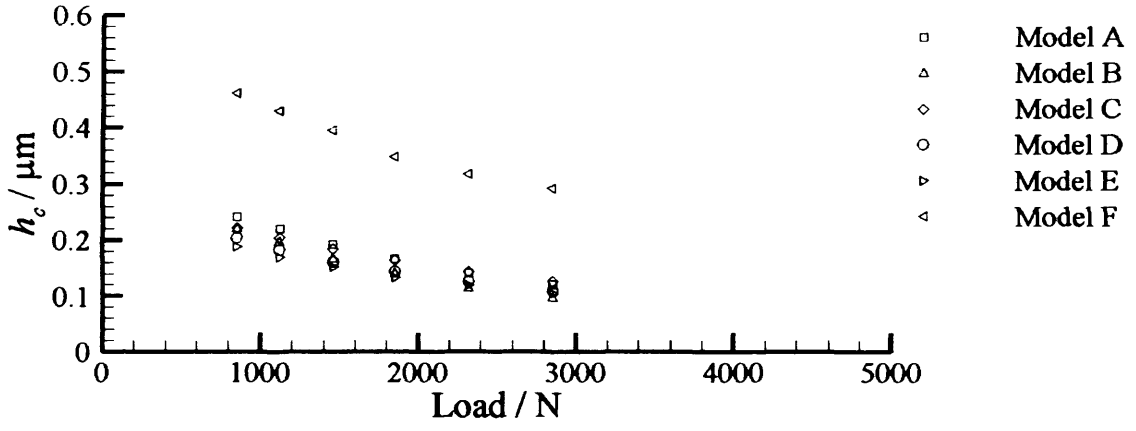

Figure 2.19: Calculated central film thickness, h_c, for test 2-2

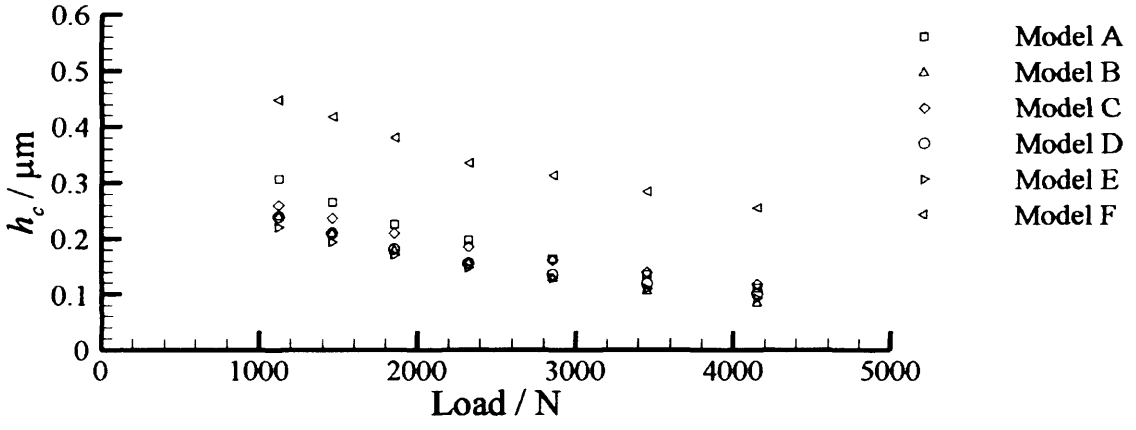

Figure 2.20: Calculated central film thickness, h_c, for test 2-5

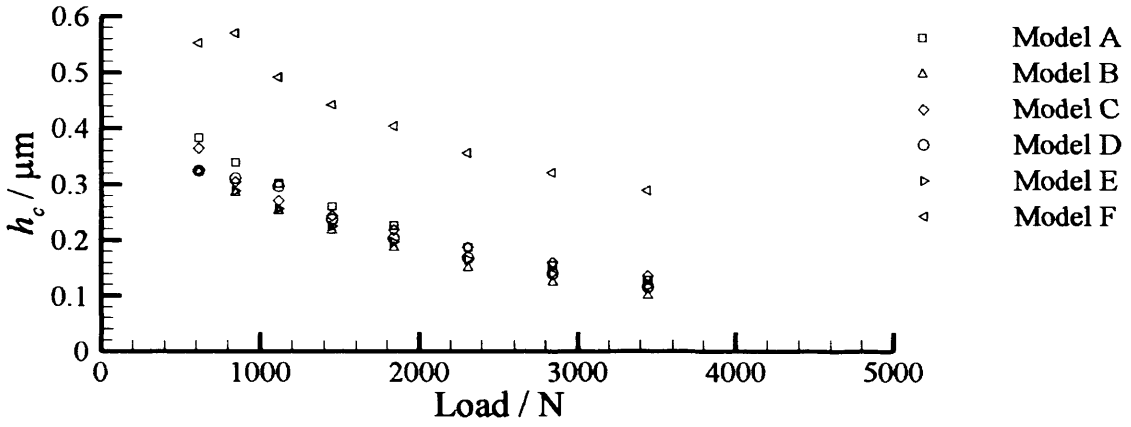

Figure 2.21: Calculated central film thickness, h_c, for test 2-11

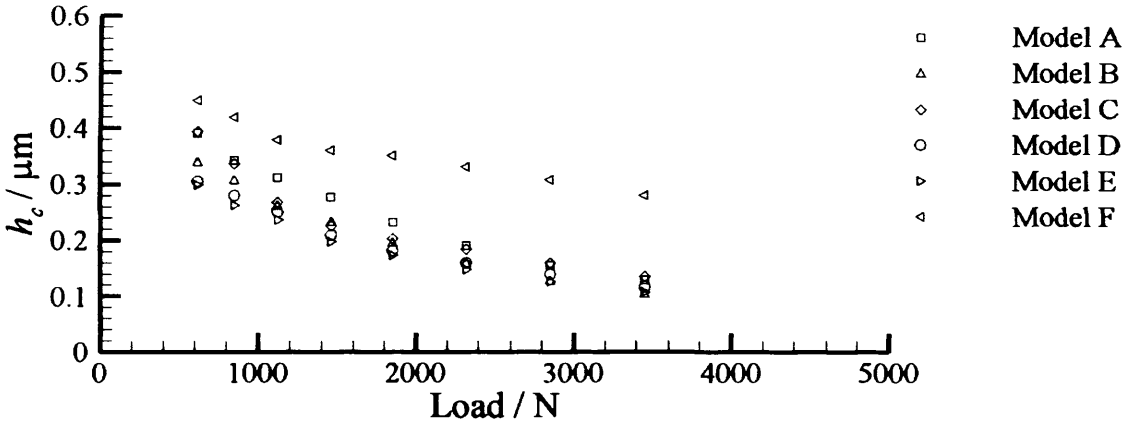

Figure 2.22: Calculated central film thickness, h_c, for test 2-13

These figures show that, in the majority of cases, the film thickness when the shear limit of the film is reached and therefore slip is occurring (i.e. when using Model F) is approximately double that of the corresponding non-slip results.

Since, when slip occurs, most of the heat is dissipated at a slip plane near to the fast surface, heat which flows into the slow surface has to be conducted across the oil film. These thicker films therefore have a higher thermal resistance across which the heat must be driven in order to reach the slow surface. In order to quantify the relative

effects of the increased film thickness and the dissipation of frictional heat along a plane adjacent to the fast surface, the analyses were repeated for experiment 2-13 with the effects of slip on the entrainment neglected. This analysis represents a case where the shear heating is dissipated adjacent to the faster surface, but where the film thickness is of a similar magnitude to the distributed shear cases (h_c = 0.13μm). Figure 2.23 shows the heat partition values calculated using this version of Model F. Also shown for reference are the results of models A to E and the trend-line of the author's earlier results.

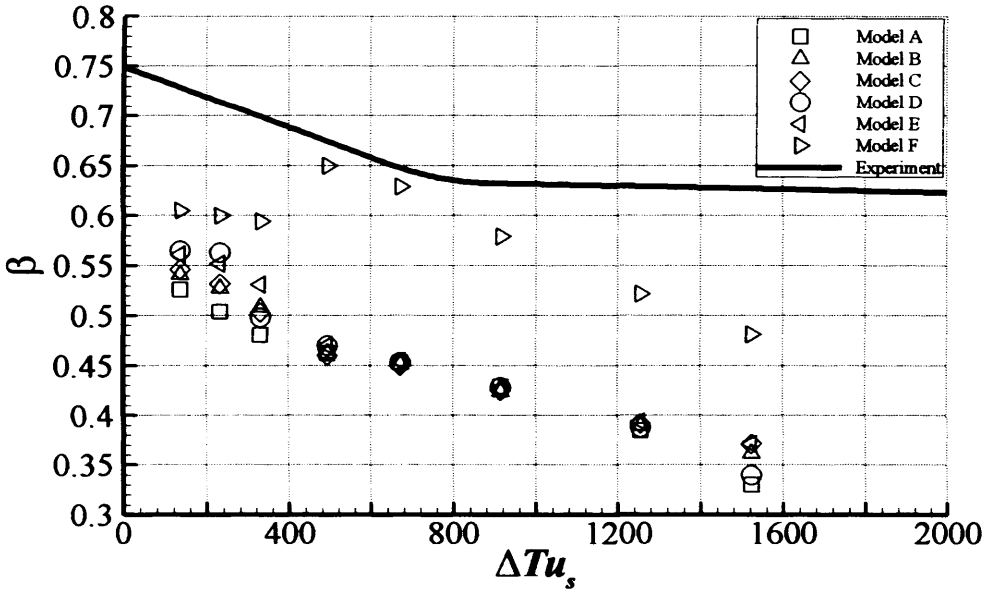

Figure 2.23: Heat partition results obtained where the effect of slip on film thickness is neglected.

It may be seen that by neglecting the reduction in entrainment when slip occurs, which leads to an increased film thickness, the amount of heat which flows into the slow surface is increased. For all load stages of test 2-13, the β value is lower than when the effect of slip on entrainment is taken into account (see Figure 2.18). For example, for the final load stage, β is reduced from 0.57 to 0.48. Whilst these results

are not in close agreement with the author's earlier results, they clearly demonstrate that even when the effect on entrainment is neglected, dissipating the frictional heat at a plane adjacent to the faster surface increases the amount of heat flowing into the surface. A comparison of Figures 2.18 and 2.23 also demonstrates that the effect of the increased thermal resistance of the thicker oil film which occurs when the effect of slip on entrainment is considered is not insignificant.

2.3.10 Influence of cross-film thermal mesh size

Since the way in which heat is generated in the film due to shear is of great importance to the partition of heat between the surfaces, as demonstrated by Figure 2.12, it is necessary to ensure that the heat partition results obtained by the EHL modelling are not overly sensitive to the number of calculation points used across the film thickness in the solution of the energy equation.

In the results presented here, the energy equation was solved with 21 cross-film mesh points (n_f=21). In order to investigate the sensitivity of the results to the value of n_f, calculations were performed using Model C (taken as being typical of the distributed shear results) and Model F for the final load-stage of test 2-13 with n_f= 11.

The results of Model C with n_f = 11 demonstrated no appreciable difference when compared to the results obtained with n_f= 21. The calculated β values were the same to two significant figures. This is because the shear heating is distributed relatively evenly across the film thickness and so the level to which the film is discretized in

order to solve the energy equation does not make a significant difference to the results.

When Model F was used, there were slight differences between the results, which are shown in Figure 2.24.

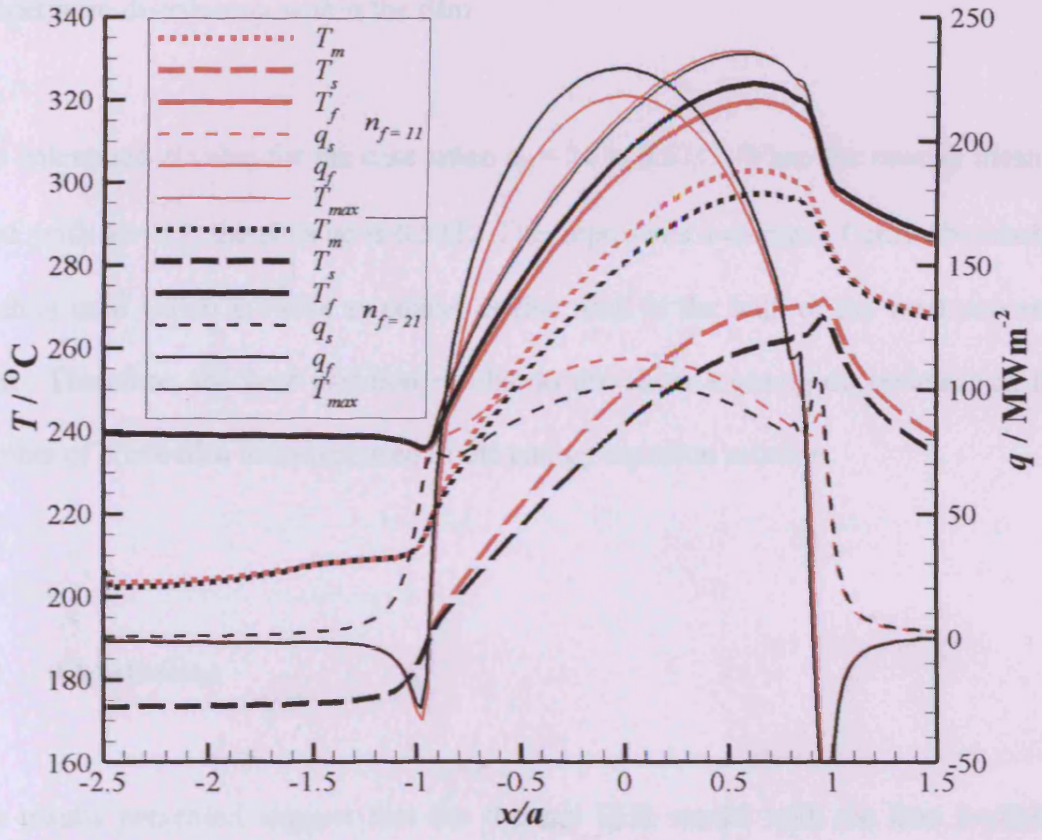

Figure 2.24: Comparison of results using Model F with $n_f = 11$ and $n_f = 21$

Inspection of Figure 2.24 shows that, when a coarser ($n_f = 11$) discretization is used for the solution of the energy equation, the temperature of the fast surface falls slightly, whilst the temperature of the slow surfaces shows a corresponding slight increase and the mid-film temperature also increases slightly. The maximum film temperatures remain at similar levels, with no clear change when the coarser solution

is used. These changes are minor – none of the surface temperatures change by more than 10°C. When the surface heat flux profiles are examined, the reason for this change in temperatures becomes clear as the heat flux at the fast surface has reduced slightly, together with a similar increase in the heat flux at the slow surface. This is because, when the coarser mesh is used, the position of the slip plane moves slightly nearer to the slower surface as the coarser mesh can less finely resolve the temperature distribution within the film.

The calculated β value for the case when $n_f = 21$ is 0.571. When the coarser mesh is used, with $n_f = 11$, the β value is 0.541. This represents a change of only 5% when a mesh is used which is twice as coarse as that used in the bulk of the work reported here. Therefore, the heat partition results do not show a strong dependence on the number of cross-film divisions used in the energy equation solution.

2.4 Conclusions

The results presented suggest that the thermal EHL model with the best available viscosity data does not predict the correct heat partition, as calculated from the previous heat transfer analysis of the disks. Four experiments have been modelled, which have a total of 29 different load stages, each of which has been analysed using the thermal EHL solver with 6 different combinations of rheological and viscosity model. The results from these analyses follow a consistent trend: only when the higher Barus viscosity is used in conjunction with a limiting shear stress rheological model, which ensures that lubricant slip takes place, do the heat partition results

favour the faster disk. The conclusion that more heat passes into the faster disk is consistent with previous disk machine work by Merritt (1962), for example.

Although the results obtained for β with model F are much closer to the values deduced from the experiments, they do not show the levelling off with increasing ΔTu_s seen in Figure 2.4. One possible explanation of this is that this feature is caused by changes to the experimental disks' heat transfer characteristics caused by relative surface temperature and relative speed in the enclosed environment of the test head.

The heat partition values determined by Clarke (2006) using a heat conduction model of the disks and shafts do contain some uncertainty regarding the assumed heat transfer coefficients from the surface of the disks and shafts. Work reported in subsequent chapters includes the development and use of a more comprehensively-instrumented disk machine, which allows the lifting of the restrictive assumptions inherent in the original modelling work.

A two-disc machine for the investigation of heat partition behaviour of high-speed elastohydrodynamic contacts

3.1 Introduction

This chapter describes the test rig used by Patching (1994) to perform the original scuffing experiments modelled in this work. It also details the modifications carried out to adapt the rig for use in the current experimental programme, where the emphasis is not on surface failure of disks but on the thermal behaviour of the oil film and contacting surfaces in a highly loaded EHL contact.

The rig is a twin-disk test rig, which is a commonly-used arrangement for investigating gear tooth contacts at a steady sliding speed without the highly transient nature of the sliding speed and the other dynamic effects present in a typical gear tooth contact.

The rig was originally constructed for use in an SERC/Rolls-Royce project to investigate scuffing failure of surfaces under conditions of sliding speed and load typical of those found in gas turbine gearing. The rig was commissioned and used for a series of scuffing tests (Snidle and Evans, 1990). The rig is not only capable of operating under high sliding and high load conditions, but also uses crowned disks, which give a self-aligning contact which avoids damaging edge-contact effects.

Patching went on to use the test rig in an experimental programme designed to investigate the scuffing performance of ground disks and super-finished disks. The rig was subsequently further developed by Alanou (2006) and Dhullipulla (2006) to investigate the effect on scuffing resistance of nitrided surfaces and various hard surface coatings.

3.2 Description of the rig

The original design of the rig was carried out in collaboration with Rolls-Royce, with the aim of reproducing the entraining speeds, slide/roll ratios and contact pressures found in typical aerospace gear meshes. The original specification of the rig is outlined in Table 3.1:

Table 3.1: Initial specification of the two-disc test rig

Sliding Speed	25 m/s maximum
Hertzian contact pressure	1.7 GPa maximum
Oil feed temperature	100°C typical, 200°C maximum
Lubricant	Mobil Jet 2 (synthetic)
Disk material	Case-carburising alloy steel to Rolls-Royce specification 6010
Heat treatment	Case-carburised, hardened and tempered to Rolls-Royce specification (RPS 371)
Surface finish	Final grinding to 0.4 μm Ra, transverse to direction of entrainment

The layout of the test head and its associated drive and loading arrangements is shown in Figure 3.1, with the test head shown in isometric projection in Figure 3.2. A photograph of the test rig as used by Patching can be seen in Figure 3.3, with the test head layout shown in Figure 3.4.

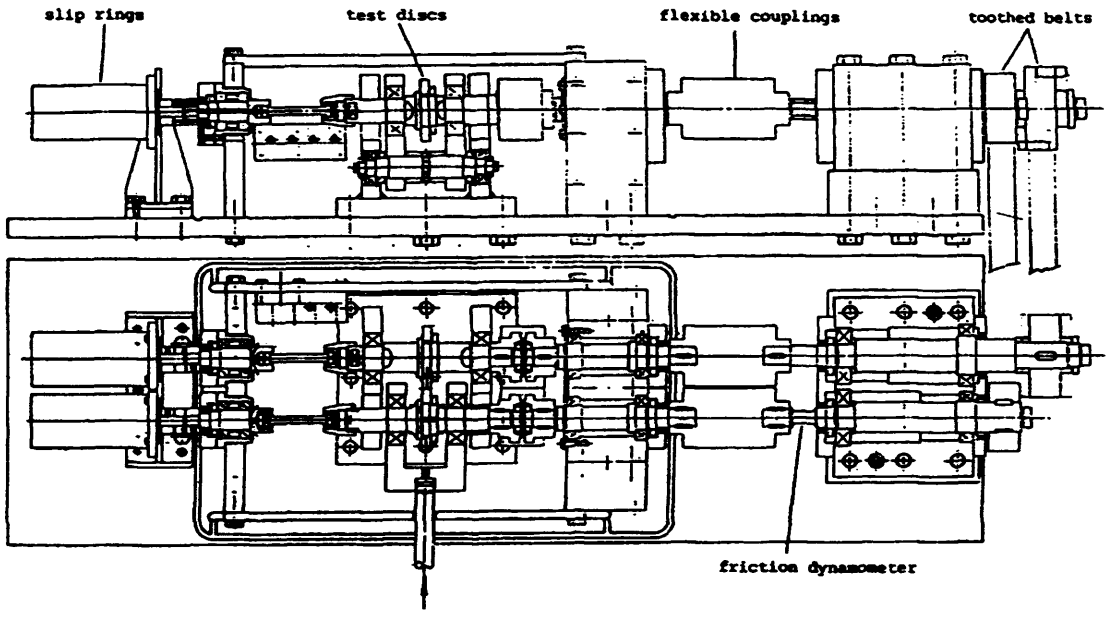

Figure 3.1: Section and plan drawing of the test head and drive arrangement of the test rig (from Patching, 1994)

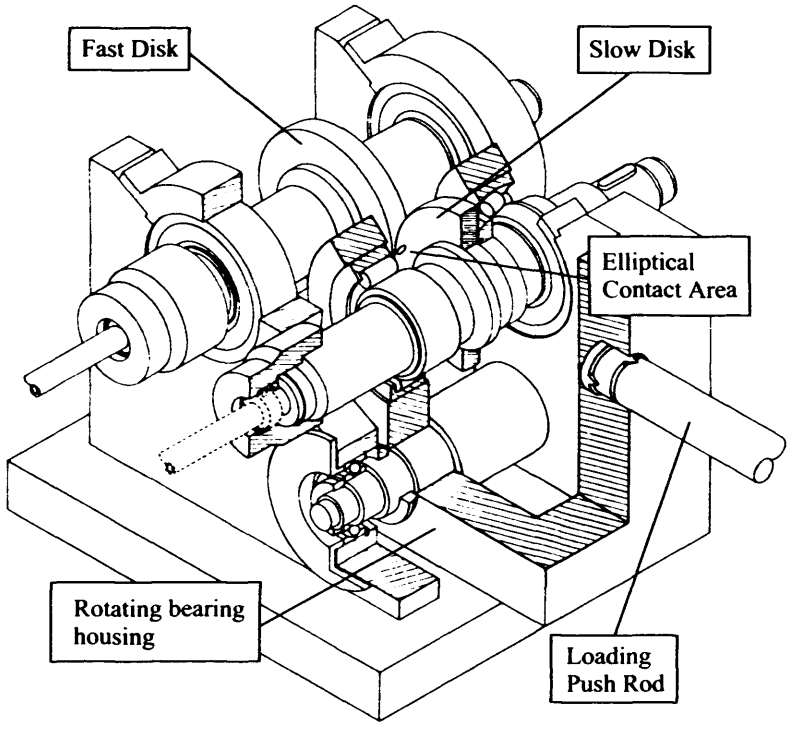

Figure 3.2: Isometric view of test head, showing the discs, shafts and bearings. Also shown is the approximate shape and area of the contact between the disks. (Adapted from Patching, 1994)

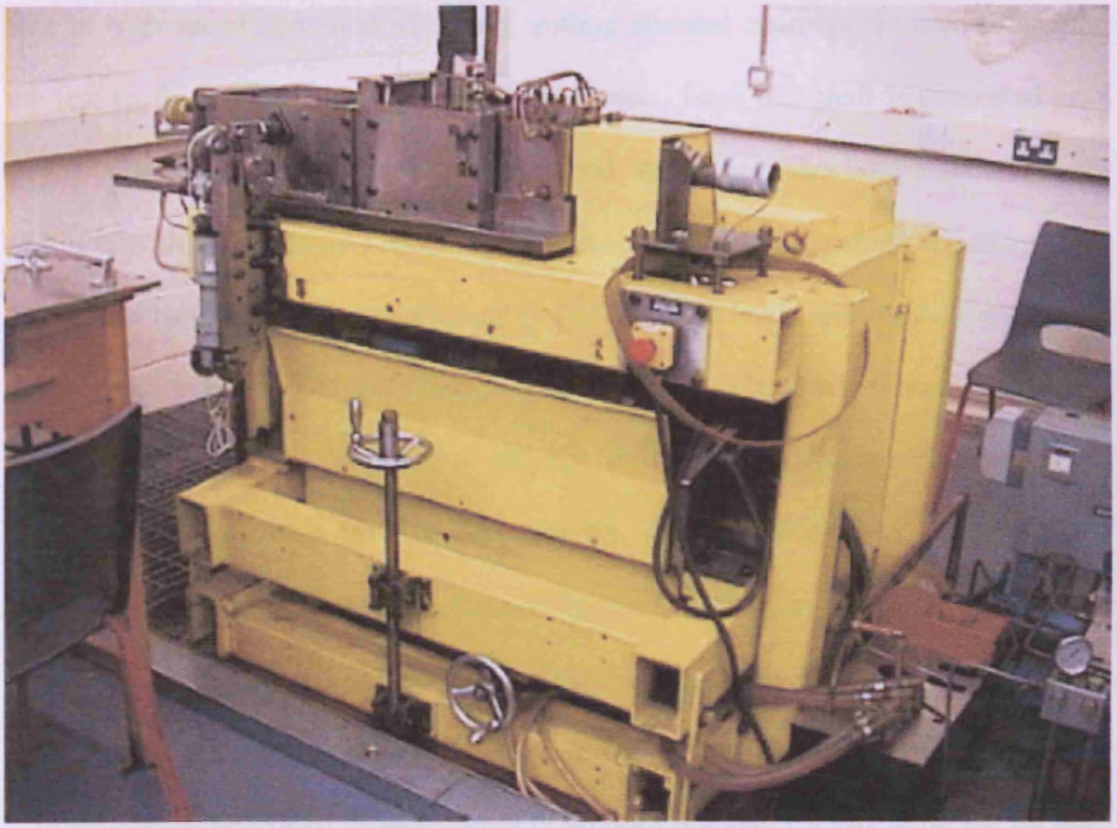

Figure 3.3: Overall view of the test rig (from Patching, 1994)

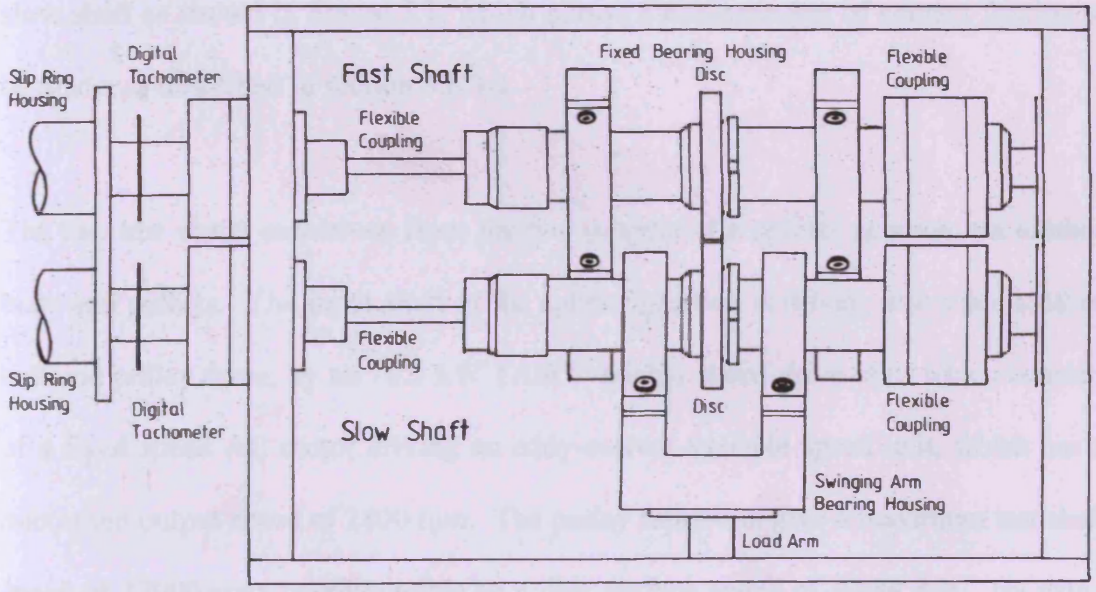

Figure 3.4: Layout of the test head (from Patching, 1994)

Due to high speed operation of the rig, rolling element bearings are used to support the test shafts in order to reduce frictional losses. Each test shaft is supported on a double row spherical roller bearing at one end, which provides both axial and radial restraint, with a cylindrical roller bearing at the other end of the shaft, which provides only radial restraint. This arrangement provides a high load capacity, whilst ensuring that thermal expansion of the shafts is unconstrained. The shafts were manufactured from EN36C steel, case-hardened to 680 Hv. They were finish ground between dead centres, ensuring a high level of concentricity. The test discs are pressed onto the shafts with a heavy diametral interference fit of between 15 and 20 μm, depending on manufacturing tolerances. Additionally, a locking nut is fitted. The shafts incorporate central and radial holes for thermocouple leads to allow measurement of disk temperature, as described in more detail in sections 3.4 and 3.5. As built, the rig used one thermocouple in each test disk, approximately 3 mm below the disk surface on the centre-line of the running track. In addition, a friction dynamometer is fitted in the slow shaft as shown in Figure 3.1, which allows a measurement of contact friction to be made, as described in section 3.6.3.3.

The two test shafts are driven from the two outputs of a splitter gearbox via toothed belts and pulleys. The input shaft of the splitter gearbox is driven, also via a toothed belt and pulley drive, by an 18.5 kW TASC variable speed drive unit, which consists of a fixed speed AC motor driving an eddy-current variable speed unit, which has a maximum output speed of 2800 rpm. The pulley ratios can give a maximum test shaft speed of 12000 rpm, corresponding to a disk surface speed of 47.88 m/s. By using different pulley ratios on the toothed-belt connection between the splitter gearbox and test shafts, the test rig is designed to allow test shaft speed ratios between 1 (pure

rolling) and 4.24, with both disk surfaces moving in the same direction relative to the contact.

If two surfaces are rolling and sliding together, with surface velocities of u_1 and u_2, then the sliding velocity is defined as

$$u_s = u_1 - u_2$$

and the mean entraining (rolling) velocity is

$$u_r = \frac{u_1 + u_2}{2}$$

The slide/roll ratio is thus given as

$$\frac{u_s}{u_r} = \frac{2(u_1 - u_2)}{(u_1 + u_2)}$$

In the test rig described here, both surfaces move in the same direction relative to the contact, as if connected by a single pair of gears (which, in effect, they are at the splitter gearbox). Therefore, the slide/roll ratio may be re-written in terms of the ratio, G, of the shaft speeds:

$$\frac{u_s}{u_r} = \frac{2(G-1)}{(G+1)}$$

The highest gear ratio available in the test rig in its current condition is 4.24, giving a slide/roll ratio of 1.24.

The test rig was designed for a maximum load of 4 kN at the contact, which corresponds to a maximum Hertzian contact pressure of 1.7 GPa for the disk geometry (76.2 mm diameter disks, with a crown radius of 304.8 mm). The load is applied by a hydraulic ram, via a bell-crank and push rod mechanism, shown in

Figure 3.5, where the hydraulic cylinder has been retracted in order to show the load cell.

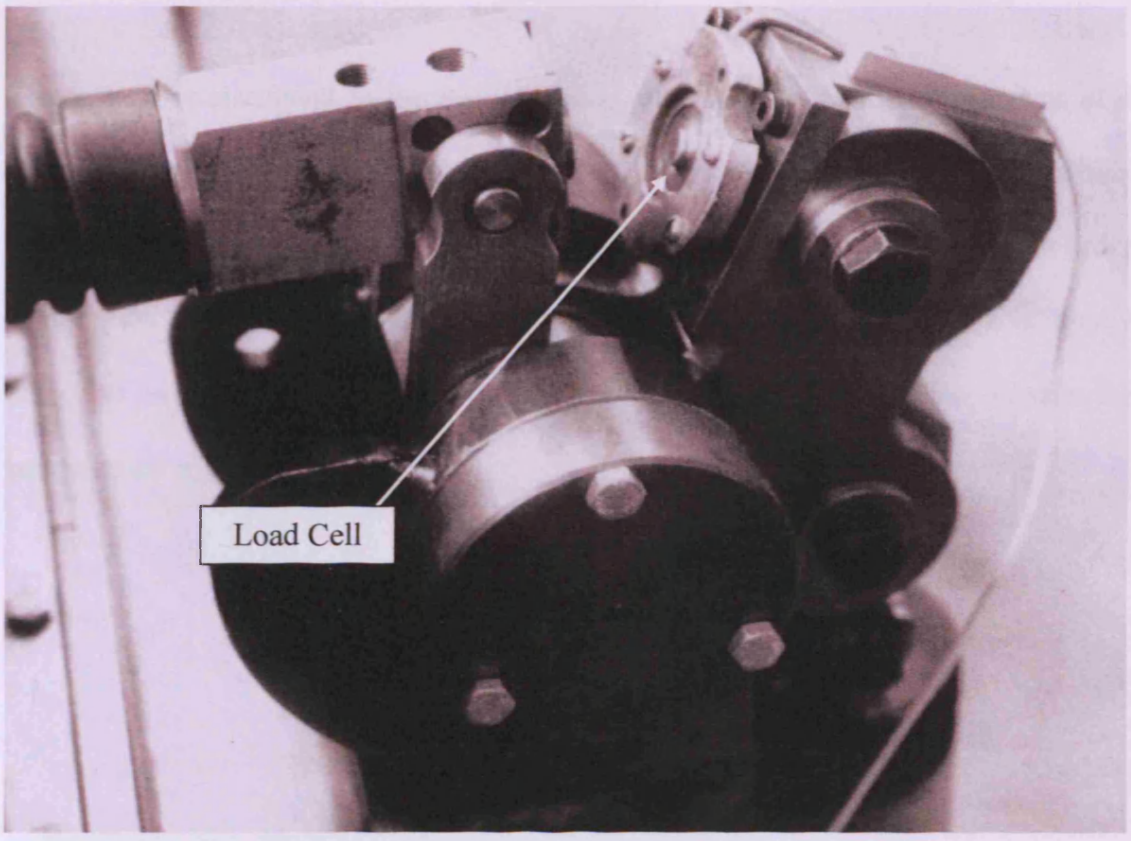

Figure 3.5: Hydraulic cylinder and loading mechanism (from Patching, 1994)

The slower shaft is mounted in a swinging yoke, which can be seen in Figure 3.2. The push rod, which transmits load to the yoke, makes contact via a crossed knife-edge, so that the load is applied at an accurately defined point. Thus any twisting of the loading mechanism (which would result in the contact point between the disks moving) is minimised, with the line of action of the loading always passing through the contact.

The load applied to the disks by this mechanism is controlled by varying the hydraulic system pressure by means of a solenoid-driven proportional valve. A load cell is

mounted on the bell crank to provide a direct measurement of the applied load. Calibration of this sensor is discussed in section 3.6.3.2.

The test oil is circulated to the test disks and shaft support bearings by means of a constant displacement pump. The oil is held in an electrically heated tank, which incorporates thermostatically controlled heating elements rated up to 4.6kW in order to maintain the oil at temperatures of up to 200°C. The oil within the tank is rapidly stirred to ensure an even temperature of the oil. A filter rated at 1μm is fitted in the test head oil supply line.

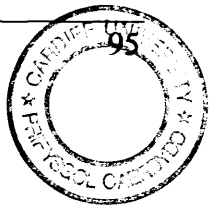

3.3 Original scuffing tests

The tests previously carried out by Patching using the test rig described here were designed to investigate scuffing failure of aerospace gear contacts. Full details of the tests are reported in Patching *et al.* (1995), but an outline of the test procedure is given here, since these tests form the basis of the initial EHL modelling of heat partition carried out by the author.

During the tests the disks were run at a constant speed. At the start of each test oil was circulated through the test head and the disks were run together at a very light load until the temperatures stabilized. At this point the first load was applied, which corresponded to a maximum Hertzian contact pressure p_0 = 0.6 GPa. This load was held constant for 3 minutes. The load was then increased to give p_0 = 0.7 GPa and held constant for a further 3 minutes. This procedure was repeated, in steps of 0.1 GPa for p_0, until scuffing occurred or the maximum load corresponding to p_0 = 1.7 GPa was reached.

Scuffing was detected by a sudden increase in friction and noise from the test head. If scuffing occurred, the load was quickly removed by means of a dump valve located in the line to the hydraulic loading system. A typical chart record showing the latter stages of a scuffing experiment can be seen in Figure 3.6 (note that time is increasing from right to left).

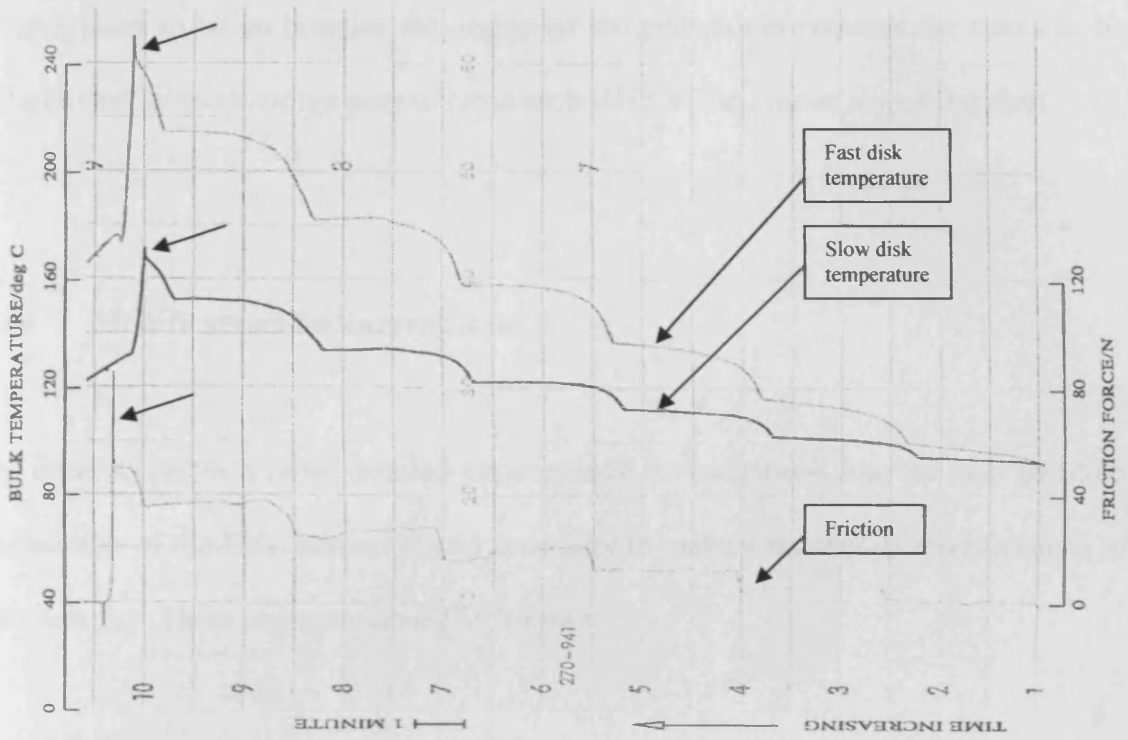

Figure 3.6: Typical chart record from scuffing experiment (from Patching, 1994)

The test trace in Figure 3.6 shows, from the top, the fast disk thermocouple temperature, slow disk temperature, and friction force. The steps in the friction and corresponding increases in the disk bulk temperatures can be clearly seen, at three minute intervals as the load is increased. The temperatures can be seen to approach steady-state conditions towards the end of each three-minute load stage. The friction force tends to decrease over each three minute load stage: the test shown here used ground disks and this friction reduction is thought to be due to running in effects in this case. The onset of scuffing may be seen in the sharp "spike" in the friction and temperature traces at the end of the test, immediately before the load is removed as arrowed. Close inspection of Figure 3.6 may suggest that the friction and temperature responses to an increase in load are offset from each other in time – this is not the case

but appears to be so because the design of the pen plotter requires the traces to be slightly offset to allow the pens to cross each other as they move across the chart.

3.4 Modifications for current tests

In order to perform more detailed experimental investigations into the heat partition behaviour of the EHL contact it was necessary to make a number of modifications to the test rig. These are summarised as follows:

1) Fitting of additional thermocouples to each disk, giving a total of 6 thermocouples per disk, at various positions near the running track. The position of these thermocouples is described in detail in section 3.5.2. The use of additional thermocouples removes the need to thermally model the entire disk and shaft assembly when computing the heat partition parameter, β, as was necessary when modelling the experiments of Patching. This is achieved by using some of the measured temperatures as boundary conditions in the thermal model of the outer annular regions of the disks.

2) The fitting of insulating washers to each side of the test disks to control axial heat flow from the sides of the disks. This simplifies the modelling of the heat transfer boundary conditions, since the washers reduce the flow of heat from the sides of the disks to a negligible amount. Thus, only one heat transfer coefficient needs to be determined – that from the running track of the disk. This can be measured using a simple run-down test, as shown in Figure 3.7. The disks are run together under load until they reach steady-state temperatures. The load is then removed, and the disks

separated from contact, such that the decay of their temperatures is only due to the convective heat transfer from the running track. The removal of the load stops the frictional heat input to the disks – there is no change to the cooling of the disks. The insulating washers are described in section 3.5.3.

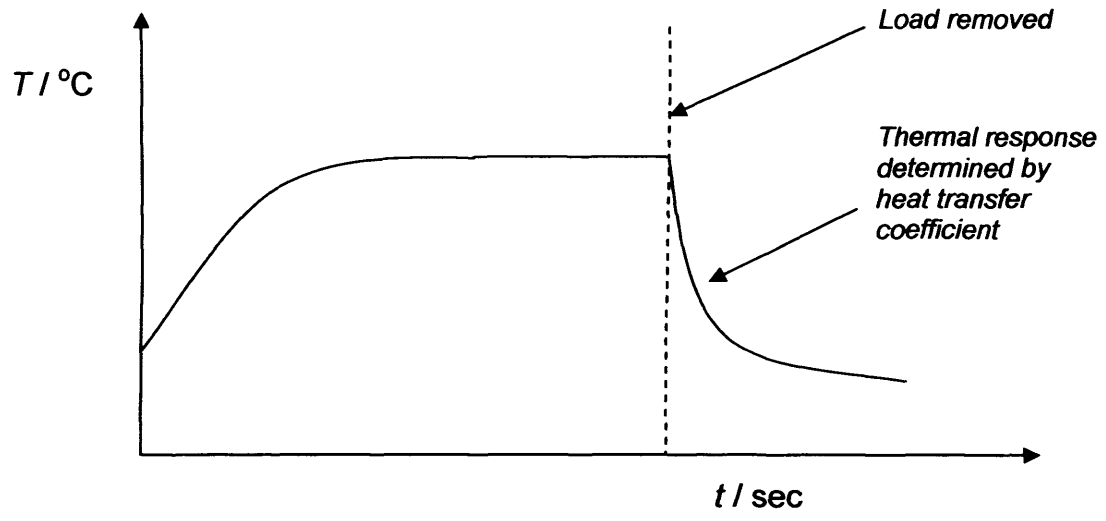

Figure 3.7: Run-down test to establish heat transfer coefficients

3) The development and installation of a new computer-based data acquisition and control system. This is described in section 3.6.

3.5 Test discs and shafts

3.5.1 Description of test discs

The test disks used in this work were of a standard geometry used for the majority of disk machine work at Cardiff. They are 76.2mm (3") in diameter with a crown radius of 304.8mm (12"). Thus, the dry Hertzian contact between the test disks is in the form of an ellipse with axis ratio of 3.91. The larger dimension (i.e. the major axis) of the contact is parallel to the shaft and disk axis, such that entrainment is in the same direction as the smaller dimension of the contact. Figure 3.8 shows the dimensions of the test disks.

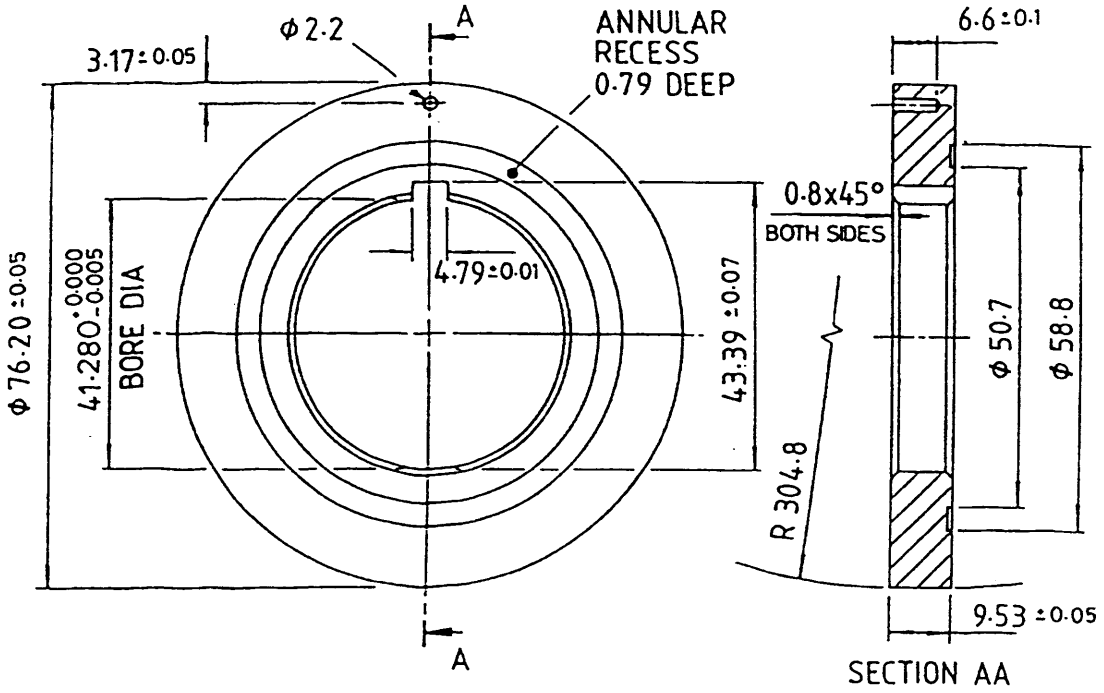

Figure 3.8: Drawing of test disks (all dimensions in mm)

The disks used in this work were manufactured from case-carburising Nickel-Chromium alloy steel supplied by Rolls-Royce, to their specification RR6010, which is given in Table 3.2.

Table 3.2: Composition of RR6010 steel (% mass)

Element	C	Si	Mn	P	S	Ni	Cr	Mo
max	0.18	0.35	0.55	0.015	0.012	4.30	1.40	0.30
min	0.14	0.10	0.25	0.0	0.0	3.80	1.00	0.20

The disks were heat treated to a typical aerospace specification, which is outlined in Table 3.3:

Table 3.3: Heat treatment specification

- Normalise @ 930°C ±10°C for 3 hours ±15 minutes
- Harden @ 850°C ±10°C for 3 hours ±15 minutes
- Temper @ 530°C ±10°C for 3 hours ±15 minutes
- Carburize @ 927°C ±10°C to yield a carburized case depth (Rc 50) of 0.036 to 0.042 inch, with a surface carbon (second 0.002" cut) of 0.65 to 0.95% Carbon
- Cool to room temperature after carburising
- Stress relieve @ 566 to 621°C for 4 hours ±15 minutes, then air cool
- Harden @ 788 to 829°C for 30 minutes, then oil quench (24 to 60°C)
- Subzero treat, within 60 minutes of quenching, for 3 hours minimum at–79°C or lower
- Temper @ 160°C ±5°C for 3 hours ±15 minutes
- Final carburized surface hardness to be HRC 60 to 63
- Case depth (HRC 50) to be 0.036 to 0.042"
- RC 60 depth to be 45% of 0.036" (0.016" of case)
- Core hardness to be HRC 36 to 41

Following heat treatment, all test samples were ground to produce an axial finish which reproduces the direction of finishing typically found on aerospace gears. Following grinding, the disks were super-finished by Metal Improvement Company,

Newbury, who kindly treated the disks free of charge. Their proprietary method uses a combination of abrasive and chemical treatment. The disks were finished to a typical Ra of 0.04μm. A super-finished disk may be seen in Figure 3.10, which clearly shows the high finish achieved.

Figure 3.10: Super-finished test disk

Following super-finishing, the circumferential roughness of the test disk running surface was measured using the Taylor Hobson Form Talysurf 2. Figure 3.11 shows the set-up used to measure circumferential profiles using the Talysurf. After the raw profiles were acquired, they were filtered in the Taylor Hobson "Ultra" software to remove the longer wavelength components of the surface finish (waviness) using a Gaussian filter with a cut-off wavelength of 0.25mm. The roughness average (Ra) was then computed. A typical roughness profile from a super-finished disk is shown in Figure 3.12 – in this case the Ra was 0.037μm.

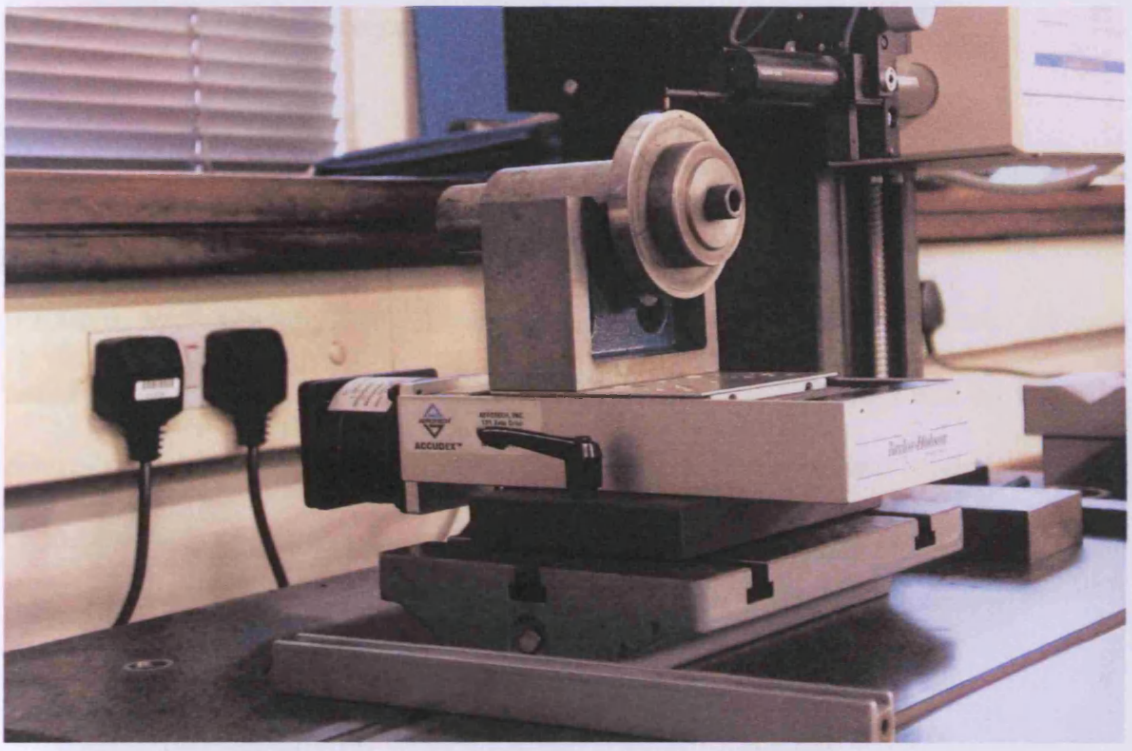

Figure 3.11: Measurement of disk surface roughness in circumferential direction

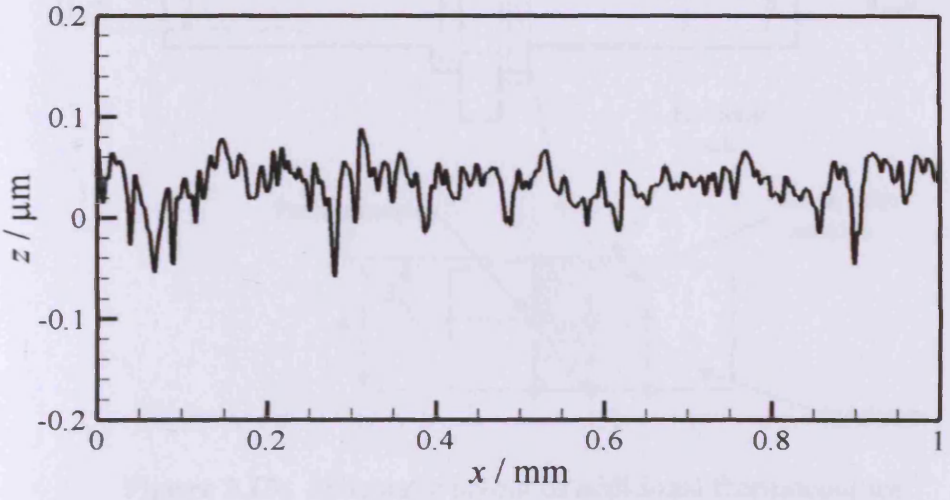

Figure 3.12: Typical circumferential roughness profile from an un-run, super-finished disk

3.5.2 Additional disk temperature measurements

In order to fit the five additional thermocouples to the test disks, it was necessary to spark-erode holes into the disks. The thermocouples were located at two radial positions, approximately 3 and 6mm below the surface of the running track. At each radial position thermocouples were located near to each disk face, and on the axial centre-line, as shown schematically in Figure 3.13 which compares modelled regions of the original, single thermocouple, disk and shaft (one-quarter cross section) with the modified disk with insulating washers.

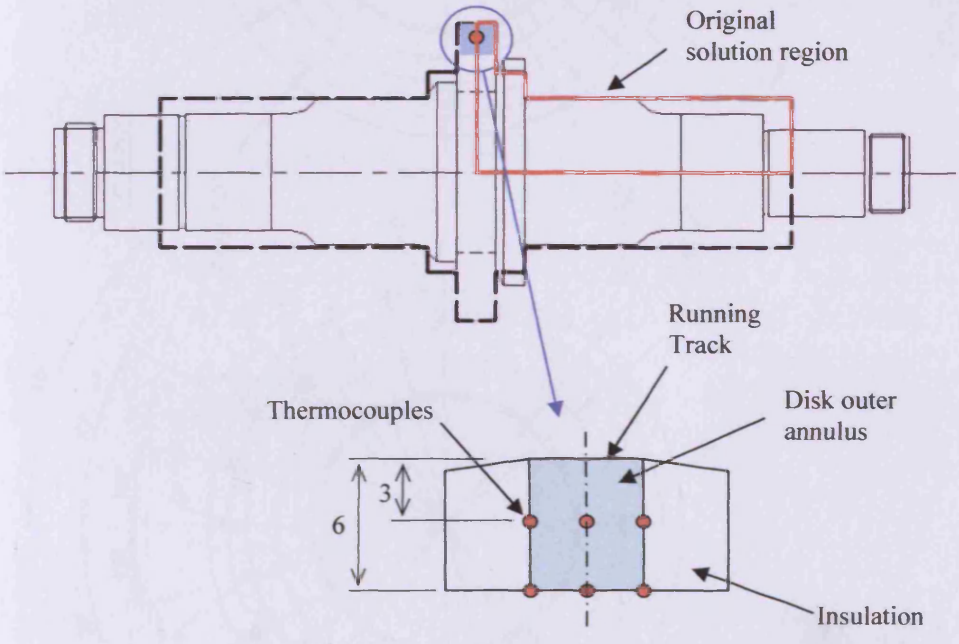

Figure 3.13: Schematic layout of additional thermocouples

Figure 3.14 shows the position and depth of the various thermocouple holes. It can be seen from the figure that there are twelve holes in each disk. This is designed to allow a replacement thermocouple to be fitted with relative ease should an existing thermocouple fail during testing.

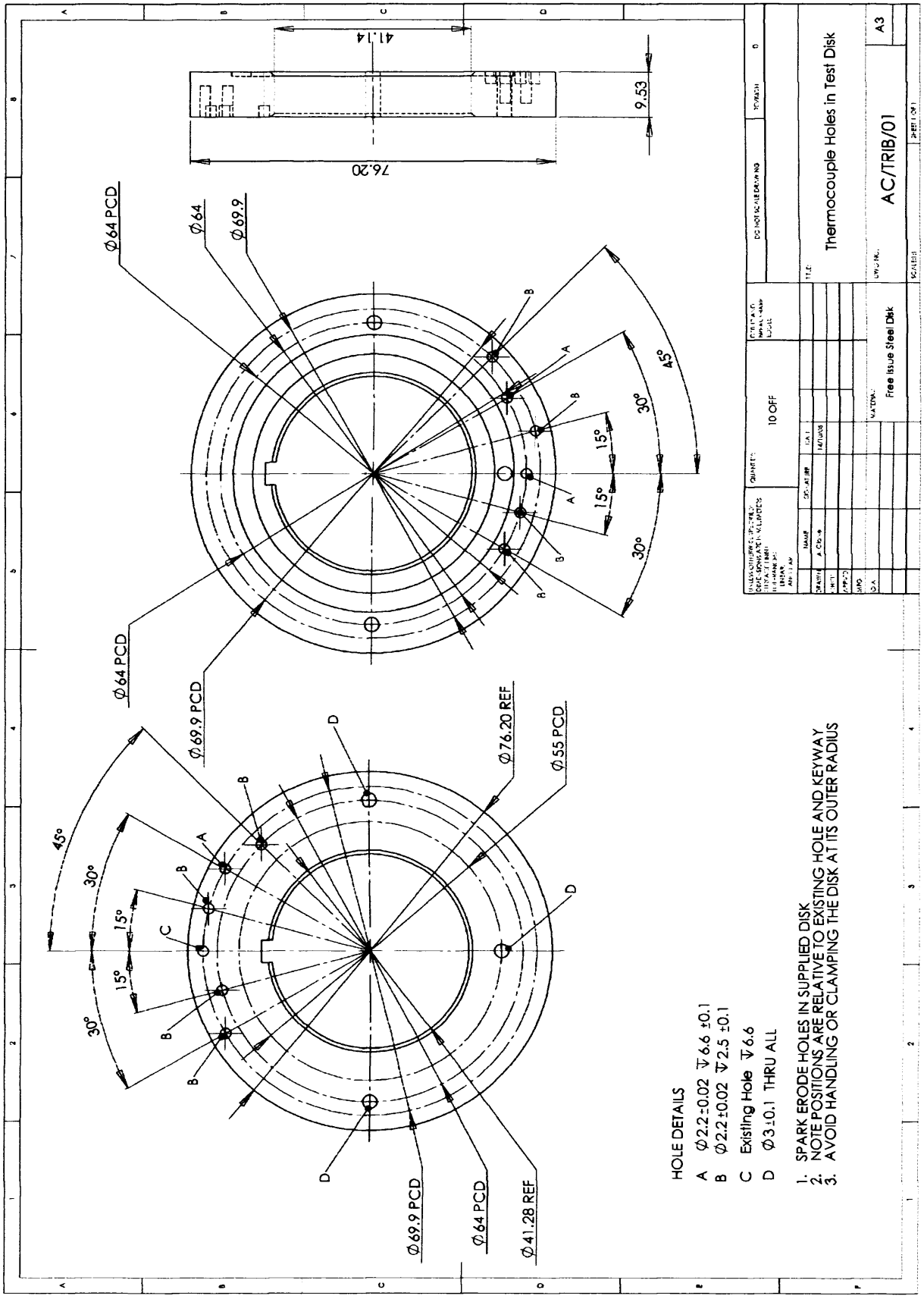

Figure 3.14: Details of thermocouple installation holes

3.5.3 Insulating washers

The insulating washers were designed to fit over either side of the test disk. They feature a central hole through which the shaft passes, together with a number of smaller holes through which the thermocouple leads pass. They have an outside diameter (76mm) which is slightly smaller than the outside diameter of the test disks (76.2mm / 3"), and are slightly tapered to ensure that the washers fitted to one disk do not come into contact with their counterparts on the other shaft. This avoids the production of wear particles which could contaminate the contact. The washers are held onto the disk using machine screws.

PTFE was originally selected for the washers as it is a highly insulating material which can withstand elevated temperatures. The material has a thermal conductivity of 0.20 $Wm^{-1}K^{-1}$ which is only 0.4% that of steel. It can operate at temperatures up to 260°C, although significant decomposition does not occur until over 400°C, which is more than sufficient for this application. The washers can be seen in Figure 3.15, and are shown fitted to a disk in Figure 3.16.

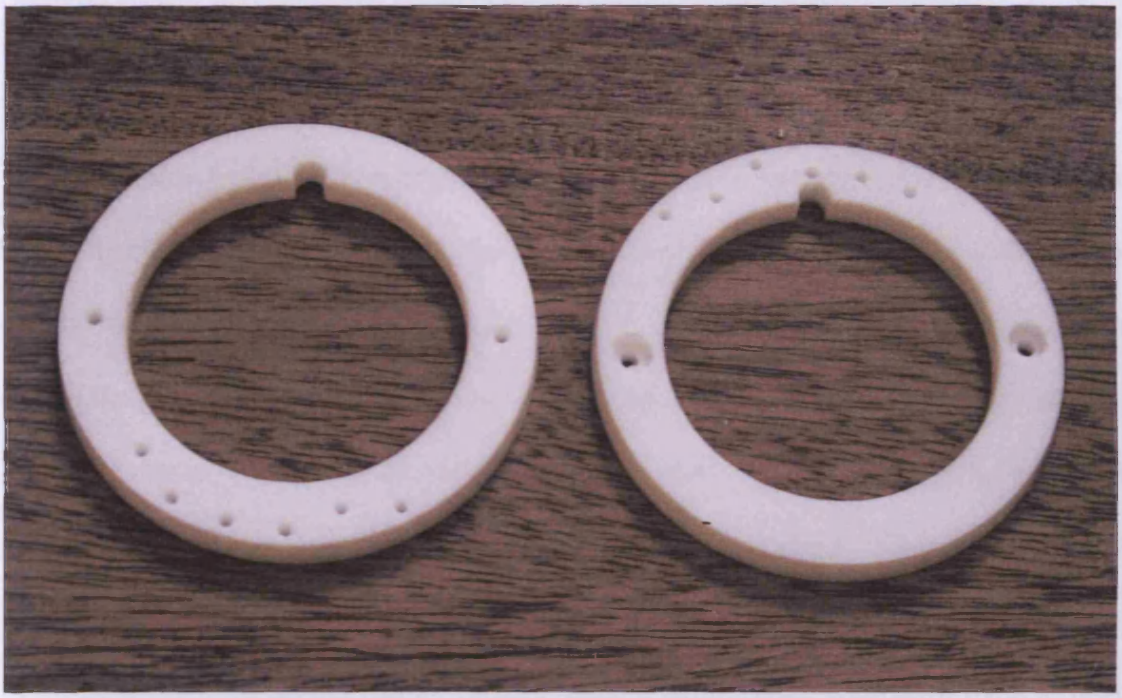

Figure 3.15: PTFE insulating washers

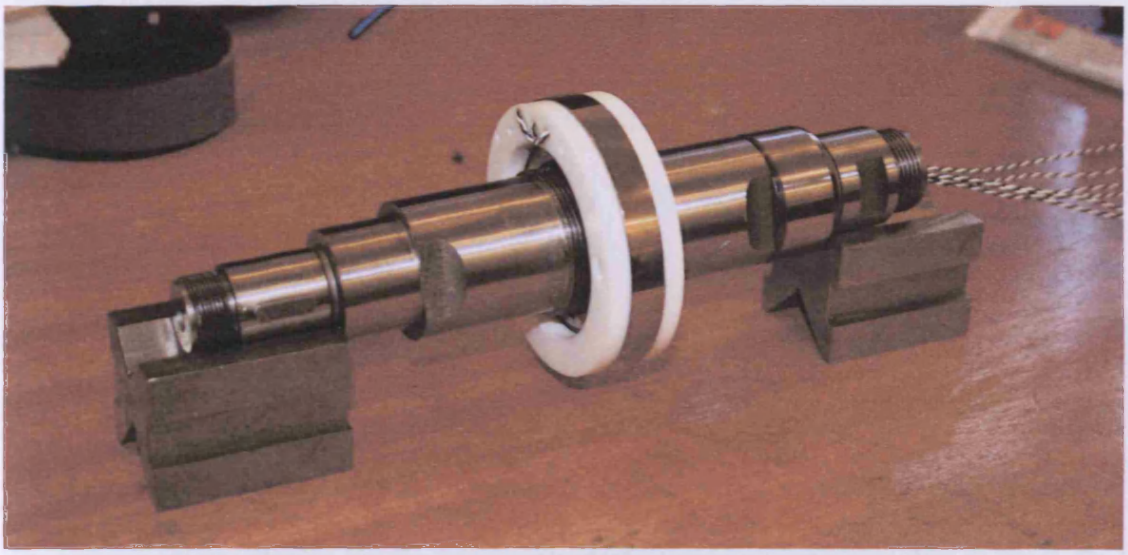

Figure 3.16: PTFE insulating washers fitted to a disk

However, following initial commissioning of the modified test rig, a number of experiments were performed which involved applying low loads to the disks at a range of sliding speeds, in order to identify any potential problems with the operation

of the test rig. During these experiments, the temperatures recorded by the thermocouples did not exceed 120°C. Unfortunately, during these tests the thermocouples failed. Upon stopping the test rig and inspecting the disks, it was found that the PTFE washers had become detached from the sides of the disks and a number of thermocouple leads had been severed. It was initially though that this was due to the failure of the nylon machine screws which were used to attach the washers. However, upon careful measurement of the washers it was found that they had expanded significantly as the temperature of the disk increased. This led to contact between the washers on the two disks around their circumference and shearing of the machine screws. A further test performed using a temperature-controlled oven to heat a PTFE washer to approximately 120°C at which point careful measurements of its diameter were taken. It was found to have expanded by up to 1mm, which makes the PTFE unsuitable for use as insulation in the test rig, where disk temperatures are likely to be even higher. This is further illustrated by consideration of the thermal expansion coefficient of PTFE (23×10^{-5} K^{-1}) which is an order of magnitude higher than that of steel (12.6×10^{-6} K^{-1}).

The failure of the insulating washers was regrettable due to the large amount of time taken to prepare disks, install and calibrate thermocouples, and install into the test rig. Thus, the material choice for the insulating washers was re-considered in order to find a more suitable and thermally stable material.

A range of materials were considered, including a fibrous material sold in sheets which would have to be clamped against the test disk with a steel retaining plate. However, the uncertainty over the thermal conductivity of this material once it

became oil-soaked when in use made it unsuitable for this application where an accurate value of the thermal conductivity of the insulating material is necessary for the accurate analysis of the experimental results.

A second option was to prepare steel washers to which a ceramic coating could be applied, such as that offered by Zircotec Ltd. These zirconia-based coatings are offered primarily to the motorsport industry to control heat losses from exhaust manifolds in order to retain heat within the exhaust gases for optimum engine power output. However, the resulting coated washers would have required measurements to determine their overall thermal conductivity which would further complicate the experimental work.

After extensive investigation of the options, a machinable ceramic material was identified as being most suitable for use as insulating washers. The ceramic, Macor, is produced by Corning Incorporated and is available in the UK from a range of suppliers. The material is, unlike most ceramics, machinable with normal metalworking tools to a high tolerance (0.01mm) and can be continuously used at temperatures of up to 800°C. Importantly, it has a coefficient of thermal expansion of 9.3×10^{-6} K^{-1}, which is of a similar magnitude to that of steel. It is an excellent thermal insulator, with a thermal conductivity of 1.46 W/mK (Corning Inc., n.d.). Following discussions with technical staff at a UK supplier of the material (Precision Ceramics Ltd.) it was decided that Macor would be a suitable material for the insulating washers. Precision Ceramics have extensive experience of machining Macor and, as such, were chosen to supply the material and finish machine the washers. The

manufacturer's data sheet on the material may be found in Appendix A. A ceramic washer can be seen in Figure 3.17.

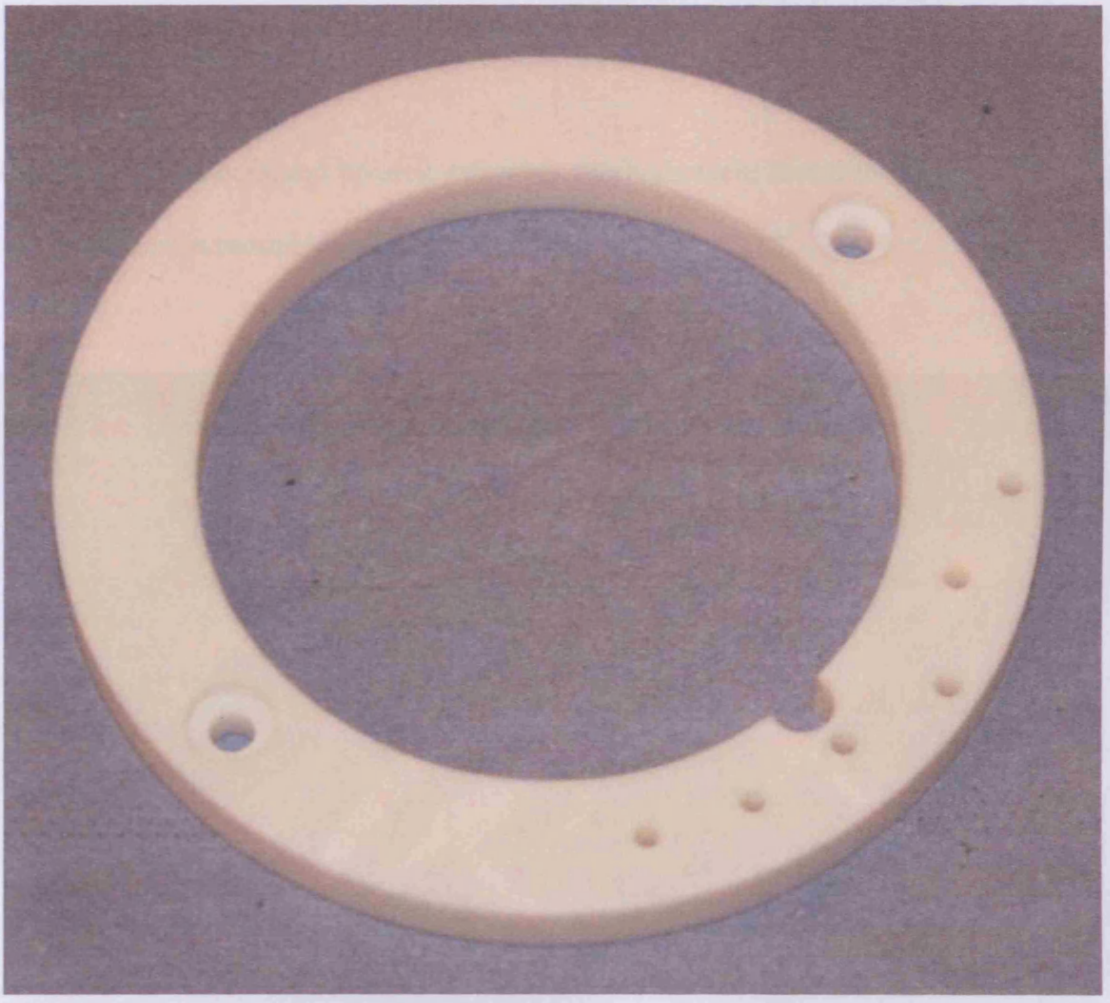

Figure 3.17: Macor machinable ceramic insulating washer

In addition to the use of a ceramic material for the washers, it was decided in consultation with Precision Ceramics to employ an adhesive bond between the ceramic washer and the disk face in addition to steel machine screws. A range of adhesives companies were consulted, and a suitable adhesive was identified in the Permabond range, ES550 grade. ES550 is a single-part heat curing rubber toughened epoxy, which is suitable for use at continuous temperatures up to 180°C (Permabond, n.d.). It is cured by heating to 120°C for 40 minutes, which allows the washers to be

accurately located on the test disks using the machine screws before the adhesive is cured. The adhesive, being rubber toughened, allows some slight relative thermal expansion between the ceramic and the steel to take place.

The ceramic washers and bonded assembly methods were found to be very effective, and may be seen mounted to the disk machine in Figure 3.18.

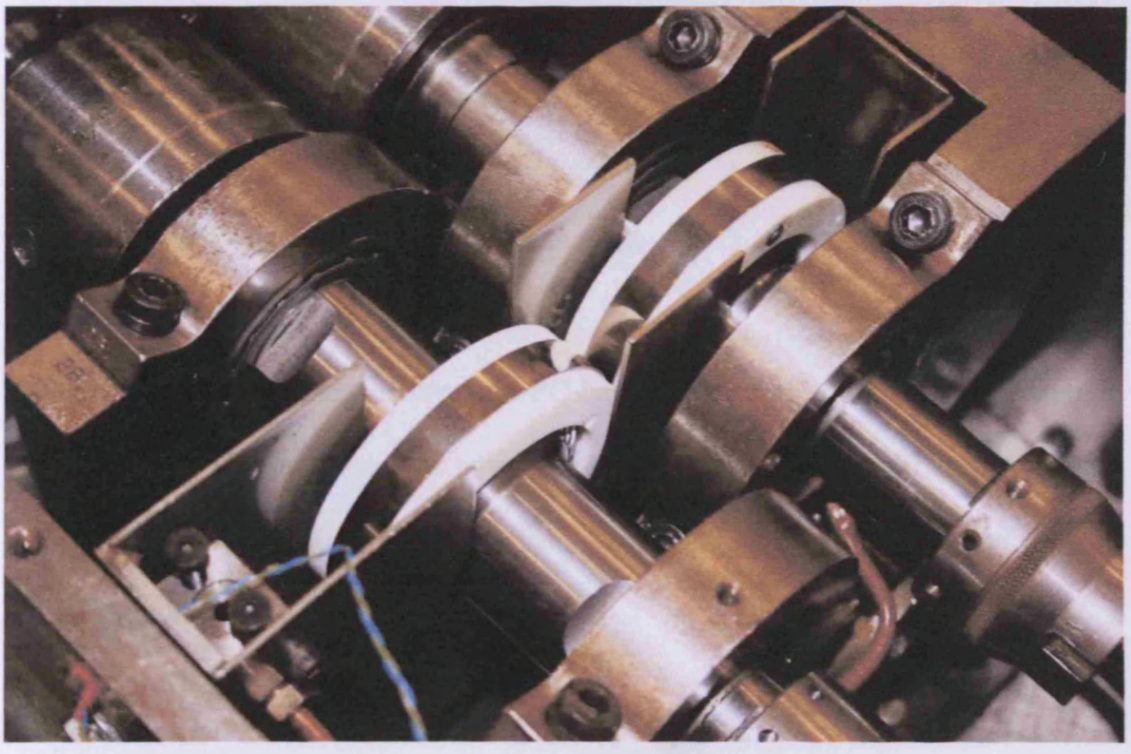

Figure 3.18: Rig with ceramic washers fitted to test disks

3.6 Instrumentation, data acquisition and control system

3.6.1 General Description of System

As discussed in Section 3.4, it was decided to replace the existing PC-based data acquisition and control system for the rig with a new system. The original system was developed in LabVIEW 4. Not only have the capabilities of PC-based data acquisition software packages improved significantly since the original system was written, but hardware chosen for interfacing the additional thermocouple signals was incompatible with the older version of LabVIEW. A new system was developed which used the inputs and outputs shown in Table 3.4.

The new system continues the previous PC-based system's use of certain components from the original control system where possible, such as the amplifier for the load measurement. The 0-10V DC output from this amplifier was connected to the data acquisition card in the PC.

Table 3.4: Inputs and Outputs to Data Acquisition System

Signal	**Type**	**Description**
Disk Temperatures (12 channels)	Thermocouple Analogue Input	6 J-Type thermocouple signals per disk
Disk oil delivery temperature	Thermocouple Analogue Input	J-Type thermocouple
Applied Load	Voltage Analogue Input	Load Cell
Friction	Voltage Analogue Input	Strain gauge torque transducer
Fast shaft speed	Digital Input	TTL signal from Optical Sensor
Slow shaft speed	Digital Input	TTL signal from Optical Sensor
Motor speed control	Analogue Output	Signal to control TASC drive unit
Load control	Analogue Output	Signal to control hydraulic proportional valve

The schematic of the system can be seen in Figure 3.19. Each sensor is described in more detail in Section 3.6.3.

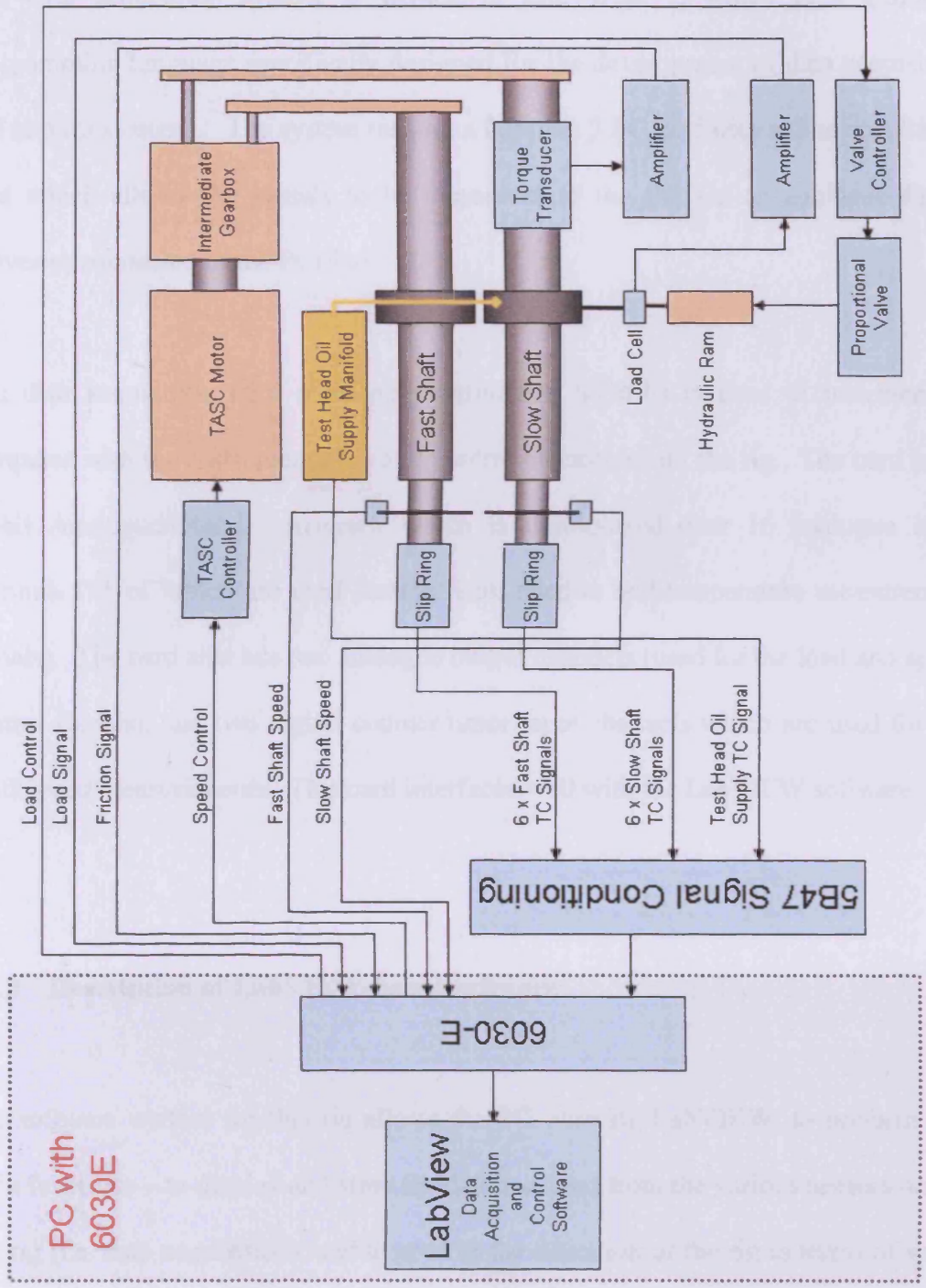

Figure 3.19: Schematic of test rig data acquisition and control system sensor layout

The data acquisition system is written in LabVIEW 7, which is a graphical programming language specifically designed for the development of data acquisition and control systems. The system runs on a Pentium 3 PC, and uses a data acquisition card which allows the signals to be connected to the PC via an analogue-digital converter connected to the PCI bus.

The data acquisition card (National Instruments 6030-E) is used to interface the computer with the instrumentation and control electronics on the rig. The card has a 16-bit Analogue/Digital converter, which is multiplexed over 16 analogue input channels (15 of which are used for the load, friction and temperature measurement signals). The card also has two analogue output channels (used for the load and speed control signals), and two digital counter/timer input channels which are used for the shaft speed measurements. This card interfaces well with the LabVIEW software.

3.6.2 Description of LabVIEW-based software

The software written for this rig allows the PC, running LabVIEW, to perform two main functions – to display and store the data received from the various sensors on the test rig (i.e. data acquisition), and to control the operation of the rig in terms of speed and load.

Software written in LabVIEW consists of two parts – the user interface (called a "Front Panel") and the code which controls the user interface (called a "Block Diagram"). The user interface developed for the test rig can be seen in Figure 3.20.

Figure 3.20: User interface ("front panel") of the LabVIEW software for the test rig

The main part of the user interface consists of three charts (designed to be similar to the original chart recorder presentation). These show a configurable number of temperatures together with the load and friction levels. Like the chart records, these charts expand over the duration of a test to show the entire test history in a graphical form. The current numerical value of each of the logged parameters is also shown on the screen, so that the current value can easily be determined without the need to estimate values from a chart. The software also compares each thermocouple signal with the allowable range for that thermocouple and displays a "thermocouple healthy" light (green) or a "thermocouple damaged" light (red) on the front panel adjacent to the numerical display of temperatures.

The LabVIEW software acquires data from the 6030E at a user-configurable rate (usually 1 – 2 Hz) for graphical display. Adopting a faster rate is unnecessary and merely records a large amount of data at a frequency far higher than required. The value of each of the logged parameters (as shown in Table 3.4) is recorded in a text file at the same rate. When it acquires the data, the software filters the signal by taking the DC value of a batch of samples in order to reduce the effects of noise.

In addition, the LabVIEW user interface allows the user to select load and speed values for control of the test rig. The control section of the block diagram is outside of the timed-loop which acquires data, so that changes made by the user to the demanded speed or load are implemented as soon as possible. Currently, control is performed in an open-loop manner, although it is possible to operate a closed-loop control scheme using functions available within LabVIEW. It is also still possible to operate the rig in manual mode, using the control gear on the original instrumentation cabinet. In this case, the LabVIEW software only performs the data acquisition functions.

3.6.3 Implementation and calibration of instrumentation

3.6.3.1 Thermocouple Construction and Instrumentation

To maintain continuity with the previous tests performed using the test rig, J-type thermocouples (iron / constantan) were used. Six were fitted in each disk, as shown in

section 3.5. The thermocouples were originally held in place using copper ferrules which are swaged into the spark-eroded holes in the disks, but this was changed to adhesive fixing using an electrically insulating cement part way through the development of the test rig for the current work in order to help reduce ground-loop problems and for ease of installation.

Previously, the two thermocouples (one per disk) were connected using J-type extension wire to two custom-built cold-junction compensation and amplification units. These units also included full channel-to-channel isolation using optical coupling. The output of these units was then fed to both a chart recorder and the original LabVIEW data-acquisition system.

During the development of the rig for the present work, a standard data-acquisition card designed to directly interface thermocouple signals to the PC was selected. The PCI-DAS-TC card, manufactured by Measurement Computing, was designed to interface all of the thermocouple measurements. It allows up to 16 multiplexed thermocouple signals to be connected, and includes a terminal block which has a built-in cold-junction sensor. The card performs linearization of the thermocouple signal and cold-junction compensation, before passing the measured temperature into the LabVIEW software. Various parameters can be adjusted by the user, such as thermocouple type (J-type for this rig), as well as settings related to on-board smoothing of the thermocouple signals. Although it is not a National Instruments product, software drivers are available to allow its use with LabVIEW. The card may be seen in Figure 3.21.

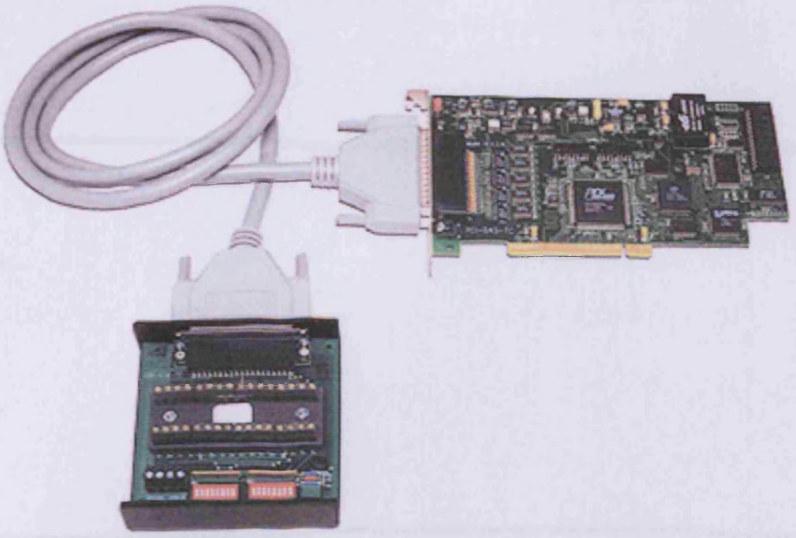

Figure 3.21: PCI-DAS-TC thermocouple card

As part of the commissioning of the card, a number of tests were carried out to investigate its performance.

A simple test was carried out to determine if there was any interaction between the thermocouple signals. Two disk specimens were prepared, each with a thermocouple fitted with a copper ferrule swaged into place. One test specimen was left at room temperature, whilst the second was placed into a glass beaker of hot water. The temperatures were continuously recorded on the PC using the PCI-DAS-TC card and LabVIEW. Once the temperatures had stabilised, the test specimens were connected electrically using a length of hook-up wire. After a timed interval, this connection was broken, and then re-made.

Figure 3.22 shows the recorded temperature trace, with periods of electrical connection indicated.

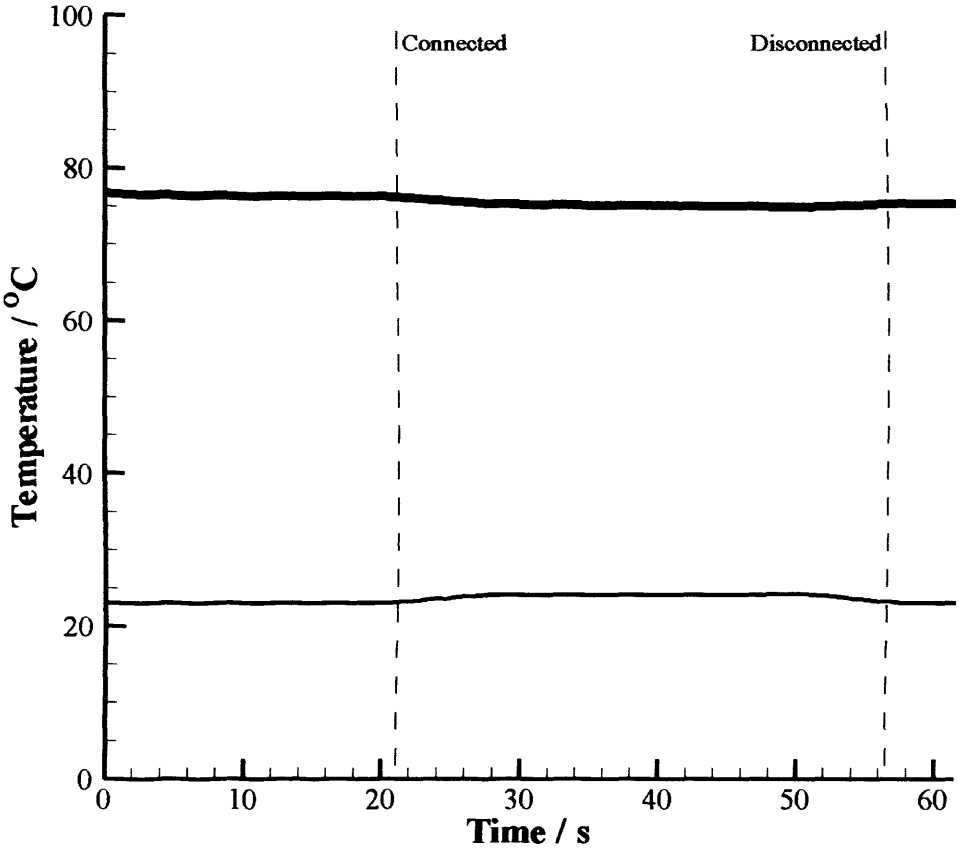

Figure 3.22: Electrical connection test using non-insulated thermocouples

Inspection of figure 3.22 clearly shows that, when the disk specimens are electrically connected, there is some interference between the temperature signals. When the specimens are connected, a clear reduction in the measured temperature of the hotter specimen can be seen accompanied by an increase in the measured temperature of the specimen at ambient temperature. When the specimens are subsequently disconnected the changes are reversed.

When installed in the test rig with copper ferrules, a (poorly defined) conduction path exists between each of the thermocouples, simulated in the simple test by connecting the two specimens. In addition, the PCI-DAS-TC only features block-isolation from the PC. The inputs are isolated from the PC after the multiplexer and digital to

analogue conversion has taken place, but the individual thermocouple inputs share a common ground at some point within the input circuitry of the card. This is done in the interests of reducing costs as simple binary opto-isolators can be used whereas more expensive linear opto-isolators are required for channel-to-channel isolation. However, this lack of full isolation means that there is the potential for the thermocouple signals to influence each other (i.e. a hotter thermocouple is able to "drive" the input of a cooler thermocouple, since it generates a higher thermal E.M.F.). In addition, ground-loops can occur as the ground at the test-rig may be at a slightly different potential to that at the PCI-DAS-TC card. Since a J-type thermocouple only generates a potential difference of approximately 42mV at its upper temperature limit of 750°C (Labfacility Temperature Handbook, 2006), even a small difference in ground potential can destroy the accuracy of the measurements.

Although the magnitude of the changes in the measured signals were not large, of the order of 2°C or less, they are very significant as they are of the order of the temperature differences which the rig described here is intended to measure.

In order to try and eliminate these problems, a new thermocouple construction technique was developed. The two strands of the thermocouple wire were twisted together, ensuring that they were in electrical contact. They were secured with solder. They were then coated with a ceramic cement. The ceramic cement is an electrical insulator but has reasonable thermal properties when compared to other materials used to isolate thermocouples, such as PTFE. Its conductivity is 1.5 $Wm^{-1}K^{-1}$ (Omega Engineering, 2006) whilst that of steel is 45 $Wm^{-1}K^{-1}$ and PTFE 0.2 $Wm^{-1}K^{-1}$. The cement has a maximum service temperature of 840°C. Once this coating of cement

had dried, the thermocouple bead was inspected to ensure that there was no exposed conductor material. This bead was then cemented into the hole in the test disk with more cement. Finally, the installed thermocouple was tested with a multimeter to ensure that it was insulated from the test disk.

The test was then repeated with two specimens fitted with the new type of thermocouple. The temperature trace may be seen in Figure 3.23.

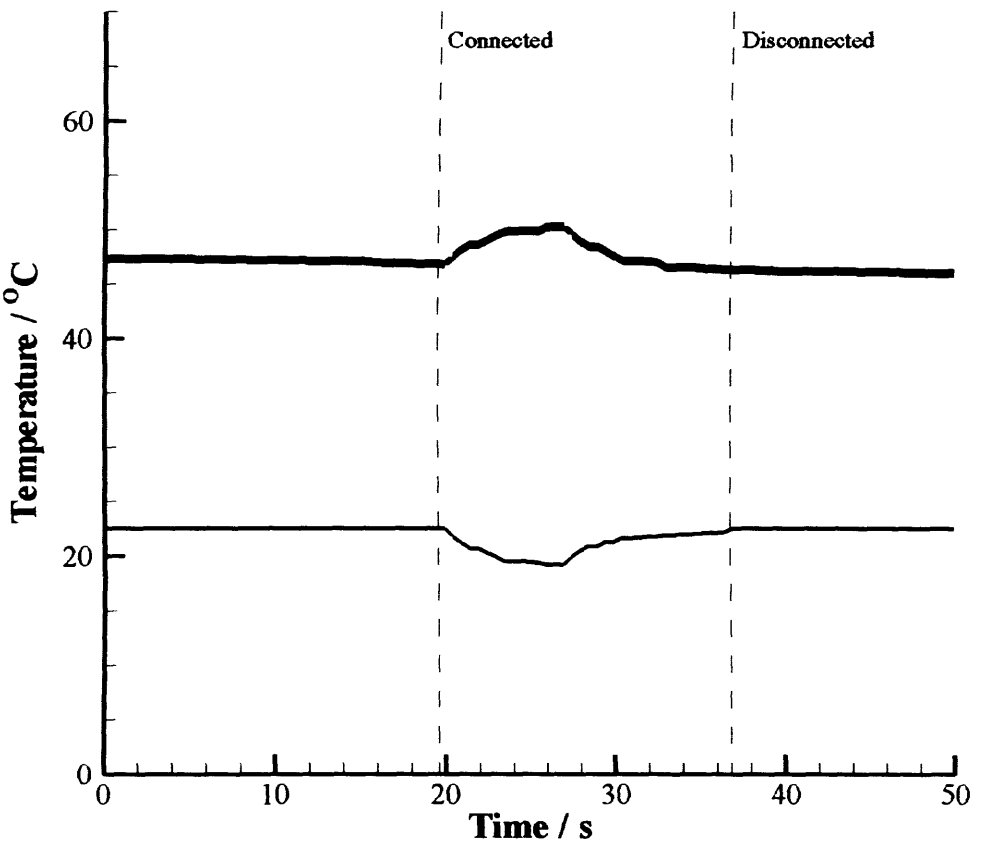

Figure 3.23: Electrical connection test using insulated thermocouples

Figure 3.23 shows that, even though the thermocouples were insulated from the test specimens, there were still measurement problems observed when the two specimens were electrically connected. Interestingly the influence between the thermocouples is now reversed when compared to figure 3.22 – the hotter disk measured temperature

increases and the measured temperature of the disk at ambient conditions appears to decrease when the disks are electrically connected. In addition, the effect of connecting the disks is not constant as the temperature can be seen to fluctuate during the period of connection. Although the effect decays during the period of connection, there seems to be a constant offset, particularly visible on the cooler disk, which disappears when the electrical connection is broken. Further testing showed that the magnitude of this offset could be up to 3°C, depending on the magnitude of the temperatures involved.

Although electrically insulating the thermocouples was expected to cure the problems, it is evident that it did not! The test was repeated a number of times with further thermocouples manufactured in the way described, with similar results. In addition, the use of shielded or non-shielded thermocouple extension cable to connect the thermocouples to the instrument was investigated, and found to have no influence.

The suppliers of the card loaned a replacement item in order to check the proper functioning of the PCI-DAS-TC card. The test, when repeated with the loan card, gave similar results. However, when a system was set up where the PCI-DAS-TC card was used to measure one temperature and a stand-alone digital thermometer was used to measure the other temperature no influence of one temperature on the other was noted. The system was effectively a two-channel system with channel-to-channel isolation (albeit one achieved by using two separate instruments). This suggested that the problems were linked to the lack of channel-to-channel isolation on the PCI-DAS-TC card, although neither the author nor the suppliers of the card have yet fully

determined the exact cause of the problem despite much extensive and time-consuming testing.

In the light of the problems described, it was decided to review the methods used to record the temperatures on the test rig, as it was clear from the tests that a device with channel-to-channel isolation was required.

A number of potential solutions were investigated, but 5B-series industrial signal-conditioning modules manufactured by Analog Devices were found to be the most cost-effective solution. These "plug-in" modules are designed for robust industrial applications, and feature isolated inputs and outputs. One module is required for each signal to be conditioned. They are designed to be slotted into "backplanes" which are a relatively straightforward method of connecting signals to and from the modules. The backplanes also offer channel-to-channel isolation as standard. Figure 3.24 shows a typical 5B module, and Figure 3.25 shows a number of such modules inserted into a common backplane.

Figure 3.24: 5B47 thermocouple signal conditioning module

Figure 3.25: 5B modules inserted into a 16-channel backplane

A large range of 5B47 thermocouple modules are available, for a range of thermocouple types and different measurement ranges. The 5B47-J-03 module was selected as being most suitable for the present work. It amplifies and filters the thermocouple signal, and performs cold-junction compensation (using platinum RTD sensors mounted on the terminal blocks on the backplane) and linearization. The module is designed to operate with J-type thermocouples over the range 0-500°C. This gives an isolated output over the 0-5V DC range which is linear with temperature, at a 10mV/°C scale. The modules also have internal low-pass filters, which reject any electrical noise above 4Hz, in order to give a very stable and low-noise signal.

In order to test the suitability of the proposed system, 2 modules were acquired. These were set up, and their DC outputs were connected to the PC using the National Instruments 6030E card. The previously described electrical connection test was carried out, and with the 5B47 signal conditioning no interference between signals was measured, as can be seen in Figure 3.26.

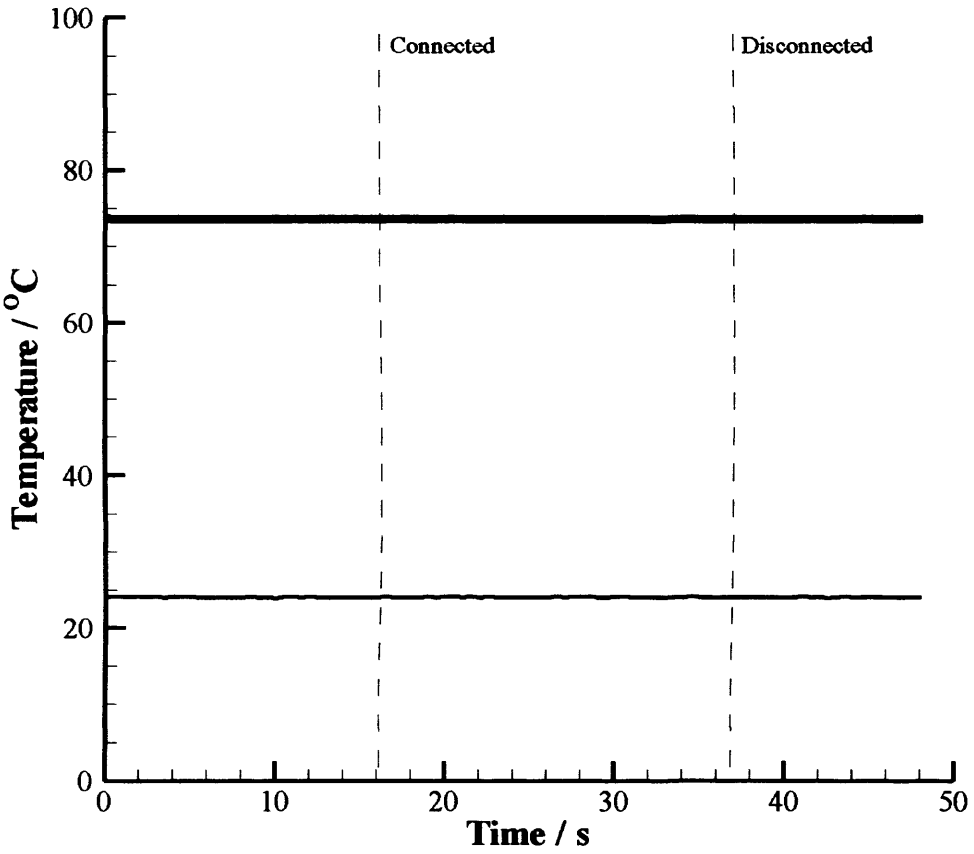

Figure 3.26: Electrical connection test with 5B47 signal conditioning

A number of repeat tests confirmed the confidence in the system, and a full 13 module system was installed, together with a 16-channel backplane. The backplane was mounted adjacent to the test rig on the wall of the laboratory.

The thermocouple signals are connected to the 5B47 modules via cabling which uses shielded J-type thermocouple extension wire and J-type plugs and sockets, to avoid errors due to parasitic thermocouple junctions. The loop resistance (total resistance across thermocouple and extension cables) was measured as 18Ω, which is significantly less than the advisable maximum loop resistance of 100Ω (Labfacility Temperature Handbook, 2006). The 0-5V DC output signals from the signal

conditioning modules are connected to the 6030E card in the PC via shielded cables, in an attempt to minimise electromagnetic interference. A photograph of the installation can be seen in Figure 3.27.

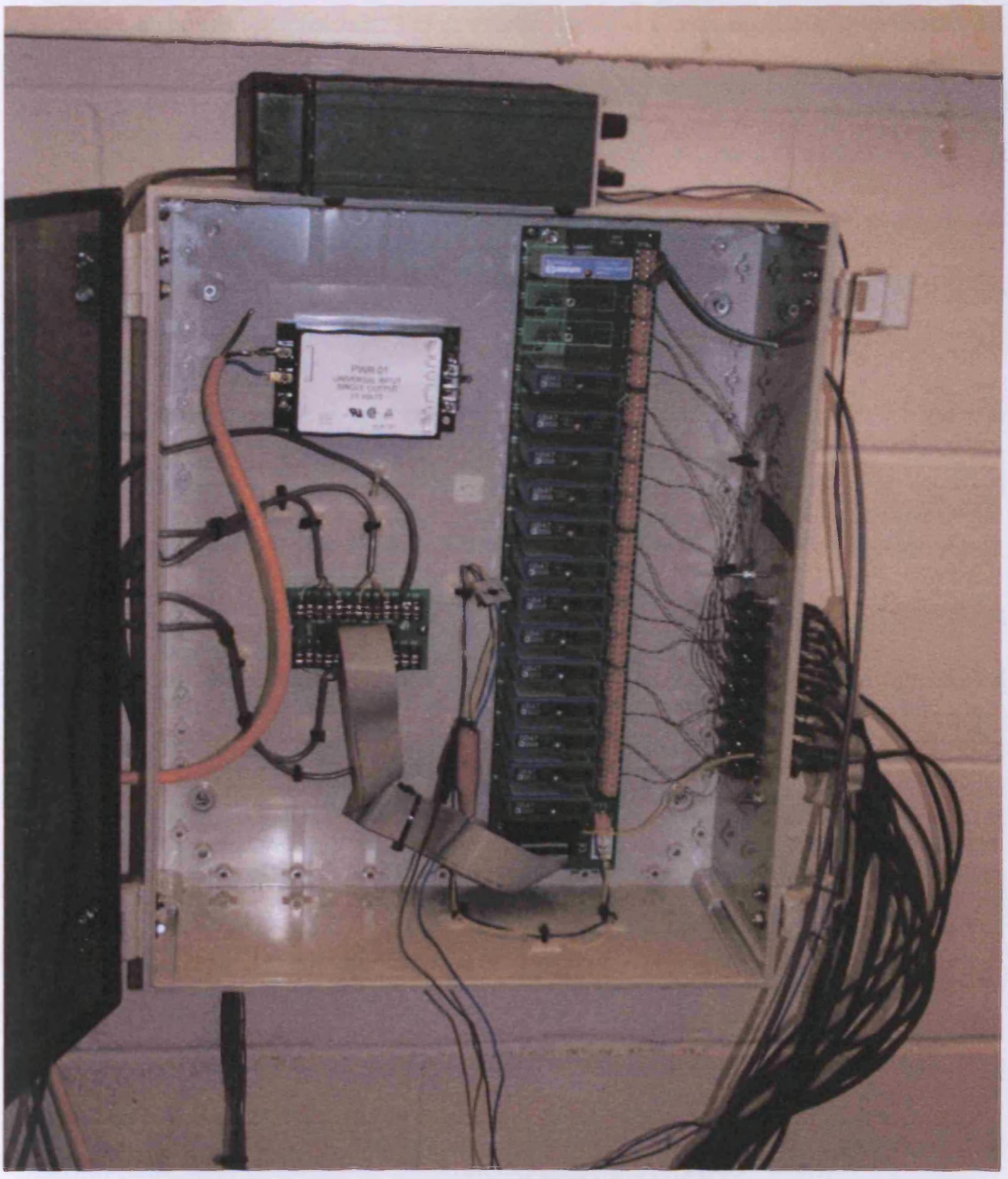

Figure 3.27: View of test rig showing thermocouple leads and signal conditioning equipment

As explained previously, a new method of installing the thermocouples into the test disks was developed using electrically-insulating ceramic cement. Although the electrical insulation was no-longer necessary following the implementation of the 5B47 signal conditioning system, the cement method of installing the thermocouples was found to be far simpler than the previous method which used a copper ferrule to secure the thermocouple. The copper ferrule required swaging into the hole using a special tool – however it was relatively easy to make an error during this process which could lead to thermocouple damage, tool breakage, or both. By contrast, the cement was relatively straightforward to use.

Therefore, it was decided to use the cement to install the thermocouples in the test disks. However, since the analysis which uses the test results requires accurate measurement of the temperature decay of the disks once the heat source is removed in order to determine the heat transfer coefficients, it was necessary to determine whether the thermal response of the thermocouple was significantly affected by the method of installation. A simple test was conducted – two identical test disks were each fitted with a thermocouple. One thermocouple used a copper ferrule, whilst the other was cemented in place. They were connected to the 5B47 signal conditioning modules, and the temperatures were logged on the PC using LabVIEW.

The test disks were lowered into a controlled, stirred hot water bath, which had previously been heated to 80°C. The bath had been left to heat over a period of some hours so that the temperature had stabilized and was constant throughout whilst the test was performed.

The recorded temperatures for each disk can be seen in Figure 3.28, which shows the temperatures of each disk rising once they have been lowered into the water bath.

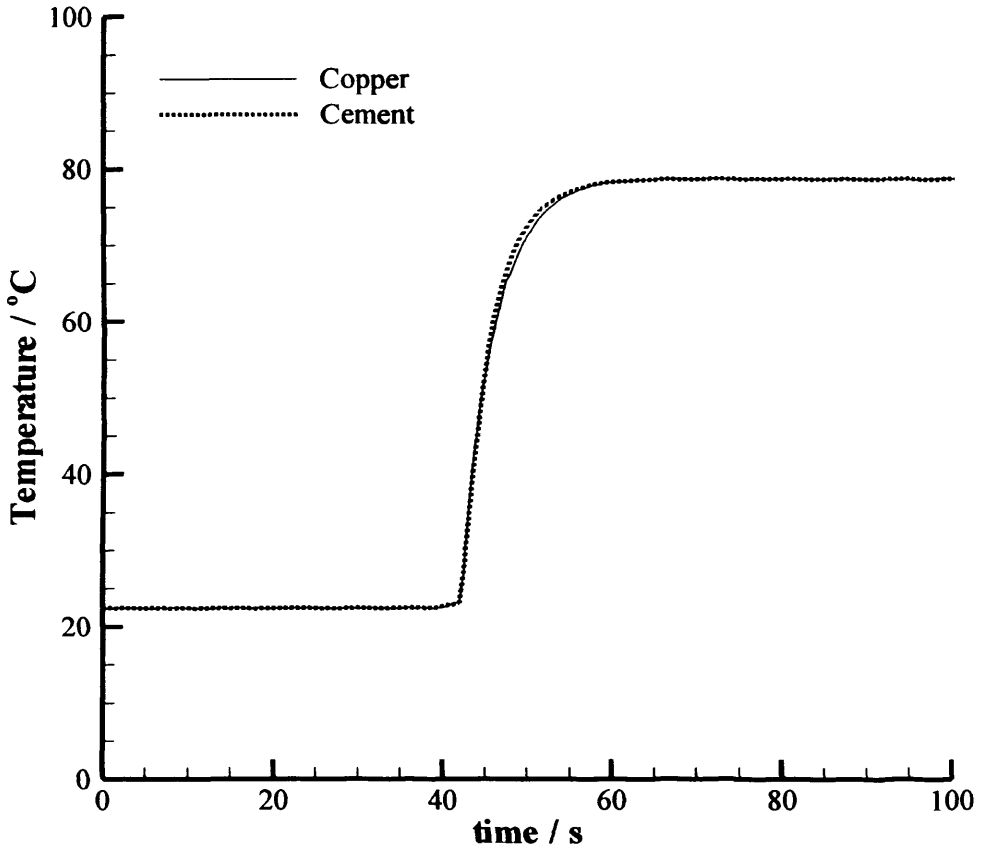

Figure 3.28: Test of copper ferrule thermocouples against ceramic coated thermocouples.

Figure 3.28 shows that there is very good agreement between the temperature rise recorded using a copper-ferule thermocouple and the rise recorded using a cemented thermocouple. During the transient stage, where the disk specimens are plunged into the hot water and are rapidly heated, the maximum temperature difference is around 2°C. When steady-state conditions are reached, there is no discernable difference between the recorded temperatures. Therefore, the cemented thermocouples offer comparable performance to the original copper-ferule design.

3.6.3.2 Calibration of thermocouples

Quoted accuracies for thermocouples used without any further calibration are approximately ±2.5°C. However, with careful calibration, accuracies better than ±1.0 °C may be achieved (Labfacility, 2006). The thermocouples in each disk were calibrated simultaneously in a temperature controlled oven. The calibration set-up is shown schematically in Figure 3.29, and in a photograph in Figure 3.30.

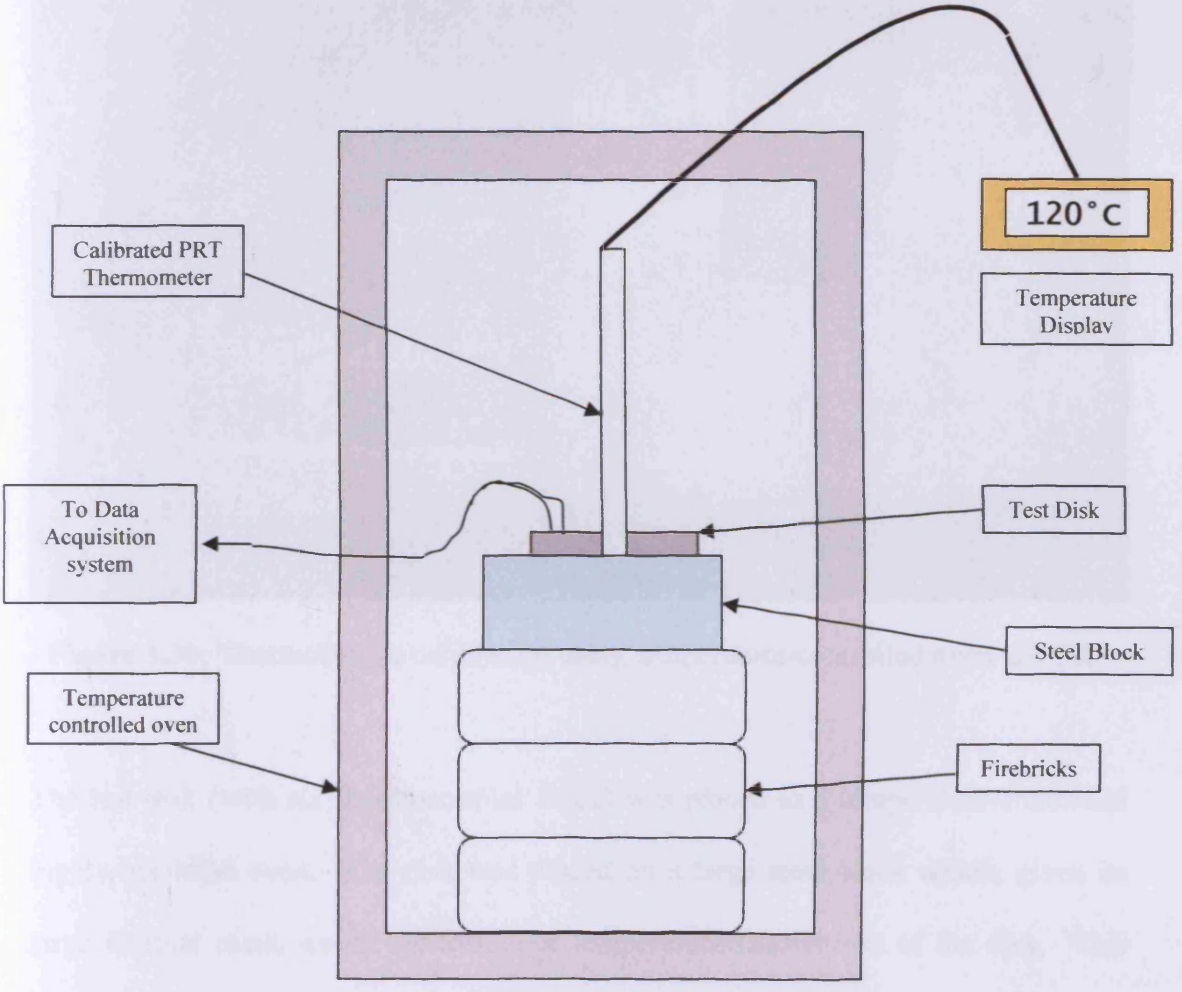

Figure 3.29: Thermocouple calibration

Figure 3.30: Thermocouple calibration using temperature-controlled oven and PRT

The test disk (with six thermocouples fitted) was placed in a temperature-controlled highly-insulated oven. The disk was placed on a large steel block which, given its large thermal mass, would act to reduce temperature fluctuations of the disk. This block, in turn, was placed in the centre of the oven on fire-bricks. This arrangement positioned the disk adjacent to the temperature sensors used by the oven control

system to monitor air temperature within the oven, in order to calibrate the disks at the position within the oven of best temperature control.

In contact with the disk was a UKAS certified platinum RTD thermometer. This measured the temperature of the disk to better than ±0.1°C. The thermocouples were connected to the data acquisition system already described. It is important to note that the connection layout *as used on the test rig* was replicated during the calibration process – i.e. the slip rings and the signal conditioning equipment were removed from the test rig and connected between the thermocouples and the PC in the same arrangement as used on the test rig.

The calibration procedure involved setting the oven set-point to a specified temperature and waiting for the temperature within the oven to stabilise. This was assessed using both the PRT thermometer and the thermocouples, and typically around one hour was required for the temperature within the oven to stabilise to within 0.1°C as indicated by the PRT thermometer. Once the temperature had stabilised, the thermocouple temperatures were recorded for a one-minute period and an average value calculated. This process was repeated at a range of temperatures between ambient temperature (around 20°C) and 160°C in steps of 20°C. This process was repeated three times. A typical set of thermocouple temperatures (in this case the outer radius, centre-line hole for a fast disk) can be seen in Figure 3.31, plotted against the PRT temperatures.

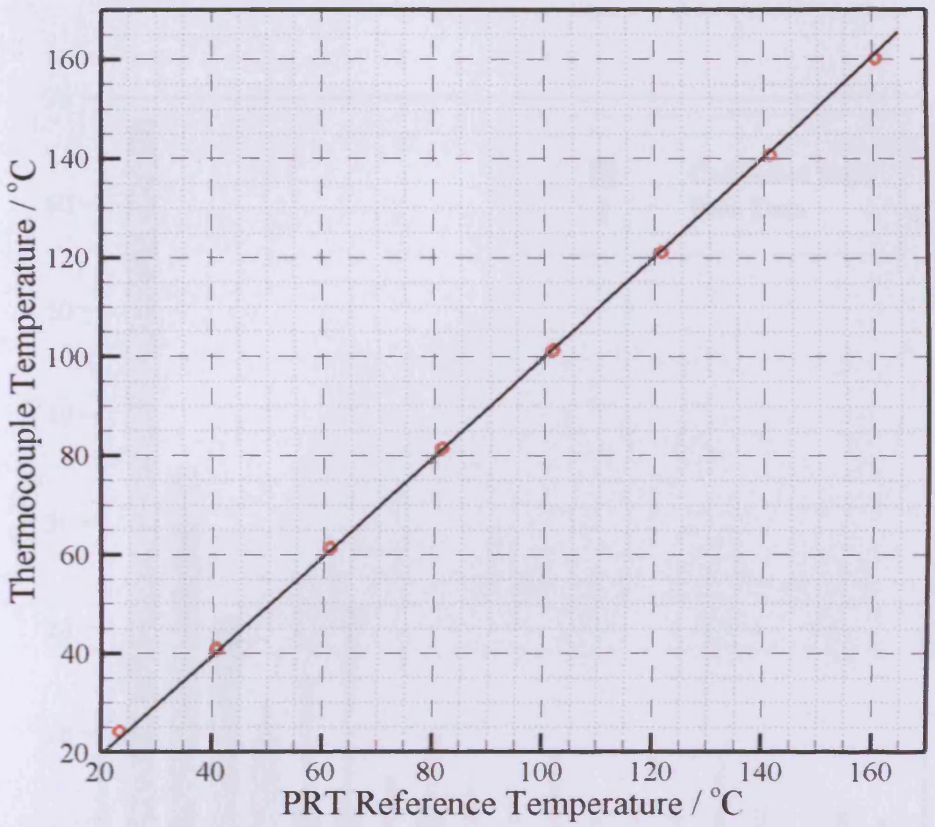

Figure 3.31: Example thermocouple calibration

Figure 3.31 also shows the least-squares trend-line fitted to the data. A similar trend-line was established for each thermocouple, and these trends are used in the LabVIEW program to calibrate the raw thermocouple signals.

In order to demonstrate the effectiveness of the calibration process, the least-squares calibrations were then applied to a typical set of raw data acquired during the calibration process. Figure 3.32 shows a histogram of the absolute errors of the thermocouple readings (against the PRT reference temperature) for the raw data and the calibrated temperatures.

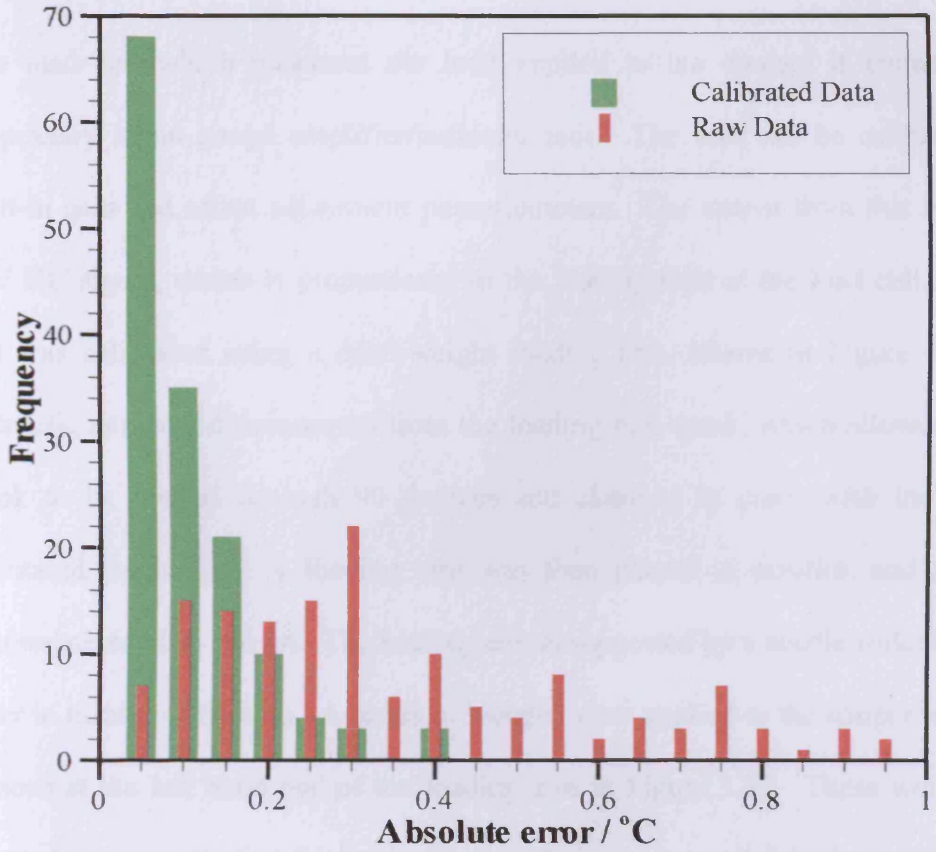

Figure 3.32: Histogram of absolute errors in calibrated and raw thermocouple readings

Some 144 one-minute averaged temperature readings are shown in Figure 3.32. It may be seen that the raw data prior to calibration have absolute errors of up to 1°C which, although seemingly high, is relatively accurate given the quoted accuracy of uncalibrated thermocouple measurements. After the calibration was applied, the worst error was 0.4°C, and the majority of the errors (134 readings, 93%) are 0.2°C or less. Thus, the calibration process can be seen to have reduced the error in the thermocouple readings by more than half when compared to uncalibrated readings.

3.6.3.3 Load Cell

The load cell which measures the load applied to the contact is connected to a proprietary strain gauge amplifier/indicator unit. The unit can be calibrated using built-in gain and offset adjustment potentiometers. The output from this unit is a 0-10V DC signal, which is proportional to the load applied to the load cell. The load cell was calibrated using a dead-weight loading arm, shown in Figure 3.33. The hydraulic ram was disconnected from the loading bell-crank, which allowed the bell-crank to be rotated through 90 degrees and clamped in place with the load cell orientated vertically. A loading arm was then placed in position and accurately counterbalanced as shown. The loading arm is supported by a needle-roller bearing in order to minimise friction. A series of weights were applied to the hanger which may be seen at the left hand end of the loading arm in Figure 3.33. These weights were selected to give a load at the load cell up to the maximum used in the test rig. Using these weights to apply a known load, the calibration of the load cell indicator/amplifier unit could be adjusted until correct readings were given. The calibration was repeated a number of times to ensure an accurate calibration was achieved.

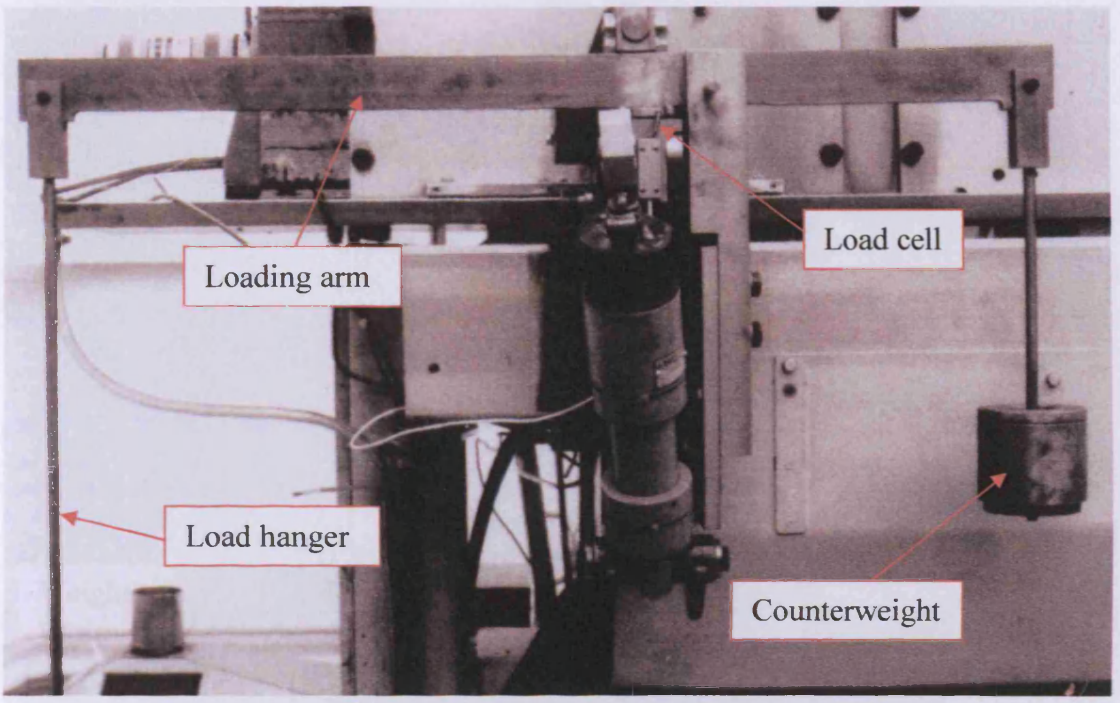

Figure 3.33: Calibration of load cell

3.6.3.4 Friction Transducer

The friction transducer consists of strain gauges applied to a reduced section of the slow speed drive shaft. These are connected to a strain-gauge amplifier, the output of which (0-10V DC) is connected to the data acquisition PC as described in section 3.6.1. During the preparatory work to develop the test rig, the original amplifier was replaced with a strain gauge module which uses one of the spare channels on the 16 channel 5B system used for the thermocouple signal conditioning. The friction transducer was calibrated using a dead-weight loading arm, as shown in Figure 3.34.

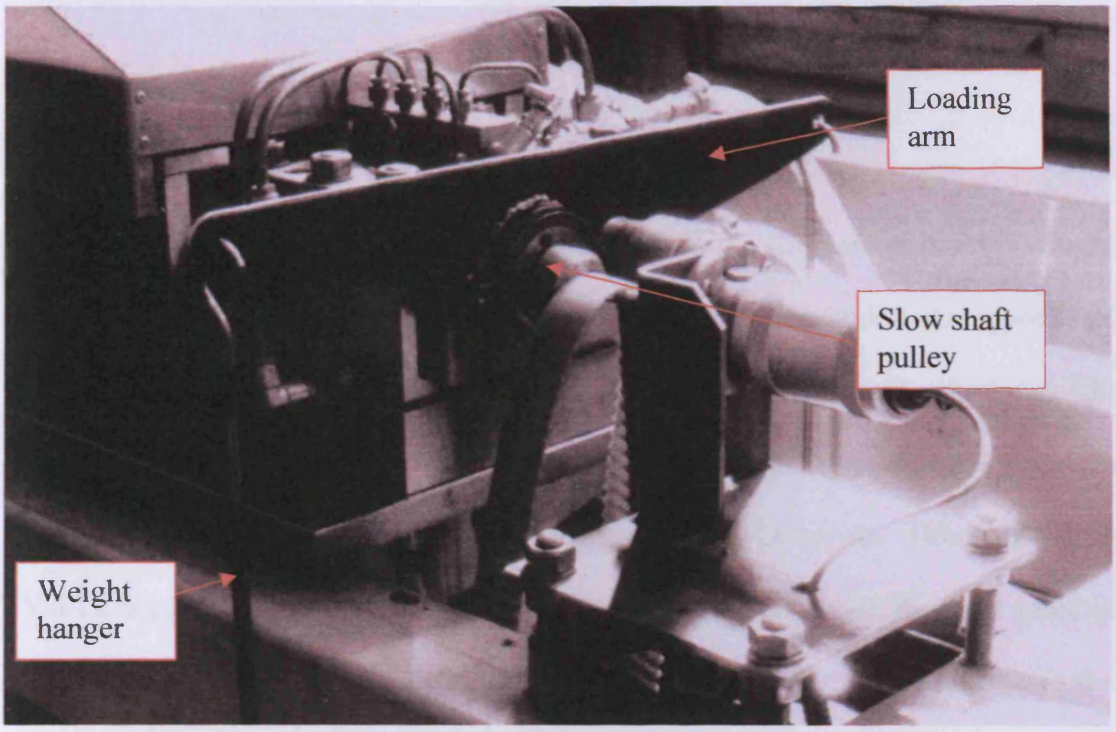

Figure 3.34: Friction calibration

The drive belt was disconnected from the slow shaft, which was then locked into position by clamping the slow shaft in the test head to prevent rotation. The counterbalanced loading arm was then clamped in a horizontal position onto the drive pulley. A series of weights were then applied to the loading arm to produce a torque in the shaft, to a level in excess of the highest frictional torque anticipated in the experiments. At each applied torque, the voltage measured by the computer was logged, and these data were used to develop a friction force - voltage characteristic which was then programmed into the LabVIEW software to covert the measured voltage into a friction force. The calibration process was repeated a number of times to ensure a reliable result. The values measured during each individual calibration process differed by no more than 1% from the mean values used to calculate the calibration equation used within the LabVIEW software.

3.6.3.5 Shaft Speed Sensors

The test rig was originally fitted with optical speed sensors. These effectively consist of a Light-Emitting Diode, which is integrally mounted in a moulded unit opposite an infra-red sensitive transistor. A trigger disk was fitted to each shaft, which has 120 slots around its periphery. As these slots pass by the sensor, they interrupt the beam of infra-red between the LED transmitter and the infra-red receiver. This creates a 0-5V TTL square wave, which has a frequency which equates to twice the shaft speed in revolutions per minute (since the trigger disk has 120 slots). The signal from the speed sensor was fed into a display unit, which displays the shaft speed.

However, it was found that the original sensors produced a poor quality TTL signal which could not be reliably measured by the computer system. Computer-based data acquisition systems are usually very susceptible to poor signals, especially in the case of these signals which were observed using an oscilloscope to have relatively long rise/fall times. Thus, new sensors were installed, using the original trigger disks. The new sensors incorporate a Schmitt trigger circuit, which ensures clean waveforms with sharp rises and falls. The original sensors and display electronics were left in place to act as a check on the new system.

The new sensors were connected to the PC via the Counter/Timer channels of the data acquisition card, and the data from them is passed into the LabVIEW program. The speeds they measured were checked using two methods – using the original sensors,

and with a hand-held digital tachometer. Both were found to give speeds in good agreement with the new optical sensors.

3.6.4 Slip Ring thermal behaviour

The slip rings are air cooled using a compressed air supply during operation. This is essential in order to avoid parasitic thermocouple voltages being generated at the slip ring rotor/brush interface. Temperature differences between the rotors and brushes will generate an additional thermo-electric EMF, which will result in incorrect temperature readings. In order to avoid this, the rig is run for a period before experimental data is acquired to allow the slip rings to reach thermal equilibrium. These problems are discussed in detail in a technical note issued by slip ring manufacturer Michigan Scientific (2008), which is shown in Appendix B.

3.7 Summary

In this chapter, the modifications made to an existing test rig in order to make it suitable for the current experimental programme have been described. These included modifications to allow the fitting of additional, carefully calibrated, thermocouples to the test disks, together with the addition of insulating washers to the sides of the disks. In addition, the instrumentation system has been completely replaced with a modern system, and a new PC-based data acquisition and control system has been developed.

Theory and formulation of numerical model of temperature distributions within test disks

4.1 The governing partial differential equation of transient heat conduction in polar co-ordinates

The heat partition modelling presented in this work is concerned with a study of the temperature distributions developed within test disks during the course of an experiment in which two disks are in rolling/sliding contact under heavily loaded EHL conditions. By matching the temperatures measured during the experiment with those predicted by a conduction model of the disks, the partition of heat between the two contacting surfaces can be determined.

4.1.1 Basis of model formulation

In order to model the temperature distributions within the test disks it is necessary to solve the partial differential equation which describes the conduction of heat within the test disks. The test disks are cylindrical, so the use of polar co-ordinates (r, θ, z) is appropriate. A small element of a test disk with dimensions δr, δz, $r\delta\theta$ is shown in Figure 4.1. The solid material is considered to be homogenous and isotropic, such that the density, specific heat capacity and thermal conductivity are the same at all points within the temperature field.

The partial differential equation which describes the temperature within the disk may be derived by performing an energy balance on the small element of test disk shown. The

element will be considered to be fixed in space, and the disk material is assumed to pass through this element as the disk rotates. Four energy terms need to be considered within a time interval δt:

a) The net heat conduction dQ_c into the volume element.

b) The net internal heat generation within the volume element, dQ_g.

c) The energy stored within the element, dQ_s, as a result of the temperature rise, dT.

d) The net heat transported into the element as a result of the disk rotation, dQ_r.

The above terms may be positive or negative, representing an increase or decrease in energy. The requirement for conservation of energy leads to equation (4.1):

$$dQ_s = dQ_c + dQ_g + dQ_r \tag{4.1}$$

Each of the four terms is now considered in detail.

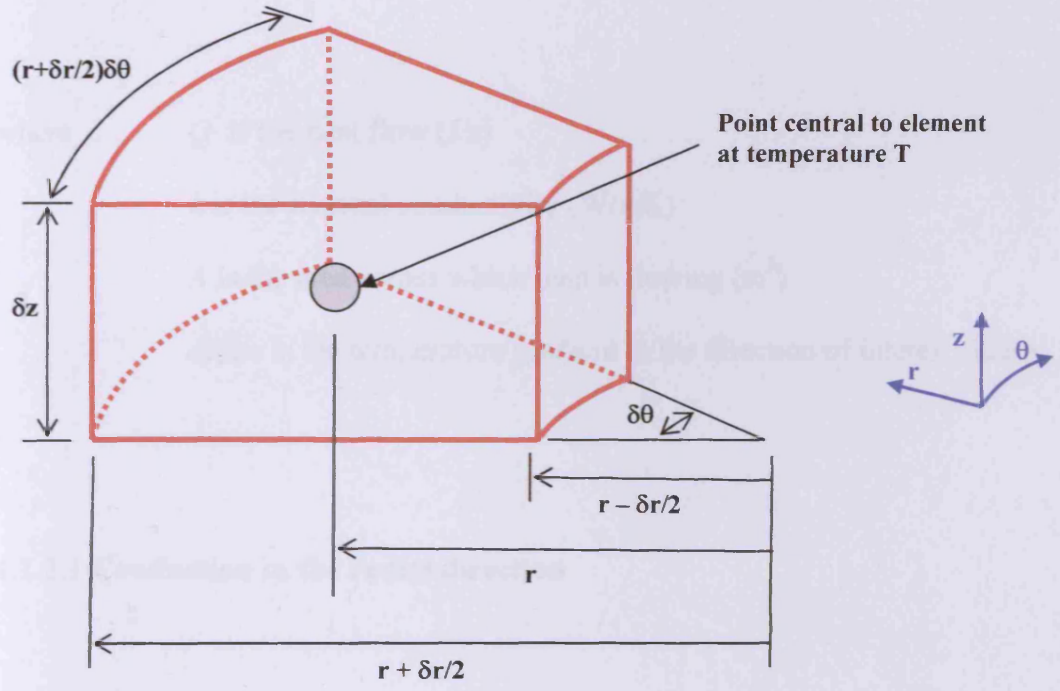

Figure 4.1: Element of Disk

4.1.2 Conduction into element

The net heat conduction dQ_c into the volume element is found by summing the net heat flow in each of the principal co-ordinate directions. These heat flows may be evaluated using Fourier's law of conduction, which states:

$$\dot{Q} = -kA\frac{dT}{dx} \tag{4.2}$$

where $Q^{'}$ is the heat flow (J/s)

k is the thermal conductivity (W/mK)

A is the area across which heat is flowing (m^2)

dT/dx is the temperature gradient in the direction of interest (K/m)

4.1.2.1 Conduction in the radial direction

Firstly, heat flow in the radial direction may be considered. Using equation (4.2), heat inflow over the innermost face over time δt is:

$$\begin{aligned} dQ_{r-\frac{\delta r}{2}} &= -k\left(\left(r-\frac{\delta r}{2}\right)\delta\theta\delta z\right)\left.\frac{\partial T}{\partial r}\right|_{r-\frac{\delta r}{2}}\delta t = -k\left(\left(r-\frac{\delta r}{2}\right)\delta\theta\delta z\right)\frac{\partial}{\partial r}\left\{T-\frac{\partial T}{\partial r}\frac{\delta r}{2}\right\}\delta t \\ &= -k\left(\left(r-\frac{\delta r}{2}\right)\delta\theta\delta z\right)\left(\frac{\partial T}{\partial r}-\frac{\partial^2 T}{\partial r^2}\frac{\delta r}{2}\right)\delta t \end{aligned} \tag{4.3}$$

The heat outflow over the outermost radial face is

$$dQ_{r+\frac{\delta r}{2}} = -k\left(\left(r+\frac{\delta r}{2}\right)\delta\theta\delta z\right)\left.\frac{\partial T}{\partial r}\right|_{r+\frac{\delta r}{2}}\delta t = -k\left(\left(r+\frac{\delta r}{2}\right)\delta\theta\delta z\right)\frac{\partial}{\partial r}\left\{T+\frac{\partial T}{\partial r}\frac{\delta r}{2}\right\}\delta t$$
$$= -k\left(\left(r+\frac{\delta r}{2}\right)\delta\theta\delta z\right)\left(\frac{\partial T}{\partial r}+\frac{\partial^2 T}{\partial r^2}\frac{\delta r}{2}\right)\delta t \qquad (4.4)$$

Thus, the net heat inflow in the radial direction (dQ_{cr}) is obtained by subtracting equation (4.4) from equation (4.3) to give

$$dQ_{cr} = dQ_{r-\frac{\delta r}{2}} - dQ_{r+\frac{\delta r}{2}} = kr\delta\theta\delta r\delta z\left(\frac{1}{r}\frac{\partial T}{\partial r}+\frac{\partial^2 T}{\partial r^2}\right)\delta t \qquad (4.5)$$

4.1.2.2 Conduction in the axial direction

Considering next the heat flow in the axial (z) direction, the heat inflow at the face (z - $\delta z/2$) is given by:

$$dQ_{z-\frac{\delta z}{2}} = -k\left(r\delta\theta\delta r\right)\left.\frac{\partial T}{\partial z}\right|_{z-\frac{\delta z}{2}}\delta t = -k\left(r\delta\theta\delta r\right)\frac{\partial}{\partial z}\left\{T-\frac{\partial T}{\partial z}\frac{\delta z}{2}\right\}\delta t$$
$$= -k\left(r\delta\theta\delta z\right)\left(\frac{\partial T}{\partial z}-\frac{\partial^2 T}{\partial z^2}\frac{\delta z}{2}\right)\delta t \qquad (4.6)$$

The heat outflow across the face at (z + $\delta z/2$) is given by:

$$dQ_{z+\frac{\delta z}{2}} = -k(r\delta\theta\delta r)\left.\frac{\partial T}{\partial z}\right|_{z+\frac{\delta z}{2}}\delta t = -k(r\delta\theta\delta r)\frac{\partial}{\partial z}\left\{T+\frac{\partial T}{\partial z}\frac{\delta z}{2}\right\}\delta t$$
$$= -k(r\delta\theta\delta z)\left(\frac{\partial T}{\partial z}+\frac{\partial^2 T}{\partial z^2}\frac{\delta z}{2}\right)\delta t \qquad (4.7)$$

The net heat inflow by conduction in the axial (z) direction is obtained by subtracting equation (4.7) from equation (4.6) to give

$$dQ_{cz} = dQ_{z-\frac{\delta z}{2}} - dQ_{z+\frac{\delta z}{2}} = -k(r\delta\theta\delta z)\left(\frac{\partial T}{\partial z}-\frac{\partial^2 T}{\partial z^2}\frac{\delta z}{2}\right)\delta t + k(r\delta\theta\delta z)\left(\frac{\partial T}{\partial z}+\frac{\partial^2 T}{\partial z^2}\frac{\delta z}{2}\right)\delta$$
$$= kr\delta\theta\delta r\delta z\left(\frac{\partial^2 T}{\partial z^2}\right)\delta t \qquad (4.8)$$

4.1.2.3 Conduction in the circumferential direction

Finally, heat flow in the circumferential direction (θ) may be considered. The heat inflow is given by:

$$dQ_{\theta-\frac{\delta\theta}{2}} = -k(\delta z\delta r)\left.\frac{\partial T}{r\partial\theta}\right|_{\theta-\frac{\delta\theta}{2}}\delta t = -k(\delta z\delta r)\frac{\partial}{r\partial\theta}\left\{T-\frac{\partial T}{\partial\theta}\frac{\delta\theta}{2}\right\}\delta t$$
$$= -k\left(\delta z\frac{\delta r}{r}\right)\left(\frac{\partial T}{\partial\theta}-\frac{\partial^2 T}{\partial\theta^2}\frac{\delta\theta}{2}\right)\delta t \qquad (4.9)$$

The heat out-flow is given by:

$$dQ_{\theta+\frac{\delta\theta}{2}} = -k(\delta z\delta r)\frac{\partial T}{r\partial\theta}\bigg|_{\theta+\frac{\delta\theta}{2}}\delta t = -k(\delta z\delta r)\frac{\partial}{r\partial\theta}\left\{T+\frac{\partial T}{\partial\theta}\frac{\delta\theta}{2}\right\}\delta t$$
$$= -k\left(\delta z\frac{\delta r}{r}\right)\left(\frac{\partial T}{\partial\theta}+\frac{\partial^2 T}{\partial\theta^2}\frac{\delta\theta}{2}\right)\delta t \qquad (4.10)$$

Thus, the net heat in-flow in the circumferential direction is obtained by subtracting equation (4.10) from equation (4.9) and is

$$dQ_{c\theta} = dQ_{\theta-\frac{\delta\theta}{2}} - dQ_{\theta+\frac{\delta\theta}{2}} = -k\left(\delta z\frac{\delta r}{r}\right)\left(\frac{\partial T}{\partial\theta}-\frac{\partial^2 T}{\partial\theta^2}\frac{\delta\theta}{2}\right)\delta t+\left(\delta z\frac{\delta r}{r}\right)\left(\frac{\partial T}{\partial\theta}+\frac{\partial^2 T}{\partial\theta^2}\frac{\delta\theta}{2}\right)\delta t$$
$$= kr\delta z\delta r\delta\theta\left(\frac{1}{r^2}\frac{\partial^2 T}{\partial\theta^2}\right)\delta t \qquad (4.11)$$

4.1.2.4 Net heat conduction into element

The total heat conduction into the element dQ_c is given by adding equations (4.5), (4.8) and (4.11):

$$dQ_c = kr\delta\theta\delta r\delta z\left[\frac{1}{r}\frac{\partial T}{\partial r}+\frac{\partial^2 T}{\partial r^2}+\frac{\partial^2 T}{\partial z^2}+\frac{1}{r^2}\frac{\partial^2 T}{\partial\theta^2}\right]\delta t \qquad (4.12)$$

4.1.3 Internal heat generation

The internal heat generation within the disk material may be taken as zero in this case, hence:

$$dQ_g = 0 \tag{4.13}$$

4.1.4 Energy stored due to temperature rise

The energy stored, dQ_s, within the element as a result of a rate of temperature rise ($\partial T/\partial t$) over a time period δt is:

$$dQ_s = \rho c_p (r\delta\theta\delta r\delta z)\frac{\partial T}{\partial t}\delta t \tag{4.14}$$

where ρ is the mass density of the material (kg/m^3)

c_p is the specific heat capacity of the material (J/kg.K)

4.1.5 Energy transported into fixed element by rotating disk material

Finally, the energy transported into the element, which is fixed in space, by allowing the material of the disk to rotate through it with angular velocity ω, must be considered. The net heat gain due to rotation for the material that is instantaneously in the fixed control volume is equal to the heat energy leaving the control volume minus that entering.

The volume of material which passes through the control element in time δt is equal to $\omega r \delta t \delta r \delta z$. The material enters the control element at temperature $T\big|_{\theta-\frac{\delta\theta}{2}}$ and leaves it at $T\big|_{\theta+\frac{\delta\theta}{2}}$, and so the net heat gain is given by:

$$dQ_r = \rho c_p \omega r \delta t \delta r \delta z \left(T\big|_{\theta+\frac{\delta\theta}{2}} - T\big|_{\theta-\frac{\delta\theta}{2}} \right) \tag{4.15}$$

The temperature difference terms can be expressed using Maclaurin's theorem:

$$T\big|_{\theta+\frac{\delta\theta}{2}} = T(\theta) + \frac{\delta\theta}{2}\frac{\partial T}{\partial\theta} + \frac{\delta\theta^2}{(4\times 2!)}\frac{\partial^2 T}{\partial\theta^2} + \frac{\delta\theta^3}{(8\times 3!)}\frac{\partial^3 T}{\partial\theta^3} + \ldots\ldots\ldots \tag{4.16}$$

$$T\big|_{\theta-\frac{\delta\theta}{2}} = T(\theta) - \frac{\delta\theta}{2}\frac{\partial T}{\partial\theta} + \frac{\delta\theta^2}{(4\times 2!)}\frac{\partial^2 T}{\partial\theta^2} - \frac{\delta\theta^3}{(8\times 3!)}\frac{\partial^3 T}{\partial\theta^3} + \ldots\ldots\ldots \tag{4.17}$$

Subtracting (4.17) from (4.16) gives, for small values of $\delta\theta$:

$$T\big|_{\theta+\frac{\delta\theta}{2}} - T\big|_{\theta-\frac{\delta\theta}{2}} = \delta\theta\frac{\partial T}{\partial\theta} \tag{4.18}$$

Thus, equation (4.18) may be substituted into equation (4.15) to give:

$$dQ_r = \rho c_p \omega r \delta r \delta z \delta\theta \frac{\partial T}{\partial\theta}\delta t \tag{4.19}$$

4.1.6 Overall partial differential equation

Equation (4.1) may now be rewritten, by substituting equations (4.12), (4.13), (4.14) and (4.19) for the four heat terms, to give:

$$\rho c_p (r\delta\theta\delta r\delta z)\frac{\partial T}{\partial t}\delta t = kr\delta\theta\delta r\delta z\left[\frac{1}{r}\frac{\partial T}{\partial r}+\frac{\partial^2 T}{\partial r^2}+\frac{\partial^2 T}{\partial z^2}+\frac{1}{r^2}\frac{\partial^2 T}{\partial \theta^2}\right]\delta t + \rho c_p \omega r\delta r\delta z\delta\theta\frac{\partial T}{\partial\theta}\delta t \tag{4.20}$$

Cancellation of the common terms gives:

$$\frac{\partial T}{\partial t} = \alpha\left[\frac{1}{r}\frac{\partial T}{\partial r}+\frac{\partial^2 T}{\partial r^2}+\frac{\partial^2 T}{\partial z^2}+\frac{1}{r^2}\frac{\partial^2 T}{\partial \theta^2}\right]+\omega\frac{\partial T}{\partial\theta} \tag{4.21}$$

where α is the thermal diffusivity (m^2/s) which is equal to $k/\rho c_p$.

Equation (4.21) will be recognised as the conduction partial differential equation in polar co-ordinates (Croft and Stone, 1977), but with the additional convective term necessary to take account of the rotation of disk material through the fixed control elements.

4.2 Finite difference numerical method

4.2.1 Background to method

The finite difference method of solving the conduction P.D.E. developed in the previous section offers a technique for the solution for complex problems where no analytical solution is available. The method replaces the derivatives in equation (4.21) with approximations in the form of finite-sized differences between temperature values at particular locations on a solution mesh. The method reduces the problem to a system of linear equations involving the temperatures at the various nodes within the mesh, which may be solved using matrix inversion or iterative techniques, depending on the scale of the problem.

4.2.2 Taylor series derivations of finite difference expressions

In order to numerically solve equation (4.21), expressions for the derivatives of a function are required in terms of function values at several neighbouring points. These can be derived intuitively (Croft and Stone, 1977) or more rigorously using Taylor series expansions. Figure 4.2 shows a function with values taken at equally spaced mesh-points. The fourth order Taylor series expansion of $f(x_1) = f(x + \Delta x)$, in terms of $\Delta x = x_1 - x_0$, is given by:

$$f_1 = f_0 + \Delta x f_0' + \frac{(\Delta x)^2}{2!} f_0'' + \frac{(\Delta x)^3}{3!} f_0''' + \frac{(\Delta x)^4}{4!} f_0^{iv} \qquad (4.22)$$

A similar expression for f_{-1} can also be obtained in terms of f_0 and its derivatives:

$$f_{-1} = f_0 - \Delta x f_0^{'} + \frac{(\Delta x)^2}{2!} f_0^{''} - \frac{(\Delta x)^3}{3!} f_0^{'''} + \frac{(\Delta x)^4}{4!} f_0^{iv} \qquad (4.23)$$

Equations (4.22) and (4.23) are truncated after the term in Δx, and re-arranged to give the so-called forward and backward difference expressions for f_0':

$$f_0' = \left.\frac{\partial f}{\partial x}\right|_{x=x_0} = \frac{f_1 - f_0}{\Delta x} - \left[\frac{\Delta x}{2} f_0^{''}\right] \qquad \text{(forward difference)} \qquad (4.24)$$

$$f_0' = \left.\frac{\partial f}{\partial x}\right|_{x=x_0} = \frac{f_0 - f_{-1}}{\Delta x} + \left[\frac{\Delta x}{2} f_0^{''}\right] \qquad \text{(backward difference)} \qquad (4.25)$$

The error terms (shown in square brackets) are of the order of Δx, and hence the forward and backward difference approximations expressed in this way are of first order accuracy.

Alternatively, equations (4.22) and (4.23) may be subtracted, which gives:

$$f_0' = \left.\frac{\partial f}{\partial x}\right|_{x=x_0} = \frac{f_1 - f_{-1}}{2\Delta x} - \left[\frac{2(\Delta x)^2}{3!} f_0^{'''}\right] \qquad (4.26)$$

This is the central difference formula, which has second-order truncation error terms (shown in the square brackets). It is thus inherently more accurate than the first-order forward or backward difference formulae.

In order to evaluate the second derivative at $x = x_0$, equations (4.22) and (4.23) are added, giving:

$$f_0'' = \left.\frac{\partial^2 f}{\partial x^2}\right|_{x=x_0} = \frac{f_1 + f_{-1} - 2f_0}{(\Delta x)^2} - \left[\frac{2(\Delta x)^2}{4!} f_0^{iv}\right] \qquad (4.27)$$

Again, it may be seen that the second derivative expression is also second-order accurate.

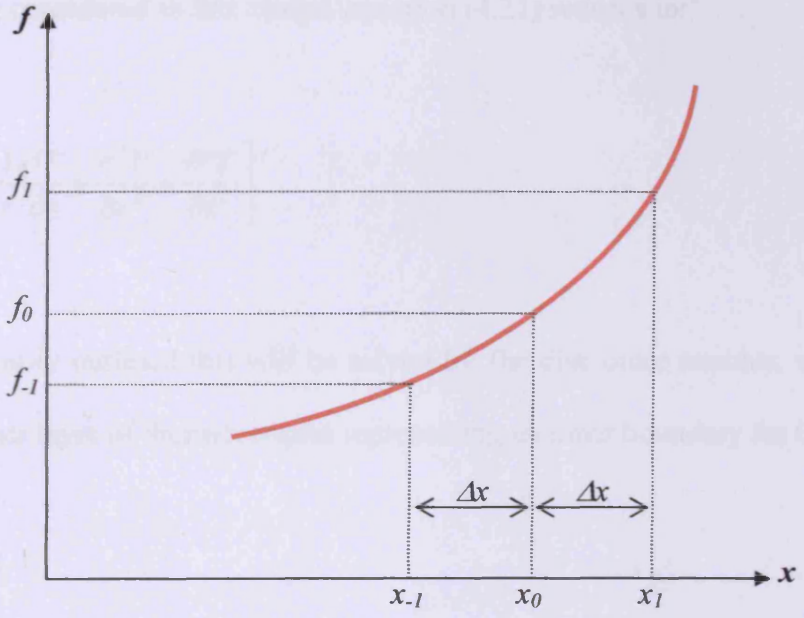

Figure 4.2: Typical $f(x)$ showing function values f_{-1}, f_0 and f_1 taken at equally spaced base points x_{-1}, x_0 and x_1

4.3 Bulk temperature two dimensional transient model

4.3.1 Simplification of P.D.E.

In order to determine the bulk (or mean) temperature within the test disks, the circumferential (or flash) temperature variation is neglected. Because the disk rotates in a period which is far shorter than that required to achieve thermal equilibrium, the frictional heat source may be considered to be evenly distributed around the periphery of the running track. The circumferential temperature variation is confined to small layers of the disk near to the running track surface (as determined using the heat penetration model of Qiao (2005), and a further model is described in section 4 to calculate the flash temperatures. Therefore, the problem reduces to one of two-dimensional transient conduction. Since the circumferential variation of temperature is not being considered in this model, equation (4.21) reduces to:

$$\frac{\partial T}{\partial t} = \alpha\left[\frac{1}{r}\frac{\partial T}{\partial r} + \frac{\partial^2 T}{\partial r^2} + \frac{\partial^2 T}{\partial z^2}\right] \tag{4.28}$$

As previously outlined this will be solved for the disk outer annulus, with the position of the inner layer of thermocouples representing an inner boundary for the model.

4.3.2 Methods for conversion of transient P.D.E. to finite difference form

In order to numerically solve equation (4.28), the temperatures within the solution region must be evaluated at discrete spatial points on the computing mesh, and at discrete time points (known as time steps). Each time step is a finite period of time (Δt) later than its predecessor. Two main types of solution method are available – the explicit and implicit methods.

4.3.3 The explicit method

This approach uses a forward difference approximation to the time derivative in equation (4.28). Therefore, the resulting finite difference equation for the temperature at an individual mesh point at the present time step is expressed in terms of the temperatures at the mesh point and its surrounding points at the previous time step. These are known values, and so the solution marches forwards in time. However, the method is not inherently stable. Too large a choice of Δt will lead to the growth of rounding errors in the calculation, rendering the results meaningless. The maximum time step for a given spatial mesh resolution can be calculated using simple stability criteria, which are discussed further in Croft and Stone (1977). Thus, fine spatial meshes, which may be necessary to achieve stability, can lead to long computational times, so the explicit method was not considered to be the most efficient solution scheme for this work.

4.3.4 The implicit method

This method uses a backward difference approximation for the time derivative in equation (4.28). This results in an equation for the temperature at each mesh point at the present time step which contains the temperatures at the surrounding mesh points, also at the present time step. As these temperatures are unknown, a set of simultaneous equations is developed, one for each mesh point, which must be solved to yield the temperature field at the current time step. The implicit method is unconditionally stable, but the use of a backward difference discretization for the time derivative makes the solution only first-order accurate.

4.3.5 The Crank-Nicolson method

This method uses a central difference approximation to the time derivative, evaluated at the time mid-way between the present time step (K+1) and the previous time step (K). The Crank-Nicolson method is a variant of the fully implicit method described in Section 4.3.4. The spatial derivatives on the right hand side of equation (4.28) are approximated by the mean of the finite difference approximations at the two time steps. It is unconditionally stable and, in addition, it has the lowest discretization error possible with the inherently stable methods. Thus, the Crank-Nicolson method is used in this work.

4.3.6 Derivation of finite difference equations

Figure 4.3 shows the general mesh layout schematically, with the nomenclature used in the following derivations. Finite difference equations must be derived for both the interior nodes and boundary nodes.

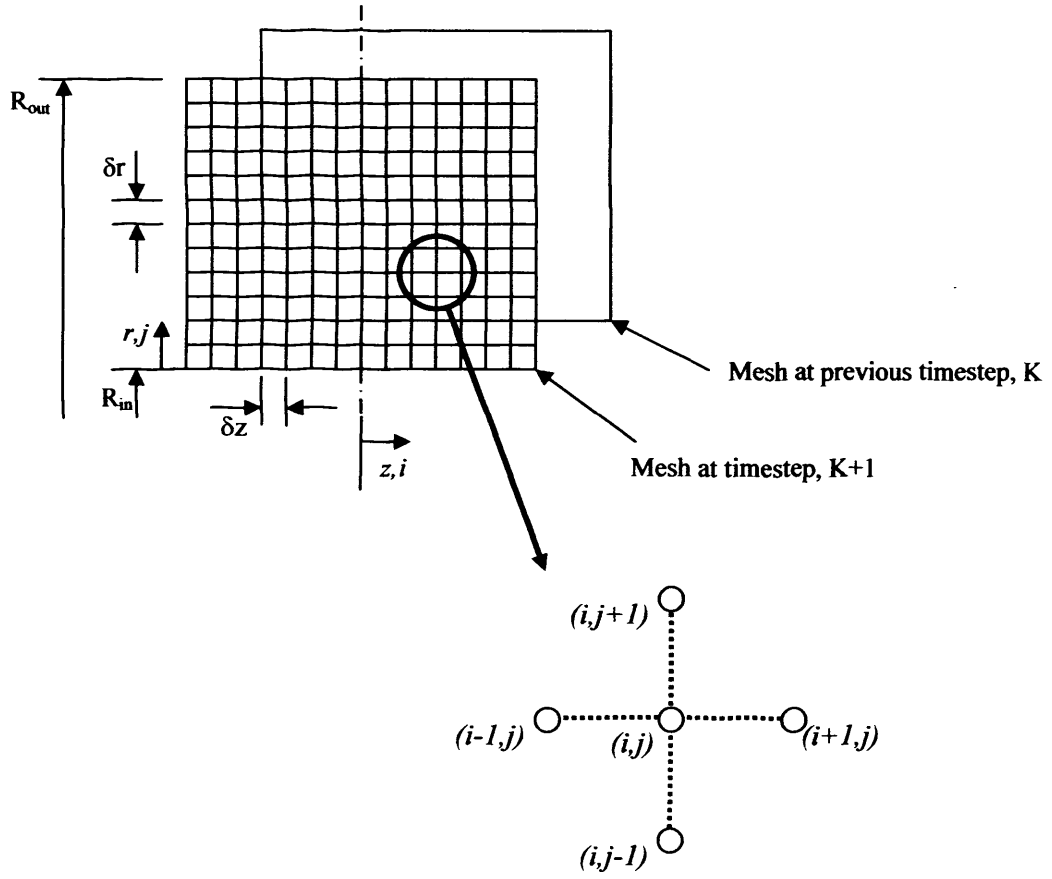

Figure 4.3: Schematic mesh layout and nomenclature

For interior nodes on the computing mesh, using the Crank-Nicolson method, equation (4.28) becomes:

$$\frac{T_{i,j}^{(K+1)} - T_{i,j}^{(K)}}{\Delta t} = \frac{1}{2}\left(\alpha\left[\frac{1}{r}\frac{\partial T}{\partial r} + \frac{\partial^2 T}{\partial r^2} + \frac{\partial^2 T}{\partial z^2}\right]_{i,j}^{(K+1)}\right) + \frac{1}{2}\left(\alpha\left[\frac{1}{r}\frac{\partial T}{\partial r} + \frac{\partial^2 T}{\partial r^2} + \frac{\partial^2 T}{\partial z^2}\right]_{i,j}^{(K)}\right) \quad (4.29)$$

where the subscripts *i,j*, represent the spatial position, and the superscript represents the time step. The following substitutions are made, from equations (4.26) and (4.27):

$$\frac{\partial T}{\partial r} = \frac{T_{i,j+1} - T_{i,j-1}}{2\delta r} \qquad \frac{\partial^2 T}{\partial r^2} = \frac{T_{i,j+1} + T_{i,j-1} - 2T_{i,j}}{\delta r^2} \qquad \frac{\partial^2 T}{\partial z^2} = \frac{T_{i+1,j} + T_{i-1,j} - 2T_{i,j}}{\delta z^2}$$

Also, the radius can be expressed in terms of the radial mesh spacing and position ($r=R_{in}+j\delta r$), giving:

$$\frac{2}{\alpha}\frac{T_{i,j}^{(K+1)} - T_{i,j}^{(K)}}{\delta t} = \left[\frac{T_{i,j+1} + T_{i,j-1} - 2T_{i,j}}{\delta r^2} + \frac{T_{i,j+1} - T_{i,j-1}}{2(R_{in} + j\delta r)\delta r} + \frac{T_{i+1,j} + T_{i-1,j} - 2T_{i,j}}{\delta z^2}\right]^{(K+1)} + \left[\frac{T_{i,j+1} + T_{i,j-1} - 2T_{i,j}}{\delta r^2} + \frac{T_{i,j+1} - T_{i,j-1}}{2(R_{in} + j\delta r)\delta r} + \frac{T_{i+1,j} + T_{i-1,j} - 2T_{i,j}}{\delta z^2}\right]^{(K)} \quad (4.30)$$

Collecting like terms, equation (4.30) may be re-written in the following general form:

$$T_{i,j}^{(K+1)} = AT_{i,j+1}^{(K+1)} + BT_{i,j-1}^{(K+1)} + CT_{i+1,j}^{(K+1)} + DT_{i-1,j}^{(K+1)} + \left[ET_{i,j}^{(K)} + AT_{i,j+1}^{(K)} + BT_{i,j-1}^{(K)} + CT_{i+1,j}^{(K)} + DT_{i-1,j}^{(K)} + F\right] \quad (4.31)$$

The coefficients *A* to *F* may be greatly simplified by expressing the inner radius as r_{in} = $s\delta r$ and setting $\varphi = \frac{\delta r^2}{\alpha \delta t}$ and $\gamma = \frac{\delta r^2}{\delta z^2}$. The coefficients in equation (4.31) then become:

$$A = \frac{s + j + 1/2}{2(s + j)(\varphi + \gamma + 1)} \qquad B = \frac{s + j - 1/2}{2(s + j)(\varphi + \gamma + 1)}$$

$$C = D = \frac{\gamma}{2(\varphi + \gamma + 1)} \qquad E = \frac{\varphi - \gamma - 1}{\varphi + \gamma + 1} \qquad F = 0$$

Equation (4.31) may be used for any internal node point to describe the temperature at the current time step in terms of temperatures at the surrounding nodes at both the current time-step (unknown values) and the previous time-step (known values). On the boundaries of the mesh the values of the coefficients *A-F* must be modified to reflect the applied boundary conditions. Boundary conditions are discussed in more detail in the following section.

4.3.7 Boundary Nodes

The various boundary conditions applied to the solution region are shown in Figure 4.4.

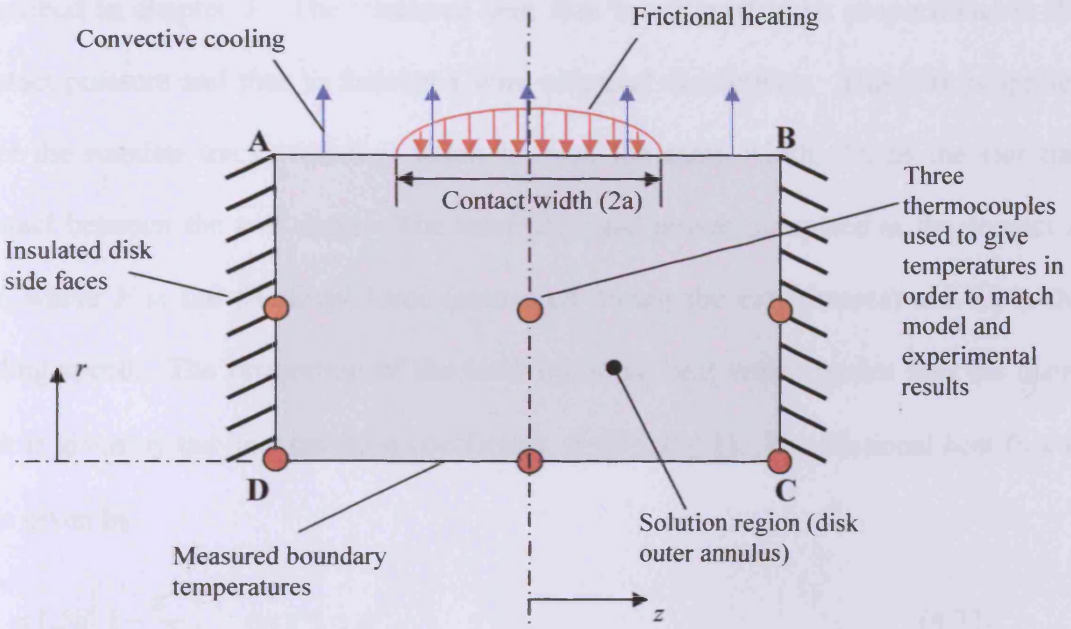

Figure 4.4: Boundary Conditions

4.3.7.1 Outer cylindrical boundary

On the disk's outer cylindrical surface (shown as line AB in Figure 4.4), the disk is subject to two flows of heat – convective cooling due to its rotation and frictional heating over the running track portion of the surface. On this boundary the point at $(i,j+1)$ does not exist and it must be eliminated from equation (4.31). This may be done by considering an energy balance at the boundary:

$$\lambda\frac{\partial T}{\partial r}=\lambda\frac{T_{i,j+1}-T_{i,j-1}}{2\delta z}=q_{fr}-h_t\left(T_{i,j}-T_a\right) \qquad (4.32)$$

where q_{fr} is the frictional heat flux, and h_t is the convective heat transfer coefficient. Thus, equation (4.32) may be re-arranged and substituted into equation (4.31) to eliminate the temperature $T_{i,j+1}$. The value of h_t can be estimated using the test rig as described in chapter 3. The frictional heat flux is assumed to be proportional to the contact pressure and thus to follows a semi-elliptical distribution. This flux is applied over the running track, which is taken to have the same width, $2a$, as the Hertzian contact between the two disks. The total frictional power dissipated at the contact is FU_s where F is the frictional force (measured during the experiments) and U_s is the sliding speed. The proportion of the total frictional heat which passes into the faster disk is given by the heat partition coefficient, β $(0 \leq \beta \leq 1)$. The frictional heat flux is thus given by

$$q_{fr} = 1.5\bar{q}\left(1 - \frac{z^2}{a^2}\right) \quad \text{on } z \leq \pm a \tag{4.33}$$

where $\bar{q} = \dfrac{\beta F U_s}{4\pi R_o a}$ for the faster disk

and $\bar{q} = \dfrac{(1-\beta) F U_s}{4\pi R_o a}$ for the slower disk.

The definition of $\bar{q}$ in equation (4.33) corresponds to the fast shaft, and is modified by replacing β with $(1-\beta)$ for the slower disk. The value of β is adjusted during the analysis process to match the measured temperatures (as shown by the orange thermocouples in Figure 4.4) with those calculated by the model. The parabolic variation of the frictional heat flux in the z direction given in equation (4.33) is obtained by integrating the semi-elliptical heat flux distribution over the disk contact to give an

equivalent distribution suitable for use in the circumferentially-averaged model described here.

4.3.7.2 Inner cylindrical boundary

This boundary (line CD in figure 4.4) is situated at radius R_{in}, where three thermocouples are installed in the test disks. The temperatures recorded during the experiment are used to provide a boundary condition along line CD. The thermocouples are installed on the disk centre-line and close to each edge of the disk, as shown schematically in Figure 4.4. A second-order polynomial is fitted to the three recorded temperatures, and used to give the temperatures at all points along this boundary.

4.3.7.3 Insulated disk faces

These faces (lines AD and BC in Figure 4.4) are insulated as described in section 5.3 of chapter 3. Considering face BC, at the boundary between the disk and the insulation the heat balance may be considered in order to eliminate $T_{i+1,j}$ from equation (4.31). The heat being conducted to the boundary through the steel must be equal to that being conducted away from the boundary through the insulating disk. The outer face of the insulating disk is taken to be at the ambient temperature of the surroundings, T_a. Therefore:

$$-\lambda\frac{\partial T}{\partial z} = -\lambda\frac{T_{i+1,j} - T_{i-1,j}}{2\delta z} = \kappa\left(T_{i,j} - T_a\right) \tag{4.34}$$

where κ is the thermal conductance of the insulating disk, and is given by $\kappa = (\lambda/d)_{Insulation}$ where d is the thickness of the insulating disk. T_a is the temperature of the heat transfer medium (in this case the oil sprayed onto the disks, the temperature of which is measured by a thermocouple in the oil delivery pipe and continuously recorded during the experiment). Equation (4.34) may be re-arranged with $T_{i+1,j}$ substituted from equation (4.31). The same method may be employed to develop an expression for $T_{i-1,j}$ at the other insulated surface shown as line AD in Figure 4.4.

4.3.8 Numerical solution of Finite Difference equations

Sections 4.2 and 4.3 describe how the partial differential equation derived in Section 1 may be converted to a system of finite difference equations. For a solution mesh with n nodes at which temperatures are unknown, then n simultaneous finite difference equations can be written. These must be solved to determine the temperature distribution at each time step. The equations may be written in matrix form, and for relatively simple problems involving a small number of unknown temperatures may be efficiently solved using direct elimination or matrix inversion methods. However, where fine meshes are used (and hence n becomes large) more efficient iterative techniques are available to solve the equations at each timestep. Two methods – Jacobi and Gauss Seidel – were considered for this work. Jacobi iteration uses the appropriate version of equation (4.31) to calculate the temperatures at each mesh point. However, during one iteration the temperatures used are always those calculated during the

previous iteration cycle. Once new temperatures have been calculated at all points, the original temperatures are replaced by the newly calculated values and the process repeated until the temperatures converge.

In the Gauss-Seidel method the newly calculated temperatures are used as soon as they are available rather than at the end of each iteration cycle. This method therefore requires less storage, is simpler to program, and quicker to converge and was therefore used to solve the transient model.

The transient model described here is solved using a numerical code written in Fortran 90. Data from the test rig (friction force, and temperatures for boundary conditions) are input to the model using a data file written by the data acquisition computer system on the test rig. The solution process of the model is described here for one disk – in reality the process runs twice in order to calculate temperatures in both the fast and slow disks. The model stores the current temperatures in an array. The values of the coefficients (A to F) in equation (4.31) are also stored in arrays since these vary with position. A program flow chart for this model is shown in Figure 4.5.

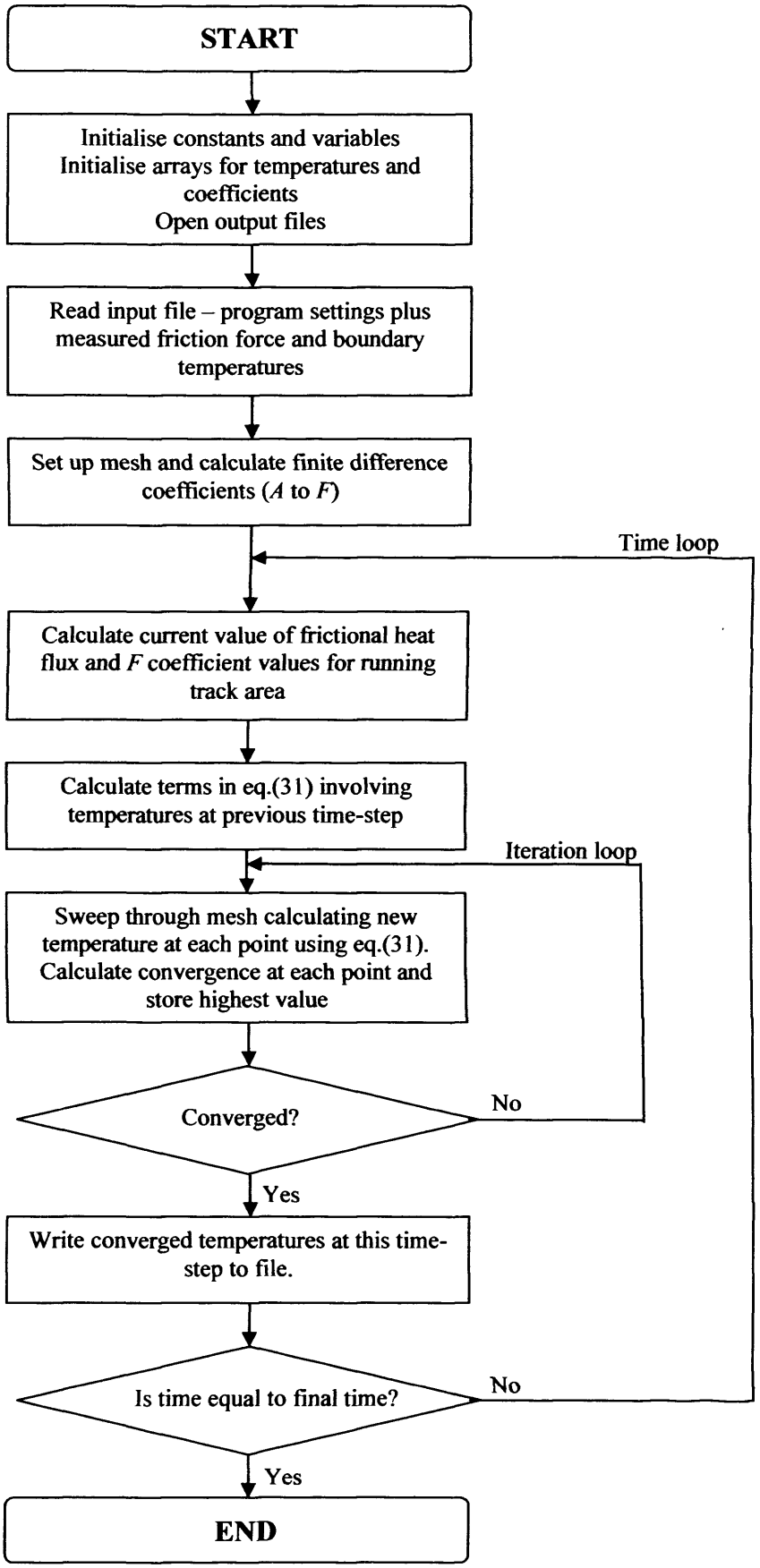

Figure 4.5: Program flow chart for two-dimensional transient model

4.4 Steady-state three-dimensional flash temperature model

The model described in Section 4.3 of this chapter was developed to allow calculation of mean temperatures and heat partition, neglecting the circumferential variation of temperature within the disk outer annulus. The frictional heat flux was assumed to be evenly distributed around the circumference of the disk. However, it is advantageous to consider the circumferential variation of temperature and hence to model the temperature of the disk surfaces as they pass through the contact. This allows for comparison with the surface temperatures calculated using a thermal EHL model of the lubricant within the contact. The model described in this section can be used to calculate the steady-state flash temperatures when the bulk temperatures of the disks have stabilised during the experiment.

As in the two-dimensional transient model, the computing mesh (and hence boundary conditions) is considered to be fixed in space and the material of the disk rotates through it. Since this is a steady-state model, equation (4.21) becomes:

$$\left[\frac{1}{r}\frac{\partial T}{\partial r}+\frac{\partial^2 T}{\partial r^2}+\frac{\partial^2 T}{\partial z^2}+\frac{1}{r^2}\frac{\partial^2 T}{\partial \theta^2}\right]+\frac{\omega}{\alpha}\frac{\partial T}{\partial \theta}=0 \qquad (4.35)$$

Figure 4.6 shows the solution region for the flash temperature model. Note that the disk outer annulus has been "unwrapped" for clarity here. The faces ABCD and EFGH are effectively the cross sections of the annulus considered in the two-dimensional model. These are shown as two faces here but are in reality at the same angular position (at $\theta = 0$ and $\theta = 2\pi$).

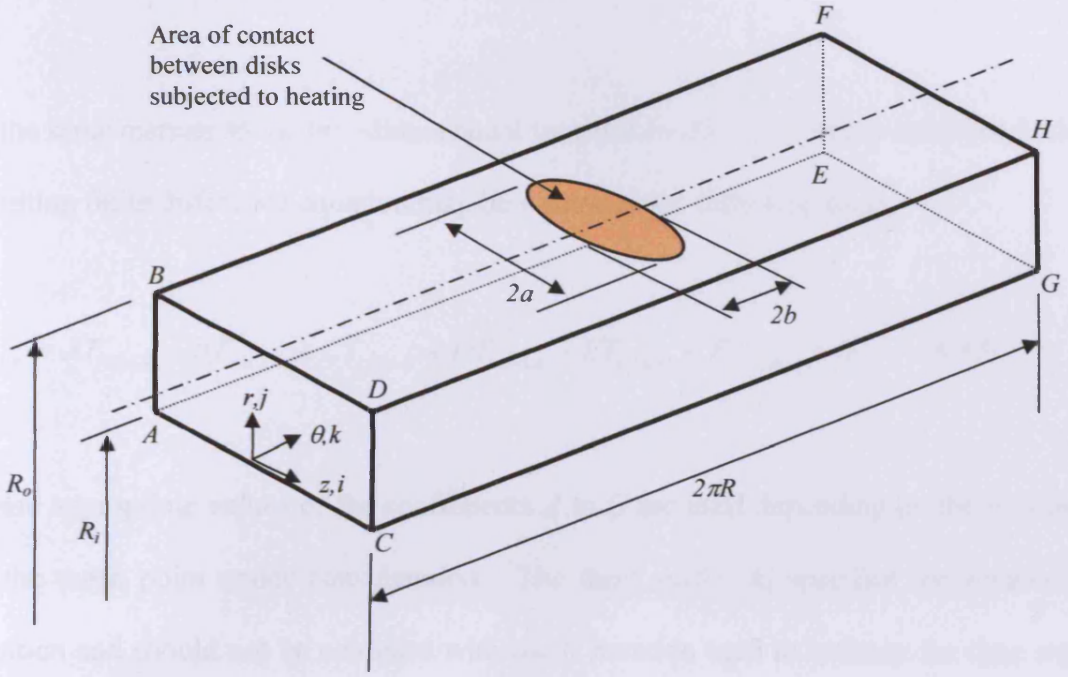

Figure 4.6: Three-dimensional flash temperature model

Equation (4.35) may be developed into a finite difference equation by representing the various partial derivatives with their finite-difference approximations. The central difference expressions as described in Section 4.2 may be used for all terms, except for the $\partial T/\partial\theta$ term which represents the rigid body convection of heat through the mesh by the rotating disk. A central difference representation of the convection term would cause the model to become unstable at high rotational speeds. This is a well known feature of equations describing convection processes and can be remedied by using backwards differences for the convective terms, referred to as "upwind differencing". Thus in order to obtain a stable numerical model of the annulus the $\partial T/\partial\theta$ term is approximated by

$$\frac{\partial T}{\partial \theta} = \frac{T_{i,j,k} - T_{i,j,k-1}}{\delta\theta} \tag{4.36}$$

In the same manner as the two-dimensional transient model described in section 4.3, the resulting finite difference equation may be written in the following form:

$$T_{i,j,k} = AT_{i+1,j,k} + BT_{i-1,j,k} + CT_{i,j+1,k} + DT_{i,j-1,k} + ET_{i,j,k+1} + FT_{i,j,k-1} + G \tag{4.37}$$

where appropriate values of the coefficients A to G are used depending on the location of the mesh point under consideration. The third suffix, k, specifies the rotational position and should not be confused with the K notation used to indicate the time step in the two dimensional transient analysis.

4.4.1 Interior nodes

The coefficients A to G may again be greatly simplified by expressing the inner radius as $r_{in} = s\delta r$ and setting $\gamma = \frac{\delta r^2}{\delta z^2}$. Thus for the interior nodes, the coefficients of equation (4.37) become

$$A = B = \gamma X \qquad C = \frac{2(s+j)+1}{2(s+j)} X \qquad D = \frac{2(s+j)-1}{2(s+j)} X$$

$$E = \frac{1}{(s+j)^2 \delta\theta^2} X \qquad F = \frac{1 + \frac{\omega \delta r^2}{\alpha} \delta\theta (s+j)^2}{(s+j)^2 \delta\theta^2} X$$

where X is a common term:

$$X = \left\{ 2(1+\gamma) + \frac{2}{(s+j)^2 \delta\theta^2} - \frac{\omega \delta r^2}{\alpha \delta\theta} \right\}^{-1}$$

4.4.2 Boundary Conditions

4.4.2.1 Inner radius of annulus

This is face ACEG shown in Figure 4.6. This face is at the same radial position R_i as the thermocouples which were used to provide a temperature boundary condition for the two-dimensional transient model. During a revolution of the disk the change in temperature on the surface as it passes through the heating zone cannot penetrate to this depth (Qiao, 2005), and so the temperature distribution on this face is taken to be independent of θ and is specified by temperatures recorded in the experiment

4.4.2.2 Outer faces of annulus

These are faces CDGH and ABEF shown in Figure 4.6. Since these faces are insulated using PTFE washers and the heat flow within the disk and away from the running track is predominantly radial, it is reasonable to assume that these temperatures are also independent of θ and are fixed using values from the two-dimensional model results at the corresponding time-step as boundary conditions.

4.4.2.3 End faces of mesh

These faces (ABCD and EFGH shown in Figure 4.6) are at the same position and so the temperatures at corresponding points on these faces are constrained to be equal to each other.

4.4.2.4 Outer surface of disk

This is the outer surface of the disk (BDFH in Figure 4.6). Here the surface is frictionally heated over the elliptical contact region, and cooled over the remainder of its area. The dimensions of the contact region are assumed to be equal to the Hertzian contact dimensions, and the heat flux is assumed to follow the same semi-elliptical shape as the Hertzian pressure distribution. The convective cooling coefficient is that determined experimentally and using the two-dimensional transient model. In addition, the heat partition parameter β is now known since it is calculated as part of the solution of the two-dimensional model of the experiment. In order to eliminate $T_{i,j+1,k}$, an approach similar to that described in section 4.3 is used, hence:

$$\lambda\frac{\partial T}{\partial r}=\lambda\frac{T_{i,j+1,k}-T_{i,j-1,k}}{2\delta z}=q_{fr}-h_t\left(T_{i,j,k}-T_a\right) \tag{4.38}$$

In the computational model, values of h_t will be set to zero for points which are within the contact ellipse. The value of q_{fr} is

$$q(\theta,z)=\hat{q}\sqrt{1-\frac{(\theta-\pi)^2R_o^2}{b^2}-\frac{z^2}{a^2}} \tag{4.39}$$

inside the contact ellipse and zero elsewhere, where a and b are the Hertzian contact ellipse semi dimensions as shown in Figure 4.6, and $\theta = \pi$ is the angular position of the centre of the contact ellipse. The value of the peak heat flux, $\hat{q}$, is

$$\hat{q} = \frac{3\beta F U_s}{2\pi ab} \qquad \text{for the fast surface}$$

$$\text{and} \quad \hat{q} = \frac{3(1-\beta) F U_s}{2\pi ab} \qquad \text{for the slow surface} \tag{4.40}$$

4.4.3 Solution of finite difference equations

The resulting set of simultaneous equations for the steady-state flash temperatures within the annular region is solved using Gauss-Seidel iteration in a numerical code written in Fortran 90. The model uses a fine mesh in the area of the contact in order to accurately resolve the flash temperature variation within the contact, but a coarser mesh is adopted away from the contact, where a fine mesh is unnecessary and would result in unnecessarily high computational overheads. A flow-chart of the solver may be seen in Figure 4.7.

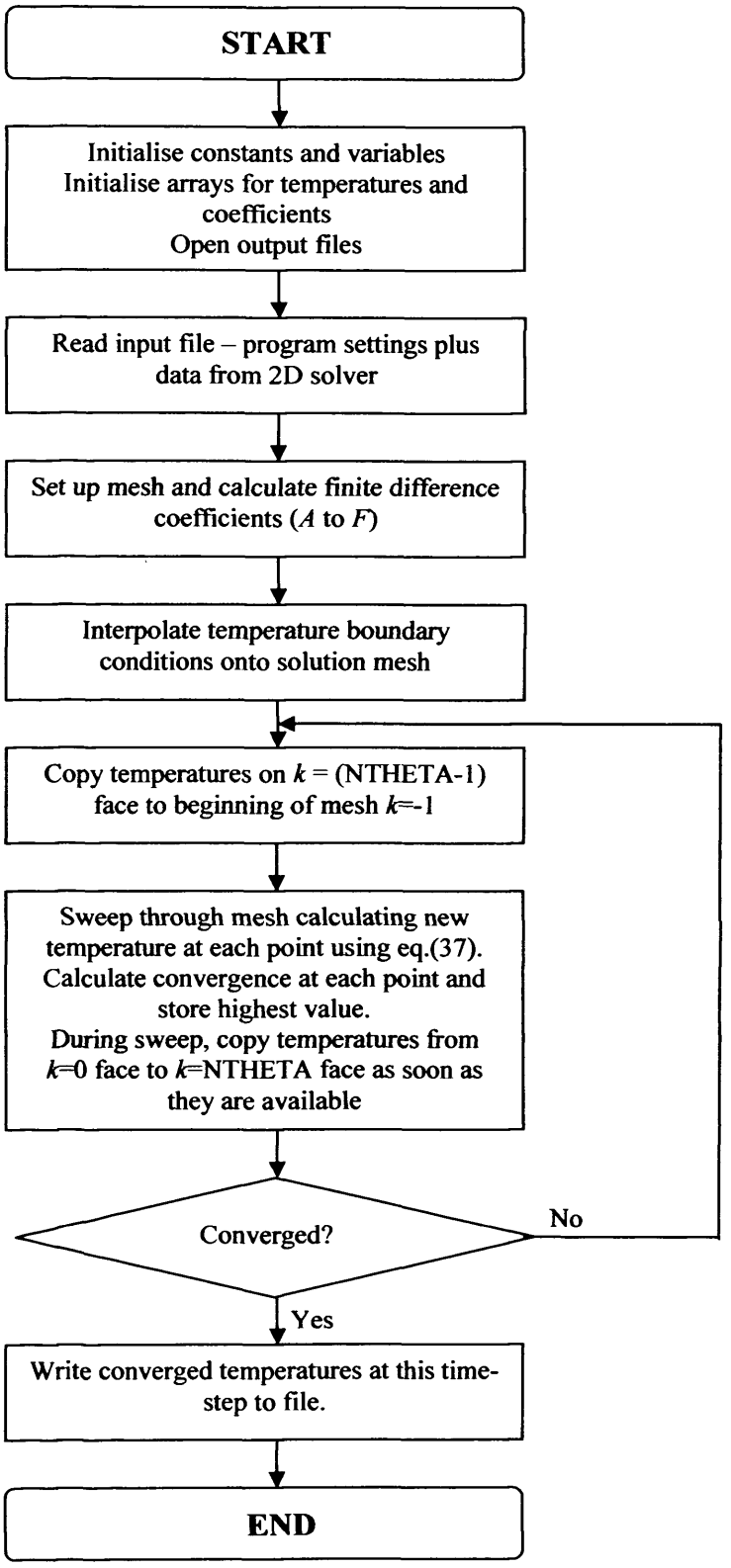

Figure 4.7: Program flow chart for three-dimensional steady-state model

Heat partition experimental results

5.1 Introduction

This chapter reports the results of a series of experiments designed to investigate the temperature distributions and division of heat between the contacting surfaces in a rolling/sliding EHL contact. The work uses the fully-instrumented test rig described in Chapter 3, in which the test disks have been fitted with six thermocouples, at radial levels 3mm and 6mm below the surface of the disk.

It should be noted that in previous experimental work carried out using this test rig (prior to its modification by the author) such as that of Patching (1994) and Dhulipalla (2006) the objective was to establish the conditions under which the test disks would experience scuffing failure. However, in the current work great care has been taken to actively *avoid* operating the test disks under conditions which could lead to scuffing, as this would then require the time-consuming calibration and installation of a new pair of disks. Reference was made to previous experimental data collected using the rig to establish "safe" maximum operating temperatures and loads in order to avoid scuffing.

5.2 Experimental procedure

At the start of a test session, the oil heaters and stirrers were switched on to allow the hydraulic, transmission and test head oil systems to reach their pre-set operating

temperatures. Their temperatures were monitored using thermocouples installed in the oil tanks, which were connected to a suitable electronic thermocouple reader. Once these had reached operating temperature, the pumps were switched on and the oil circulated through the test head of the disk machine with the shafts stationary. A warm-up period of around one hour was found to be sufficient to allow the test head temperatures to stabilise. During this period, a visual check was made on each oil-delivery point within the test head to ensure that oil was reaching all the bearings. Towards the end of the warm-up period, the cooling air for the slip rings was turned on and the main drive started with the shafts being brought up to the required speed for the first test. At this point, the data acquisition system was used to monitor the temperatures of the embedded thermocouples, and once these had stabilised the actual test could be started, with the data acquisition system being set to log data to a file.

At the beginning of a test, the disks are run with no load for 60 seconds, and then the required load is applied by closing the hydraulic system dump valve and adjusting the servo-valve potentiometer (or control voltage if operating under computer control) until the required load is set. At this point, a rapid rise in disk temperatures is observed. The load is held constant for a sufficient period for approximately steady-state thermal conditions to be reached within the test disks. After a period of experimentation, it was found that a total elapsed time from the start of the test of 1100 seconds was sufficient for steady-state to be achieved. At 1100 seconds, the hydraulic dump-valve is opened to remove the load from the contact. At the same time, the slow shaft yoke is manually retracted against its stop to ensure that the test disks are fully separated. Once the load is removed, the temperatures of the test disks drop rapidly as they cool, and the test continues for a period of time sufficient to allow

the disks to return to steady-state thermal conditions. A total elapsed time of 2250 seconds was found to be sufficient for the cooling phase to reach steady-state temperatures. At this point, the data acquisition is stopped, and the file checked to ensure that it has been correctly written by the data acquisition software. Following each test, a visual check was made on the test disks to ensure no significant surface degradation had occurred and that there were no problems with the ceramic insulating washers (in view of the issues with the failure of the original PTFE washers).

5.3 Experimental programme

Experiments were run at four sliding speeds – 10 ms^{-1} (Series A), 13 ms^{-1} (Series B), 16 ms^{-1} (Series C) and 20 ms^{-1} (Series D) – with the gearing set to give a slide/roll ratio of 1.24. At each of these sliding speeds, tests were carried out with loads increasing from an initial load of 850 N, giving a maximum Hertzian contact pressure between the disks of 1.0 GPa. Rather than setting a maximum load, previous experimental data collected using super-finished disks in scuffing experiments with the same kinematic conditions were analysed, and the lowest fast disk bulk temperature at which scuffing occurred was determined for each speed. The lowest scuffing temperature was approximately 180°C, and so the experiments were limited to a maximum fast disk temperature of 160°C in order to avoid scuffing. The sequence of loads used is given in Table 5.1 along with the corresponding maximum Hertzian contact pressure. The temperature limit was reached in some of the test series at loads below 3450N and the sequence of loads applied limited accordingly.

Table 5.1: Loading sequence

Load / N	p_0 / GPa
850	1.0
1460	1.2
1850	1.3
2320	1.4
2850	1.5
3450	1.6

In all, some 20 separate experiments were carried out, together with two repeat experiments to ensure that the recorded temperatures were repeatable. The experiments were carried out with an oil-feed temperature of 60°C. This temperature was chosen as opposed to the value of 100°C used by Patching as a further measure to reduce the likelihood of scuffing.

5.4 Bearing friction measurement

The friction force measured by the torque transducer fitted to the slow shaft includes friction in the bearings supporting the slow shaft and "windage" losses due to shaft rotation. During operation the drive belt acts to brake the slow shaft as the traction force at the sliding disk contact is trying to increase the speed of the slow shaft. Thus, since the bearing friction and windage oppose motion of the shaft, the true traction force at the contact is higher than that recorded by the torque transducer. The parasitic friction must be measured to allow a suitable correction to be applied to the recorded data. This is achieved by disconnecting the coupling between the fast shaft and the drive pulley and running the disks together in free rolling conditions. In this situation the slow shaft pulley is driving the disks against the friction in the (identical) sets of bearings which support the fast and slow shafts, and the measured friction will

be equal to twice the total parasitic losses of the slow shaft. These parasitic losses were measured as a function of load at slow shaft speeds of 774 rpm, 1005 rpm, 1238 rpm and 1546 rpm which correspond to the sliding speeds of 10 ms^{-1}, 13 ms^{-1}, 16 ms^{-1} and 20 ms^{-1} used in this work. The results obtained are shown in figure 5.1

Inspection of figure 5.1 shows that, at each sliding speed, the parasitic frictional losses increase with load as expected in a linear manner. For each sliding speed, a linear best-fit between friction force and applied load was calculated (as shown by the heavy lines in figure 5.1) which are used to adjust the friction force recorded during experiments accordingly.

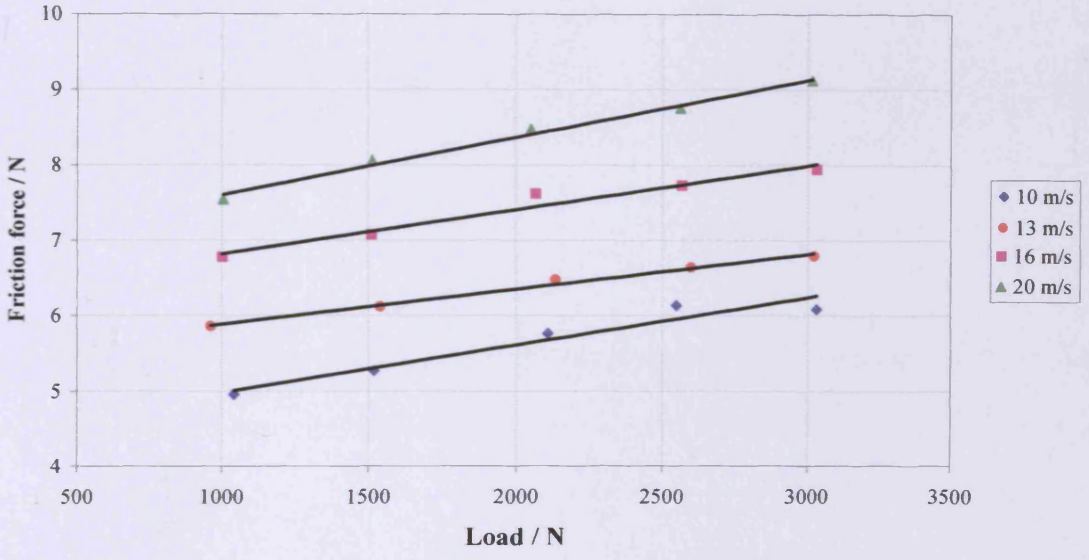

Figure 5.1: Parasitic friction force due to bearings and windage losses in slow shaft

The values given in figure 5.1 are for speeds corresponding to the slow shaft speed during the experiments described in subsequent sections. It should be noted that during these experiments the fast shaft is rotating at over four times the speed of the slow shaft, and consequently the bearing frictions at the fast shaft support bearings

will be higher than those at the slow shaft bearings. This can be seen by extrapolating the trends shown in figure 5.1 to higher speeds.

5.5 Experimental Results

The results from each experimental series are now presented in turn. In all cases, the six thermocouple positions in each disk are denoted by a letter, as shown in Figure 5.2.

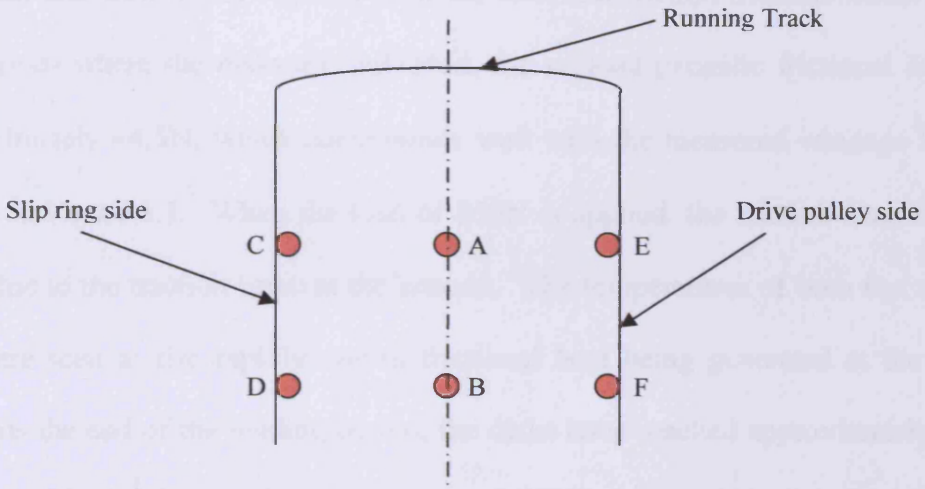

Figure 5.2: Thermocouple positions within test disks

In addition, all of the temperature traces from the experiments are presented to the same scale to allow direct comparison between the temperature results. None of the friction force measurements presented in this chapter have been adjusted for bearing friction.

5.5.1 Series A tests – 10 ms^{-1} sliding speed

In this series of tests, the slow shaft was rotating at 774 rpm, which corresponds to a sliding speed of 10 ms^{-1} and a mean entraining speed of 8.06 ms^{-1}. Figure 5.3 shows the centre-line thermocouple temperatures at positions A and B (see Figure 5.2) for both fast and slow disks, together with the load and friction measurements. During the periods where the disks are unloaded, the no-load parasitic frictional losses are approximately –4.5N, which corresponds well with the measured windage losses as shown in Figure 5.1. When the load of 850N is applied, the friction rises to around +5N, due to the traction force at the contact. The temperatures of both fast and slow disks are seen to rise rapidly due to frictional heat being generated at the contact. Towards the end of the loading period, the disks have reached approximately steady-state conditions, with the fast disk at around 80°C and the slow disk reaching 66°C. The slow disk thermocouple at position A (3mm below the running track) reaches a temperature of 66.3°C whereas the thermocouple at position B (6mm below the running track) reaches 65.9°C. This appears to suggest a flow of heat from the disk surface towards the shaft, as would be expected from a cursory consideration of problem. However, when the fast disk data are examined, the thermocouple at position A is at a lower temperature (79.8°C) than that at position B (81.1°C). The basic premise that heat flows from the surface where it is generated in a broadly radial direction would suggest that the thermocouple at position A, being nearer the surface, should be at a higher temperature than that at position B. Further consideration is given to this apparent contradiction later in this chapter, following presentation of the remaining experimental results.

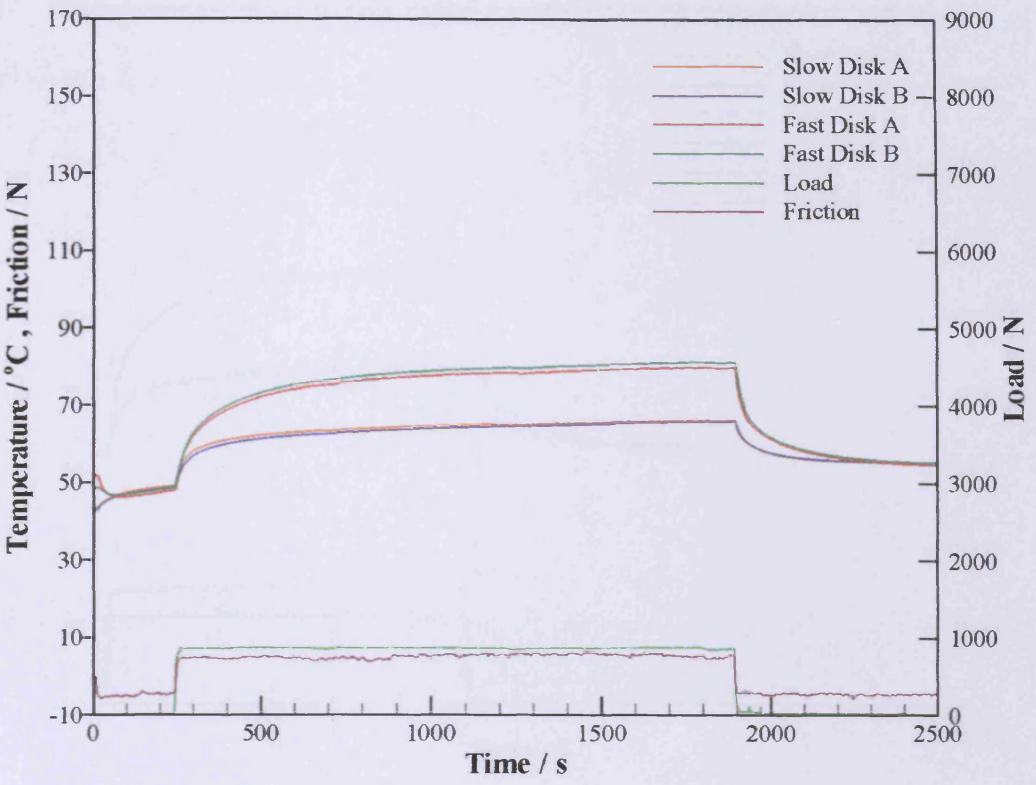

Figure 5.3: Test A1 (774rpm, 850N)

Figure 5.4 shows the results of test A2 where the disks were loaded to 1460N, equivalent to a maximum Hertzian contact pressure (p_0) of 1.2 GPa. Again, the initial no-load friction measurements are consistent with those recorded during measurements of parasitic losses. At the steady-state conditions immediately before the load is removed (t = 1070 s), the slow disk has temperatures at positions A and B of 77.3°C and 76.4°C respectively. This is a larger radial gradient than that measured in test A1, which is consistent with the higher frictional power being dissipated in test A2. The fast disk has temperatures at positions A and B of 101.6°C and 101.9°C respectively. Whilst the thermocouple nearest the surface is still at a lower temperature than that further below the surface, the difference between these measurements is only 0.3°C, compared to a difference of 1.4°C recorded in test A1.

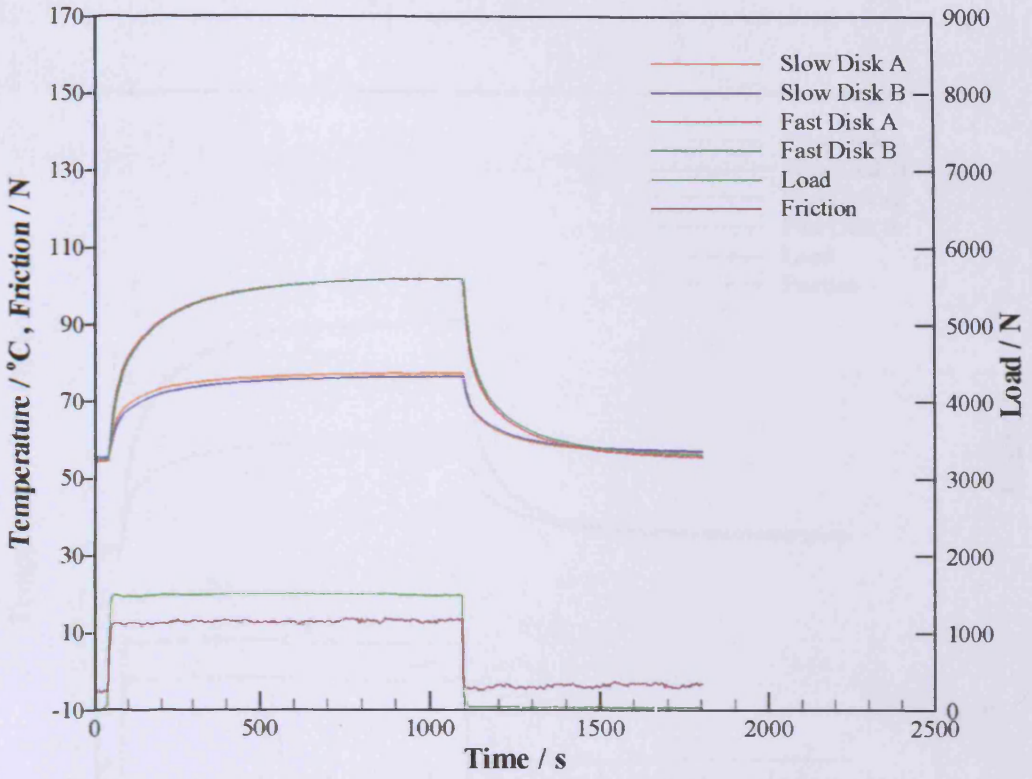

Figure 5.4: Test A2 (774rpm, 1460N)

Consideration of the temperatures at the end of the cooling period during both experiments shows that the thermocouple at position B is always at a slightly higher temperature than that at position A, nearer the running track. This behaviour can be seen in both the fast and slow disks in experiments A1 and A2, and is consistent with a radial outflow of heat within the disk as the disk and shaft cool back to ambient temperature and suggests that the fast temperatures recorded during the loaded phase of these experiments cannot be simply explained by an offset in the thermocouple signals. It is also of interest to study the temperatures during the initial phases of the load stage. At 130 seconds, some 70 seconds after the load was applied, the temperatures in the slow disk at positions A and B were 70.8°C and 69.4°C, and in the fast disk were 85.3 and 84.5°C respectively, both indicating centre-line heat flows into the disks from the surface during the initial phase of the load stage.

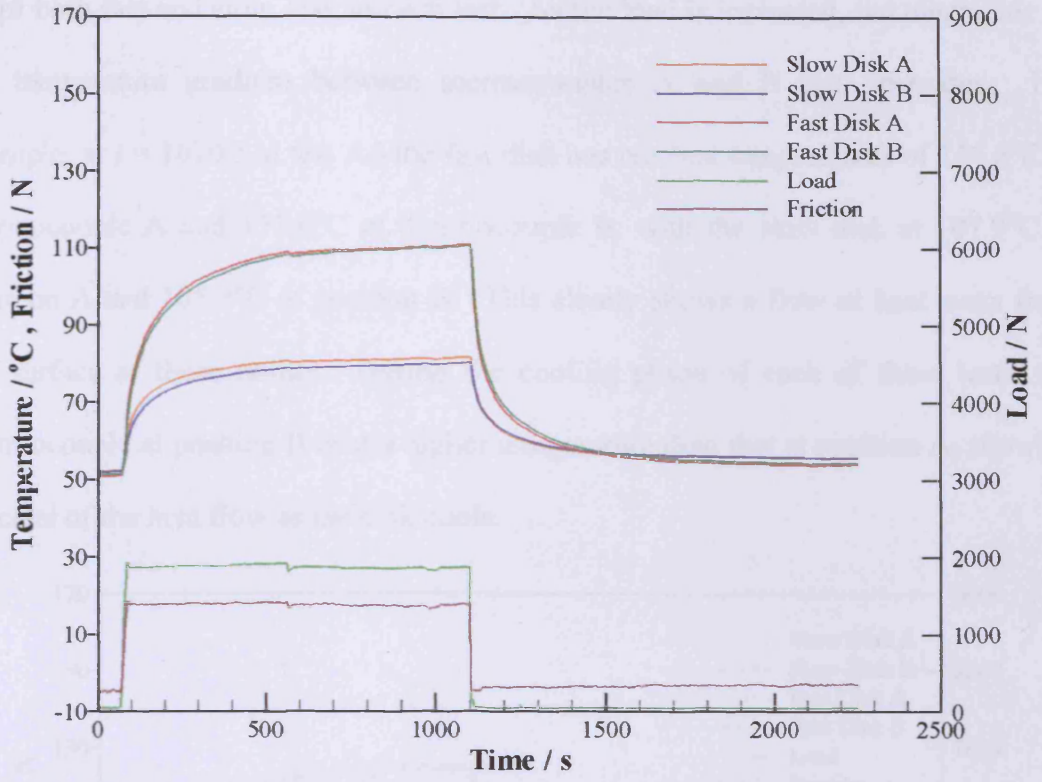

Figure 5.5: Test A3 (774rpm, 1850N)

Figure 5.5 shows the results of test A3, at a load of 1850 N. The temperature distributions within this experiment are also of interest. At all times whilst the load is applied, the temperatures at position A (nearest the surface) are higher than those at position B for both fast and slow disks. At t = 1070 s, the temperatures at positions A and B are 81.7°C and 80.2°C for the slow disk, and 110.9°C and 110.3°C for the fast disk. The apparently contradictory fast disk temperature behaviour is no longer seen, with the thermocouple nearer the surface being at a higher temperature in both disks.

Figures 5.6, 5.7 and 5.8 present the results of the final three experiments in this series, with loads of 2320 N (p_0 = 1.4 GPa), 2850 N (p_0 = 1.5 GPa) and 3450 N (p_0 = 1.6 GPa) respectively. In each case, the temperature behaviour is consistent, with the

highest temperatures at the end of the loading period being observed at thermocouple A for both fast and slow disk in each test. As the load is increased, the magnitude of the temperature gradient between thermocouples A and B also increases. For example, at t = 1070 s in test A6 the fast disk has reached temperatures of 156.6°C at thermocouple A and 153.6°C at thermocouple B, with the slow disk at 107.9°C at position A and 105.2°C at position B. This clearly shows a flow of heat away from the surface at these points. During the cooling phase of each of these tests, the thermocouple at position B is at a higher temperature than that at position A, showing reversal of the heat flow as the disk cools.

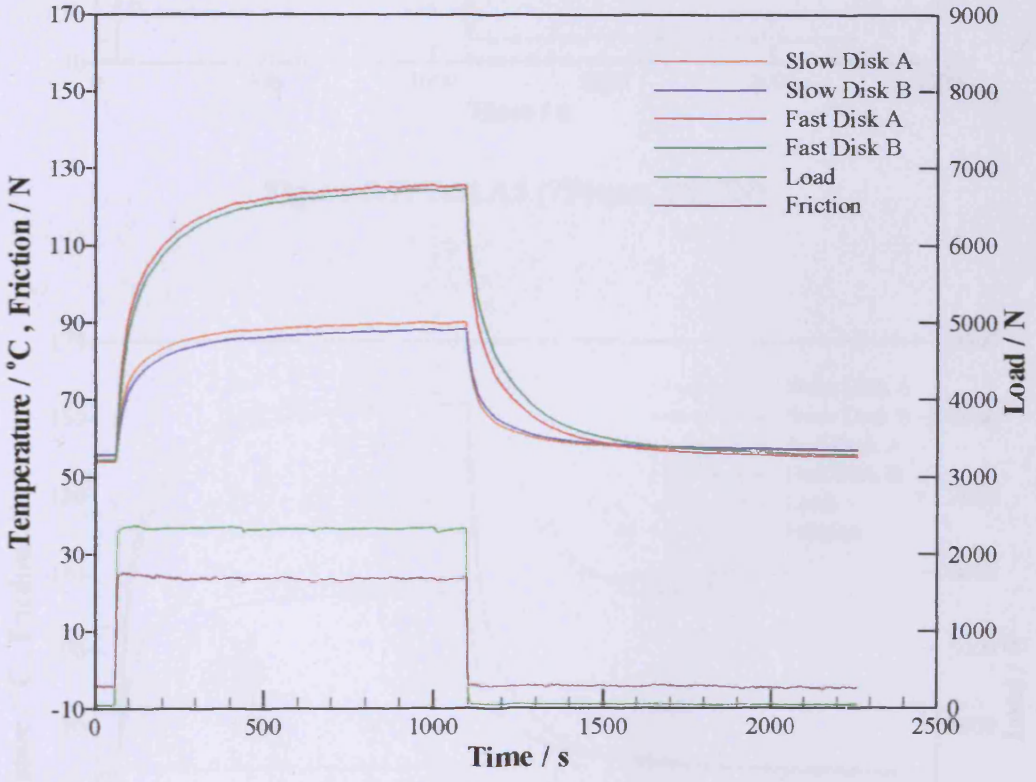

Figure 5.6: Test A4 (774rpm, 2320N)

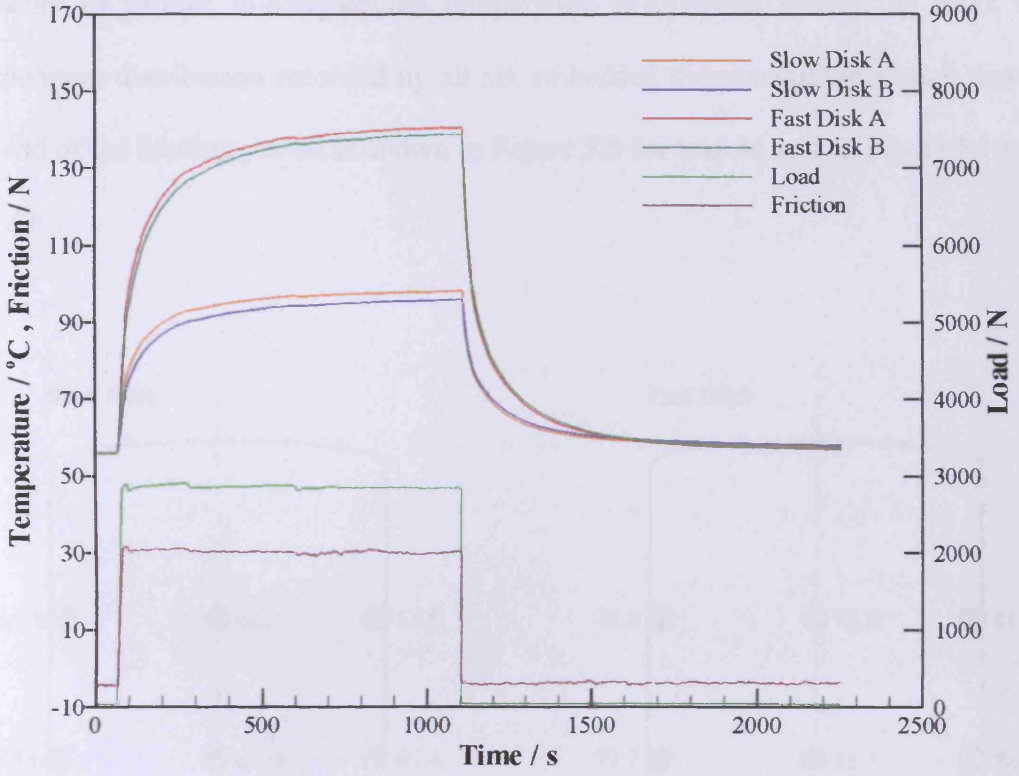

Figure 5.7: Test A5 (774rpm, 2850N)

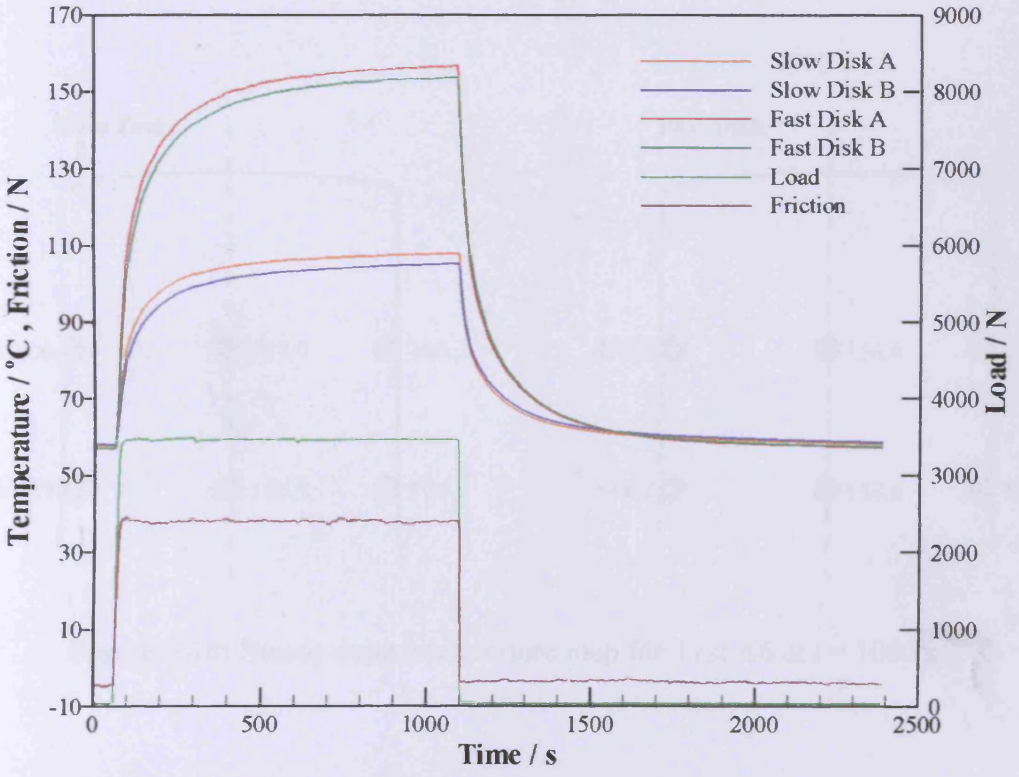

Figure 5.8: Test A6 (774rpm, 3450N)

In order to further investigate the temperature distribution within the disks the temperature distribution recorded by all six embedded thermocouples in each disk at the end of the loading period is shown in Figure 5.9 for test A1 and in Figure 5.10 for test A6.

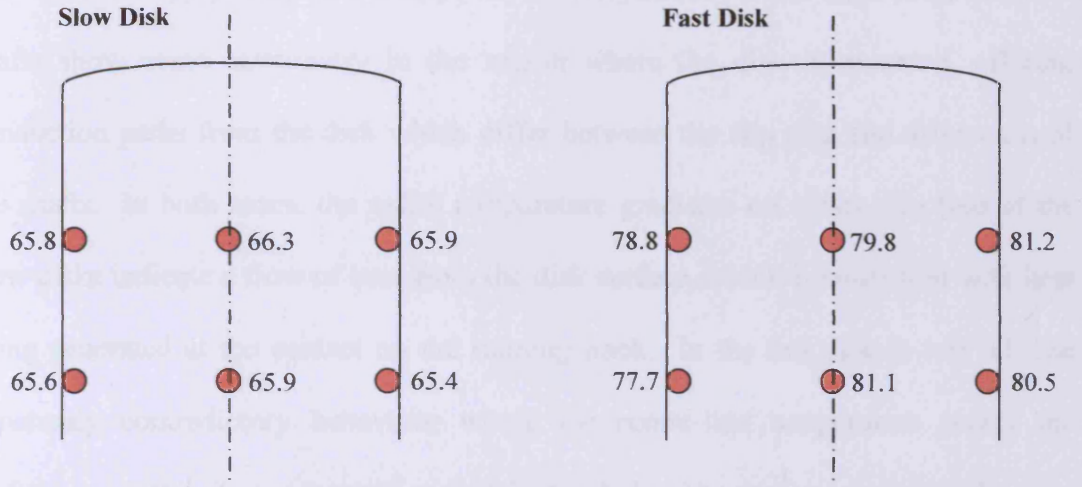

Figure 5.9: Steady-state temperature map for Test A1 at t = 1880 s

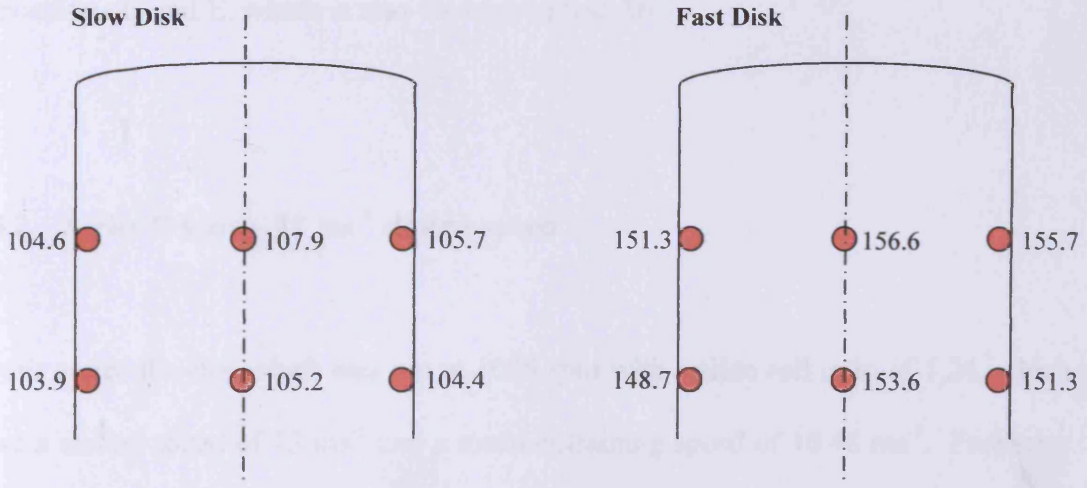

Figure 5.10: Steady-state temperature map for Test A6 at t = 1080 s

Inspection of Figures 5.9 and 5.10 shows that the temperature distribution within both fast and slow disks displays some asymmetry, particularly at higher loads (figure 5.10). The temperatures at positions E and F, on the drive side of the disks, are noticeably higher than those at positions C and D, on the slip ring side, in all cases except the slow disk in figure 5.9 although temperatures here are only marginally above the oil supply temperature of 60°C. This asymmetry is not surprising, since the shafts show some asymmetry in the region where the disk is mounted, offering conduction paths from the disk which differ between the slip ring and drive ends of the shafts. In both cases, the radial temperature gradients on either side face of the slow disks indicate a flow of heat from the disk surface, which is consistent with heat being generated at the contact on the running track. In the fast disk in test A1, the apparently contradictory behaviour where the centre-line temperature nearer the surface at position A was lower than that further below the surface at position B is not repeated in the temperatures recorded at either side of the fast disk. On both side faces, the highest temperatures are recorded by the thermocouples nearest the surface, at positions C and E, which is also the case in test A6.

5.5.2 Series B tests – 13 ms^{-1} sliding speed

In this series the slow shaft was run at 1005 rpm with a slide roll ratio of 1.24, which gave a sliding speed of 13 ms^{-1} and a mean entraining speed of 10.48 ms^{-1}. Five tests were conducted, up to a maximum load of 2850 N, which corresponds to a maximum Hertzian contact pressure of 1.5 GPa. Results are presented in figures 5.11 to 5.15 in the same format as the series A tests previously described.

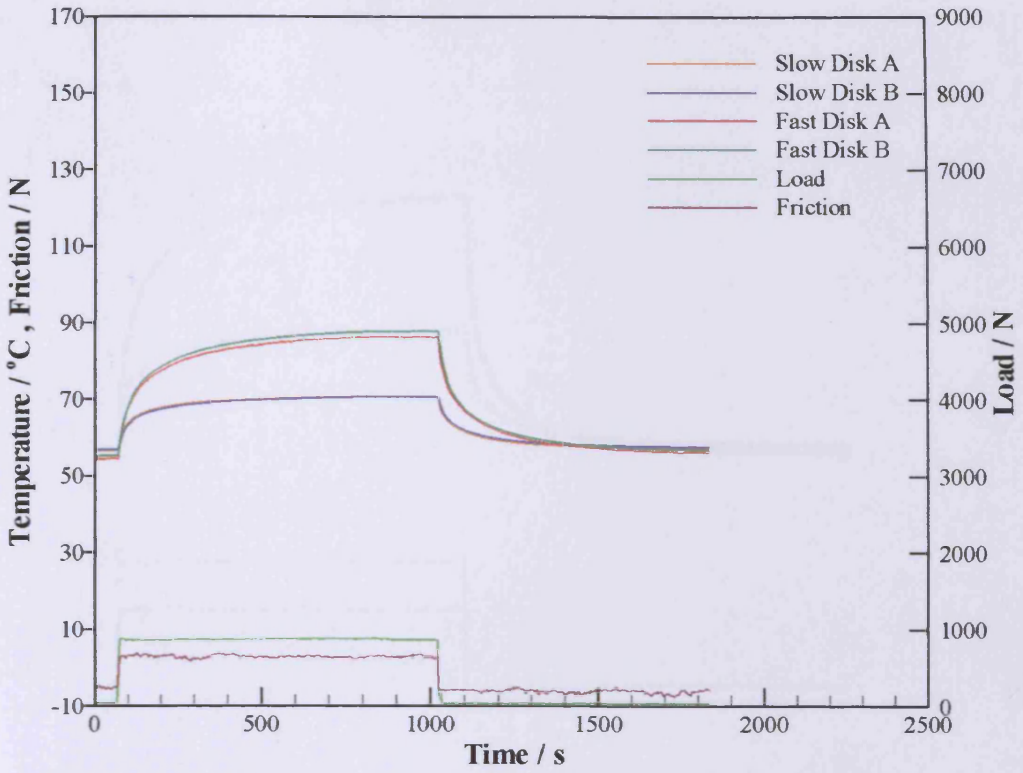

Figure 5.11: Test B1 (1005rpm, 850N)

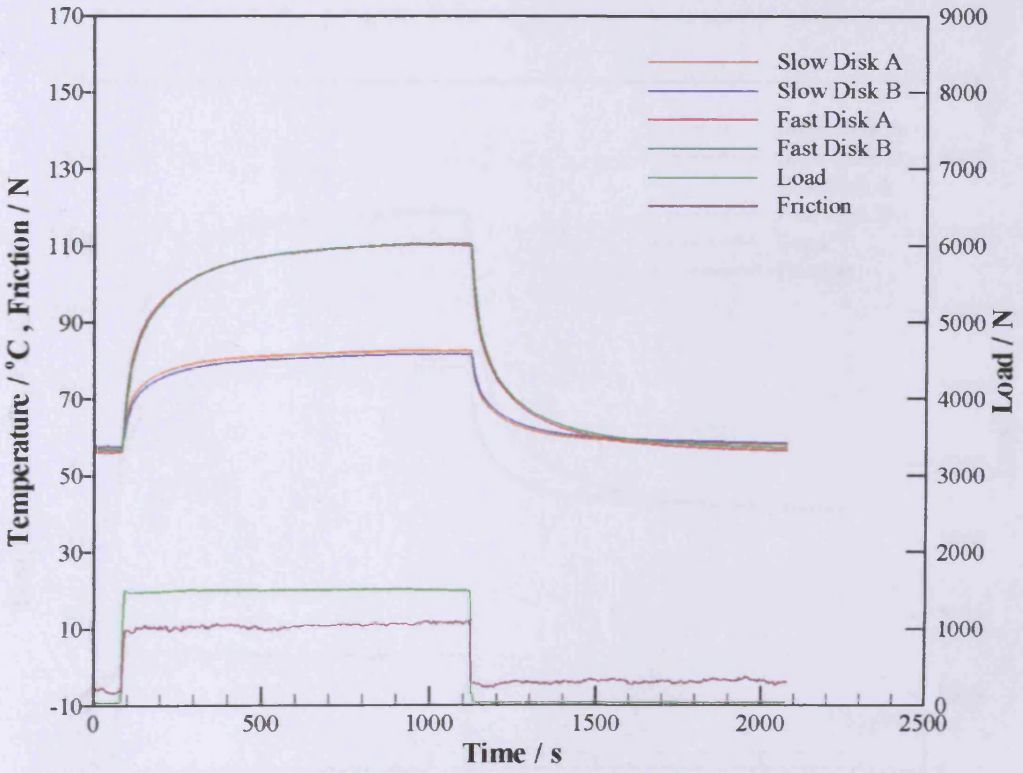

Figure 5.12: Test B2 (1005rpm, 1460N)

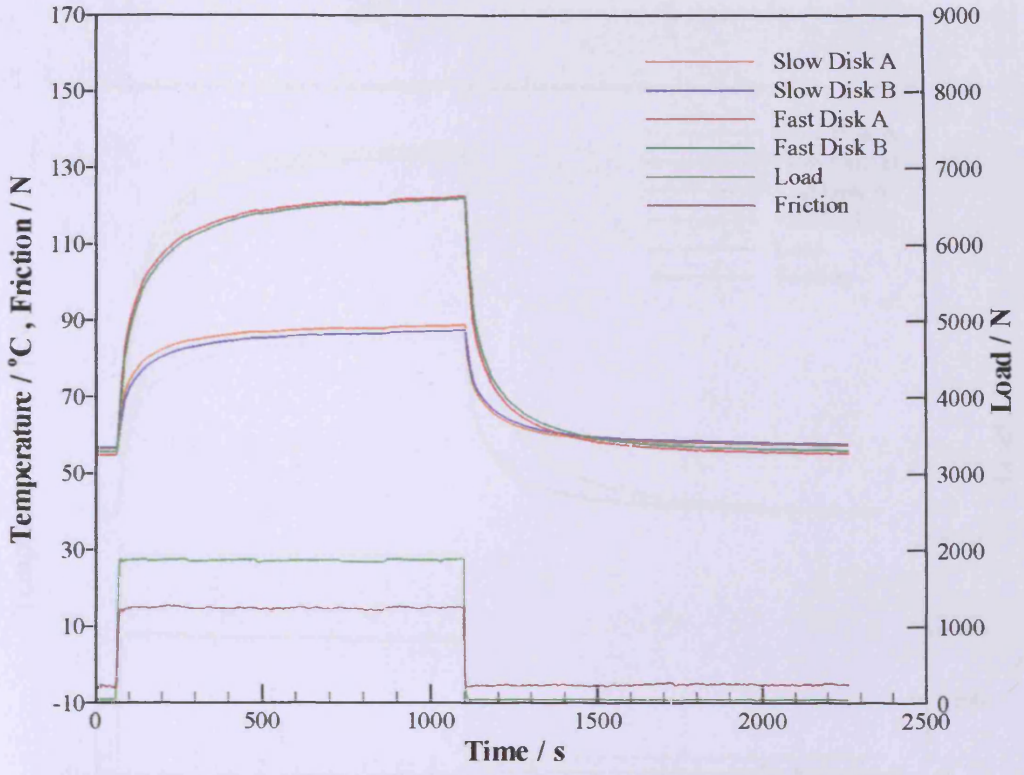

Figure 5.13: Test B3 (1005rpm, 1850N)

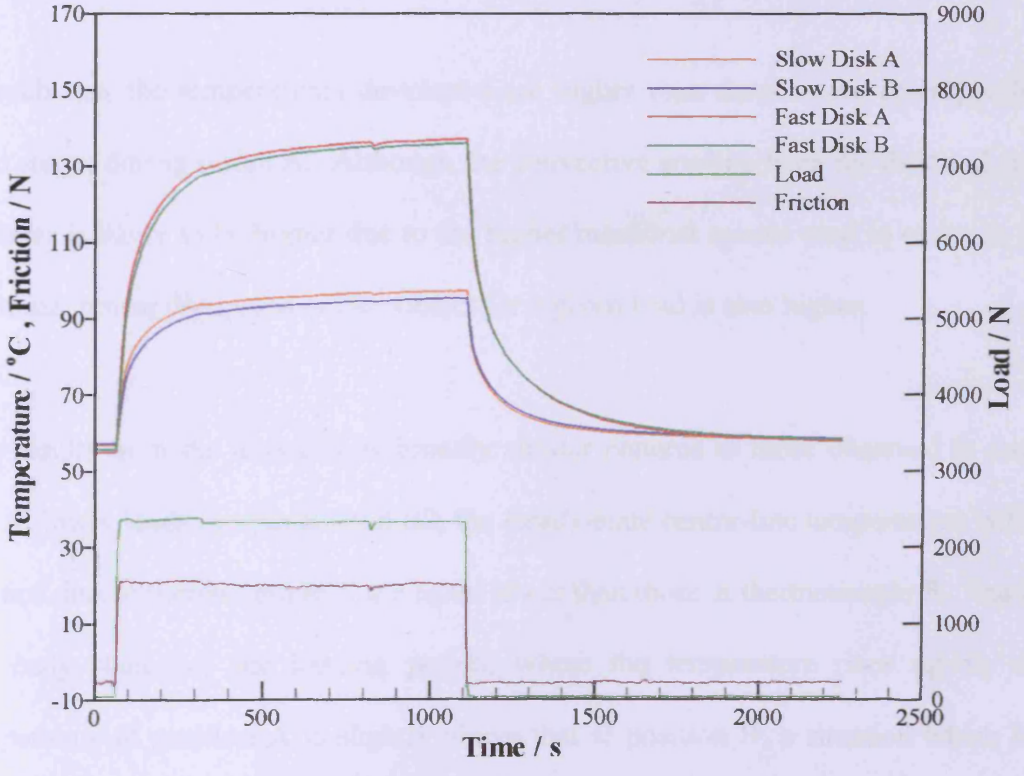

Figure 5.14: Test B4 (1005rpm, 2320N)

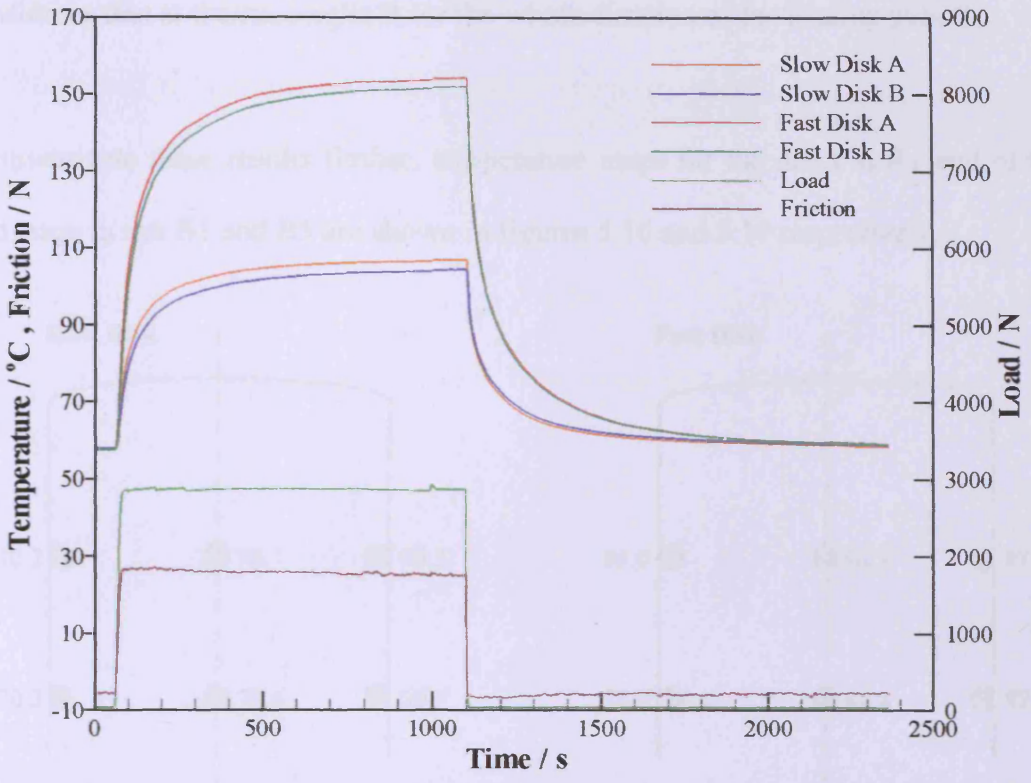

Figure 5.15: Test B5 (1005rpm, 2850N)

In each test, the temperatures developed are higher than those at the corresponding load stages during series A. Although the convective cooling from the disk and shaft surfaces is likely to be higher due to the higher rotational speeds used in series B, the frictional power dissipated at the contact for a given load is also higher.

The results from the tests follow broadly similar patterns to those observed in series A. At lower loads in tests B1 and B2, the steady-state centre-line temperatures within the fast disk at thermocouple A are again lower than those at thermocouple B. During the early stages of the loading period, where the temperature rises rapidly the temperature at position A is slightly above that at position B, a situation which has reversed by the time steady-state conditions are reached. This behaviour reverses in

the tests at higher loads (B3, B4 and B5), where the temperature at thermocouple A rises above that at thermocouple B for the whole duration of the loading period.

To investigate these results further, temperature maps for the disks at the end of the load stage in test B1 and B5 are shown in figures 5.16 and 5.17 respectively.

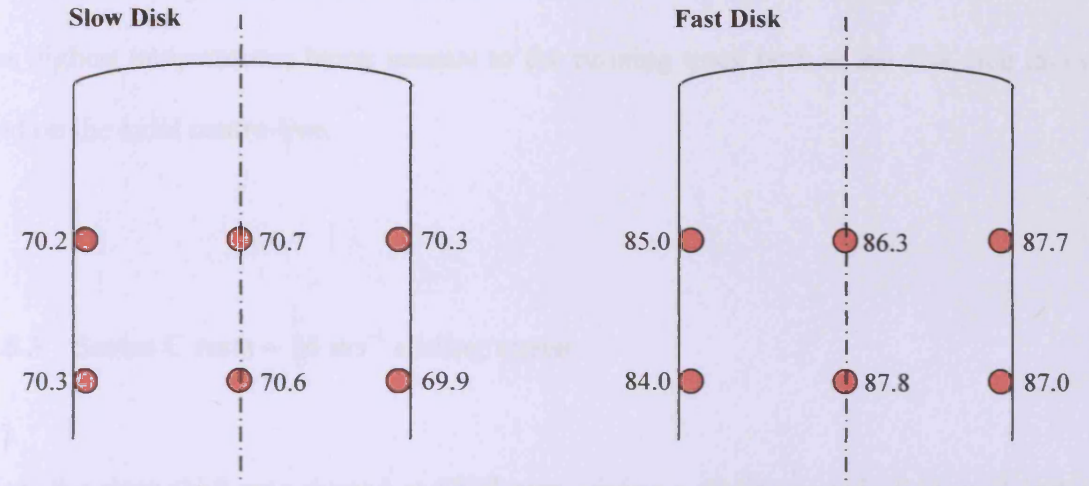

Figure 5.16: Steady-state temperature map for Test B1 at t = 1020 s

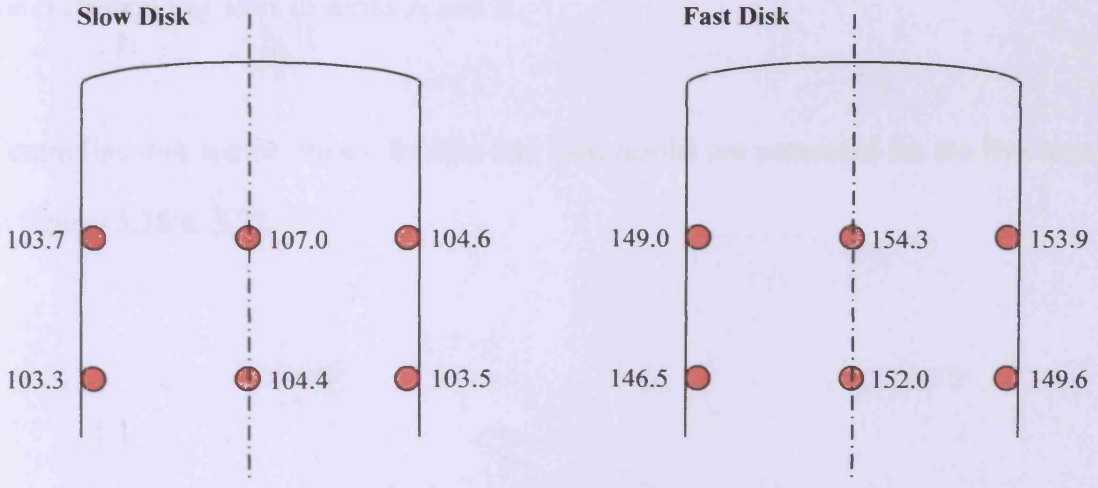

Figure 5.17: Steady-state temperature map for Test B5 at t = 1070 s

As observed in series A, there is some asymmetry in the temperatures, with those at the drive side of the disks being generally slightly higher than those at the slip ring side. The fast disk temperature distributions are also similar to those in series A in that in test B1 the highest temperatures on the sides of the disks are nearest the running track surface whereas those at the disk centre-line are highest further away from the running track. In test B5, the centre-line behaviour has again reversed, with the highest temperatures being nearest to the running track both at the disk side faces and on the axial centre-line.

5.5.3 Series C tests – 16 ms^{-1} sliding speed

Here the slow shaft was rotated at 1238 rpm, giving a sliding speed of 16 ms^{-1} and a mean entraining speed of 12.90 ms^{-1}. Five tests were carried out, with a maximum load of 2850 N in test C5. Disk temperatures at each load were higher than those in the corresponding tests in series A and B.

Centre-line disk temperatures, friction and load results are presented for the five tests in figures 5.18 to 5.22.

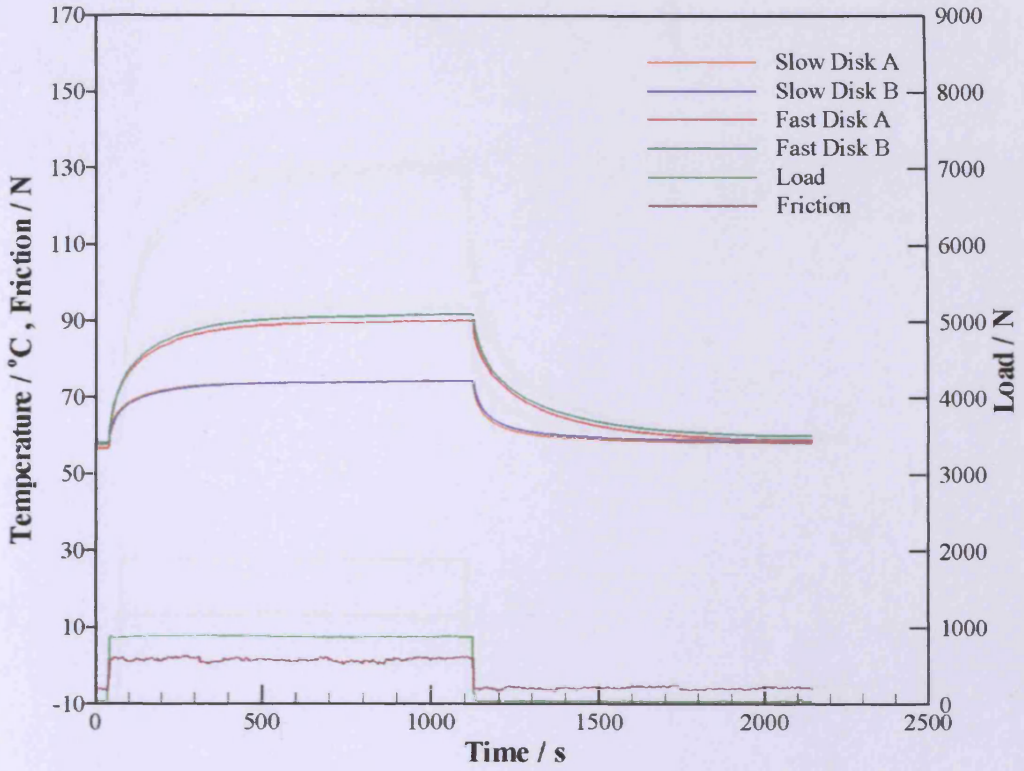

Figure 5.18: Test C1 (1238rpm, 850N)

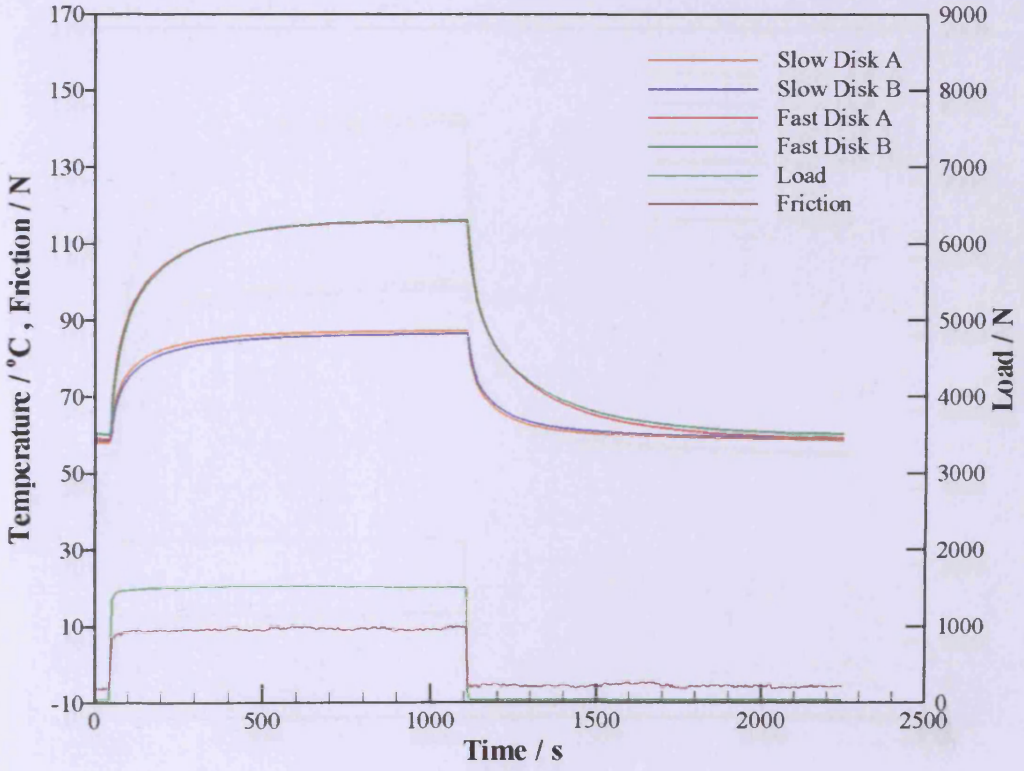

Figure 5.19: Test C2 (1238rpm, 1460N)

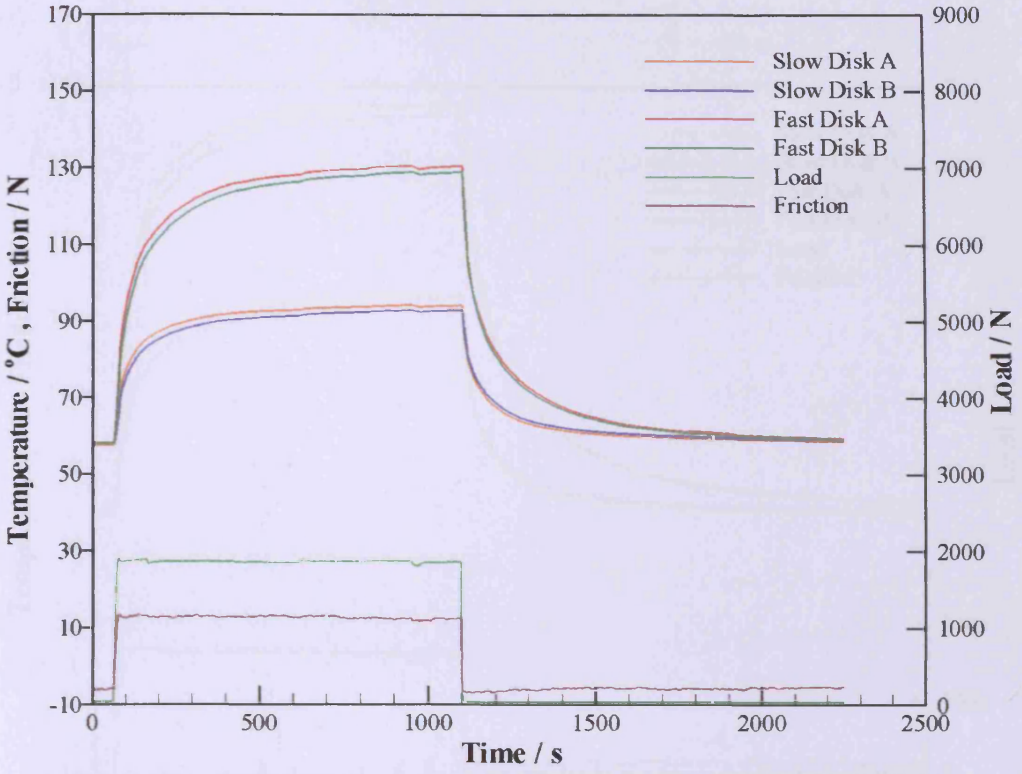

Figure 5.20: Test C3 (1238rpm, 1850N)

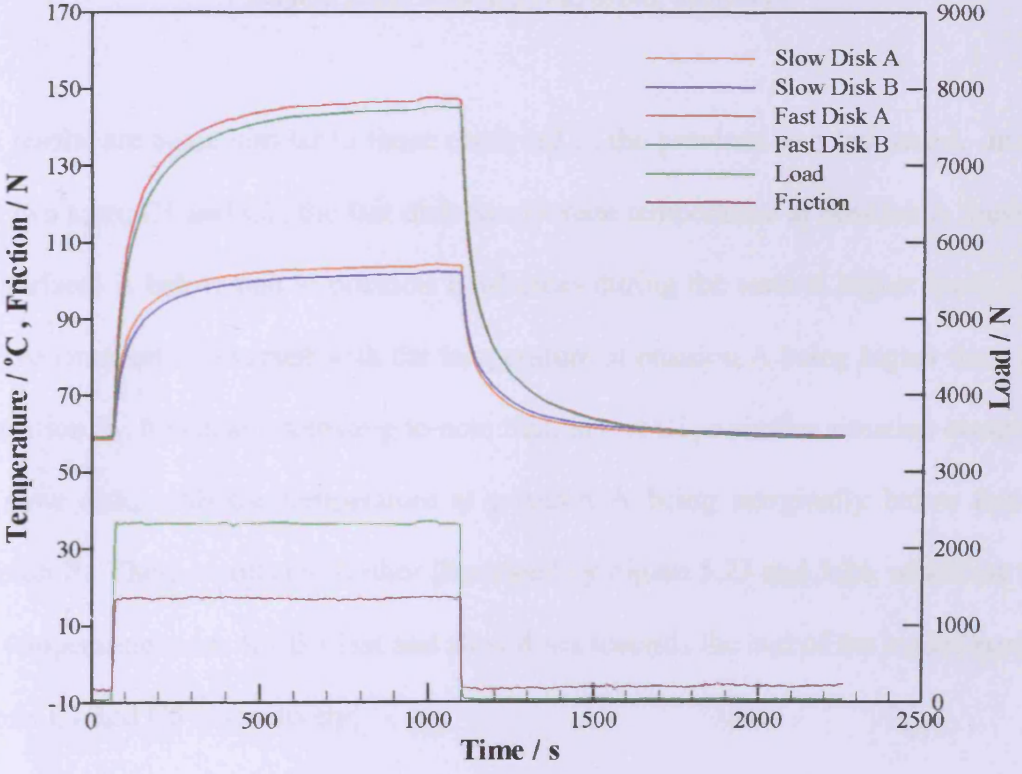

Figure 5.21: Test C4 (1238rpm, 2320N)

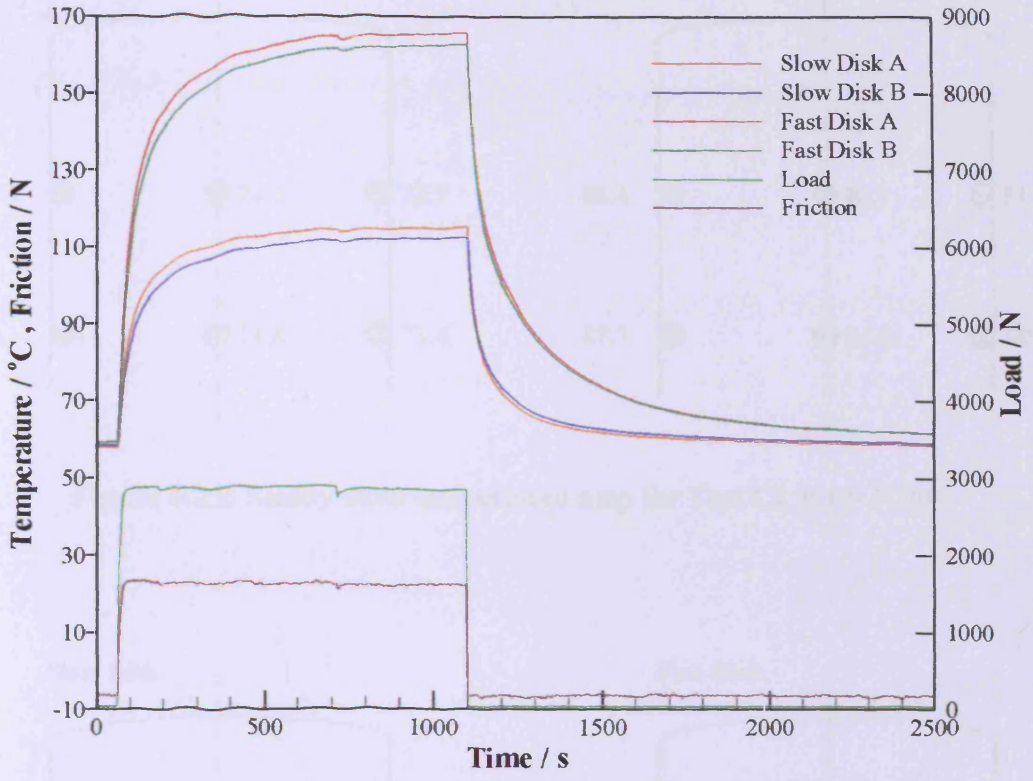

Figure 5.22: Test C5 (1238rpm, 2850N)

The results are again similar to those observed in the previous two test series. In the first two tests, C1 and C2, the fast disk steady-state temperature at position A (nearest the surface) is below that at position B whereas during the tests at higher loads, C3-C5, the situation is reversed with the temperature at position A being higher than that at position B. It is also interesting to note that, in test C1, a similar situation occurs in the slow disk, with the temperature at position A being marginally below that at position B. These results are further illustrated by Figure 5.23 and 5.24, which are the full temperature maps for the fast and slow disks towards the end of the loaded period in tests C1 and C5 respectively.

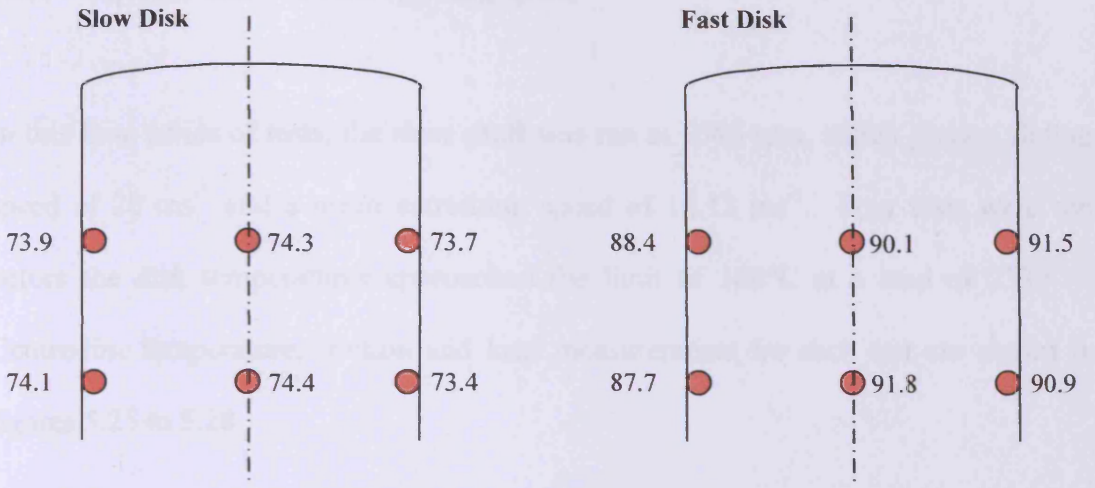

Figure 5.23: Steady-state temperature map for Test C1 at t = 1070 s

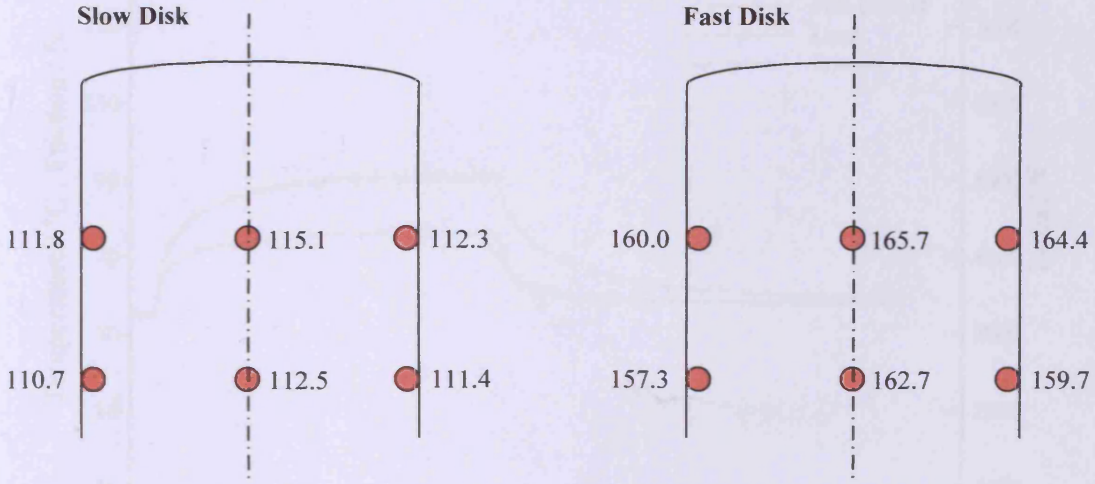

Figure 5.24: Steady-state temperature map for Test C5

Again, the temperature map for test C1 (figure 5.24) show the centre-line temperature to be lower nearer the surface in the fast disk whereas the side temperatures are higher nearer the surface. Interestingly, the slow disk temperatures in this test also show a similar trend with lower temperatures nearer the surface on both the centre-line and slip-ring side, although the temperature differences involved are small.

5.5.4 Series D tests – 20 ms^{-1} sliding speed

In this final series of tests, the slow shaft was run at 1546 rpm, which gives a sliding speed of 20 ms^{-1} and a mean entraining speed of 16.13 ms^{-1}. Four tests were run before the disk temperatures approached the limit of 160°C at a load of 2330 N. Centre-line temperature, friction and load measurements for each test are shown in figures 5.25 to 5.28.

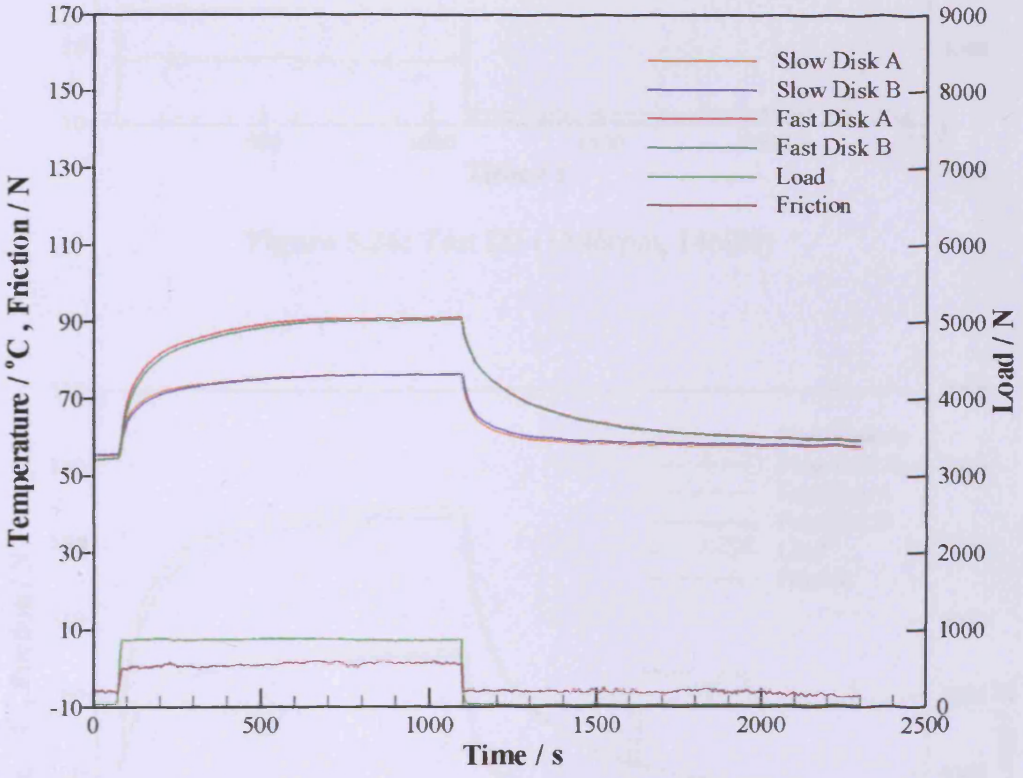

Figure 5.25: Test D1 (1546rpm, 850N)

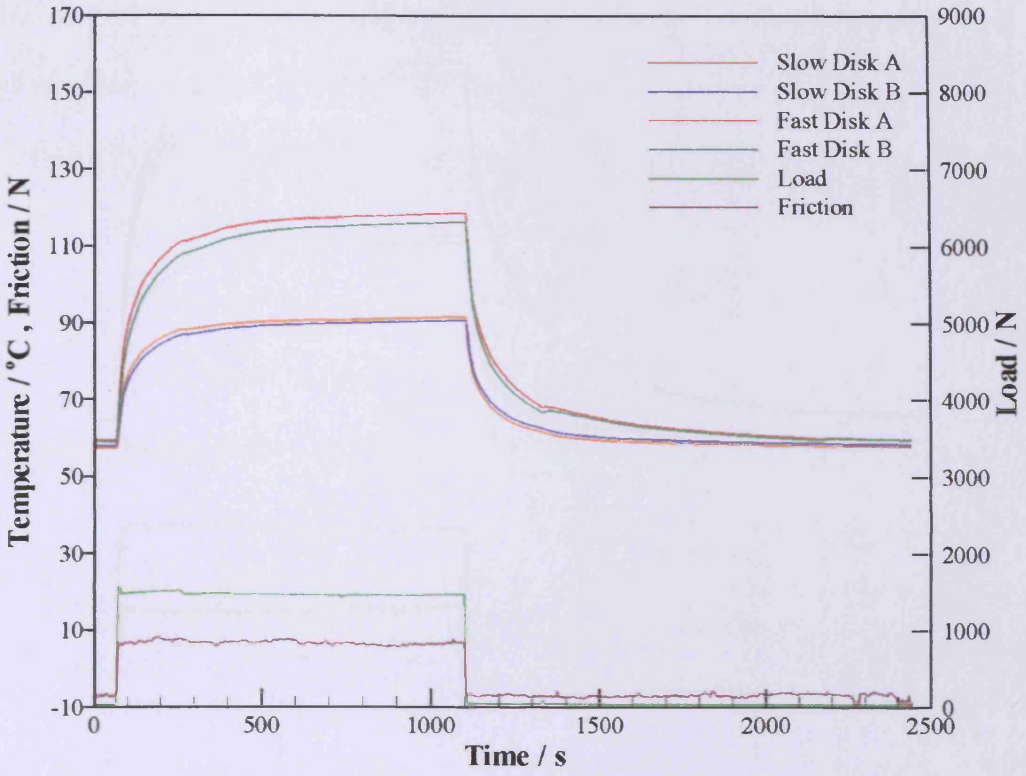

Figure 5.26: Test D2 (1546rpm, 1460N)

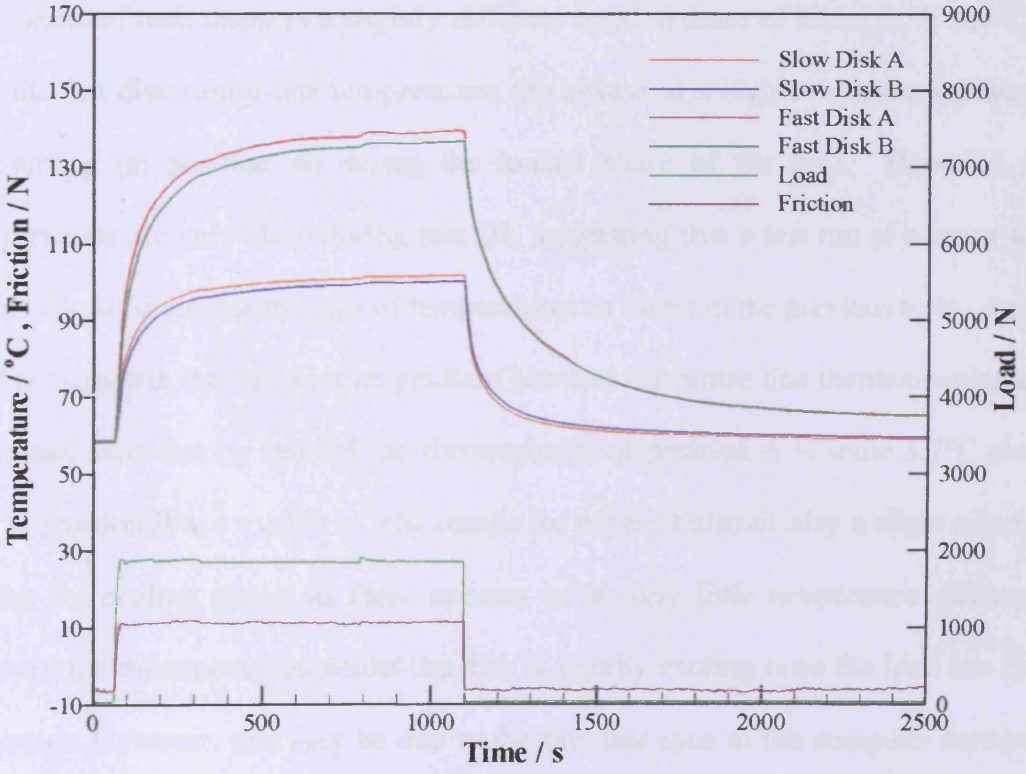

Figure 5.27: Test D3 (1546rpm, 1850N)

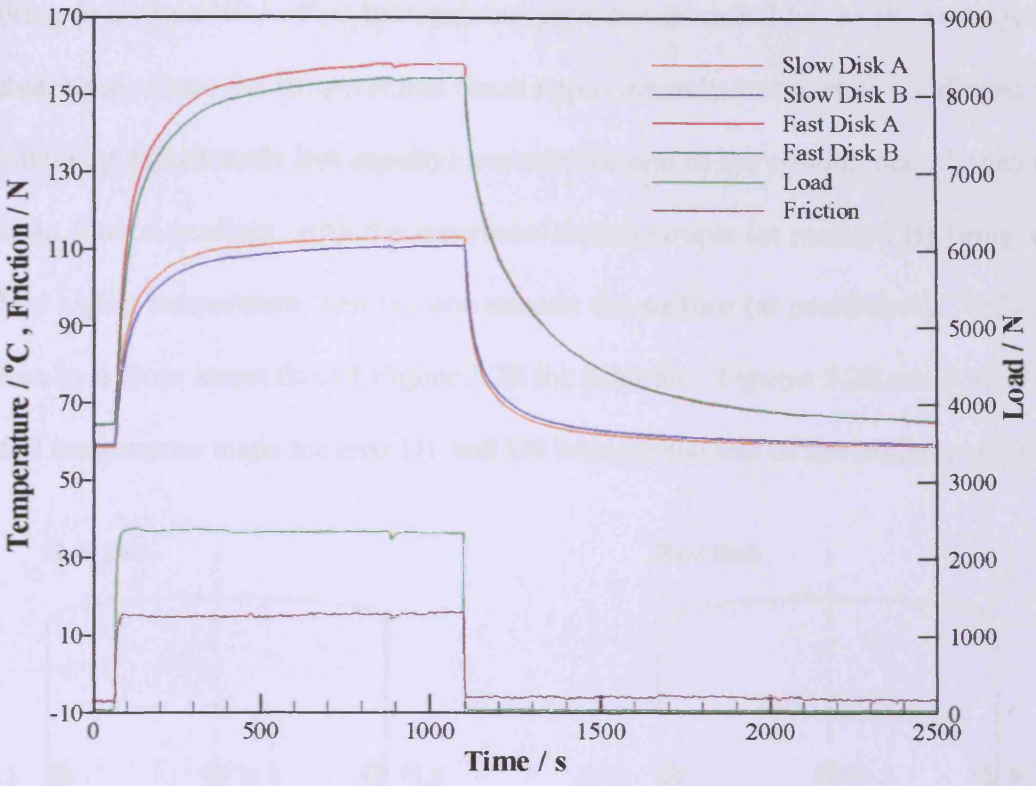

Figure 5.28: Test D4 (1546rpm, 2320N)

This series of tests displays a slightly different trend to those of series A, B and C, in that the fast disk centre-line temperatures are always at a higher temperature nearest the surface (at position A) during the loaded phase of the tests. However, the temperatures are very close during test D1, suggesting that a test run at a lower load would display a similar reversal of temperatures as found in the previous tests. As the load is increased, the temperature gradient between the centre-line thermocouples also increases, such that by test D4 the thermocouple at position A is some 3.7°C above that at position B at t = 1070 s. The results for series D also display a slight anomaly during the cooling phase, as there appears to be very little temperature difference between the thermocouples whilst the disk is rapidly cooling once the load has been removed. However, this may be due to the fact that (due to the computer hardware available) the channels are multiplexed rather than being simultaneously sampled,

resulting in a slight time offset between temperatures recorded by the PC at the same nominal time. Once the temperatures reach approximately steady state conditions (or are changing significantly less rapidly) towards the end of the cooling period, then the disks do show a gradient, with the innermost thermocouple (at position B) being at a slightly higher temperature than the one nearest the surface (at position A). This can be seen by a close inspection of Figure 5.28 for example. Figures 5.29 and 5.30 show the full temperature maps for tests D1 and D4 towards the end of the loaded period.

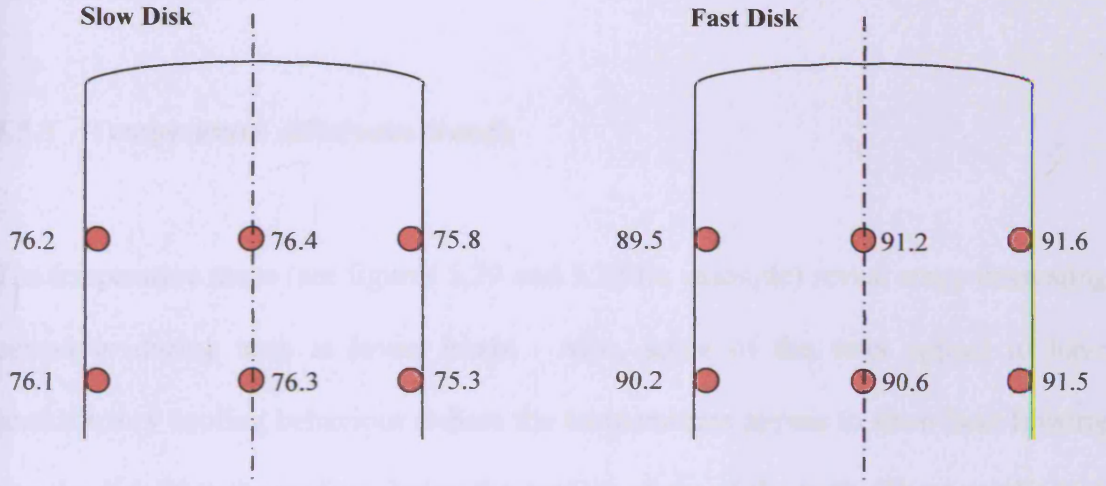

Figure 5.29: Steady-state temperature map for Test D1 at t = 1070 s

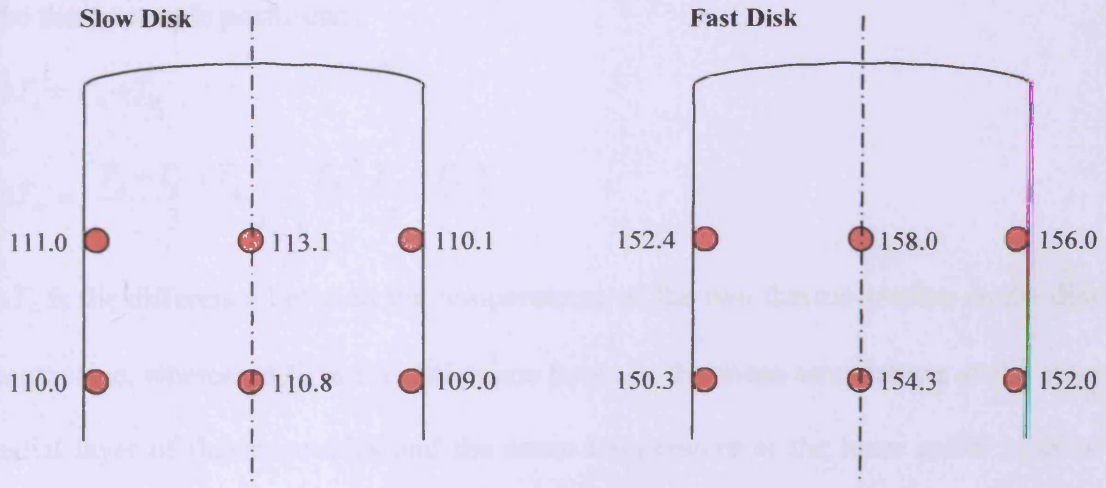

Figure 5.30: Steady-state temperature map for Test D4 at t = 1070 s

The temperature map in figure 5.29, for test D1, confirms that the fast disk centre-line temperature is now higher at position A (nearest the surface) than position B, but displays a slight anomaly in the slip ring side temperatures, with the thermocouple at position C being at a slightly lower temperature than that at position D. This behaviour has not been previously observed. The temperature maps for test D4, shown in figure 5.30, are consistent with previous results for heavily loaded tests. In particular, the fast disk displays the previously observed asymmetry in the temperature distribution.

5.5.5 Temperature difference trends

The temperature maps (see figures 5.29 and 5.30 for example) reveal some interesting behaviour during tests at lower loads. Also, some of the tests appear to have contradictory cooling behaviour (where the temperatures appear to show heat flowing into the disk from the surface during the cooling phase of the test). These results may be investigated further by defining two measures of temperature difference between the thermocouples, ΔT_c and ΔT_m in terms of the six temperatures, T_A to T_F at each of the thermocouple positions:

$$\Delta T_c = T_A - T_B$$

$$\Delta T_m = \left(\frac{T_A + T_C + T_E}{3}\right) - \left(\frac{T_B + T_D + T_F}{3}\right)$$

ΔT_c is the difference between the temperatures of the two thermocouples on the disk centre-line, whereas ΔT_m is the difference between the mean temperature at the outer radial layer of thermocouples and the mean temperature at the inner radial layer of thermocouples. Positive values of ΔT_c and ΔT_m mean that the thermocouples nearest

the disk running track are at a higher temperature than those furthest away from the running track. These temperature differences have been calculated for each of the tests at four times – at 200 seconds which is during the early part of the loaded phase when the disk temperatures are rising rapidly; at 1000 seconds when the disk temperatures have reached approximately steady-state conditions; at 1150 seconds which is during the period of rapid cooling which immediately follows the load removal; and at 2000 seconds which is when the disk temperatures are once again at approximately steady-state conditions. These temperature differences may be seen in figures 5.31 to 5.34 plotted against load for the tests in Series A to D respectively.

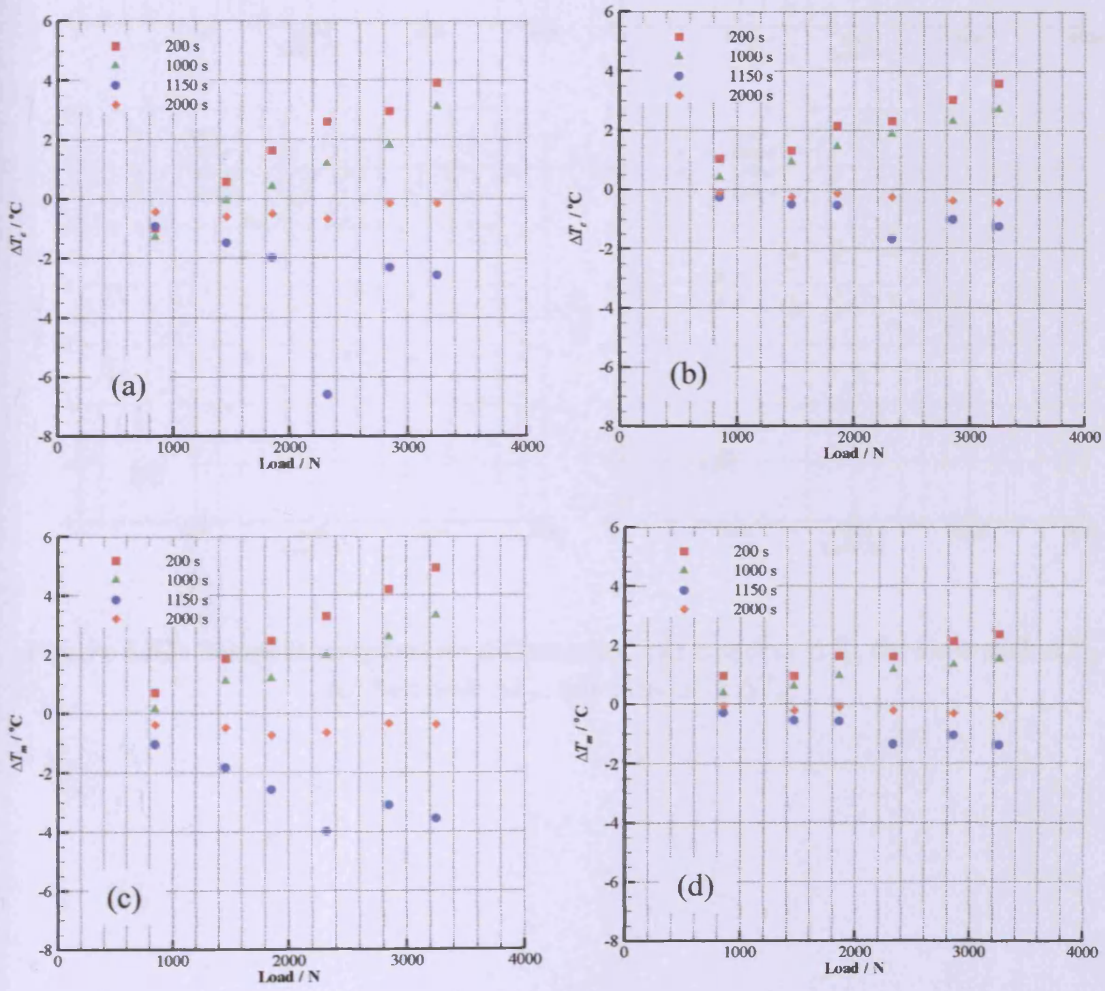

Figure 5.31: Series A temperature differences. (a) fast disk ΔT_c, (b) slow disk ΔT_c, (c) fast disk ΔT_m, (d) slow disk ΔT_m.

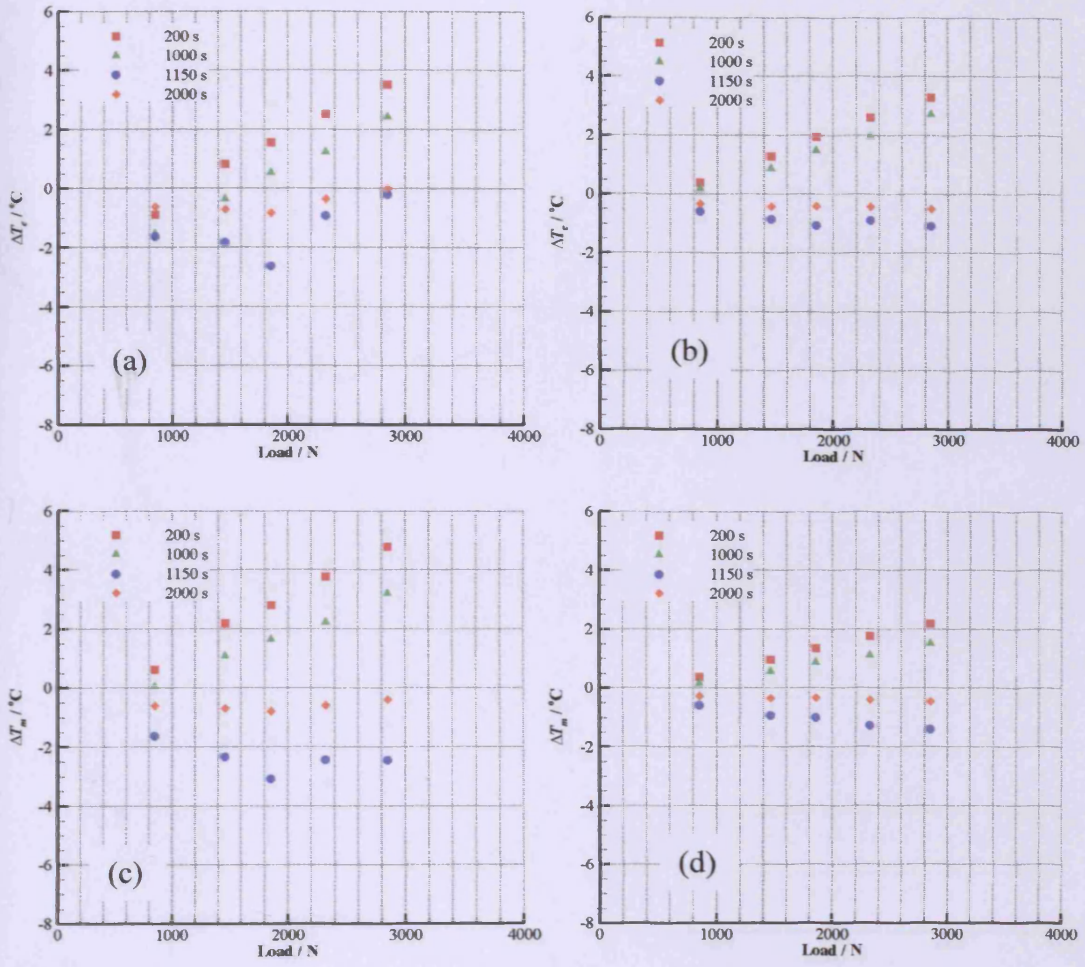

Figure 5.32: Series B temperature differences. (a) fast disk ΔT_c, (b) slow disk ΔT_c, (c) fast disk ΔT_m, (d) slow disk ΔT_m.

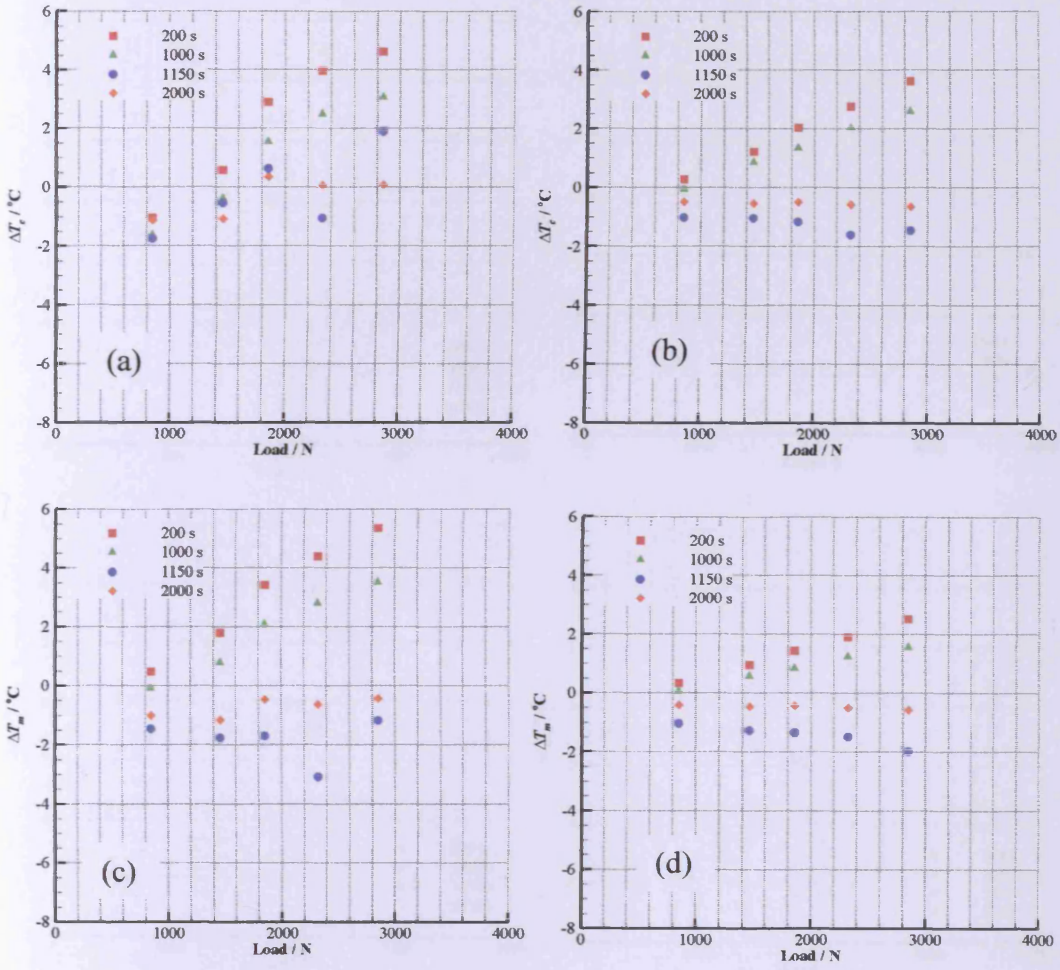

Figure 5.33: Series C temperature differences. (a) fast disk ΔT_c, (b) slow disk ΔT_c, (c) fast disk ΔT_m, (d) slow disk ΔT_m.

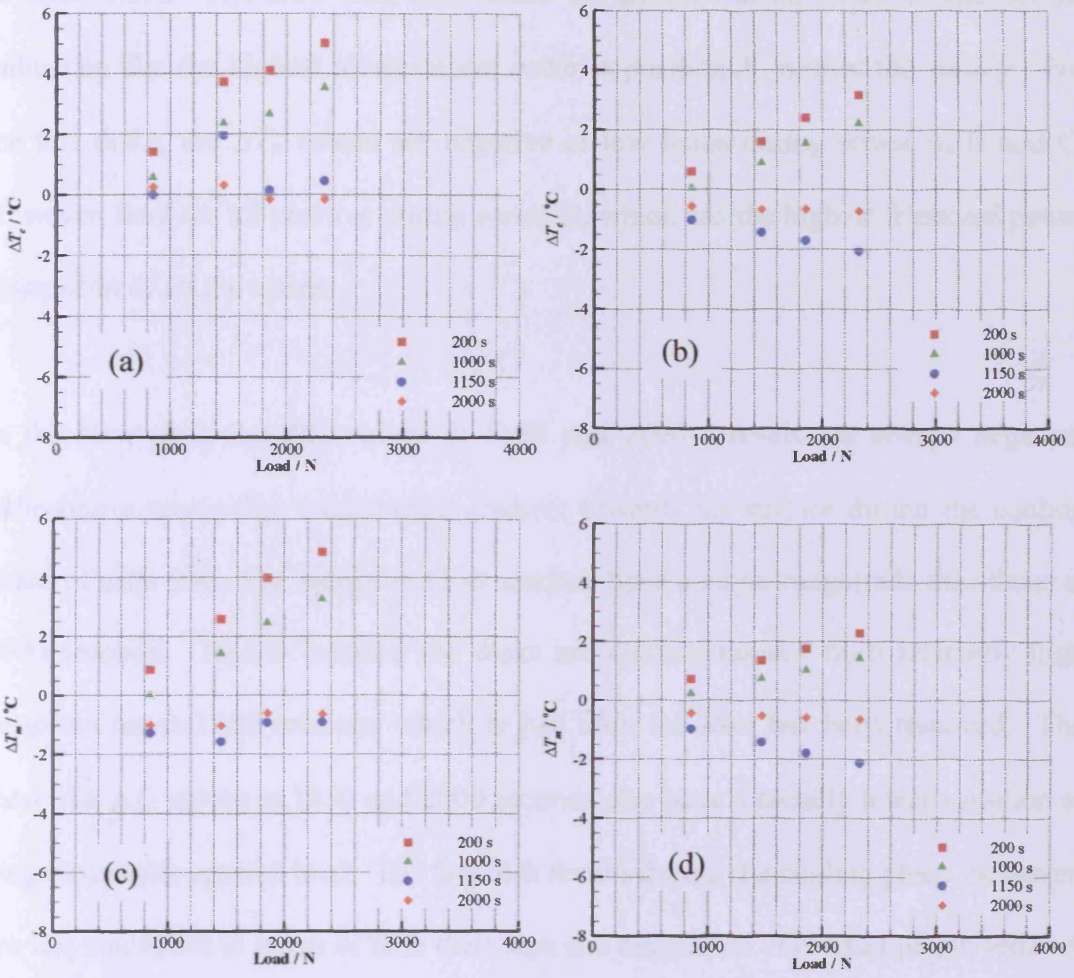

Figure 5.34: Series D temperature differences. (a) fast disk ΔT_c, (b) slow disk ΔT_c, (c) fast disk ΔT_m, (d) slow disk ΔT_m.

Consideration of the central temperature differences, ΔT_c, for the fast and slow disks at both 200 and 1000 seconds show consistent results for all four series of tests. The ΔT_c values follow broadly linear trends with increasing load. The fast disks show larger ΔT_c values than the corresponding slow disk data at both 200 and 1000 seconds in each series. The slow disk ΔT_c values are positive at all loads in each series, indicating that the highest temperatures occur at position A, nearest the surface. For the fast disks, the ΔT_c values are negative at low loads during series A, B and C. However, they are all positive during series D, which has the highest frictional power dissipation of all the series.

In the slow disk, the ΔT_c values at 1150 and 2000 seconds are always negative, indicating a centre-line temperature gradient towards the surface during the cooling phase of each test. The values at 1150 seconds have a larger magnitude than those at 2000 seconds. This is because the disks are cooling rapidly from relatively high temperatures at 1150 seconds, which is just after the load has been removed. The slow disk ΔT_c values at 1150 and 2000 seconds also have a broadly linear variation in magnitude with applied load. The fast disk results during the cooling phase, however, are less consistent in terms of both their sign and magnitude. For example, in series A the fast disk values are all negative as expected, and appear to be linear with the exception of the values at 2320N load, where the magnitude of the ΔT_c value at 1150 seconds is approximately three times that which could be reasonable expected from the trend shown by the results at higher and lower loads. Inspection of figure 5.6 also shows that the cooling behaviour is different for this test in the series, with a greater difference between the centre-line temperatures during the rapid cooling phase for test A4 than the other tests in the series. Series B shows less consistent results. Although

all the ΔT_c values during the cooling phase are negative for this series they display no linear trend as observed with the slow disk results. The tests at 2320 N and 2850 N show much smaller temperature gradients than those at lower loads, which is also unexpected. The fast disk ΔT_c results at 1150 and 2000 seconds for series C and D are also inconsistent, with many of the values being positive which does not appear to be consistent with the behaviour shown in the other test series.

When the mean temperature differences, ΔT_m, are considered broadly similar trends to the ΔT_c results are shown. The slow disk results are consistent during both loading and cooling phases of each test, with linear trends for all four times under consideration. In addition, the temperature differences are consistently positive during the loading phase of the tests and negative during the cooling phase. Again, the fast disk results are less consistent. However, when the ΔT_m values are considered, all tests show negative differences during the cooling phase although the fast disk ΔT_m values show less clear trends with load than the slow disk results.

5.5.6 Repeat tests

Two repeat tests were carried out – one (B1) which displayed the lower fast disk temperatures at thermocouple position A when compared to position B, and a second test (B4) which displayed higher temperatures at position A than at position B. In both cases, similar temperature levels developed in the disks as the original experiments. In order to further quantify the repeatability of the temperature

distributions being recorded the ΔT_c and ΔT_m values were calculated and are shown in table 5.2 and 5.3 for test B1 and B4 respectively.

Table 5.2: Comparison of original and repeat test B1 temperature differences

	Fast Disk				Slow Disk			
	ΔT_c		ΔT_m		ΔT_c		ΔT_m	
Time / s	Original	Repeat	Original	Repeat	Original	Repeat	Original	Repeat
200	-0.9	-1.2	0.6	0.5	0.4	0.5	0.4	0.4
1000	-1.5	-1.5	0.0	0.0	0.2	0.2	0.1	0.2
1150	-1.6	-0.4	-1.6	-1.2	-0.6	-0.5	-0.6	-0.5
2000	-0.6	0.3	-0.6	-0.4	-0.3	-0.2	-0.3	-0.2

Table 5.3: Comparison of original and repeat test B4 temperature differences

	Fast Disk				Slow Disk			
	ΔT_c		ΔT_m		ΔT_c		ΔT_m	
Time / s	Original	Repeat	Original	Repeat	Original	Repeat	Original	Repeat
200	2.5	3.1	3.8	4.1	2.6	2.8	1.8	1.9
1000	1.2	1.3	2.2	2.4	2.0	2.1	1.1	1.1
1150	-0.9	-4.0	-2.5	-3.9	-0.9	-1.1	-1.3	-1.4
2000	-0.4	-0.1	-0.6	-0.5	-0.4	-0.4	-0.4	-0.4

It can be seen that the slow disk behaviour is reasonably repeatable during both the loaded and cooling phases of the tests. This reinforces the consistent behaviour of the slow disk temperature distributions as shown in figures 5.31 to 5.34. However, the fast disk behaviour is less repeatable, which adds further weight to the suspicion that the recorded data has some anomalies present. In order to further investigate the repeatability of the recorded data, a further series of repeat rests was conducted. Test D4 was repeated nine times and the ΔT_c and ΔT_m values were calculated for each test. The first four tests were straightforward repeat runs, with all instrumentation connected in the intended manner. Tests five to nine were carried out with the software set to not apply any calibrations to the thermocouple data in order to eliminate any effects of the calibration on the data. In tests seven to nine, the

connections from the slip rings to the amplifiers were reversed in order to determine if the data acquisition system was affecting the results. In normal operation, the six slow disk thermocouples are connected to channels 0 to 5 of the system, with channels 6 to 11 carrying the fast disk signals. In tests seven to nine, these connections were reversed such that the slow disk signals were now connected to channels 6 to 11 and *vice versa*. Figures 5.35 to 5.38 show the calculated differential temperatures at during the nine repeat tests.

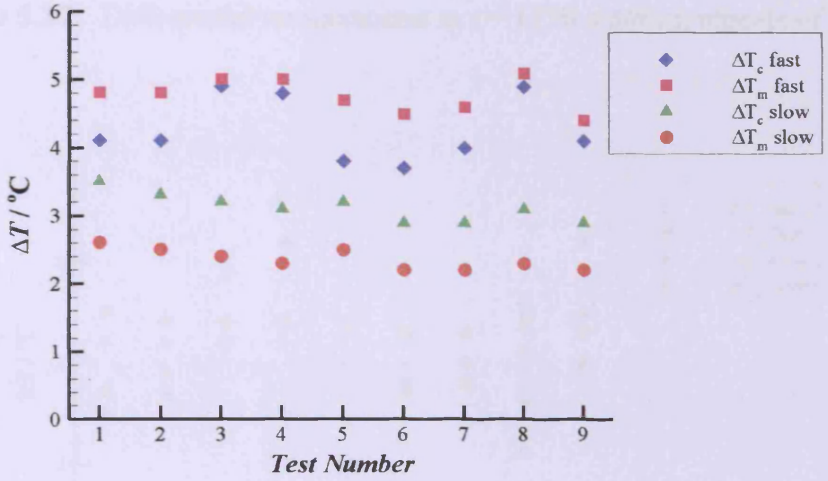

Figure 5.35: Differential temperatures at t = 200 s during repeats of test D4

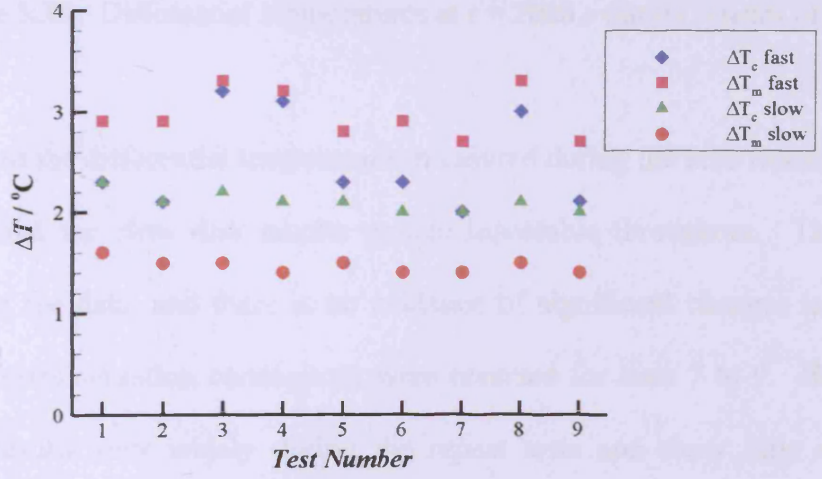

Figure 5.36: Differential temperatures at t = 1000 s during repeats of test D4

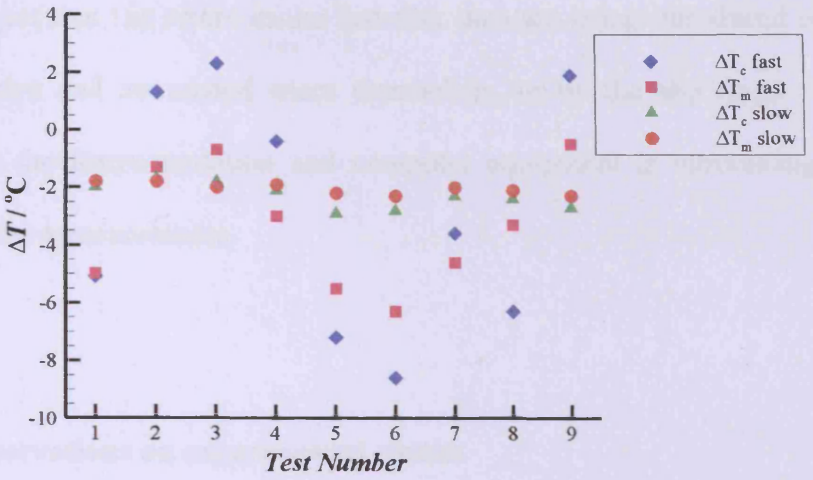

Figure 5.37: Differential temperatures at t = 1150 s during repeats of test D4

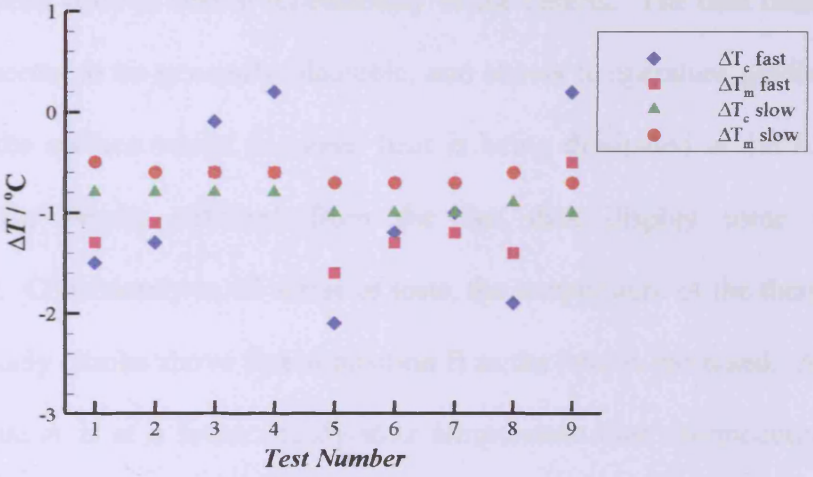

Figure 5.38: Differential temperatures at t = 2000 s during repeats of test D4

Inspection of the differential temperatures measured during the nine repeat runs of test D4 show that the slow disk results remain repeatable throughout. There is little variation in the data, and there is no evidence of significant changes in the results when the instrumentation connections were reversed for tests 7 to 9. However, the fast disk results vary widely during the repeat tests and show little evidence of repeatability. In addition, the removal of the calibrations or the reversal of the instrumentation connections has not improved the repeatability of the data. This

would suggest that the errors in the fast disk data are being introduced either by the thermocouples and associated wires themselves, or by the slip rings. It does not appear that the instrumentation and computer equipment is introducing significant errors into the measurements.

5.6 Observations on experimental results

Four series of tests have been carried out, totalling some 20 separate tests together with two check tests to ensure repeatability of the results. The data obtained for the slow disk seems to be generally plausible, and shows temperature gradients into the disk from the surface whilst frictional heat is being dissipated at the EHL contact. However, the results obtained from the fast disk display some unexplained phenomena. Consistently in all series of tests, the temperature of the thermocouple at position A only climbs above that at position B as the load is increased. At low loads, thermocouple A is at a lower steady-state temperature than thermocouple B. This situation reverses (and becomes at first glance more plausible) as the load is increased. This curious behaviour is not shown in the thermocouple pairs on the two sides of the disks.

There are a number of potential explanations for this behaviour. There could be an error in the thermocouple readings. However, a simple offset in the reading of either thermocouple A or B does not explain these results. The only source of such an offset could be a differential temperature rise in the brush/rotor tracks of the slip rings, but the error introduced by such a temperature differential would be unaffected by the

removal of the disk load. In the majority of tests the temperature gradient during cooling shows a flow of heat towards the disk surface (which is to be expected). Thus, if there was an offset error which could explain the temperatures measured during the loaded phase, correction of such an error would result in the cooling behaviour of the disks becoming implausible.

Additionally, it should be noted that the thermocouples were very carefully calibrated, with a number of repeat calibration runs, as described in section 3.6.3.2 in chapter 3. The calibration took place with the thermocouples connected to the data acquisition system through the slip rings, and great care has been taken to ensure that adequate cooling is provided to the slip rings whilst they are in operation.

In order to rule out any errors in either the construction, installation or calibration of the thermocouples it would be necessary to carry out a repeat test with a newly fitted fast disk. This should ideally be connected through different channels on the slip rings to the current configuration, in order to rule out any possible errors being introduced by the slip rings. Unfortunately, due to the large number of problems which arose during the development of the test rig and data acquisition system, it has not proved possible to carry out this validation work within the time constraints of this project.

On the assumption that the temperatures are correct it follows that the flows of heat within the test disks are more complex than a basic consideration of the problem would suggest. It is interesting to note that the behaviour is only noticeable in the fast disk, where speeds are significantly higher and friction generated at the shaft support

bearings will be correspondingly higher. Previous work with superfinished disks has noted that at low loads the friction being dissipated at the bearings is of a similar magnitude to that being dissipated by oil shearing at the EHL contact (Patching, 1994). Thus, one potential explanation for these results may be that, at low loads, the frictional heat being generated by the bearings is flowing up the test disk (which is acting like a cooling fin on a heat exchanger or radiator tube) and disturbing the flow of heat within the disk. As the loading is increased, the contact friction increases to a level where it swamps the bearing friction and thus the behaviour is no longer seen.

However, it is clear from both the temperature maps (such as figure 5.29) and the temperature difference measurements shown in figures 5.31 to 5.34 that the slow disk temperature behaviour is self-consistent between experiments. The slow disk behaviour also appears logical when the likely flows of heat within the test disks are considered. However, it is also clear that the fast disk temperatures are less consistent, with particularly curious behaviour during tests at lower loads and during the cooling phases of the tests. Thus, it must be considered that there is either a source of error present in the fast disk data or that the thermal behaviour of the disks and test rig is more complex than first thought.

In Chapter 6, these results are analysed using the heat conduction model of the disks developed in Chapter 4.

Numerical modelling of heat partition experiments

6.1 Introduction

In this chapter the numerical model of heat conduction within the test disks developed in Chapter 4 is applied to the experimental data presented in Chapter 5. The model is used to determine both the heat transfer from the running track and the partition of heat necessary between the disks to match the temperatures calculated by the model to the experimental data.

6.2 Analysis procedure

Due to the uncertainties about the fast disk temperatures, as discussed in Chapter 5, it was decided to treat the fast and slow disk data as two independent means of determining the division of heat between the disks. Thus, the transient, two-dimensional, bulk temperature model, described in Section 4.3, was applied separately to each disk. As explained in Section 4.3, the model uses measured temperatures (at thermocouple positions B, D and F) as boundary conditions. The running track heat transfer coefficient (h_t) and heat partition value (β for the fast disk and $1-\beta$ for the slow disk) are then adjusted in order to match the calculated temperatures at positions A, C and E with the experimental data. Modelling the fast and slow disks separately gives two measures of the partition of heat between the disks – i.e. one based on the measured thermal behaviour of the slow disk and a second based on the measured behaviour of the fast disk.

In order to assess the agreement between the numerical results and the measured temperatures an objective measure of simulation error was developed. At 100 second intervals throughout the test the absolute percentage error between the calculated temperature and experimental data at positions A, C and E are evaluated. These three errors (e_A, e_C and e_E) at each 100 second interval are then combined to determine an overall error for the simulation, e, given by

$$e = \frac{1}{n}\sum_{i=1}^{i=n}\left(\frac{2e_A + e_C + e_E}{4}\right)_{t=100i}$$

where n is the number of 100 second intervals within the test. For a typical test of duration 2250 seconds, $n = 22$. In order to determine the optimum values of h_t and β for each test, such that the calculated error (e) was minimised, the model was optimised for efficient running by removing as many instances of writing to files and the screen as necessary. In addition, the evaluation of error described was incorporated into the code. The numerical model was then placed as a sub-routine within a control program, which was able to perform successive runs with a series of h_t and β value combinations. The control program ran the model for all possible combinations of β and h_t values (within specified ranges) and thus it was possible to determine the optimum values of each parameter in order to minimise the error between calculated and experimental temperatures. After a period of development a suitable range of investigation for the running track heat transfer coefficient, h_t, was found to be $100 \leq h_t \leq 1200$ W/m^{2}K. The control program ran the model with h_t varying over this range in steps of 100 W/m^{2}K. By definition, the maximum quantity of frictional heat which passes into either disk cannot exceed the total heat dissipated

at the contact. Thus, for the fast disk the range $0.05 \leq \beta \leq 1$ was investigated in steps of 0.05. For the slow disk, the range $0.05 \leq (1-\beta) \leq 1$ was used (since β is defined as the fraction of the total frictional heat passing into the *fast* disk) also in steps of 0.05. Thus, for each disk the control program ran a total of 240 simulations with each possible β / h_t combination.

The approach of using a multivariable optimisation procedure to analyse the results was not used as the time available to complete the study did not give an opportunity to develop such a method. The approach adopted was selected as it was seen as a robust first stage evaluation, especially in light of the concerns regarding measurement accuracy identified in Chapter 5.

The approach outlined here differs from that adopted by the author's previous heat partition modelling work (Clarke *et. al,* 2006) in one important aspect. In this thesis the data from the two disks are used to give two independent measurements of the partition of heat. Thus, the value of β determined by analysis of the fast disk data and the value of $(1-\beta)$ obtained from the slow disk analysis are not necessarily constrained to sum to unity. This approach was deemed the most appropriate in the light of the uncertainty in the fast disk data discussed in Chapter 5.

6.3 Example analysis results (test A5)

In this section, as an example, the results of the numerical analysis of test A5 are shown and described in some detail. The experimental results of the test can be seen

in Figure 5.7 in Chapter 5. The analyses in this chapter were carried out with 25 radial mesh points and 40 axial mesh points, and with a time step of 1 second. This gives a mesh with δz = 0.238 mm and δr = 0.244mm. The sensitivity of the results to both mesh density and time-step is discussed further in Section 6.5.

The analysis procedure described in Section 6.2 was followed in order to determine the optimal heat transfer and heat partition values to match the experimental data. Figure 6.1 shows contours of the error value, e, against h_t and β values for the fast disk analysis.

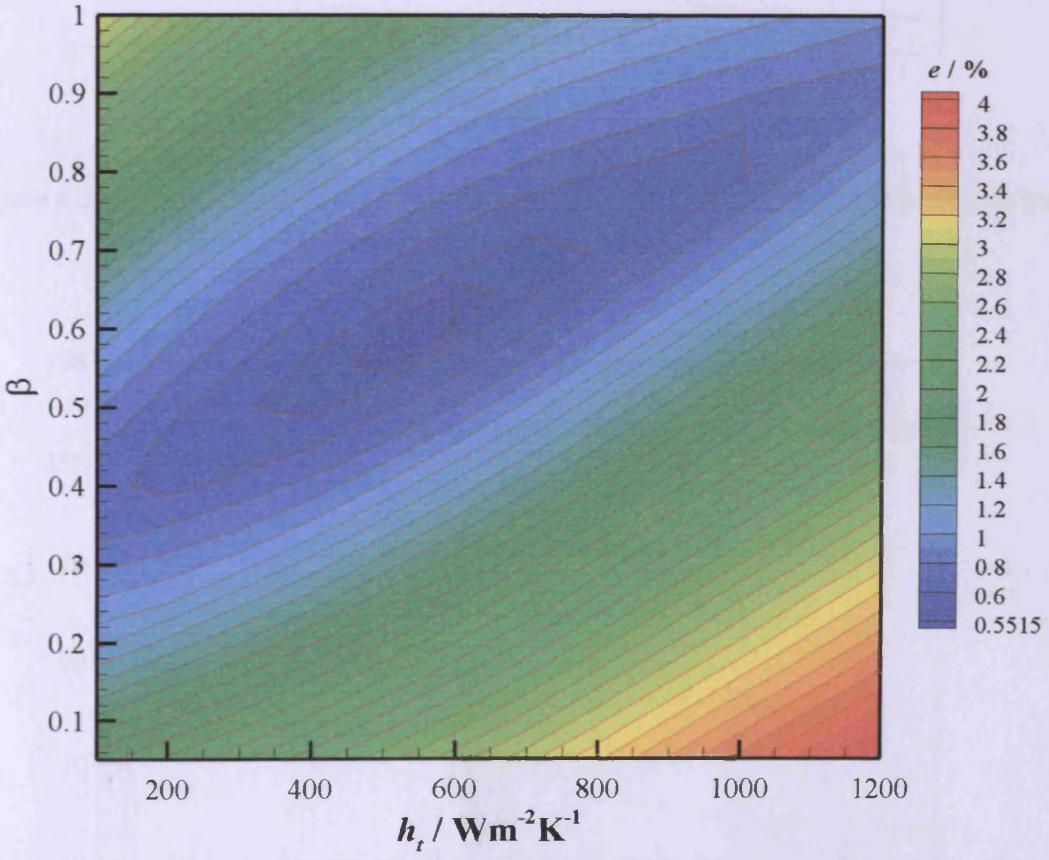

Figure 6.1: Contours of calculated error value, e, for test A5 (fast disk)

From Figure 6.1 it can be clearly seen that the minimum error between calculated and experimental temperatures occurs when $\beta = 0.60$ and $h_t = 600$ W/m^{2}K. This gives a minimum error of 0.55%. Figures 6.2, 6.3 and 6.4 compare the calculated temperatures with the experimental data at thermocouples A, C and E respectively.

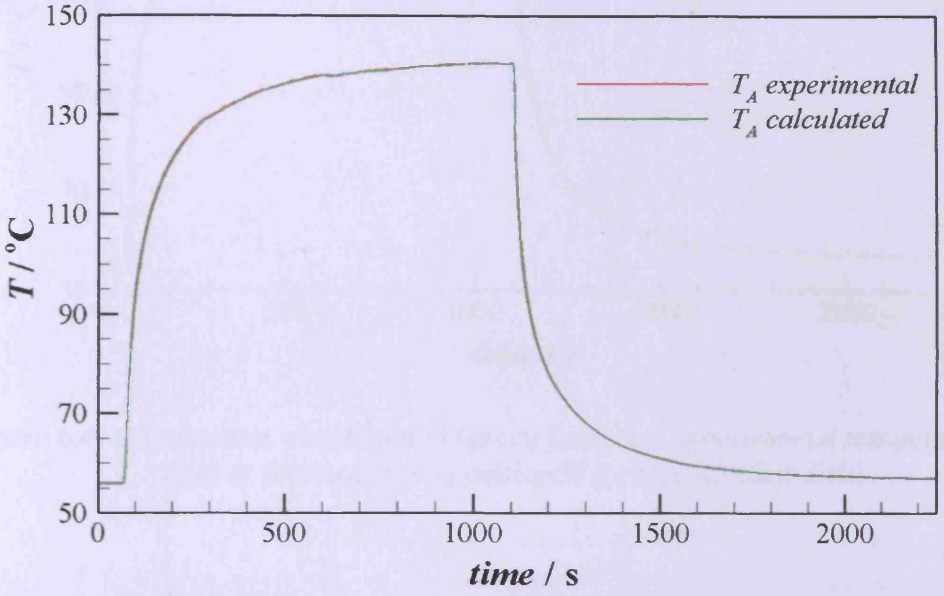

Figure 6.2: Comparison of calculated (green line) and experimental temperatures (red line) at thermocouple position A for test A5 (fast disk)

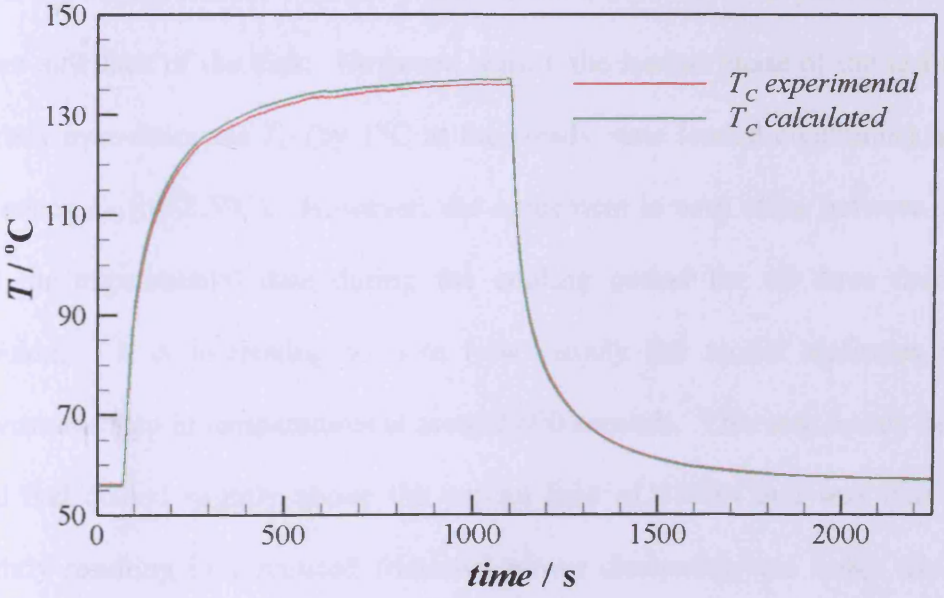

Figure 6.3: Comparison of calculated (green line) and experimental temperatures (red line) at thermocouple position C for test A5 (fast disk)

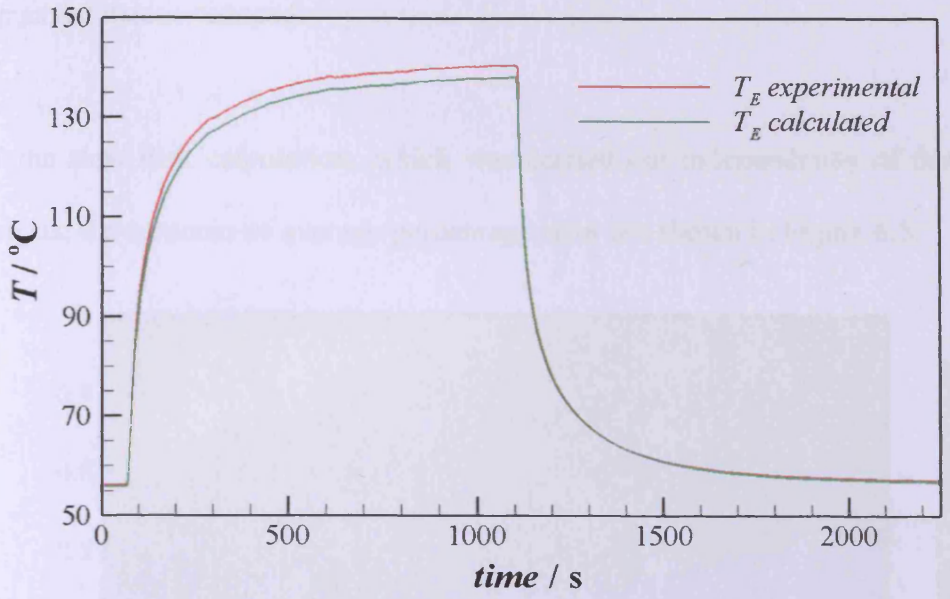

Figure 6.4: Comparison of calculated (green line) and experimental temperatures (red line) at thermocouple position E for test A5 (fast disk)

Figure 6.2 shows that the central thermocouple temperature, T_A, is very closely predicted by the model over the entire duration of the experiment. Figures 6.3 and 6.4 show a good agreement with the experimental temperatures at positions C and E on either side face of the disk. However, during the loaded phase of the test the model slightly over-estimates T_C (by 1°C at the steady state loaded conditions) and under-estimates T_E (by 2.5°C). However, the agreement is very close between the model and the experimental data during the cooling period for all three thermocouple positions. It is interesting to note how closely the model replicates the slight downwards step in temperatures at around 600 seconds. This step occurs because the load had drifted slightly above the pre-set load of 2850N and was thus corrected slightly resulting in a reduced frictional power dissipation and hence the observed temperature step. The model replicates this behaviour because the experimental

friction trace is used as an input to the model, and it contains a corresponding small step as the load is reduced.

For the slow disk calculation, which was carried out independently of the fast disk analysis, the contours of average percentage error are shown in Figure 6.5.

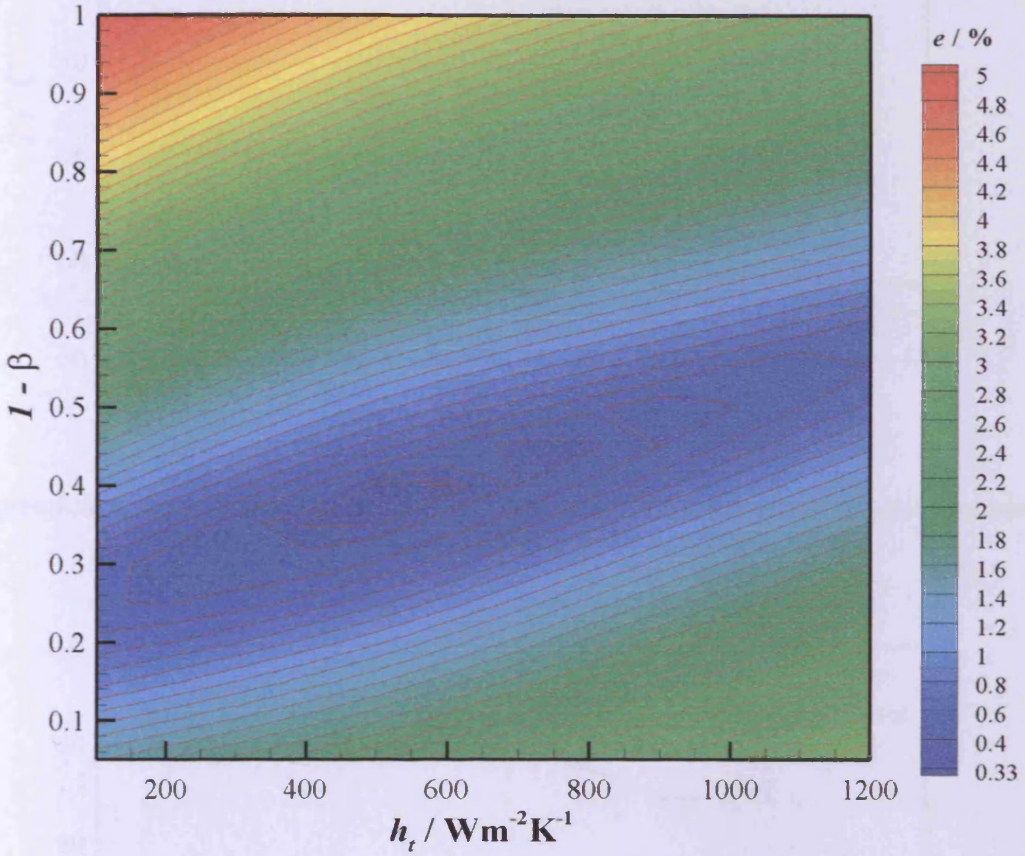

Figure 6.5: Contours of calculated error value, e, for test A5 (slow disk)

For the slow disk, the minimum error value of 0.32% occurred when the analysis was performed using $(1-\beta) = 0.40$ and $h_t = 600$ W/m^{2}K. In this example, the heat partition between the two disks is consistent – the analysis of the fast and slow disks both independently predict that $\beta = 0.60$ for this test. However, conclusions cannot be drawn from this single analysis until the complete results from analysis of all 20 tests

are examined. Figures 6.6, 6.7 and 6.8 compare the calculated and experimental temperatures at the three thermocouple positions.

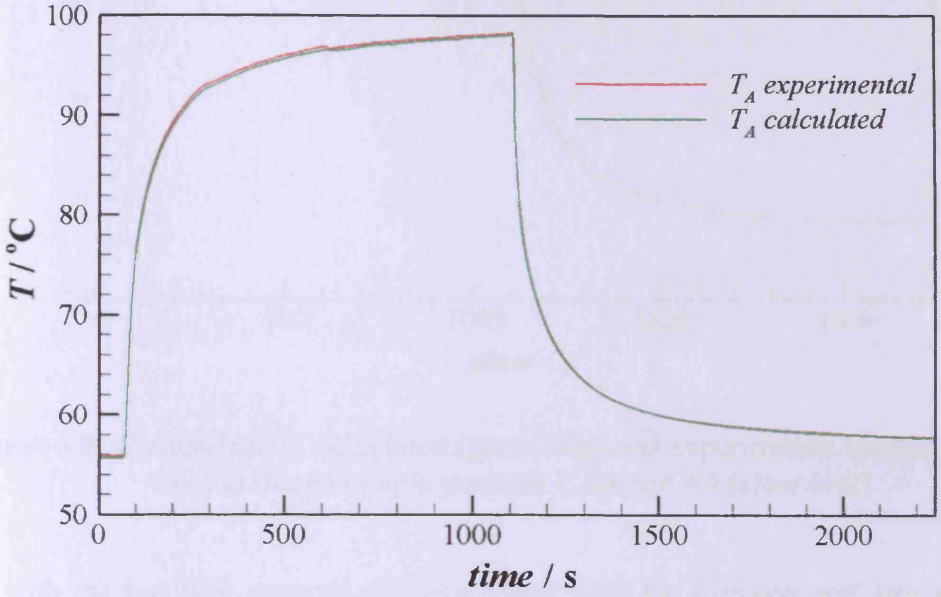

Figure 6.6: Comparison of calculated (green line) and experimental temperatures (red line) at thermocouple position A for test A5 (slow disk)

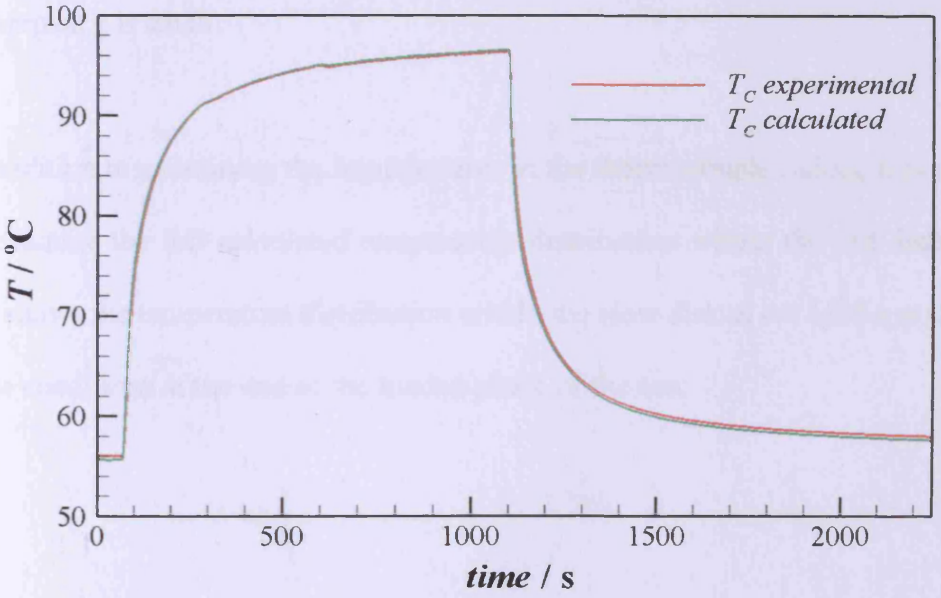

Figure 6.7: Comparison of calculated (green line) and experimental temperatures (red line) at thermocouple position C for test A5 (slow disk)

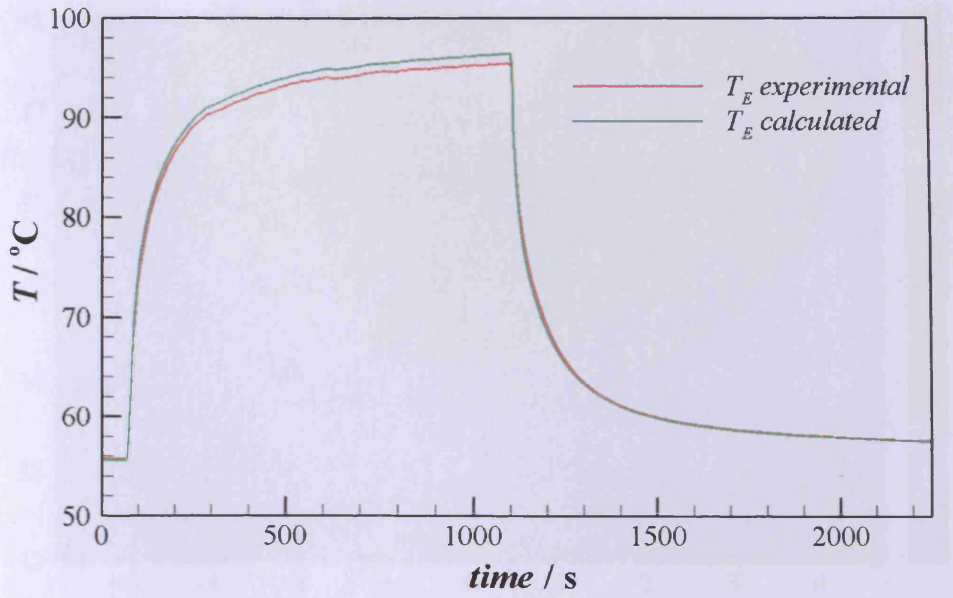

Figure 6.8: Comparison of calculated (green line) and experimental temperatures (red line) at thermocouple position E for test A5 (slow disk)

As with the fast disk analysis, the agreement with the experimental temperatures is very close during both loading and cooling phases of the test. The temperature at position E is, however, slightly higher than the experimental temperature although the discrepancy is small.

In addition to examining the temperatures at the thermocouple points, it is interesting to examine the full calculated temperature distribution within the test disks. Figure 6.9 shows the temperature distribution within the slow disk at t = 1100 s at the steady-state conditions at the end of the loaded phase of the test.

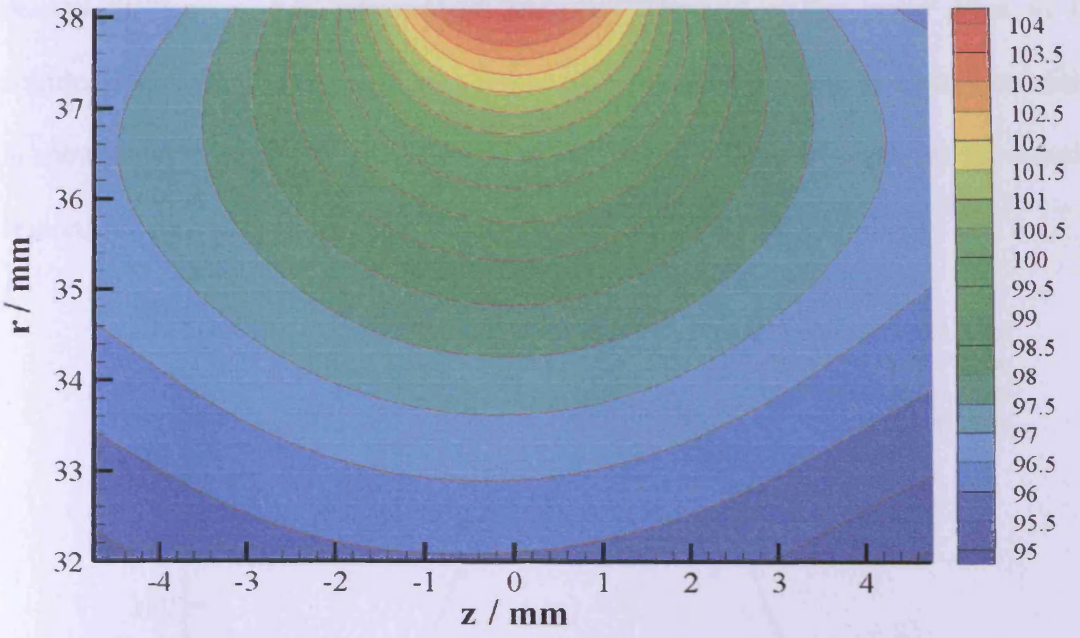

Figure 6.9: Contours of temperature in slow disk at t = 1100 s

Heat flows normal to the isotherms from the contact on the running track. On the running track regions away from the contact zone, heat flows radially towards the surface as the surface is cooled. It is also interesting to examine a number of radial and axial temperature profiles. Figure 6.10 shows four axial temperature profiles at three positions within the slow disk. The profile at r = 38.0 mm is 0.1 mm below the running track surface and hence shows a large peak of temperature due to frictional heating at the running track, with the temperature on the disk centreline being 7°C above that at the edges at this radial position. The profile at r = 35.5 mm is some 2.6 mm below the running track and shows a much flatter temperature profile, with a maximum variation of 1.8°C between the centreline and disk sides. The third profile at r = 33.0 mm is 5.1 mm below the running track. At this depth the temperature profile displays only slight variation with axial position as the heat flow has changed from a two-dimensional flow near to the disk surface to a predominantly one-dimensional radial flow at this position. All three profiles show slight asymmetry,

due to the asymmetric temperature boundary imposed at the lower edge of the solution region by the experimental boundary temperatures. This boundary condition is shown by the profile at r = 32.0 mm which is at the inner boundary of the solution region.

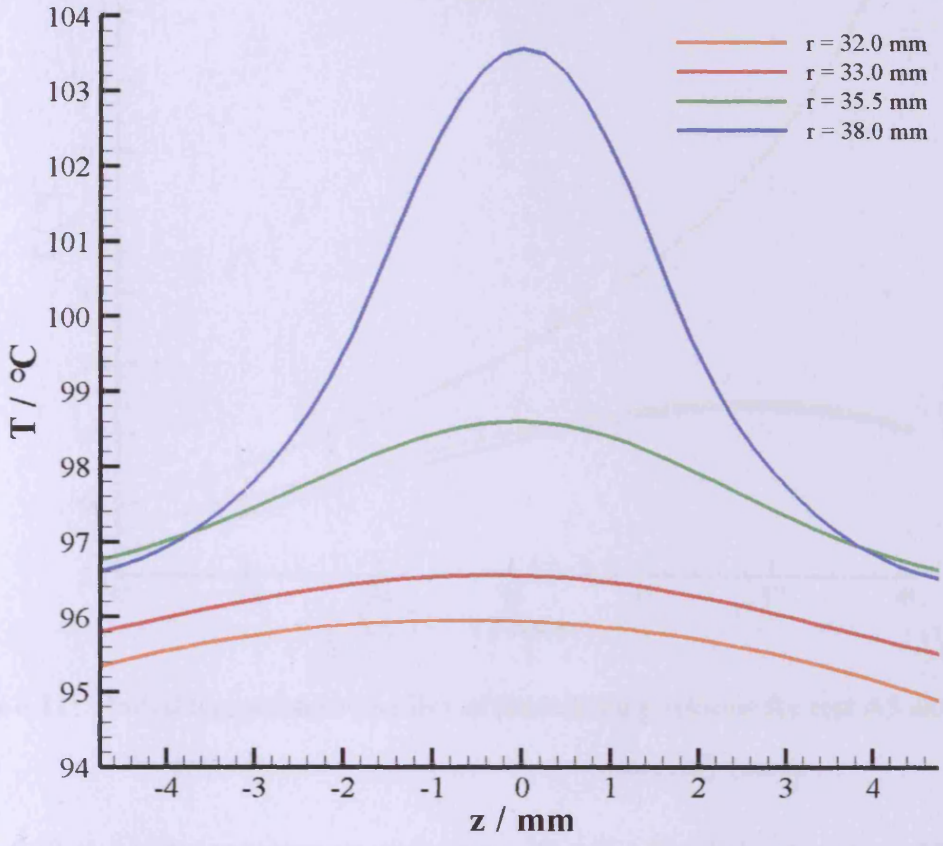

Figure 6.10: Axial temperature profiles at three radial positions for test A5 slow disk

Figure 6.11 shows three radial temperature profiles – on the disk axial centre-line, and at z = +/– 3.6 mm. For the centreline profile the large temperature gradient near the disk running track can be seen which is due to the frictional heat input at the surface centred at z = 0 mm. The other two profiles, at z = +/– 3.6 mm, show heat flowing out of the disk at the running track surface (since these axial positions are outside the contact zone and hence experience cooling rather than net heating). As the radial

position moves away from the running track, the difference between the three temperatures reduces as the flow of heat becomes predominantly radial.

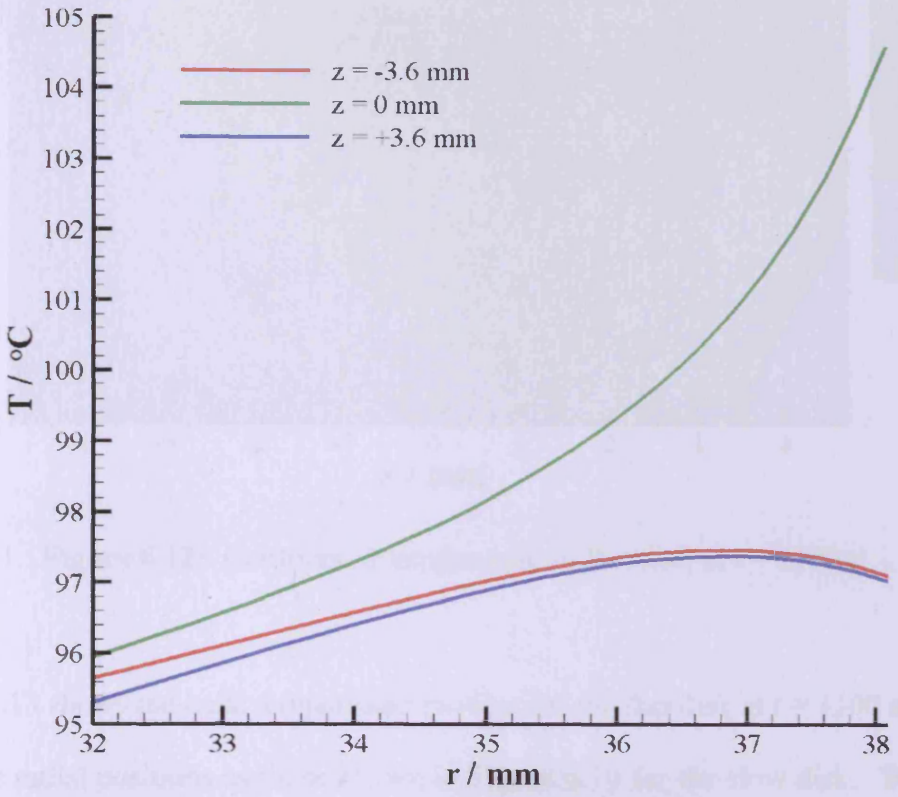

Figure 6.11: Radial temperature profiles at three axial positions for test A5 slow disk

Figure 6.12 shows the temperature contours within the fast disk, also at t = 1100 s at the end of the steady-state loaded phase. In comparing these results with the corresponding slow disk results it is apparent that the temperature distribution within the fast disk displays a higher degree of asymmetry than that in the slow disk, with a significant skewing of the isotherms at inner radial positions away from the running track. This occurs within the model due to the asymmetrical boundary conditions imposed on the inner radius using the experimental temperatures measured at that radius. The heat transfer coefficients on either side face of the disk are equal, being determined from the insulating washer's thermal conductivity and thickness as described in Chapter 4.

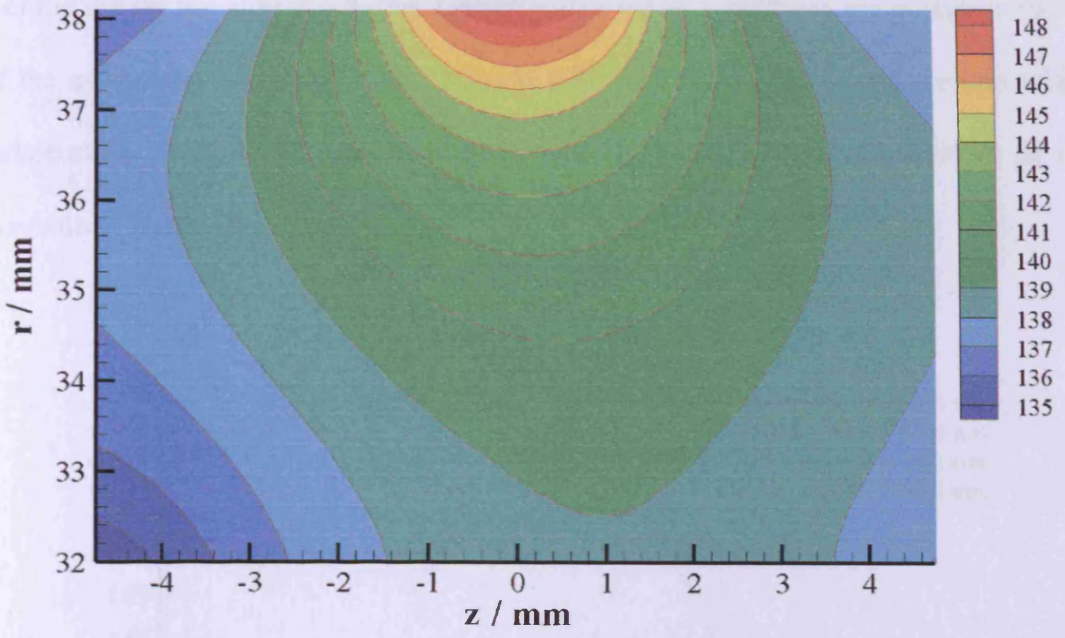

Figure 6.12: Contours of temperature in fast disk at t = 1100 s

Figure 6.13 shows the axial temperature profiles for the fast disk at t = 1100 s taken at the same radial positions as those shown in Figure 6.10 for the slow disk. Whilst the profiles are similar to those shown in Figure 6.10, the axial asymmetry is more pronounced in the fast disk results, with the axial profile at the innermost radial position (r = 33.0 mm) showing a difference of 2°C between the temperatures at the sides of the disk. The position of the maximum temperature moves from the centreline for the profile at r = 38.0 mm (due to the frictional heating having the greatest magnitude at the centreline) to z = +1 mm for the innermost profile at r = 33.0 mm. This may be either due to errors in the experimental data being used as boundary conditions (shown in the r = 32.0 mm profile), or due to an asymmetry in the conduction path or cooling at the two sides of the disk. Approximately 1mm below the innermost boundary of the solution region there is a shallow groove on the side of the disk at which the higher temperatures occur. Also, the disk is located against a shoulder which is an integral part of the shaft at one side, but retained by a separate

locking nut on the side at a higher temperature. These conditions are potential causes of the asymmetry observed here. Figures 6.10 and 6.13 both show the slope of the temperature profiles reducing near the edges of the disk, due to the effect of the insulating layer at these faces.

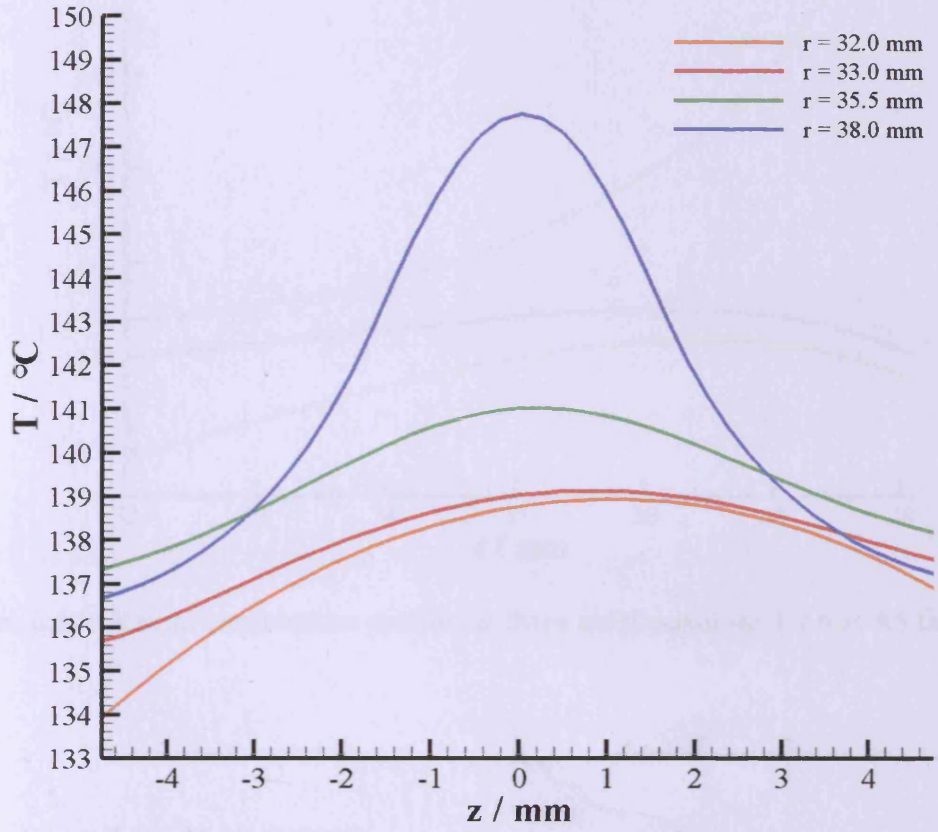

Figure 6.13: Axial temperature profiles at three radial positions for test A5 fast disk

Radial temperature profiles for the fast disk are shown in Figure 6.14, at positions corresponding to those in Figure 6.11. Overall, the fast disk temperature profiles are similar to those for the slow disk, with a large temperature gradient at the surface on the centreline indicating frictional heat flowing into the disk. The two profiles at +/– 3.6 mm again display cooling behaviour at the surface. However, it is noticeable that the temperatures do not approach each other as closely as the slow disk temperatures

as the radial position moves into the disk away from the surface, due to the asymmetry present in the results.

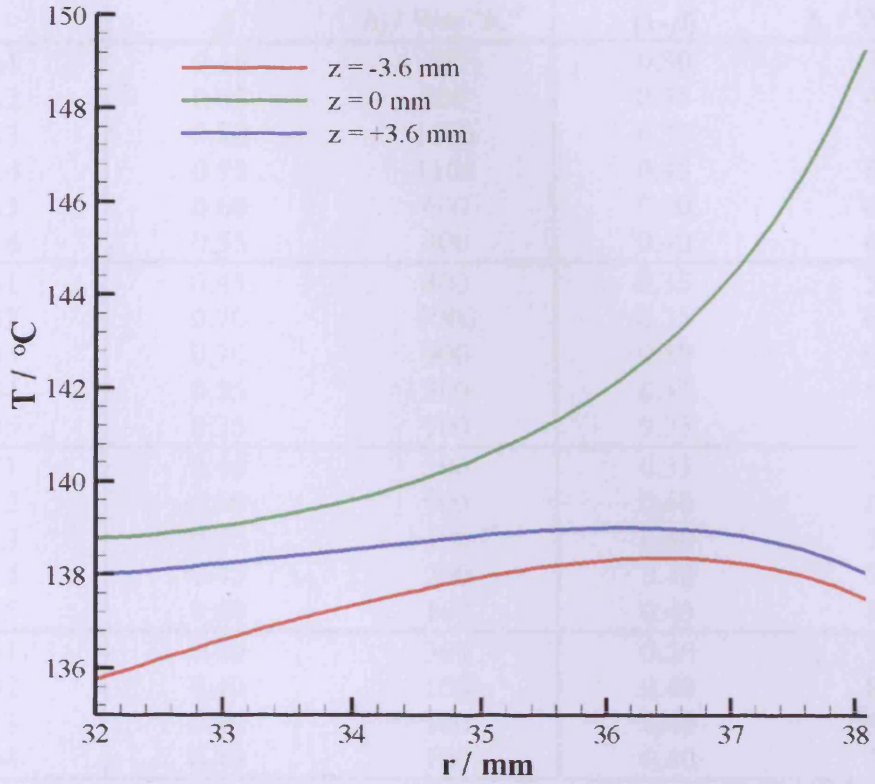

Figure 6.14: Radial temperature profiles at three axial positions for test A5 fast disk

6.4 Overall results and trends

The analysis procedure outlined in Section 6.2 and given as a detailed example in Section 6.3 was carried out for all of the twenty tests. As in the case of the example given in Section 6.3, the slow and fast disks were analysed separately, in order to give two independent estimates of the partition of heat between the disks. Table 6.1 shows the results from the analysis.

Table 6.1: Optimal heat partition and running track heat transfer coefficients obtained from conduction analysis of fast and slow disks

Test	Fast Disk Analysis		Slow Disk Analysis	
	β	h_t / $Wm^{-2}K^{-1}$	$(1-\beta)$	h_t / $Wm^{-2}K^{-1}$
A1	0.10	600	0.30	300
A2	0.65	800	0.35	400
A3	0.80	1100	0.35	300
A4	0.95	1100	0.45	600
A5	0.60	600	0.40	600
A6	0.55	400	0.40	600
B1	0.45	800	0.35	500
B2	0.70	1000	0.35	600
B3	0.70	900	0.40	600
B4	0.55	300	0.45	600
B5	0.35	100	0.35	600
C1	0.40	100	0.35	600
C2	0.60	900	0.40	800
C3	0.40	100	0.40	700
C4	0.45	200	0.40	700
C5	0.40	100	0.45	800
D1	0.40	300	0.50	900
D2	0.40	100	0.40	800
D3	0.40	100	0.40	900
D4	0.40	100	0.40	700

Inspection of Table 6.1 shows the results of the slow disk analyses to be more consistent than those obtained from the fast disk analyses. The heat partition values from the slow analysis fall within the range $0.30 \leq (1-\beta) \leq 0.50$, indicating that the majority of the frictional heat passes into the fast disk. However, for the fast disk analysis the range of values is much wider, such that $0.10 \leq \beta \leq 0.95$. Figures 6.15 and 6.16 show histograms of the heat partition values obtained for the fast and slow disks respectively. It can clearly be seen that whilst the slow disk results give heat partition behaviour which falls within a narrow range of values for all experiments, the fast disk behaviour shows no clear trend with a wide spread of heat partition values.

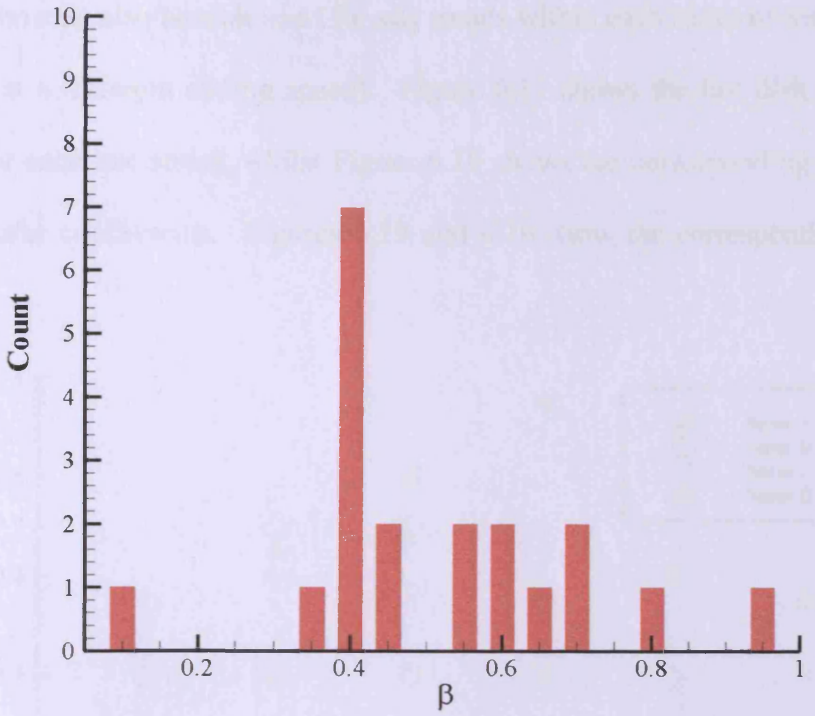

Figure 6.15: Histogram of β values from fast disk analysis

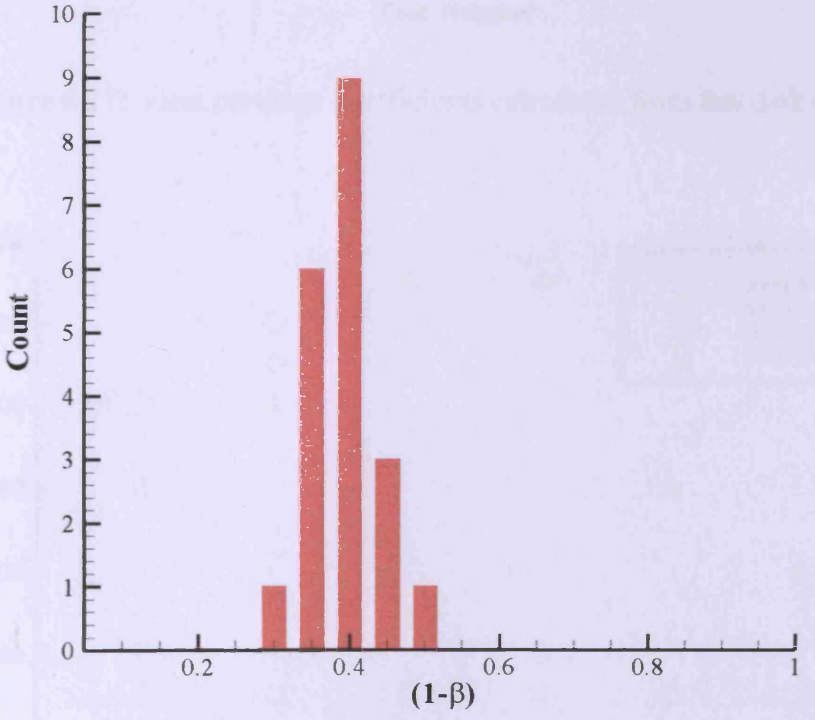

Figure 6.16: Histogram of $(1-\beta)$ values from slow disk analysis

The results may also be examined for any trends within each series of tests (since each series is at a different sliding speed). Figure 6.17 shows the fast disk heat partition values for each test series, whilst Figure 6.18 shows the corresponding running track heat transfer coefficients. Figures 6.19 and 6.20 show the corresponding slow disk data.

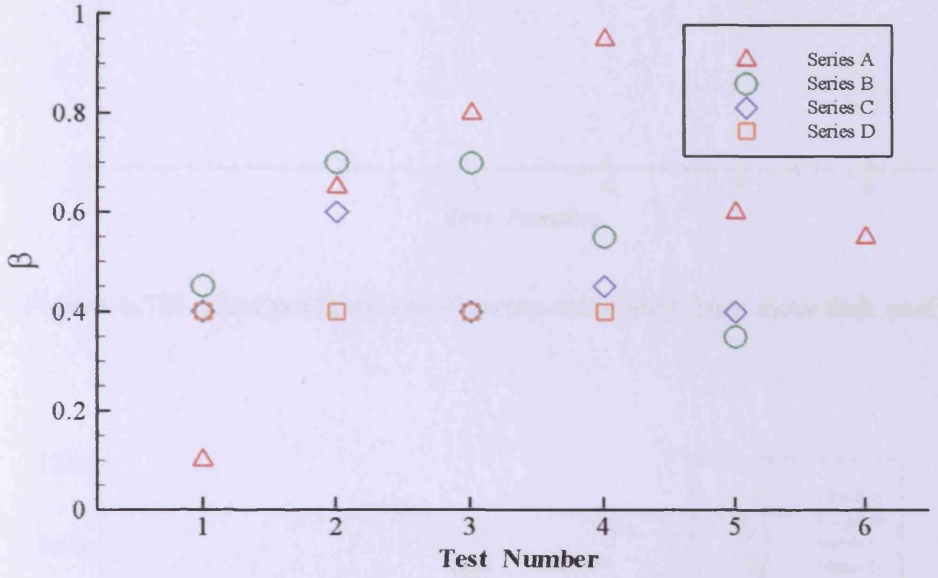

Figure 6.17: Heat partition coefficients calculated from fast disk analysis

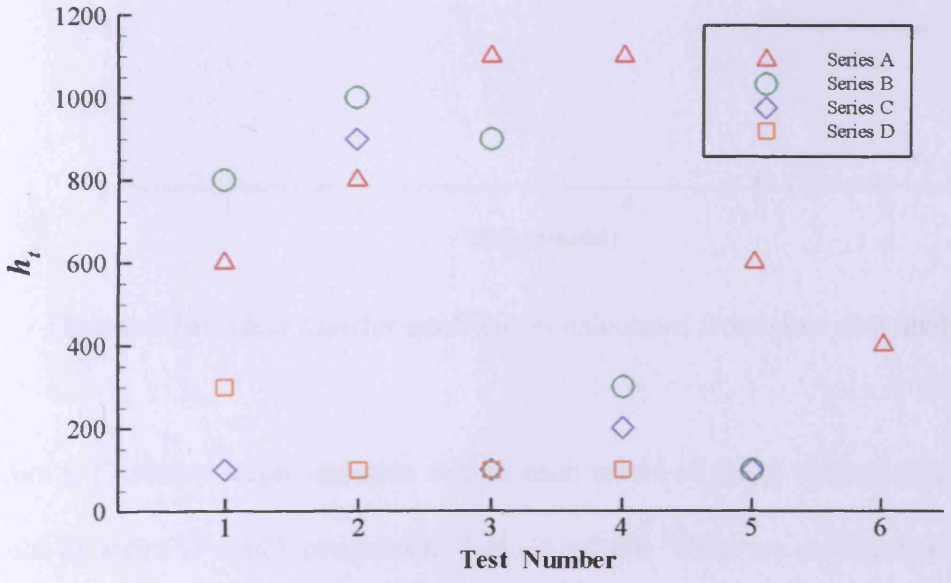

Figure 6.18: Heat transfer coefficients calculated from fast disk analysis

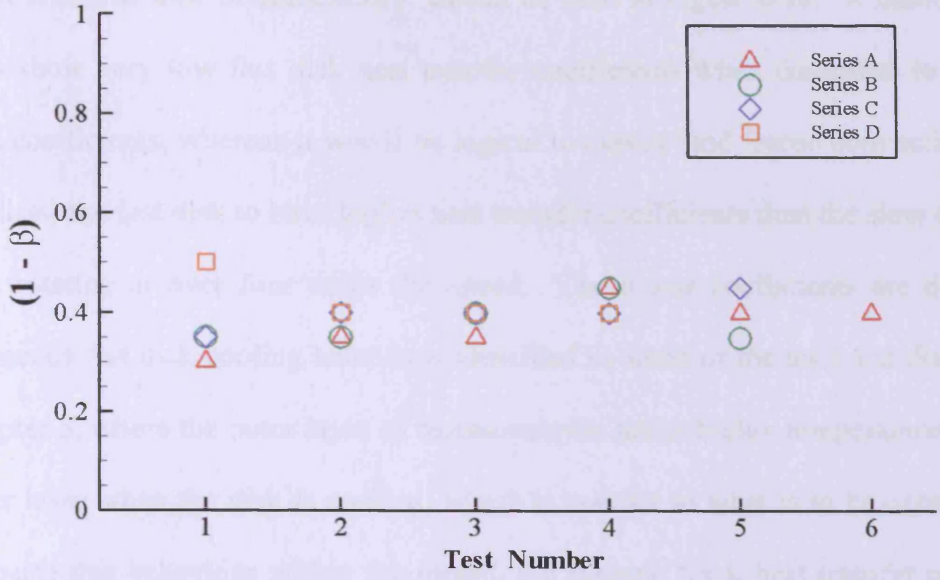

Figure 6.19: Heat partition coefficients calculated from slow disk analysis

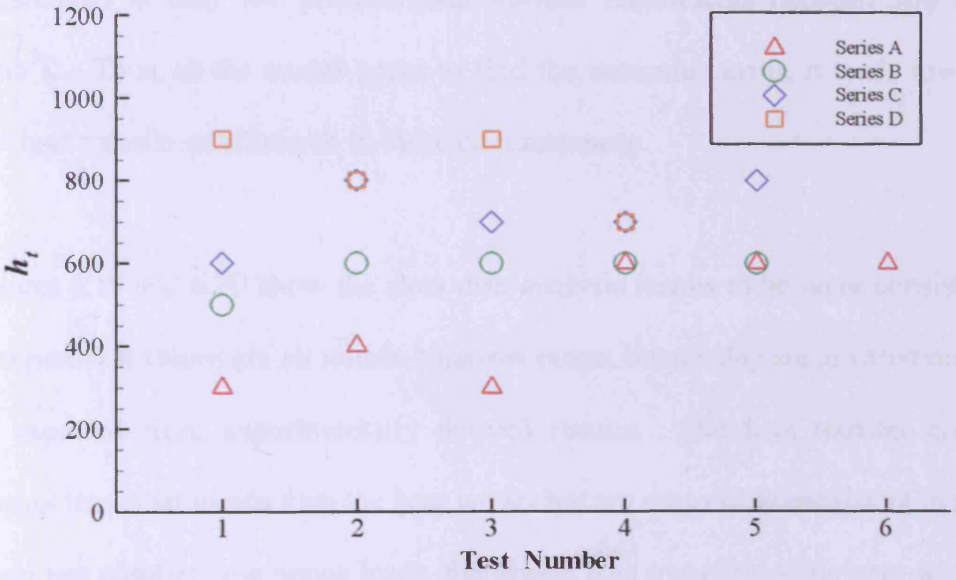

Figure 6.20: Heat transfer coefficients calculated from slow disk analysis

Figure 6.17 shows large variation within each series of the β values, except for the results of series D which consistently have $\beta = 0.40$. There are no clearly discernible trends within each of the series of tests. The running track heat transfer coefficients

show a similar lack of consistency, as can be seen in Figure 6.18. A number of the tests show very low fast disk heat transfer coefficients when compared to the slow disk coefficients, whereas it would be logical to expect (and forced convection theory predicts) the fast disk to have higher heat transfer coefficients than the slow disk since it is rotating at over four times the speed. These low coefficients are due to the erroneous fast disk cooling behaviour identified in some of the tests and discussed in Chapter 5, where the outer layer of thermocouples are at higher temperatures than the inner layer when the disk is cooling, which is counter to what is to be expected. To replicate this behaviour within the model, the running track heat transfer coefficient would have to be negative in order to generate a heat flux into the disk away from the running track surface. However, since this is not physically possible, the model is constrained to only use positive heat transfer coefficients between 100 and 1200 W/m^2K. Thus, as the model seeks to find the minimum error, it tends towards very low heat transfer coefficients in these circumstances.

Figures 6.19 and 6.20 show the slow disk analysis results to be more consistent. The heat partition values are all within a narrow range, but display some variation as might be expected from experimentally derived results. The heat transfer coefficients display less clear trends than the beta values but are reasonable consistent in that, for a given test number (and hence load), the lowest heat transfer coefficients occur for the test with the lowest shaft speeds (Series A). The heat transfer coefficients increase with shaft speed and, although there is some variability in the results, this trend is broadly followed by the whole set of slow disk results. The average heat transfer coefficient for each test series may be seen as a function of sliding speed in Figure 6.21.

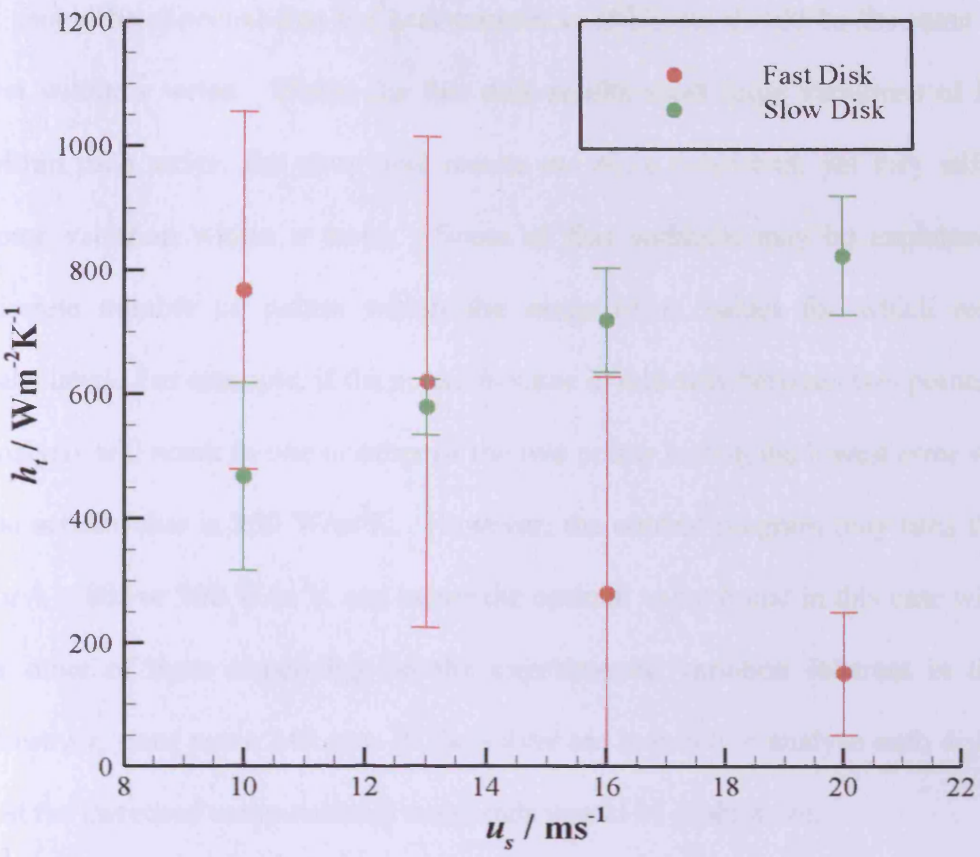

Figure 6.21: Mean heat transfer coefficients (h_t) for fast and slow disks as a function of sliding speed (u_s). Error bars show +/– 1 standard deviation

In Figure 6.21, the slow disk average heat transfer coefficient has an increasing trend with sliding speed (and hence slow shaft rotational speed). Since the disk is cooled by an oil jet and due to its rotating in an oil mist at a lower temperature than its surface, then this is a logical relation. The error bars show +/– 1 standard deviation as an indication of the range of the heat transfer coefficients. Whilst the fast disk data appears to have a *decreasing* trend with sliding speed, the error bars are very large when compared to the slow disk data and thus the validity of any trend derived from data with such a wide variation must be questioned.

Although the solver finds the optimum heat transfer coefficient for each disk in each test independently, tests within one series are all run at the same shaft speeds and thus

it should be expected that the heat transfer coefficients should be the same for each test within a series. Whilst the fast disk results show large variations of h_t values within each series, the slow disk results are more consistent, yet they still display some variation within a series. Some of this variation may be explained by the discrete number of points within the range of h_t values for which results are calculated. For example, if the actual h_t value is mid-way between two points then the analysis will result in one or other of the two points having the lowest error value (i.e. the actual value is 850 W/m^{2}K. However, the control program only runs the solver for h_t = 800 or 900 W/m^{2}K and hence the optimal value found in this case will be one or other of these depending on the experimental variation inherent in the data). However, since some 240 runs of the solver are required to analyse each disk in each test the increased computational overheads would be prohibitive.

A cursory inspection of Figure 6.5 (error contours for test A5 slow disk) would suggest that the error value is less sensitive to heat transfer coefficient than it is to heat partition. Figure 6.5 is typical of the error contours for the slow disk results. Given that there is some variation within a test series of the calculated heat transfer coefficient (h_t) and that heat transfer theory suggests that the value should be constant for a constant shaft speed (i.e. within a test series), further analysis of the slow disk results has been carried out to determine the sensitivity of the results to the heat transfer coefficient.

Each test series has a range of slow disk h_t values predicted by the analysis. For example, in the case of Series A the values range from 300 to 600 W/m^{2}K. For each value of h_t (i.e. 300, 400, 500 and 600 W/m^{2}K) the value of $(1-\beta)$ for each test was

found which gives minimum error, given that the heat transfer coefficient is fixed for the whole test series at a particular value. This heat partition value is found by plotting the error values as a function of $(1-\beta)$ at the particular h_t value under consideration using the analysis results already obtained for use in plotting the error contours. For example, in test A5 for h_t = 300 W/m^{2}K the error values are shown plotted against $(1-\beta)$ in Figure 6.22.

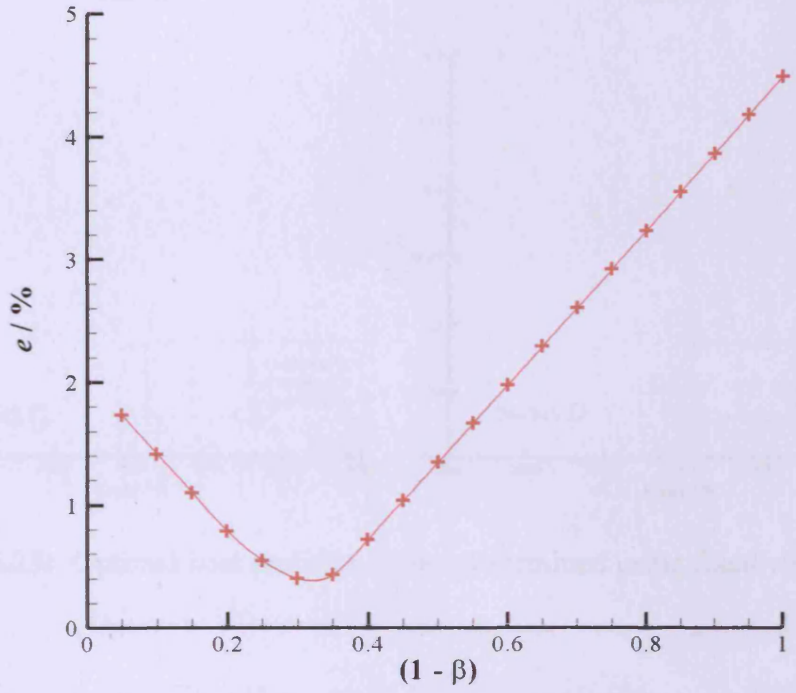

Figure 6.22: Error value versus heat partition for fixed h_t = 300 W/m^{2}K

The use of a spline curve fitted between the data points using the graphing package Tecplot, as seen in Figure 6.22 allows the value of $(1-\beta)$ which gives the minimum error value to be located at $(1-\beta)$ = 0.32. This process was repeated for the other tests at each of the possible h_t values within each series. Figure 6.23 show the results of this analysis for each series.

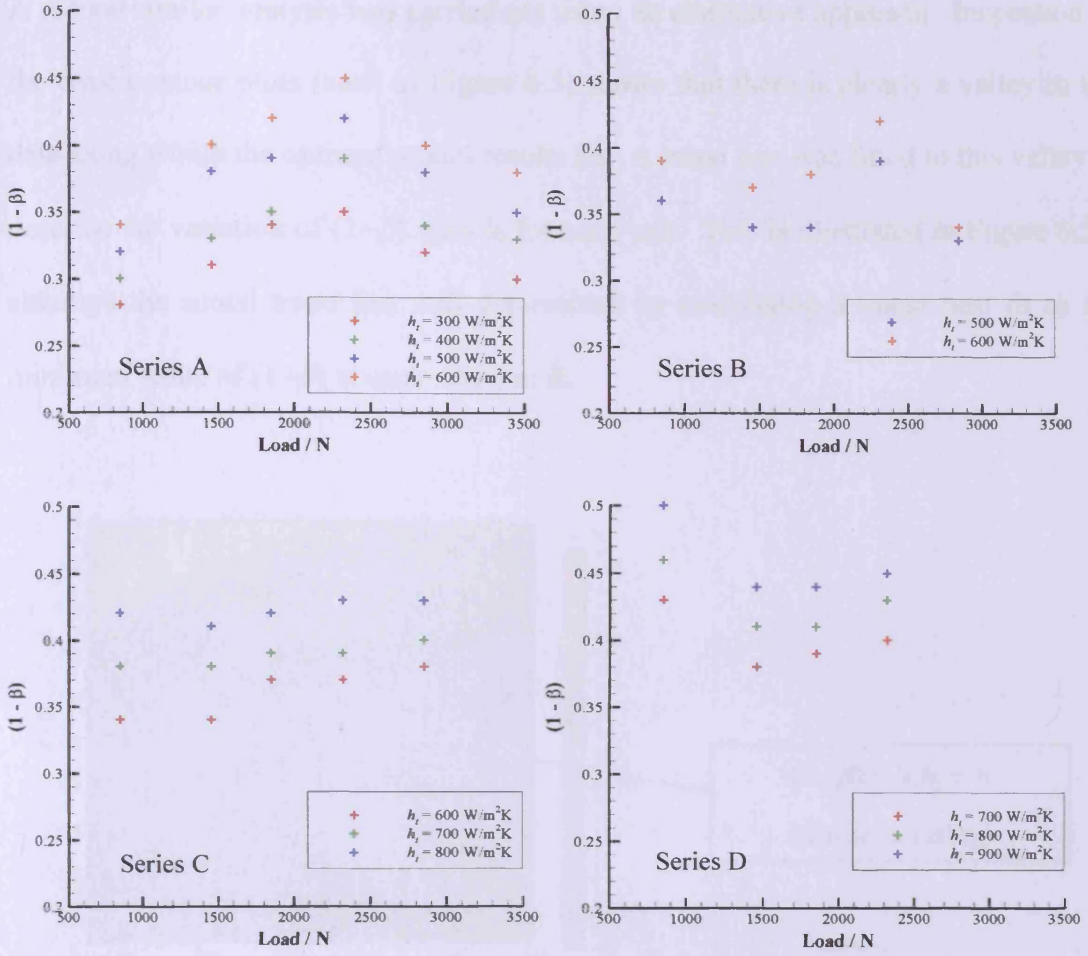

Figure 6.23: Optimal heat partition values determined using fixed values of h_t

The results given in Figure 6.23 show that, as the heat transfer coefficient is increased and more cooling takes place at the running track, more heat input (i.e. a larger value of $(1-\beta)$ is necessary to best match the experimental temperatures. However, more importantly, the Figure shows that as the value of h_t is varied through the possible values predicted by the original analysis the values of $(1-\beta)$ do not change by large amounts - in other words, if any of the predicted h_t values for a particular test series are used throughout that series then the overall result that the heat partition favours the fast disk remains unchanged.

A second similar analysis was carried out using an alternative approach. Inspection of the error contour plots (such as Figure 6.5) shows that there is clearly a valley in the data along which the optimal model results lie. A trend line was fitted to this valley to describe the variation of $(1-\beta)$ with h_t for each test. This is illustrated in Figure 6.24, although the actual trend line was determined by calculating a linear best fit to the minimum value of $(1-\beta)$ at each value of h_t.

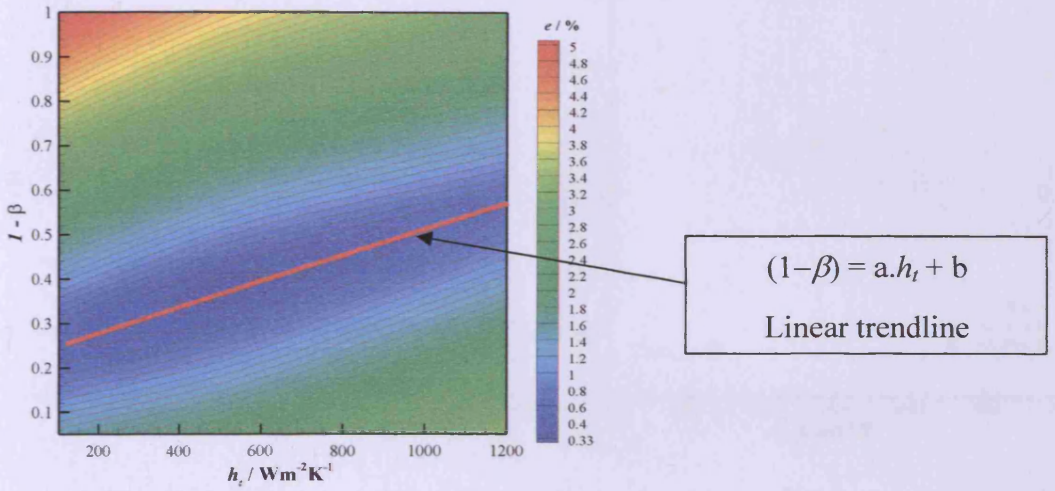

Figure 6.24: Linear trend line fitted to valley of minimum error

This trend line was then used to calculate the value of $(1-\beta)$ using each of the possible values of h_t predicted by the original analysis. The procedure was then repeated for the slow disk in each test in the series, giving the results shown in Figure 6.25.

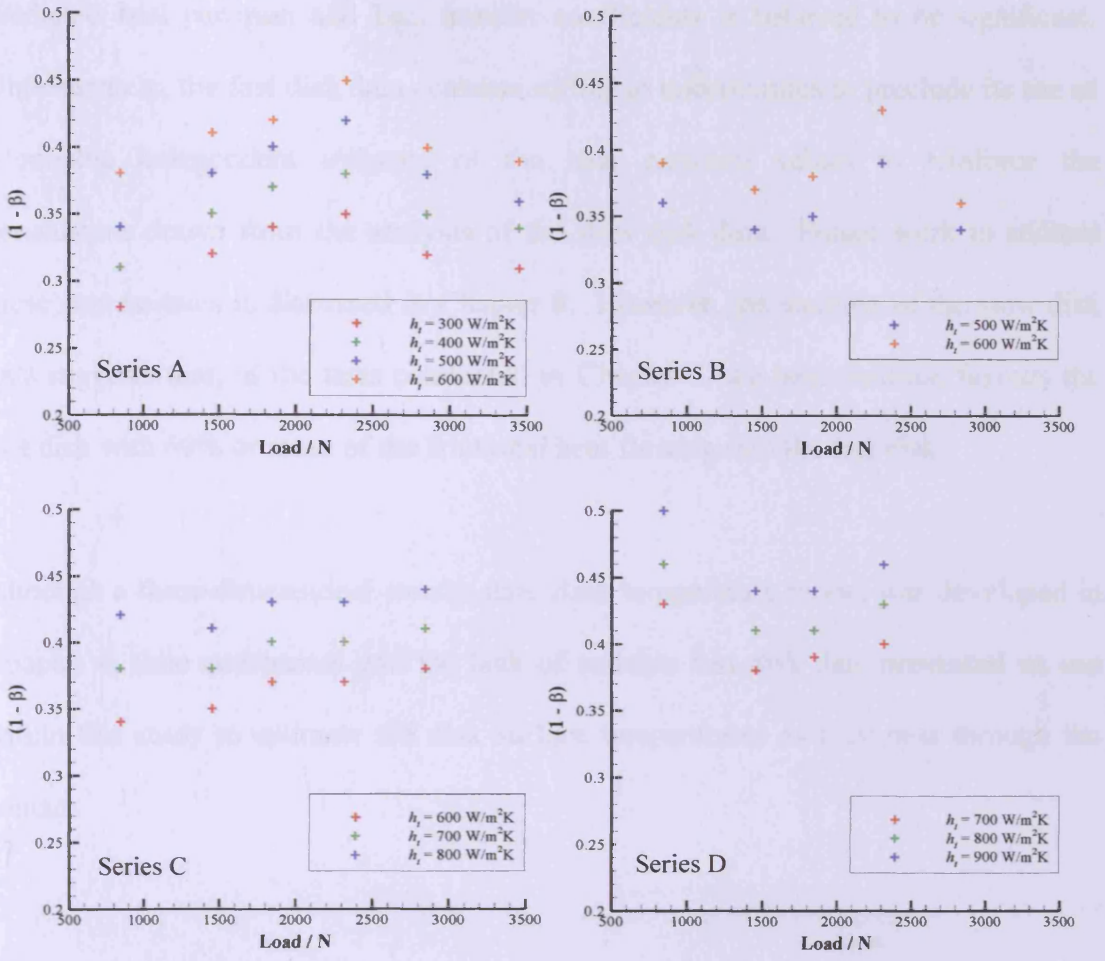

Figure 6.25: Optimal heat partition values determined using linear trend-line analysis of slow disk results

The results in Figure 6.25 show similar trends to those in Figure 6.23 in that, for all values of h_t within the range predicted by the original analysis of a series, the optimal fit to the experimental data is still obtained where the majority of the heat flows into the fast disk.

The analysis presented in this chapter reinforces the observations made in Chapter 5 concerning the errors and uncertainty in the fast disk data. However, the slow disk analysis shows consistent behaviour and, it is believed, provides a good estimate of the partition of heat between the contacting surfaces. The narrow spread of the

predicted heat partition and heat transfer coefficients is believed to be significant. Unfortunately, the fast disk data contains sufficient uncertainties to preclude its use as a reliable independent estimate of the heat partition values to reinforce the conclusions drawn from the analysis of the slow disk data. Future work to address these uncertainties is discussed in Chapter 8. However, the analysis of the slow disk data suggests that, in the tests conducted in Chapter 5, the heat partition favours the fast disk with 60% or more of the frictional heat flowing into the fast disk.

Although a three-dimensional steady-state flash temperature model was developed in Chapter 4, time constraints and the lack of suitable fast disk data prevented its use within this study to estimate the disk surface temperatures as they pass through the contact.

6.5 Sensitivity of results to time step and mesh density

In order to have confidence in the analysis results it is necessary to assess the sensitivity of the results to the time-step and mesh size used in the simulation. Firstly, the A5 fast disk results used as an example in Section 6.3 were re-calculated using a range of time-steps from 0.1 s to 20 s. The calculated temperature at thermocouple position A is shown in Figure 6.26 for these time steps. No significant difference can be seen between the results and thus the time-step of 1.0 s used for this work represents an acceptable trade-off between accuracy and computational efficiency.

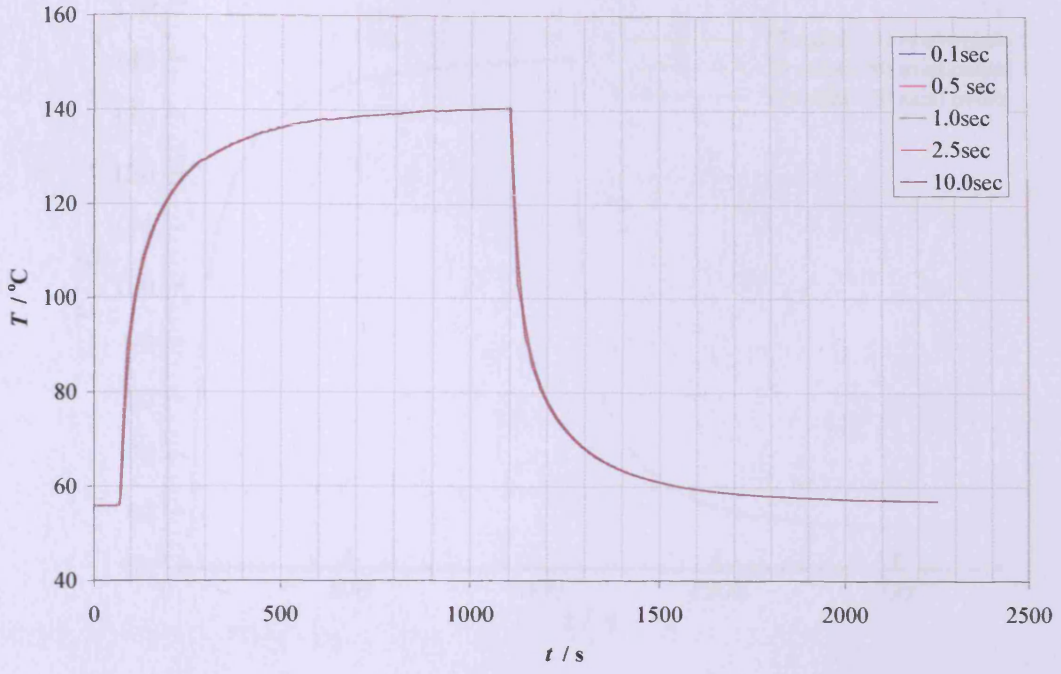

Figure 6.26: Calculated temperature at thermocouple A for a range of time-steps for test A5 fast disk

In order to assess the effect of mesh size, further calculations were performed using a time-step of 1.0s. Three mesh sizes were used – the original mesh size of 25 radial points and 40 axial points; a mesh twice as fine with 50 radial points and 80 axial points; and a mesh approximately twice as coarse with 13 radial points and 20 axial points. The calculated temperature at position A for each mesh can be seen in Figure 6.27. It is clear than the results of the model are not, at this scale, significantly affected by mesh size.

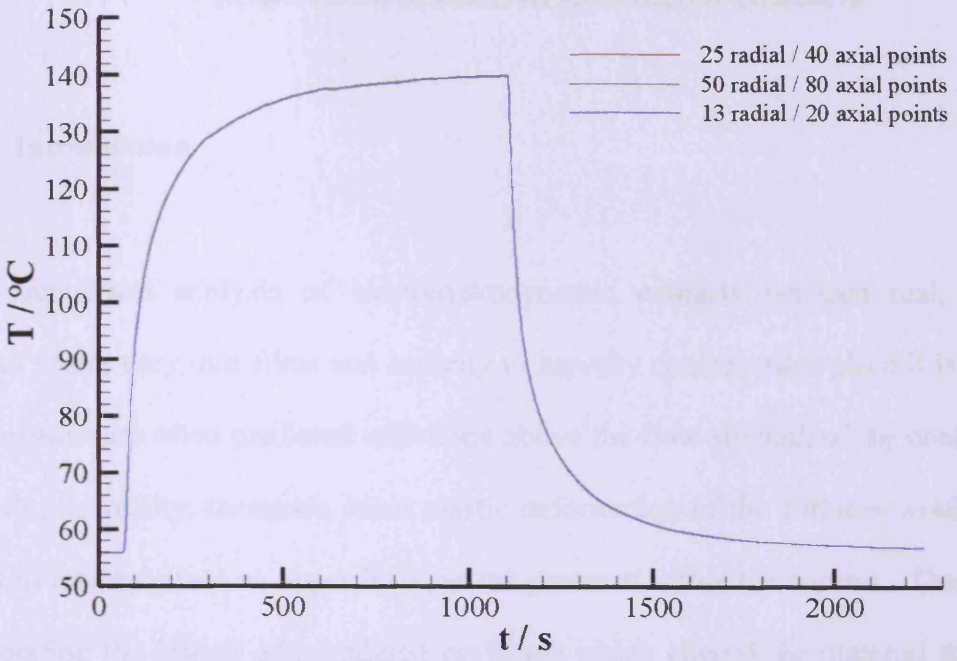

Figure 6.27: Calculated temperature at thermocouple A for a range of mesh sizes for test A5 fast disk

6.6 Summary

In this chapter, the two-dimensional transient heat conduction model of the outer annular section of the test disks (developed in Chapter 4) has been applied to the heat partition experimental results of Chapter 5. The results from the fast and slow disks were treated independently. The analysis procedure adjusted the heat partition and convective cooling coefficients until the error between calculated temperatures and those recorded during the experiments was minimised. Whilst the uncertainties currently present in the fast disk data prevented any meaningful conclusions being drawn from these results, the slow disk analysis clearly shows that the partition of heat in these experiments favours the faster disk. Around 60% of the total frictional heating dissipated at the contact passes into the faster disk.

Plastic deformation in lubricated contacts

7.1 Introduction

In the numerical analysis of elastohydrodynamic contacts between real, rough surfaces where very thin films and asperity to asperity contact takes place it is found that pressures are often predicted which are above the flow strength of the contacting materials. In reality, therefore, local plastic deformation of the surfaces would take place and thereby place an upper limit on the pressure within the contact. Therefore, incorporating the effects of calculated pressures which exceed the material strength within an EHL solution is necessary to achieve a more realistic model of the lubricated contact of real rough surfaces. Such a model would be of great interest in the study of the running-in and wear of rough surfaces, for example.

This chapter presents a review of work reported in the literature to incorporate elastic-plastic material behaviour in both lubricated and dry contacts, together with a model for the plastic deformation of contacting surfaces based on the results of finite element analysis (FEA). Finally, some suggestions are made on how the proposed model could be incorporated into an EHL (or elastic-plastic) solver code.

The work described in this chapter was intended to form a parallel programme of work with the heat-partition study which forms the bulk of this thesis. However, it became clear that to incorporate the models developed herein into an EHL solver was of sufficient complexity to warrant a separate study. The work reported here is therefore included to aid subsequent developments in the field.

7.2 Previous work

7.2.1 Dry contact – statistical models

The majority of the work reported in the literature on plastic deformation of asperities concerns dry contact. It covers a wide range from analytical studies of simple geometry to complex numerical solvers to simulate the dry contact of real surfaces.

Early work on contacts which featured plastic deformation of asperities was reported by Abbot and Firestone (1933) who developed their widely known model for a fully plastic contact, known as the surface microgeometry model. Their model assumes that the deformation of a rough surface against a rigid flat is equivalent to the truncation of the un-deformed surface by the rigid flat held at the same separation – i.e. that the contact area between the plastically deformed asperities and the flat is equivalent to the asperity tips being "cut off" by the flat. The contact pressure at these contacts is taken to be the material flow pressure. Whilst this model is simple and easily used, it does not conserve material volume.

The contact of real rough surfaces has been studied by many workers using statistical methods to represent real roughness by idealised equivalent distributions of asperities. The pioneering contribution to the field was made by Greenwood and Williamson (1966) who developed a model for the elastic contact of rough surfaces. In their model a rough surface was represented by hemispherically-tipped asperities (all with a common radius of curvature) whose heights followed a Gaussian (normal) distribution. They assumed that the contacts between the individual asperities and a smooth plane followed Hertzian elastic theory, and on this basis they derived

relationships for the total area of contact and the total load as functions of the separation between the surfaces. However, the Greenwood and Williamson model is limited to cases where the majority of contacting asperities deform elastically. In their experimental work which attempted to validate the Greenwood and Williamson model, Powierza *et al.* (1992) found that the model is relatively good at predicting *elastic* contact phenomena, but that when the applied load exceeded about half of the yield point load, their experimental results deviated significantly from those predicted by the Greenwood and Williamson model.

A number of workers have attempted to bridge the extremities of predominantly elastic deformation (as represented by the Greenwood and Williamson model) and fully plastic deformation (Abbott and Firestone). For example, Chang *et al.* (1987) proposed an elastic-plastic contact model for rough surfaces, based on the volume conservation of plastically deformed asperities. Chang *et al.*'s work was based on a similar statistical approach to that of Greenwood and Williamson. However, their model only allows an individual asperity to have two states – either it deforms elastically or is subject to fully plastic deformation. Whilst their model can analyse cases where on a macroscopic level the contact is in the elastic-plastic transition regime, it does not incorporate such effects at the individual asperity level. This is unfortunate, since Johnson (1985) has demonstrated that the elastic-plastic transition region is both long and significant. His work showed that, for the contact of a sphere and a rigid plane, the load must be increased by a factor of 400 from the point of initial yielding until full plastic flow conditions are reached. The Chang *et al.* model was subsequently extended to cover surfaces with elliptical asperities by Horng (1998) in order to represent manufactured surfaces with a predominant direction of finish, but the inherent simplifications were not addressed.

Other workers (e.g. Zhao *et al.*, 2000; Jeng and Wang, 2003; Schofield and Thornley, 1977; Jackson *et al.*, 2003) have developed models which use the same basic approach as Greenwood and Williamson, that is to represent a surface statistically by a distribution of similar asperities, but which incorporate the range of deformation cases for each asperity, from elastic deflection, through elastic-plastic deformation to unconstrained plastic flow.

7.2.2 Dry contact – numerical models

However, all of these models by their very nature deal with the macroscopic behaviour of the whole contact and offer little insight into the details of the deformation of individual asperities. In order to incorporate elastic-plastic and fully plastic deformation of asperities into an EHL model detailed information on the deformation of asperities both during and after loading is required. A range of studies have been carried out by various workers using the finite element method to study in detail the elastic-plastic deformation of asperities in a wide range of situations. The use of the finite element method allows the simplifying assumptions inherent in the work discussed in Section 7.2.1 to be removed.

Beghini *et al.* (1992) carried out a finite element study of asperity deformation and sub-surface residual stresses using a commercial finite element code (ABAQUS). Their model was used to simulate contact between two surfaces, one of which featured a single asperity. The material model used was an elastic-perfectly plastic model, with no attempt to incorporate strain-hardening of the material. Their finite

element results showed the residual deformation after a loading and unloading cycle, and also displayed the characteristic "piling-up" of material outside the loading region. They used their results for residual deformation and stresses to simulate the over-rolling of a dent in a bearing raceway and to assess such a defect's influence on the fatigue life of the bearing.

Kogut and Etsion (2002) used finite element analysis to consider the classical contact mechanics problem of the contact of a deformable sphere and a rigid flat. They used this as a simple approximation to an asperity contact, and used an elastic-perfectly plastic material model. They obtained results at a range of interference ratios, ω/ω_c, defined as the ratio of the interference between the plane and the sphere to the interference at the onset of yielding. They found that, for $(\omega/\omega_c) < 6$ the plastic zone is fully surrounded by elastic material. As the interference is increased above $(\omega/\omega_c) = 6$, the plastic zone grows until, at $(\omega/\omega_c) = 68$, the contact region is fully plastic and the mean contact pressure is equal to the material hardness. A similar analysis of the elastic-plastic contact of a sphere and a rigid flat was carried out by Jackson and Green (2003) who presented results which are in broad agreement with those of Kogut and Etsion.

Kogut and Etsion went on to obtain non-dimensional curve-fits to their finite element results to describe the evolution of mean contact pressure, contact load and contact area with interference from the initial elastic behaviour through to the fully plastic behaviour. They also used these dimensionless relations in a statistical model for the contact of rough surfaces (Kogut and Etsion, 2003) which followed a similar approach to Greenwood and Williamson and subsequent workers in that it used a statistical distribution of similar asperities to simulate a real rough surface. Their finite-element

based statistical model was subsequently extended to take into account adhesion, and hence allow an estimation of friction between sliding rough surfaces (Kogut and Etsion, 2004).

Faulkner and Arnell (2000) also considered asperity friction in their statistical model of two rough surfaces sliding past each other. The model was based on finite element simulations of two single hemispherical asperities sliding past each other at a fixed separation. Both asperities used elastic-plastic materials models, with one asperity being aluminium and the other high speed steel (HSS). The results of their transient analysis of the asperities sliding past each other gave both shear and normal forces acting on the asperities and hence allowed the friction coefficient to be estimated. These results were then incorporated into their statistical model which assumed an exponential distribution of asperity heights. They found their model to give lower predictions of friction force than previous work which had modelled asperities as cylindrical bodies. Other finite element simulations of sliding asperity contacts including the effects of friction have been reported by Zhang *et al.* (2003), who presented detailed results for the evolution of the plastic zone in a sliding asperity contact at various loads.

The combination of a finite element model of an idealised asperity with a statistical model of a real rough surface is a popular one, with similar work to that of Kogut and Etsion and Faulkner and Arnell carried out by Kucharski *et al.* (1994) and Xuesheng *et al.* (2004).

Further finite element work was carried out by Krall and co-workers (Krall *et al.*, 1993, 1995 a & b), in order to investigate the tribological contacts which occur in

magnetic data-storage disks. They initially analysed the evolution of residual stresses, residual deformation and contact pressure distribution during repeated loading cycles of an elastic-plastic body by a spherical indenter (Krall *et al.*, 1993). They investigated the effect of the elastic modulus and strain-hardening parameters used in their material model, and presented detailed results for the evolution of the plastic zone with increasing load, up to fully plastic conditions. The model was subsequently extended to include a hard coating on the surface of the elastic-plastic body, as commonly used in magnetic disk applications (Krall *et al.* 1995a, 1995b). They presented results for surface and sub-surface residual stresses, together with residual deformations and the evolution of the plastic zone for a range of coating thicknesses and material properties.

Advances in available computing power allowed Komvopoulos and Ye (2002) to extend their analysis of layered media in magnetic storage devices to multiple asperity contacts. Their model simulated indentation of an elastic-perfectly plastic layered body (representing a computer magnetic storage disk) by a rigid rough body (representing the read-write head). They investigated the effect of the coating thickness and material properties on the stress distribution in the layered body. They found the shape of the asperity to be of importance – sharper asperities with a small radius of tip curvature were found to give plastic deformation directly below the micro-contact in the coating layer, whereas asperities with a larger tip radius led to plastic flow within the substrate itself. In addition, they investigated the beneficial effects of residual stresses in the coating caused by the sputtering process by which it is applied to the magnetic substrate.

A similar study was carried out by Tao *et al.* (2001), who also modelled the head/disk interface in computer storage media using an elastic-plastic finite element model. They investigated three different representations of the rough surface – using fractals, Fourier series and polynomial functions – and found that the high frequency components of the surface roughness (which are retained by the fractal and Fourier series representations but eliminated by the polynomial function) were important in determining the stress distribution in the coating layer.

The work reviewed here generally used commercial finite element software, such as ABAQUS or ANSYS, to simulate the elastic-plastic deformation of asperities. A number of workers have developed bespoke numerical or semi-analytical codes to evaluate the stresses and deflections at the contact of rough surfaces. For example, Mayeur *et al.* (1995) developed a semi-analytical code using the boundary integral method. They split the problem into two parts – an elastic part which was analysed using classical elastic contact methods, and the plastic deformation part solved using an iterative method. Their model used a strain-hardening material model, and was capable of dealing with real rough surface profiles. Their results showed flattening of asperity tips after loading cycles during which the contact pressures exceeded the flow strength of the material.

The numerical model for elastic-plastic contact of Liu *et al.* (2001) is based on a Fast Fourier Transform (FFT) method, and calculates the surface and subsurface stresses during the running-in process. Their model was used to investigate the modification of surface profiles and contact pressures by plastic deformation, with comparison measurements taken during running-in experiments. Other numerical models capable of analysing the multiple-asperity elastic-plastic contact of real rough surfaces have

been developed by Prodan and Diaconescu (2003) and Liu *et al.* (2001, 2006), for example.

7.2.3 Lubricated contacts

The majority of the reported work on elastic-plastic deformation of rough surfaces is concerned with dry contact, for example in computer hard disk applications. However, some work has been reported by Xu *et al.* (1996) in developing an EHL line contact solver which includes the effects of plastic deformation under high lubricant pressures. Xu's work involved analysing a smooth surface with a superimposed dent, designed to replicate damage caused by rolled-in debris on the raceways of rolling element bearings. In an EHL analysis of a dented surface, Xu found that the pressure spikes caused by the dent exceeded the hardness of the material and thus permanent plastic deformation of the surface could be expected. In order to include this behaviour in the EHL solution the film thickness equation was modified by the inclusion of an additional term to account for the plastic deformation as follows:

$$h(x,t) = h_0 + \frac{x^2}{2} + h_{elastic} + h_{plastic}$$

where h_0 is the separation of the surfaces; $h_{elastic}$ is the elastic deflection of the surfaces determined from a pressure integral; and $h_{plastic}$ is the extra term to represent the additional deformation of the surfaces due to plastic yielding.

In order to evaluate $h_{plastic}$, Xu used a commercial FEA package, ABAQUS, to model a semi-infinite body subject to an arbitrary pressure loading on its top surface. During the convergence process of the EHL solution the calculated pressure distribution was passed to the FEA model at regular intervals. Two FEA analyses were performed –

one where elastic material properties were used, and one where an elastic-plastic linear kinematic hardening material model was used. The difference between the deflections calculated from these two analyses was the deflection due to plastic yielding, $h_{plastic}$. This is then included in the film thickness equation, and the solution is iterated until no change in the plastic deformation occurs. They considered a range of cases, with both a stationary and moving dent. They also investigated the effect of using different degrees of strain hardening in their material model, from no hardening (elastic-perfectly plastic) to levels typical of bearing steels. In all cases, the inclusion of plastic deformation in the film thickness equation led to reductions in the magnitude of the pressure spikes. In one of the cases which was analysed with a dent in the surface and an elastic-perfectly plastic material model, the maximum pressure decreased from 3.59 times the maximum Hertzian smooth surface pressure to 2.46 times the maximum Hertzian pressure when plastic deformation was taken into account.

Whilst the approach of Xu *et al.* must be commended since they are among the first workers to report the results of, as they term it, an elastoplastohydrodynamic lubrication (EPHL) analysis, their method does display some shortcomings. In the work described, the dent is relatively large compared to the EHL contact half-width (a), approximately $0.3a$ wide. Thus, relatively coarse meshes may be used in both the EHL and finite element solutions without sacrificing the accuracy of the computed results. In order to resolve accurately a real rough surface, a significantly finer mesh would be necessary in both the EHL and the finite element models, which would lead to significantly increased computational overheads. Thus, to extend Xu's solver to a full rough surface solution would, in the author's opinion, be prohibitively expensive in terms of computing requirements given that the method described employs the

solution of two finite element models a number of times during the convergence of the EPHL solution.

The lack of any subsequent publications from Xu or his co-workers on their EPHL model could be construed as indicative of the inherent problems of extending their approach further. Recent developments in high performance and parallel computing methods could alleviate these problems, but not without access to such expensive computing resources.

The use of finite element results from models of the elastic-plastic deformation of semi-infinite bodies in order to develop closed-form solutions for the plastic deformation term in a modified film thickness equation seems a possible way forward in attempting the study of real roughness under elastic/plastic/lubricated conditions. This approach is developed by the author in the following sections.

7.3. Plastic yielding in Hertzian contacts

7.3.1 Hertzian elastic contact theory

It is instructive to briefly review the work of Hertz in analysing the elastic contact of semi-infinite bodies. Analysis of the stresses at the contact of two elastic solids was first carried out by Hertz (1882), who was studying optical interference fringes between glass lenses, and wanted to take account of the possible deformation of the lenses due to the contact pressure between them.

Hertz made the following assumptions and simplifications:

1) **The contact area is, in general, elliptical.** This assumption was likely to have been guided by his observations of the interference fringes with which his work was concerned.

2) **Each body can be regarded as an elastic half-space** for the purpose of calculating local deformations. Thus, the highly localized contact stresses are treated separately from the general stress distribution in the bodies. In order for this assumption to hold, the contact dimensions must be small compared with:
    1. the dimensions of each body – so that the stress field calculated assuming an infinite solid is not seriously influenced by the proximity of boundaries and other features on the real body.
    2. the radii of relative curvature of the surfaces - to ensure that the surfaces immediately outside the contact region are approximately equal to the plane surfaces of an elastic half-space, and so that strains within the contact region are sufficiently small that linear elastic theory may be applied.

3) **The surfaces are assumed to be frictionless**, so that only a normal pressure is transmitted between them. In reality, the contact pressure must act perpendicularly to the interface between the two surfaces which, due to the deformation between the surfaces, need not necessarily be planar. However, the linear elastic theory does not allow for changes in the boundary forces due to the deformation which they produce, and so this assumption must be followed.

In this section, the treatment presented of the work of Hertz is based on that published by Johnson (1985) in his seminal work on contact mechanics. A co-ordinate system is adopted for this section, whereby the *x-y* plane is the common tangent plane to the two surfaces, and the *z* axis lies along the common normal projected into the lower surface, positive into the lower surface.

The surfaces are considered to be smooth, such that the profile of surface 1 close to the origin may be given by

$$z_1 = A_1x^2 + B_1y^2 + C_1xy + \ldots \tag{7.1}$$

A similar expression may be developed for the other surface. The separation between the two surfaces is given by $h = z_1 - z_2$, and the axis set can be chosen such that the xy term disappears:

$$h = Ax^2 + By^2 = \frac{1}{2R'}x^2 + \frac{1}{2R''}y^2 \tag{7.2}$$

R' and R'' are defined as the principal radii of relative curvature. The situations must now be considered where a normal compressive load is applied to the two solids, and the point of contact expands into an area. Consider two corresponding surface points $S_1(x,y,z_1)$ and $S_2(x,y,z_2)$, the separation between which is given, before deformation, by equation (7.2). Figure 7.1 shows the deformed shape of the two bodies:

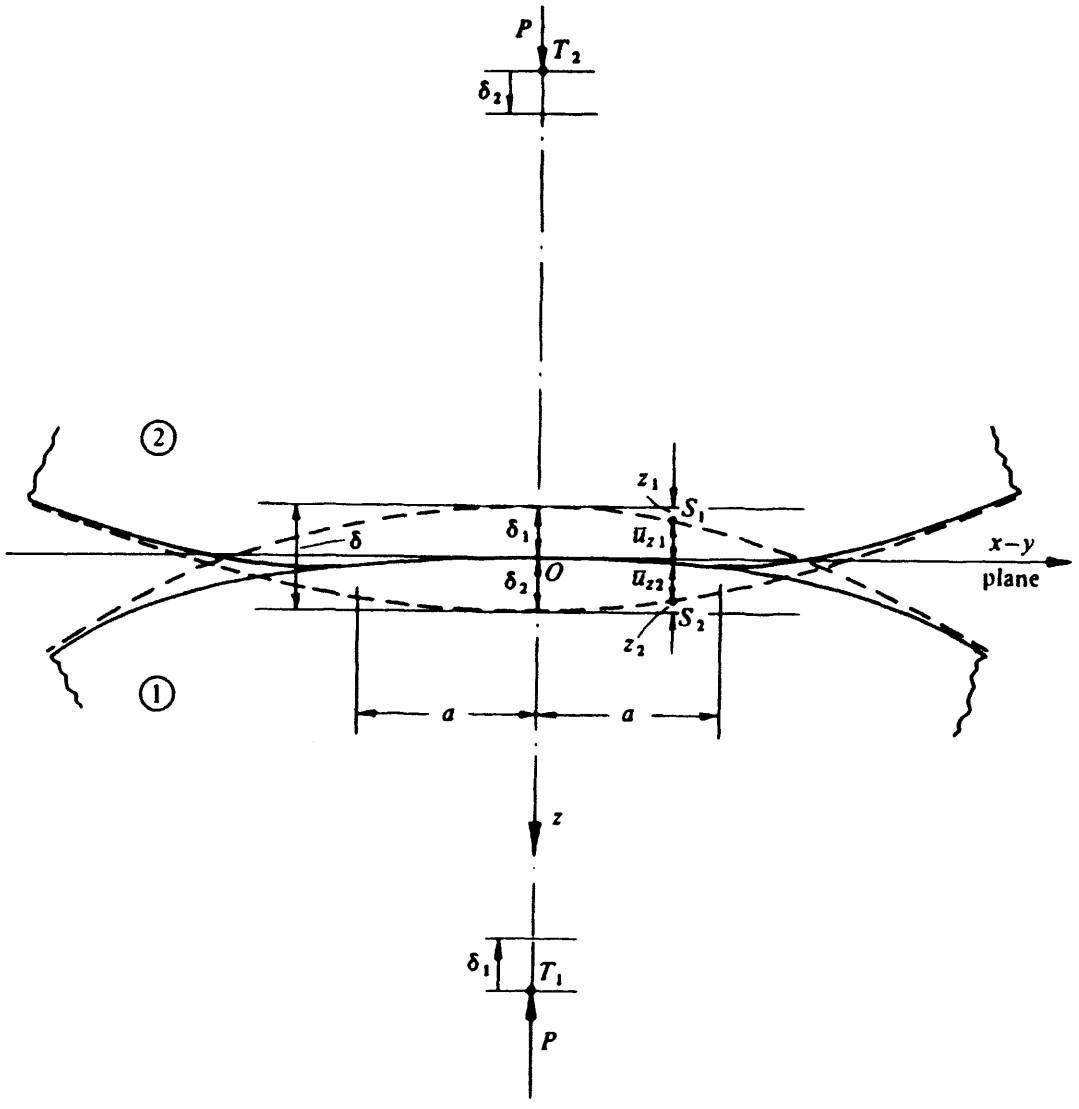

Figure 7.1: Deformation of two elastic bodies (from Johnson, 1985)

When the load is applied, distant points in each body, T_1 and T_2, move by displacements δ_1 and δ_2, respectively. If no deformation occurred, then the bodies would overlap as shown by the dotted profiles in Figure 7.1. Due to the contact pressure, the surface of each body is deformed by a distance u_{z1} and u_{z2}, relative to T_1 and T_2. If the points S_1 and S_2 are within the contact zone, on the surface of each body, then:

$$u_{z1} + u_{z2} + h = \delta_1 + \delta_2 \tag{7.3}$$

By using equation (7.2), and writing $\delta = \delta_1+\delta_2$, then an expression for the elastic displacements can be written:

$$u_{z1}+u_{z2}=\delta-Ax^2-By^2 \tag{7.4}$$

Equation (7.4) holds for all points within the contact zone, otherwise, equation (7.5) must be satisfied:

$$u_{z1}+u_{z2}>\delta-Ax^2-By^2 \tag{7.5}$$

Thus, the distribution of contact pressure must be determined such that the resulting elastic displacement satisfies equation (7.4) within the contact area, and equation (7.5) outside it.

For the particular case of line contact (i.e. normal contact between two long cylinders of radii R_1 and R_2), $B = 0$ since the radius of relative curvature in the y direction is infinite ($R'' = 0$). The radius of relative curvature in the x direction is given by:

$$\frac{1}{R}=\frac{1}{R_1}+\frac{1}{R_2} \tag{7.6}$$

Thus, for points on the surfaces of the unloaded cylinders, co-incident in the x direction, equation (7.2) becomes:

$$h=Ax^2=\frac{1}{2R}x^2 \tag{7.7}$$

For points within the contact region after loading, equation (7.4) becomes:

$$u_{z1}+u_{z2}=\delta-Ax^2=\delta-\frac{1}{2R}x^2 \tag{7.8}$$

and equation (7.5), for points outside the contact region, becomes

$$u_{z1}+u_{z2}>\delta-\frac{1}{2R}x^2 \tag{7.9}$$

By differentiating equation (7.8), an expression for the surface gradients may be obtained:

$$\frac{\partial u_{z1}}{\partial x}+\frac{\partial u_{z2}}{\partial x}=-\frac{x}{R} \tag{7.10}$$

Using the method of stress functions, and satisfying the conditions of equilibrium, compatibility and Hooke's Law, the problem of an elastic half-space loaded by normal pressure *p(x)*, may be considered. The expression, obtained using the method of stress functions, for surface displacement due to the pressure is given by:

$$u_z=-\frac{2\left(1-\nu^2\right)}{\pi E}\int_a^a p(s)\ln|x-s|\mathrm{d}s \tag{7.11}$$

In addition, the expressions for the stress components due to the applied pressure loadings are given by equations (7.12), (7.13) and (7.14).

$$\sigma_x=-\frac{2z}{\pi}\int_a^a \frac{p(s)(x-s)^2\mathrm{d}s}{\left\{(x-s)^2+z^2\right\}^2} \tag{7.12}$$

$$\sigma_z=-\frac{2z^3}{\pi}\int_a^a \frac{p(s)\mathrm{d}s}{\left\{(x-s)^2+z^2\right\}^2} \tag{7.13}$$

$$\tau_{xz}=-\frac{2z^2}{\pi}\int_a^a \frac{p(s)(x-s)\mathrm{d}s}{\left\{(x-s)^2+z^2\right\}^2} \tag{7.14}$$

Equation (7.11) may be differentiated, giving another expression for the surface gradients:

$$\frac{\partial u_z}{\partial x}=-\frac{2\left(1-\nu^2\right)}{\pi E}\int_a^a \frac{p(s)}{x-s}\mathrm{d}s \tag{7.15}$$

By substituting equation (7.15) into equation (7.10), an integral equation for the contact pressure distribution in a line contact is found:

$$\int_a^a \frac{p(s)}{x-s}\mathrm{d}s=\frac{\pi E^*}{2R}x \tag{7.16}$$

This may be solved to give an expression for the contact pressure distribution:

$$p(x)=\frac{2P}{\pi a}\left(1-\left(x/a\right)^2\right)^{1/2}=p_0\left(1-\left(x/a\right)^2\right)^{1/2} \tag{7.17}$$

Now that the pressure distribution is known, it may be substituted into equations (7.12), (7.13) and (7.14) to give expressions for the stress components. Along the z axis, the integrals may be evaluated, giving equations (7.18) to (7.21):

$$\sigma_x = -\frac{p_0}{a}\left\{\left(a^2+2z^2\right)\left(a^2+z^2\right)^{-1/2} - 2z\right\} \tag{7.18}$$

$$\sigma_z = -p_0 a\left(a^2+z^2\right)^{-1/2} \tag{7.19}$$

$$\sigma_y = \nu\left(\sigma_x + \sigma_z\right) \tag{7.20}$$

$$\tau_1 = -\frac{p_0}{a}\left\{z - z^2\left(a^2+z^2\right)^{-1/2}\right\} \tag{7.21}$$

It should be noted that σ_x and σ_z are principal stresses, and hence τ_1 is the principal shear stress. The maximum value of τ_1 is $0.30p_0$, at a position z=$0.78a$.

7.3.2 Onset of plastic yielding in a Hertzian contact

The yielding of ductile materials is usually predicted by either von-Mises' shear strain-energy criterion or by Tresca's maximum shear stress criterion. These can be related to the yield stress, Y, of the material in a simple tensile test. Von-Mises' criterion states that yielding occurs according to:

$$\sqrt{\frac{1}{2}\left\{\left(\sigma_1-\sigma_2\right)^2+\left(\sigma_2-\sigma_3\right)^2+\left(\sigma_3-\sigma_1\right)^2\right\}} = Y \tag{7.22}$$

Where σ_1, σ_2 and σ_3 are the principal stresses. Tresca's criterion suggests that yielding takes place according to the following criterion:

$$\max\left\{\left|\sigma_1-\sigma_2\right|,\left|\sigma_2-\sigma_3\right|,\left|\sigma_3-\sigma_1\right|\right\} = Y \tag{7.23}$$

Experimental evidence tends to support the von-Mises criterion as being the more accurate whereas the Tresca criterion is simpler to use. The two criteria represent upper and lower bounds of the range within which yielding occurs. By using the von-Mises and the Tresca criterion, the onset of yielding can be predicted for the line-contact case.

The Tresca criterion is governed by the maximum principal stress difference (the maximum shear stress), since σ_y is the intermediate principal stress. The maximum principal stress, $\tau_1 = \frac{1}{2}|\sigma_z - \sigma_x|$ has a maximum value of $0.30p_0$, at a depth of $z = 0.78a$. Substituting this into the Tresca criterion, equation (7.23) gives:

$$0.60p_0 = Y \tag{7.24}$$

$$(p_0)_Y = 1.67Y \tag{7.25}$$

Thus, first yielding takes place at a point $0.78a$ below the surface, when the maximum Hertzian pressure, p_0, reaches a value of 1.67 times the yield strength. Alternatively, using the von-Mises criterion, yield begins at a point $0.70a$ below the surface, when $p_0 = 1.79Y$.

After the onset of yielding, and plastic flow has begun, the plastic zone is fully contained by the surrounding material which remains elastic. The plastic zone lies beneath the surface, and the plastic strains are constrained to be of the same order of magnitude as the elastic strains of the surrounding material. Eventually, the plastic zone breaks out to the surface, and the displaced material is free to flow plastically to the sides of the loaded area. This "uncontained" mode of deformation takes place where p_0 reaches a value of around $3.8Y$ (Johnson, 1985).

7.4 Finite element modelling of the elastic-plastic deformation of a semi-infinite body

This section describes a series of finite element analyses performed using the commercially available code ABAQUS, to assess the elastic-plastic deformation of a semi-infinite solid. Non-dimensional relations for the residual deformation due to plastic yielding have been developed and their incorporation into an EPHL solution is described subsequently in Section 7.5.

7.4.1 Outline of Problem

The initial work was carried out for a fixed contact size and contact pressure, to establish the modelling methodology. A semi-elliptical pressure loading, with a maximum value of p_o = 1 GPa was applied to a body, over a contact of semi-dimension a = 0.5 mm, and the resulting stresses and deflections were analysed using ABAQUS FEA software with a plane-strain model. The material was modelled including plastic behaviour, and the load was ramped up over a period of time, and then removed in the same manner, to allow the residual deflection and stresses to be seen.

The problem analysed can be seen in Figure 7.2, shown schematically and not to scale.

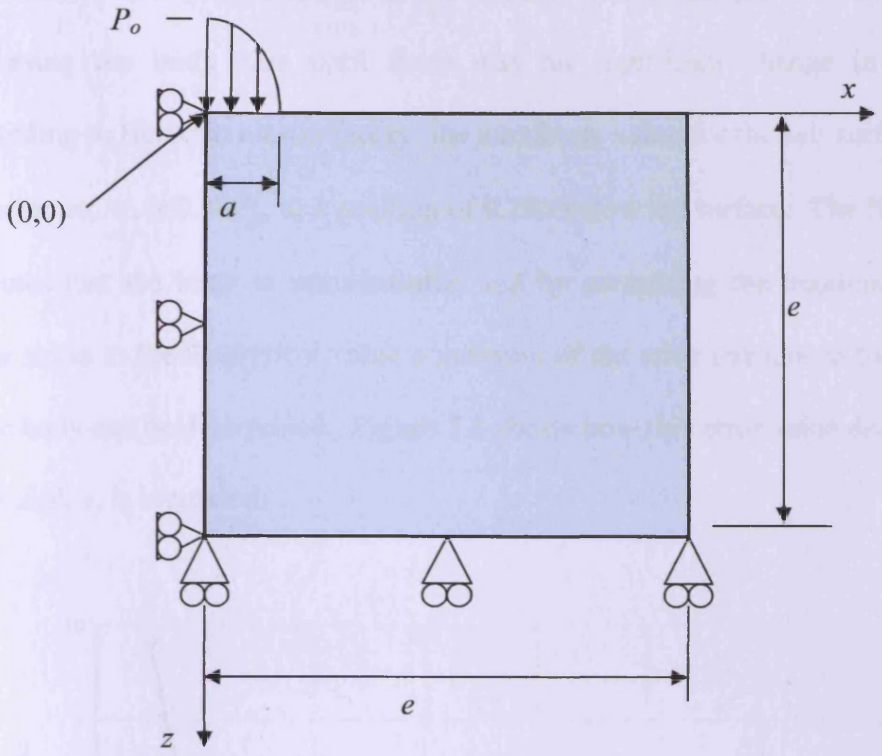

Figure 7.2: Boundary and loading conditions

7.4.2 Model verification against elastic results of Johnson

An elastic model of the above problem was used initially to determine the required dimensions of the body to give results independent of body size, and also to verify the mesh and element choices by comparing to the analytical expressions for sub-surface stresses in a Hertzian contact given by Johnson (1985), and outlined earlier as equations (7.18) to (7.21).

User defined loading routines were used within ABAQUS to apply the load in a semi-elliptical distribution, as given by Hertzian theory and shown in equation (7.17).

The size of the body relative to the contact half-width (a) was determined by increasing the body size until there was no significant change in the results. According to Hertzian elastic theory, the maximum value for the sub-surface principal shear stress, τ_1, is $0.30P_o$, at a position of $0.78a$ below the surface. The Hertzian work assumes that the body is semi-infinite, and by comparing the maximum computed shear stress to the theoretical value a measure of the error introduced by modelling a finite body can be determined. Figure 7.3 shows how this error value decreases as the body size, e, is increased.

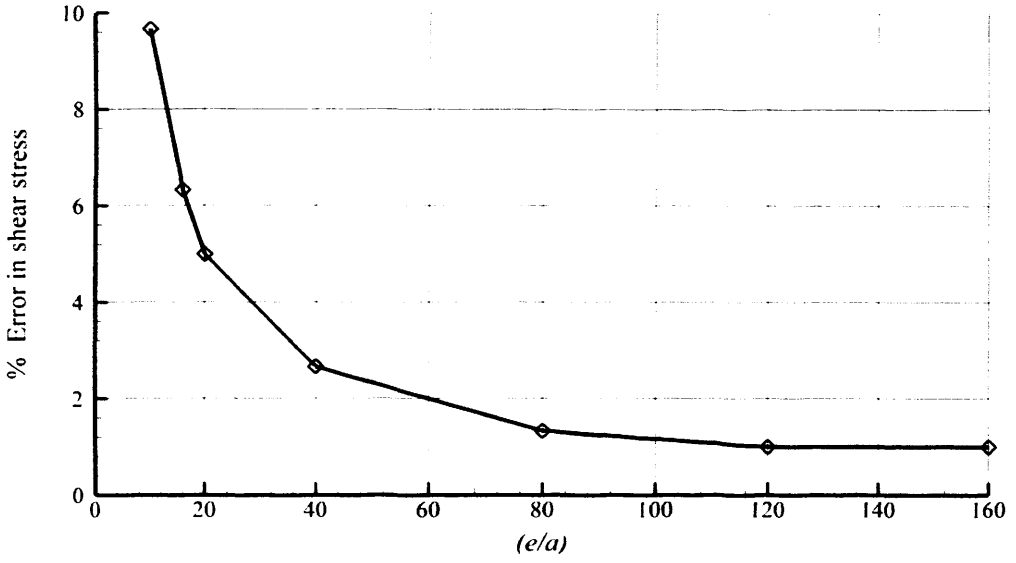

Figure 7.3: Error in shear stress

Thus, from Figure 7.3, it can be seen that the error in the shear stress is around 1% for $e/a \geq 80$. Increasing the e/a value further than 80 is unnecessary, as the computational overheads increase for little further reduction in error.

With e/a fixed at 80, the appropriate element type was investigated. ABAQUS offers a number of plane strain elements, and two were investigated: CPE4 (4 noded linear element) and CPE8 (8 noded quadratic element). The CPE8 elements were found to

give results which matched the theory more closely, and so they were selected for use in this work.

Finally, the results from the elastic model were verified by detailed comparison with the theoretical results from Johnson (1985), given earlier in equations (7.18) to (7.21). Figure 7.4 shows a comparison between the finite element results and theory, for the three principal direct stresses, σ_x, σ_y and σ_z, and the principal shear stress, τ_1, along the z axis.

The computed stresses along the vertical centre-line of the contact, where $x = 0$, are compared in Table 7.1 to values given by Johnson (1985) from the analytical formulae.

Table 7.1: Comparison of stresses along $x = 0$ line from analytical and FEA results

	Values from Johnson				**Values from FEA**			
z/a	σ_x/P_o	σ_y/P_o	σ_z/P_o	τ_1/P_o	σ_x/P_o	σ_y/P_o	σ_z/P_o	τ_1/P_o
0	-1.00	-0.60	-1.00	0	-0.99	-0.60	-1.00	0.00
0.2	-0.66	-0.49	-0.98	0.16	-0.65	-0.49	-0.98	0.16
0.4	-0.43	-0.41	-0.93	0.25	-0.42	-0.40	-0.93	0.26
0.6	-0.28	-0.34	-0.86	0.29	-0.27	-0.34	-0.86	0.29
0.8	-0.18	-0.29	-0.78	0.30	-0.17	-0.29	-0.78	0.30
1.0	-0.12	-0.25	-0.71	0.29	-0.11	-0.25	-0.71	0.30
1.5	-0.05	-0.18	-0.56	0.25	-0.04	-0.18	-0.56	0.26
2.0	-0.03	-0.14	-0.45	0.21	-0.02	-0.14	-0.45	0.22

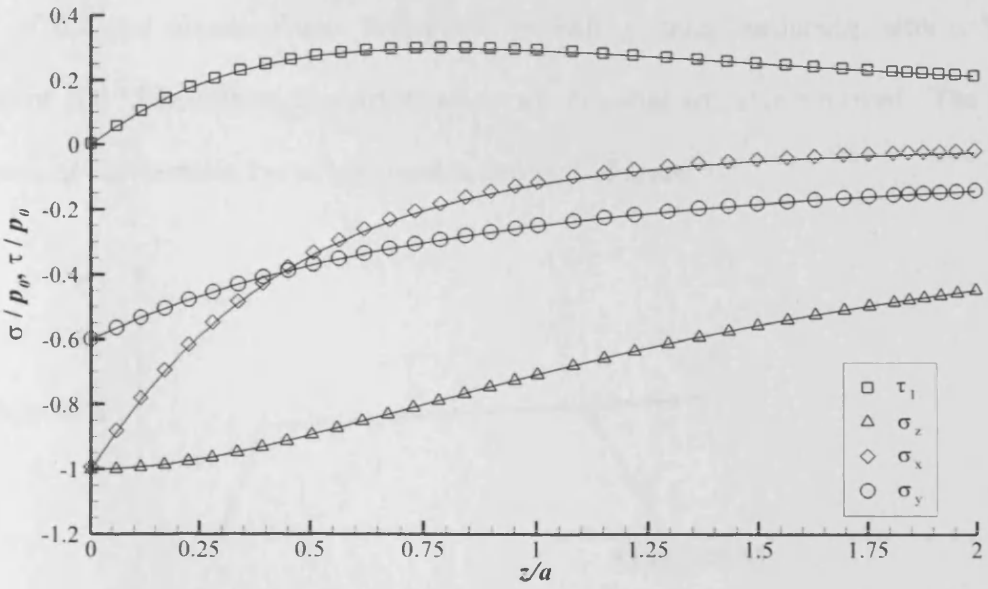

Figure 7.4: Comparison of FEA and analytical results
(Solid lines are theoretical results, symbols are data from FEA model)

It can be seen from Figure 7.4 and Table 7.1 that the finite element results are in good agreement with the theory, for elastic material behaviour.

7.4.3 Elastic-plastic behaviour

Following verification of the elastic model, elastic-plastic material behaviour was incorporated, together with time-dependent loading and unloading, in order to study the residual stresses and deflection after the applied load is removed. In all the work reported here, the loading and model geometry were the same as the elastic model. The value of p_0 = 1.0 GPa used for these initial model tests is greater than the value for the onset of yield given by the von-Mises criteria (approximately 900 MPa) and so plastic deformation was expected to occur.

The material was selected as steel with a Young's Modulus of 200 GPa, Poisson's ratio of 0.3 and elastic-plastic behaviour, including strain hardening, with a Yield Stress of 500 MPa, although restrictions on the material are later removed. The form of material stress-strain curve assumed is shown in Figure 7.5.

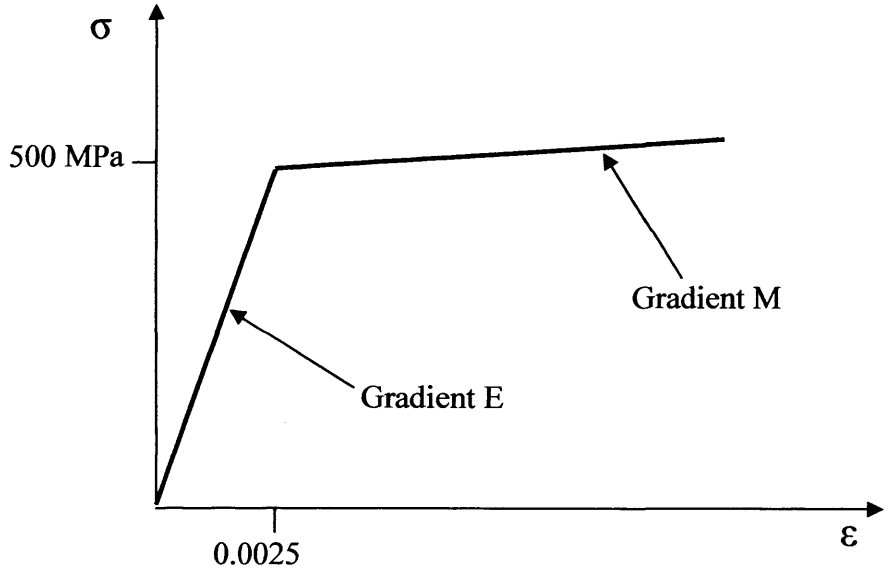

Figure 7.5: Stress – Strain curve for elastic-plastic material

The plastic modulus (slope of the plastic portion of the stress-strain curve shown in Figure 7.5), *M*, of 4 GPa was selected such that the material model used was comparable to that of Xu *et al.* (1996).

In order to assess the residual deformation and stress field following loading beyond the yield point, a transient loading cycle was incorporated into the finite element model. The loading sequence is represented in Figure 7.6, and consists of an initial phase, during which the loading is ramped linearly to its maximum value. This load is then held constant for a period, after which the load is removed in a linear fashion. The loading sequence can be summarised as:

1)	0 to 0.75 s	Linearly ramp load to maximum value
2)	0.75 to 1.25 s	Hold load constant
3)	1.25 to 2.00 s	Linearly ramp load down to zero
4)	2.00 to 2.25 s	Hold load at zero

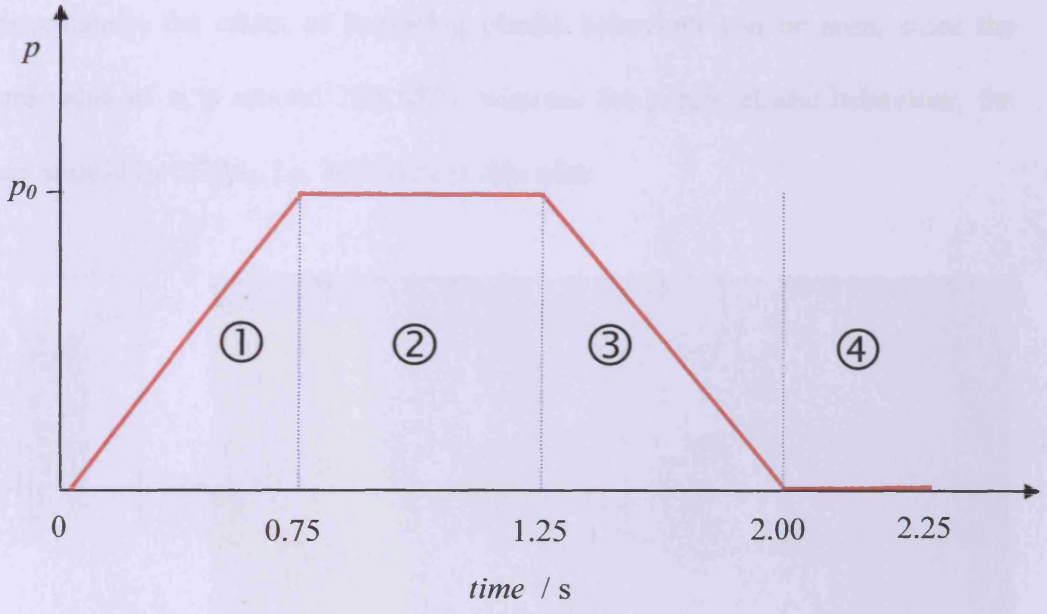

Figure 7.6: Loading Cycle

A number of tests were carried out with a range of loading cycles, with different time periods for each stage of the load cycle. Duration of these time periods was observed to have no effect on the maximum deflection during phase 2 of the cycle, or on the residual plastic deflection and residual stress at the end of the load cycle. It should be noted that the material model contains no time dependence and the use of a time-dependent loading cycle is merely the simplest way to implement variable loadings within the ABAQUS software. Various durations were investigated for each of the loading phases and were found to have no influence on the results obtained.

Initial results were obtained for contact width a = 0.5 mm, using the material behaviour shown in Figure 7.5, with the loading sequence shown in Figure 7.6, with a maximum pressure, p_o, of 1.0 GPa.

The contours of principal shear stress, τ_1, at the maximum load, can be seen in Figure 7.7. Immediately, the effect of including plastic behaviour can be seen, since the maximum value of τ_1 is around 280 MPa, whereas for purely elastic behaviour, the maximum should be $0.30p_0$, i.e. 300 MPa in this case.

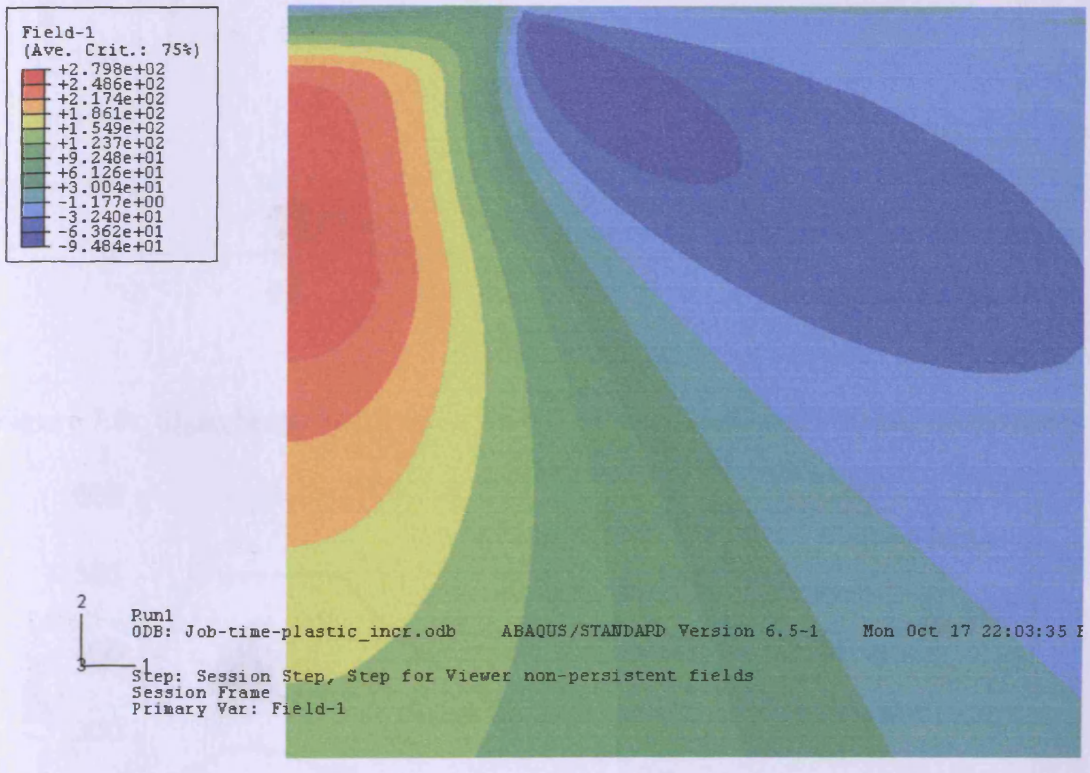

Figure 7.7: Contours of shear stress, τ_1, for p_0 = 1.0 GPa

The difference between elastic and elastic-plastic behaviour is further illustrated by Figure 7.8, where the distribution of principal shear stress, τ_1, along the z axis is compared for both cases, under fully loaded conditions. The flattening of the shear stress curve can be seen, in the region of $z = 0.78a$ = 0.39 mm, which is where the

maximum shear stress occurs under elastic conditions. The FEA results have a maximum value of τ_1 = 304 MPa for the elastic case, whereas when elastic-plastic behaviour is considered, the maximum value of τ_1 is reduced to 280 MPa.

In addition, the effect of the plastic yielding on the distribution of von-Mises stress along the z axis can be seen in Figure 7.9.

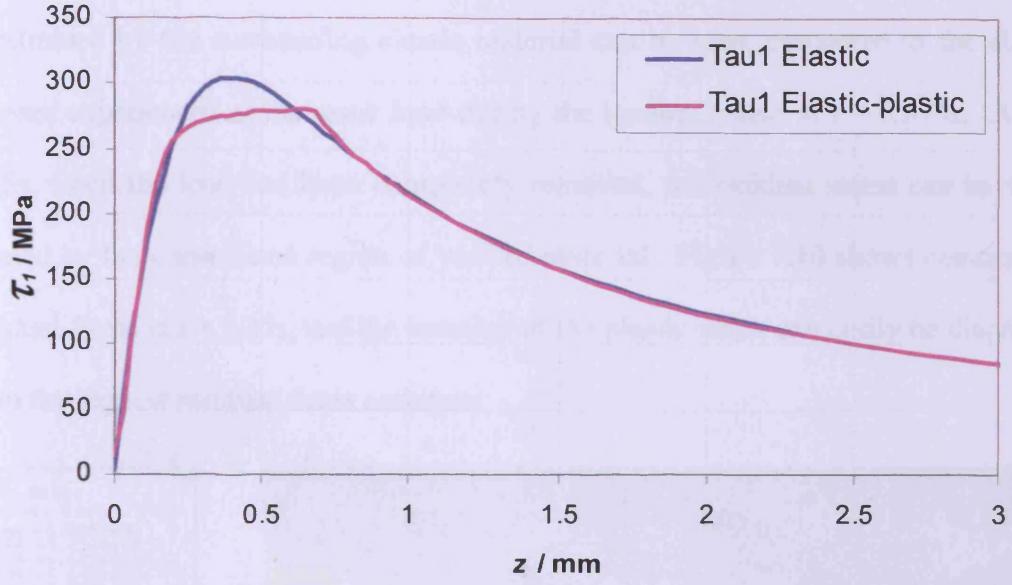

Figure 7.8: Shear Stress distribution along *z* axis, for elastic and elastic-plastic cases

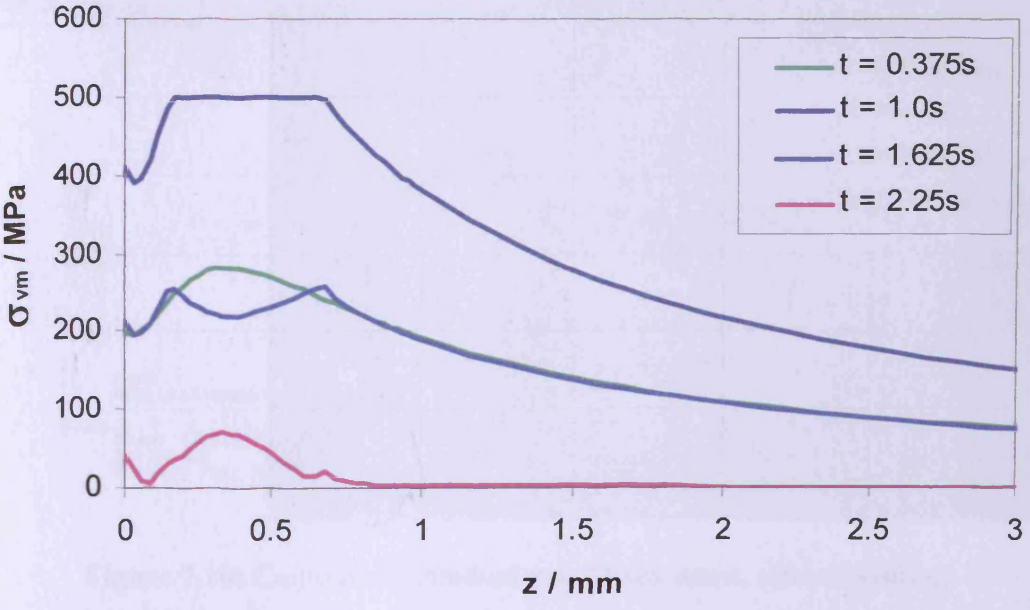

Figure 7.9: von-Mises stress distribution along *z* axis during loading cycle

The effect of the elastic-plastic behaviour can be seen in Figure 7.9. As the load is applied, at t = 0.375s, the value of p_0 has only reached 500 MPa, which is below the threshold for plastic deformation, and so the behaviour is fully elastic. At t = 1.0s, the value of p_0 has reached 1 GPa, and the effect of the material yielding can be seen, as the von-Mises stress is limited to the yield stress, of 500 MPa. During the unloading phase, at t = 1.625s, the residual stress caused by the yielded material being constrained by the surrounding elastic material can be seen, compared to the elastic stresses experienced at the same load during the loading phase, at t = 0.375s. At t = 2.25s, when the load has been completely removed, the residual stress can be seen, created by the constrained region of yielded material. Figure 7.10 shows contours of residual stress at t = 2.25s, and the location of the plastic strain can easily be discerned from the highest residual stress contours.

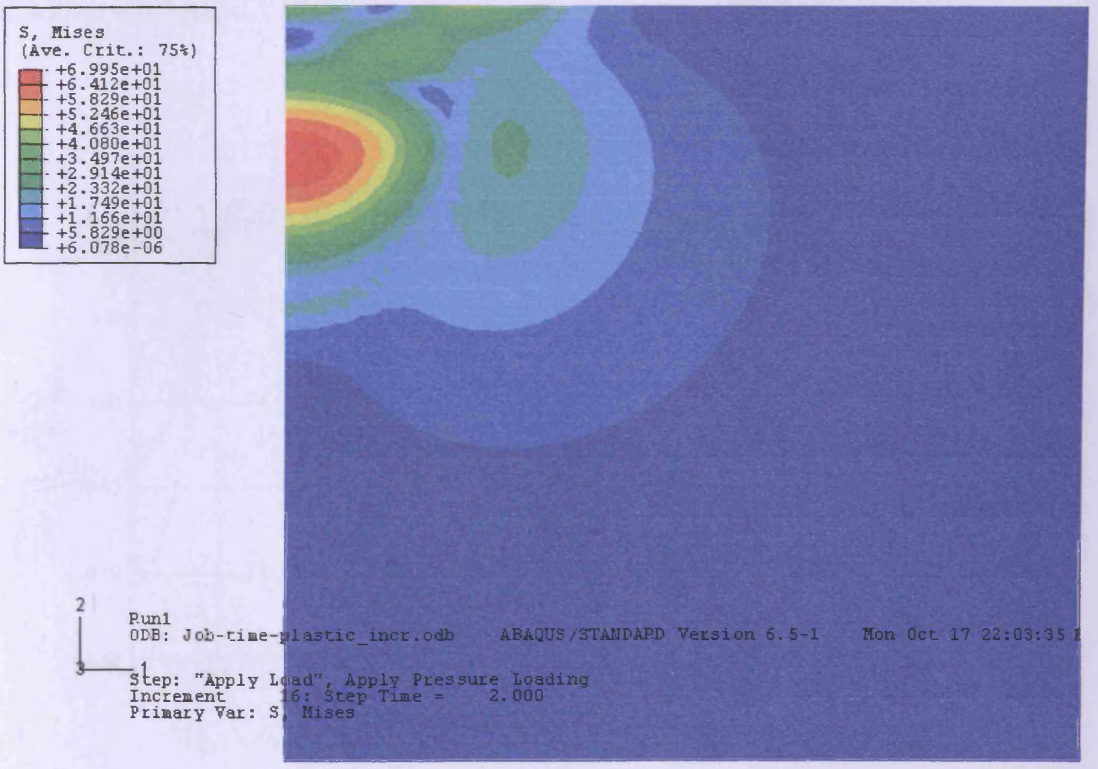

Figure 7.10: Contours of residual von-Mises stress, after unloading

7.4.4 Shape and magnitude of plastic deformation

In this section, a variety of analyses were performed, with a range of contact widths, a, and a range of maximum pressures, p_0. The results of these analyses were used to characterise both the shape and magnitude of the residual deformation due to the applied load.

7.4.4.1 Residual deformed shape

The residual deformation at the surface (along the line $z = 0$) after a full loading cycle can be seen in Figure 7.11, for a range of p_0 values from 1.5 to 2.1 GPa, at $t = 2.25$s, all with $a = 0.5$mm

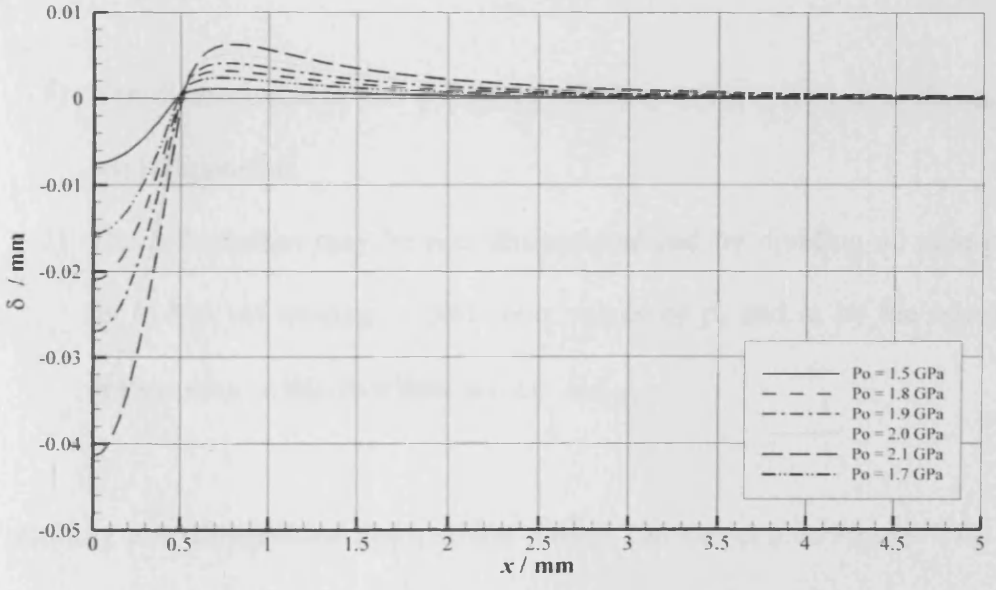

Figure 7.11: Residual Deformation at surface

The deformation increases in magnitude as the value of p_0, and hence the total load, is increased. A "piling up" of the material displaced by the plastic deformation, outside of the loaded area can also be seen. This is expected, and is described by Tabor (1951) as being due to flow of material away from the loaded area, as it is displaced by the deformation of the material under the applied load. It is also interesting to note that the transition from the section of surface with a negative deflection under the applied load, to the area which has "piled up" occurs at the same position, at the edge of the loaded area, regardless of the magnitude of the applied load. The results obtained here for the shape of the residual deformation are very similar to those reported by Beghini *et.al.* (1992).

In order to incorporate the shape of the residual deformation into the EHL model, to allow for plastic deformation of the asperities, it is necessary to find the non-dimensional shape of the deformation curve. The curve may be non-dimensionalized by the following manipulations:

1) Non-dimensionalize the x axis by plotting (x/a), where a is the contact semi-dimension.
2) The deformation may be non-dimensionalized by dividing all data points for a data set relating to particular values of p_0 and a, by the maximum deformation within that data set, i.e. δ/δ_{max}.

The resulting non-dimensional deformation curves can be seen in Figure 7.12, with data from load widths a = 0.3 mm and a = 0.5 mm included.

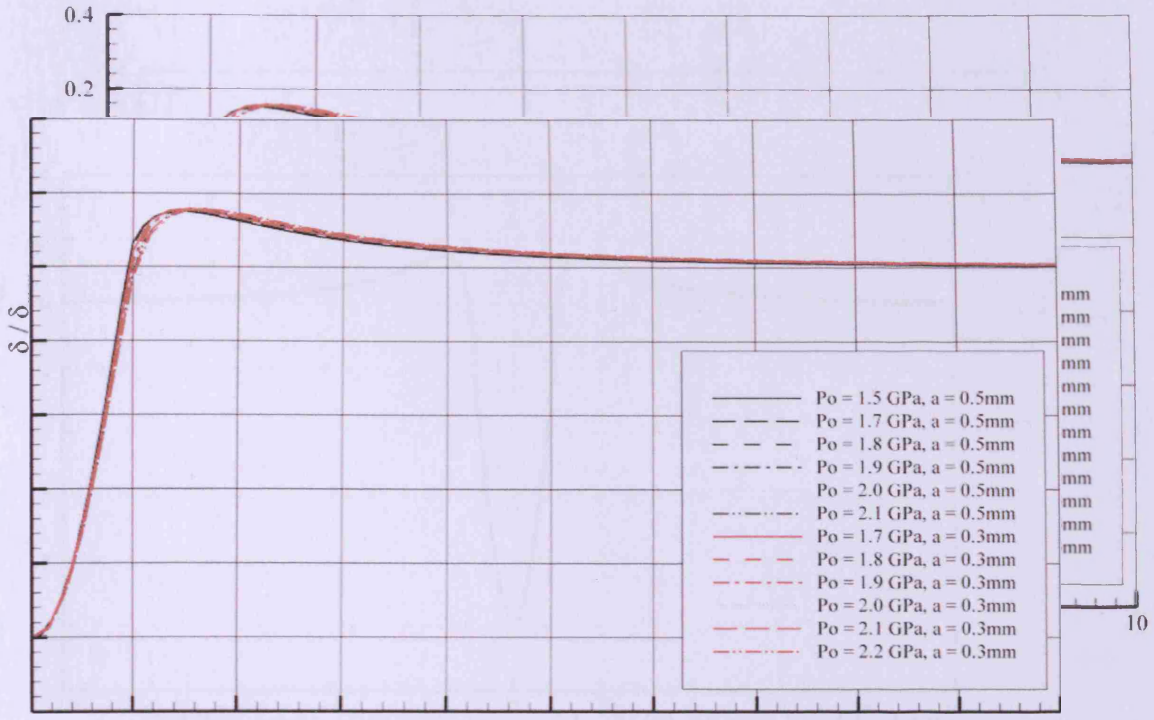

Figure 7.12: Non-dimensional residual deformation curve

Figure 7.12 shows that the shape of residual deformation at the surface after a load cycle does not depend to any great extent on the magnitude of the load.

The deformed surface has a transition from negative deformation within the loaded area to "piling up" immediately outside the loaded area. This "piling up" has a maximum magnitude of around 15% of the maximum deformation, and occurs at $(x/a) \approx 1.5$. The "piling-up" has decayed to zero by about $(x/a) = 10$. Figure 7.13 shows the average deflection curve, and has been mirrored about its centre-line to show the shape of the residual deformation produced by a semi-elliptical load.

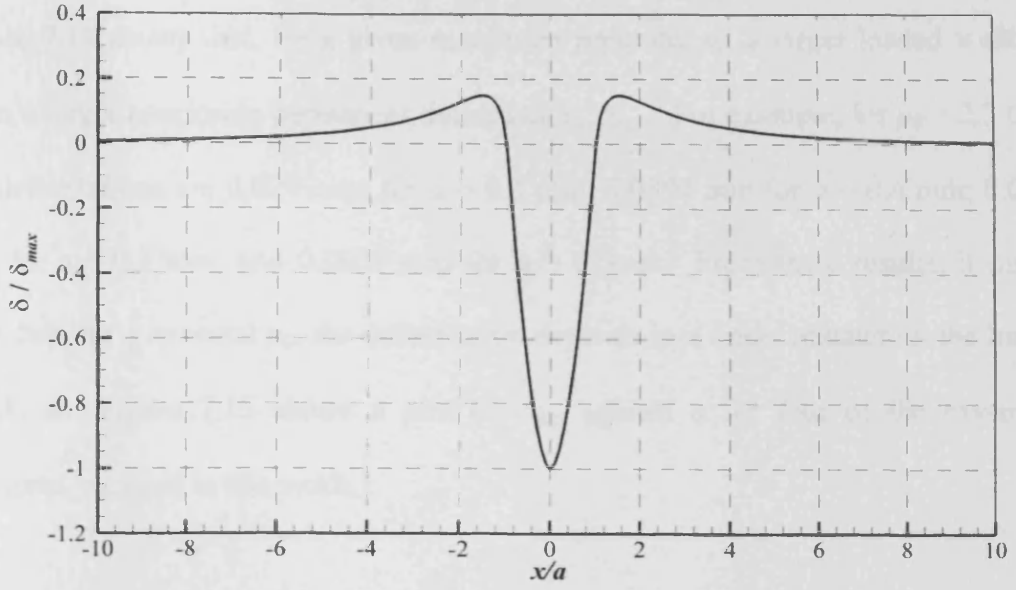

Figure 7.13: Non-dimensional residual surface deformation

7.4.4.2 Magnitude of Residual Deformation

The magnitude of the maximum deflection (δ_{max}) is plotted for a range of p_0 and a values in Figure 7.14.

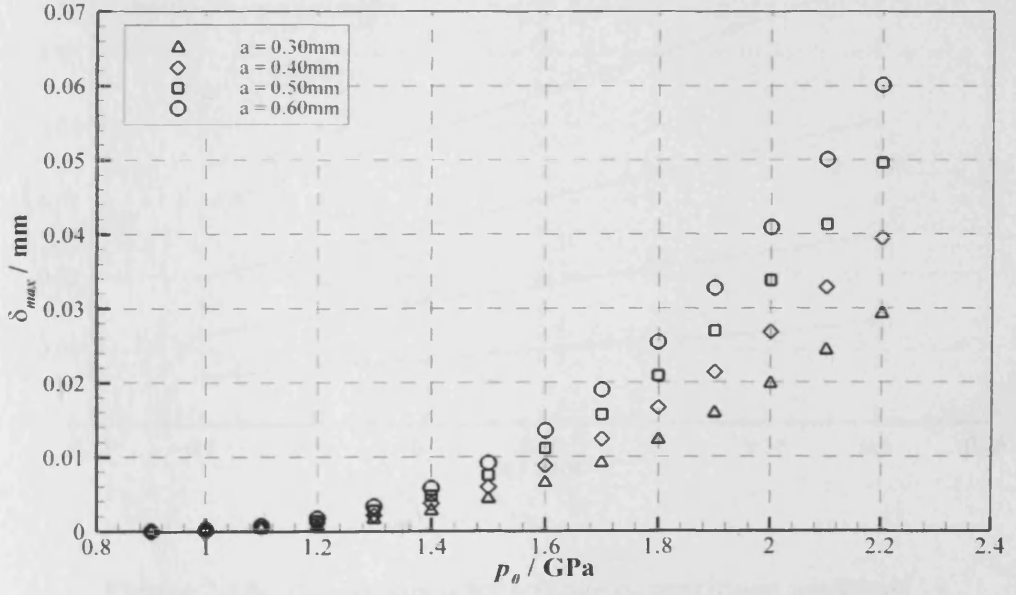

Figure 7.14: δ_{max} versus p_0 for a range of load widths (a)

Figure 7.14 shows that, for a given maximum pressure, p_0, a larger loaded width, a, gives a larger maximum permanent deformation, δ_{max}. For example, for p_0 = 2.2 GPa, the deformations are 0.0292mm for a = 0.3 mm; 0.0394 mm for a = 0.4 mm; 0.0496 mm for a = 0.5 mm; and 0.0601 mm for a = 0.6mm. From these results, it can be seen that, for a constant p_0, the deformation depends in a linear manner on the loaded width, a. Figure 7.15 shows a plot of δ_{max} against a for four of the maximum pressures, p_0, used in this work.

Thus, it can be seen that the maximum deformation, δ_{max}, may be non-dimensionalized by dividing it by the loaded width, a. This makes the four separate trends shown in Figure 7.14, for each loaded width, fall on one curve, as shown in Figure 7.16.

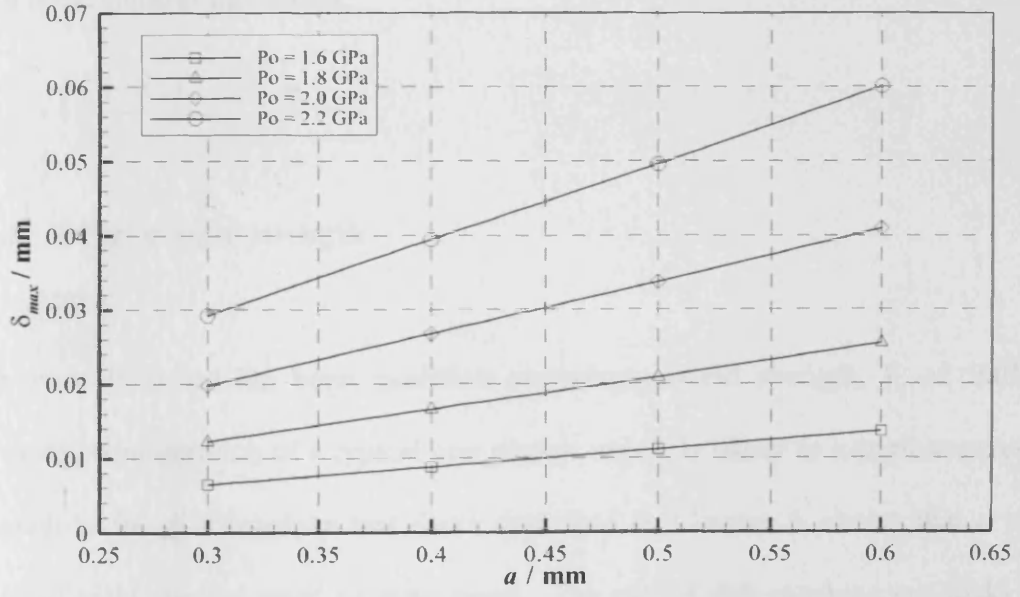

Figure 7.15: δ_{max} versus a for a range of maximum pressures

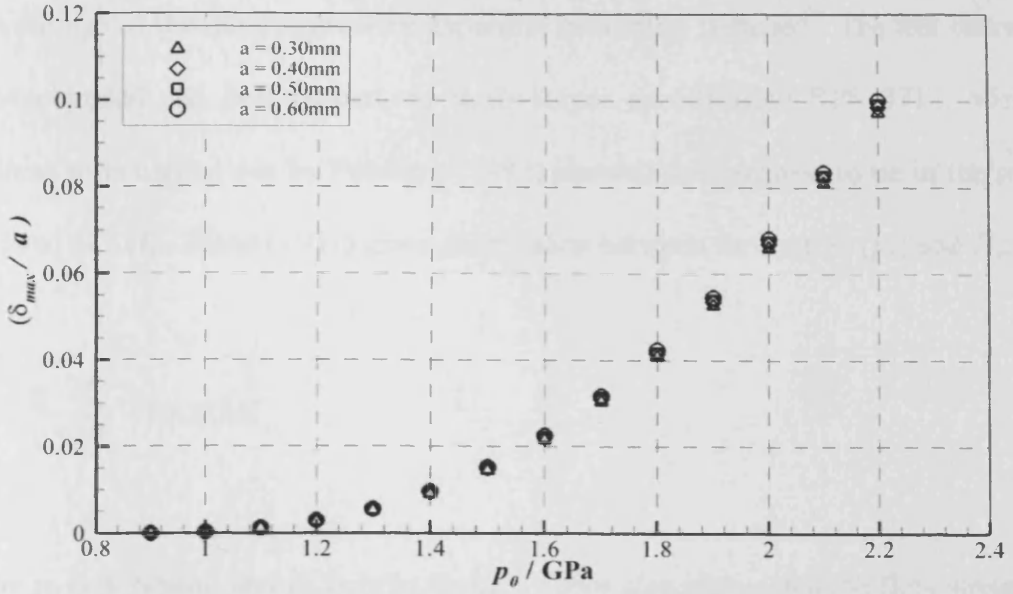

Figure 7.16: Non-dimensionalized permanent deformation, δ_{max}/a, versus p_0 for a range of loaded widths, a.

Thus, by using Figures 7.16 and 7.13, both the magnitude and shape of the permanent deformation caused by an applied load can be predicted, using these results obtained from finite element modelling.

7.4.5 Effect of yield strength

The work discussed has been modelled assuming a yield strength, Y, of 500MPa. However, consideration of a typical component which is likely to experience running in, such as the disk machine test disks described in Chapter 3, shows that a wider range of yield stresses must be considered. The use of disk machine test disks as a typical material is because the work of Davies (2005), who developed a method of measuring surface roughness profiles on test disks *in-situ* at various stages during a

running-in test. His results showed the evolution of the surface during running-in, with the tips of the most aggressive asperities becoming flattened. The test disks are case-carburised and heat treated, to Rolls-Royce specification RPS 371. Vickers hardness tests carried out by Patching (1992) showed the hardness to be in the range of 634 to 642 H_v. Tabor (1951) gives the relation between flow stress (p_p) and H_v:

$$p_p = \frac{g \cdot H_v}{0.927} = 10.583 H_v$$

where p_p is in N/mm^2 and H_v is in kgf/mm^2. Tabor also shows that the flow stress, p_p, is approximately 3 times the yield stress, Y. Thus, for the disk material, the yield stress is within the range of 2237 to 2265 MPa, and a typical value of Y = 2250MPa may be taken.

In order to investigate the effect of different yield strengths on the results, a number of additional analyses were carried out, using yield strengths of 1000MPa and 2000MPa, in addition to the data for Y=500 MPa already obtained. The values of Young's Modulus, E, and the plastic modulus, M, were left unchanged from the values described in section 7.4.3. The stress-strain curves used for this work can be seen in Figure 7.17.

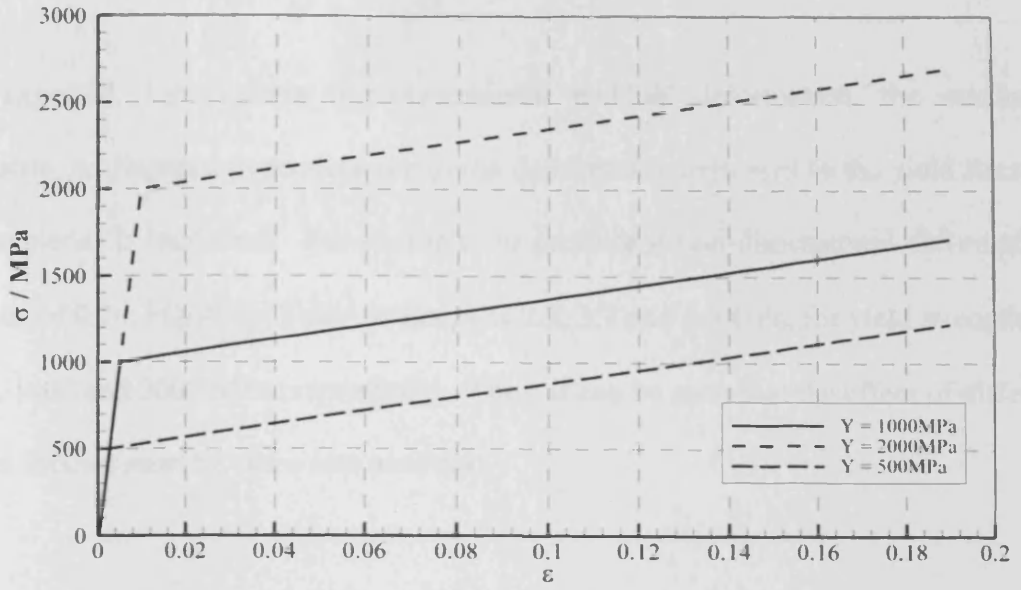

Figure 7.17: Stress – Strain curves for elastic-plastic material

Analyses were performed over a range of loads, with p_0 values between $1.8Y$ and $4.4Y$ (although in the case of Y = 2000 MPa the model failed due to excessive strains at values of p_0 above $3.6Y$). The results may be seen Figure 7.18.

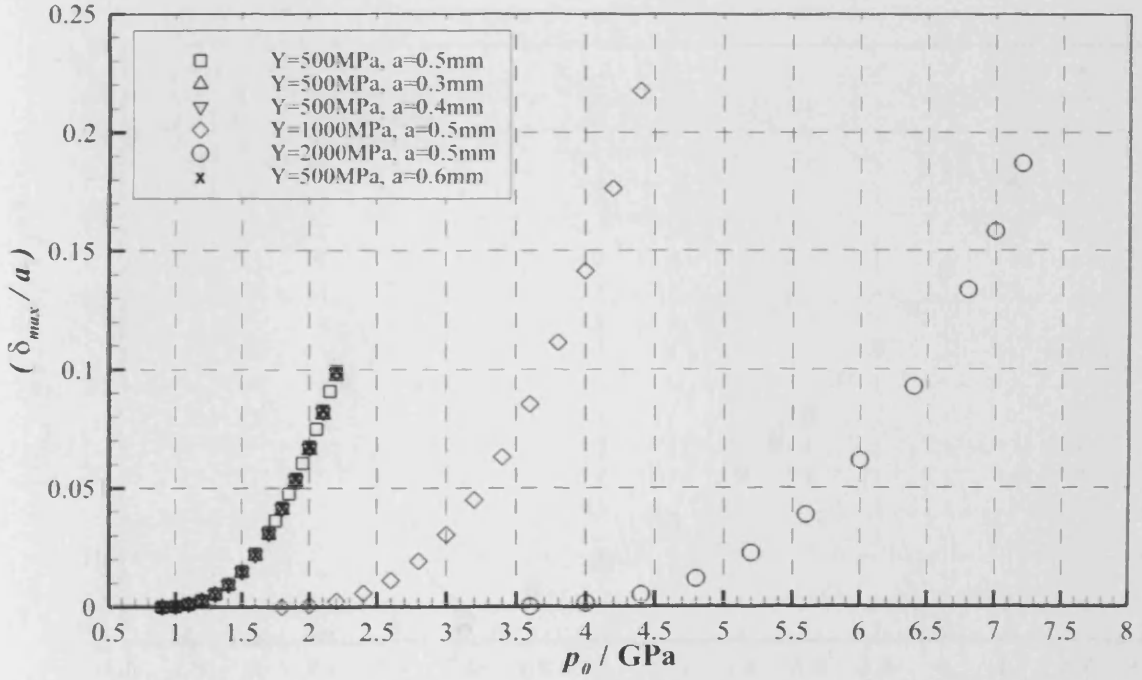

Figure 7.18: Magnitude of permanent deformation for Y = 500, 1000 & 2000 MPa

As expected, for a given non-dimensional residual deformation, the maximum pressure, p_0, required to produce the given deformation increases as the yield stress of the material is increased. For example, to produce a non-dimensional deformation, δ_{max}/a, of 0.10, Figure 7.18 shows that p_0 is 2.2, 3.7 and 6.5 GPa, for yield strengths of 500, 1000 and 2000 MPa respectively. Thus, it can be seen that the effect of different yield stresses must be taken into account.

To have separate functions to describe the relationship between (δ_{max}/a) and p_0 for a range of different yield strengths would make the incorporation of these results into an elastic-plastic hydrodynamic lubrication (EPHL) model more cumbersome, and the results have been combined into one trend, as shown in Figure 7.19. The value of the power of the (E / Y) term was obtained such that it gave the minimum deviation between the three data points at each (p_0 / Y) value.

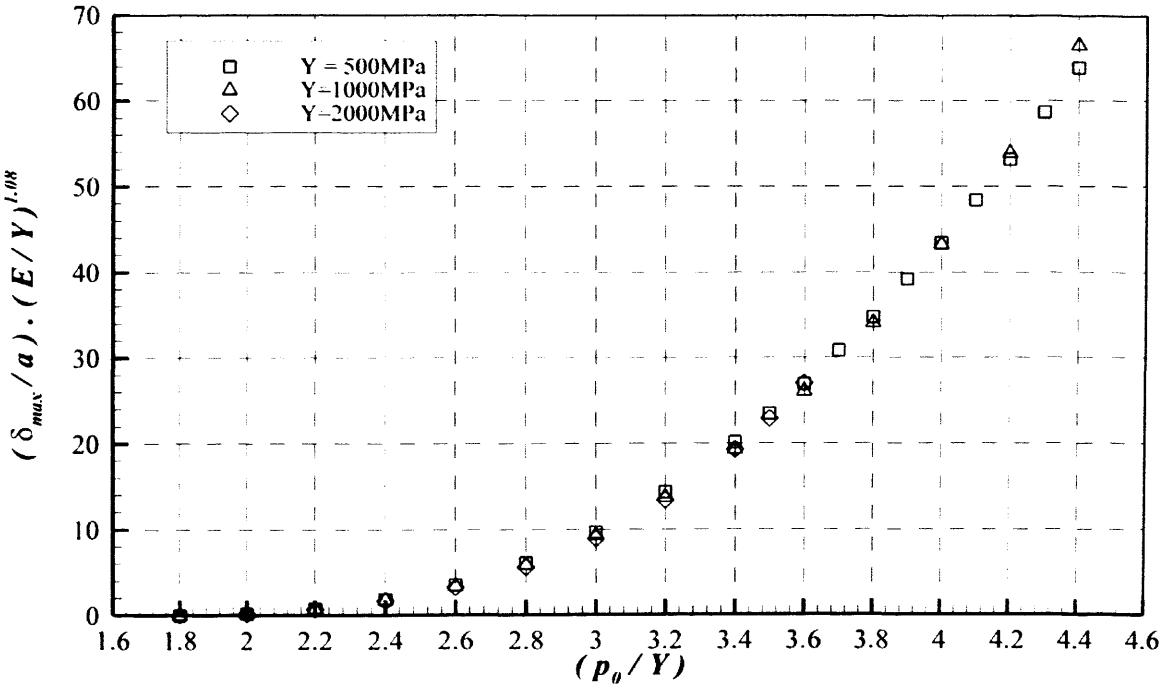

Figure 7.19: Maximum deformation results for a range of Yield Strengths

7.4.6 Analyses using measured material stress-strain curve

An alternative material model was also investigated, based on data published by Abudaia *et al.* (2005). They experimentally measured the yield strength of through-hardening steel specimens which were heat treated to give mechanical properties very similar to those of the case-carburised layer in the disk machine test disks, with a nominal yield strength of 2000 MPa and strain hardening properties. Figure 7.20 shows the measured stress-strain data.

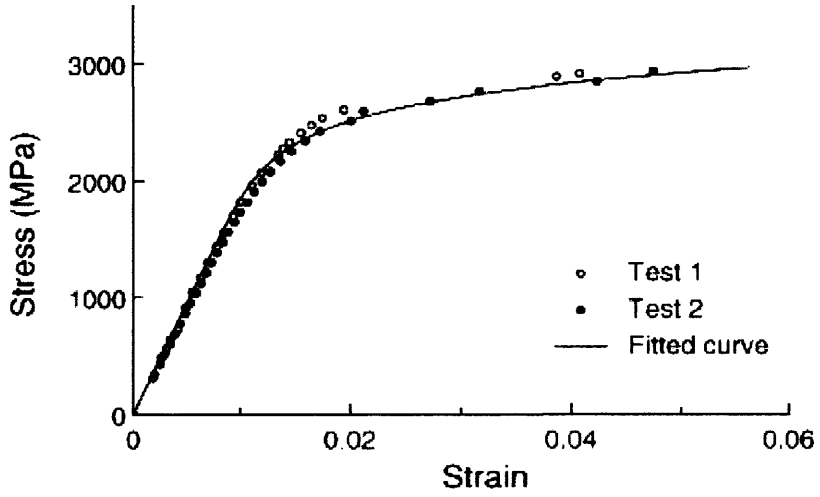

Figure 7.20: Measured stress-strain data for high strength steel from Abudaia *et al.* (2005)

In order to incorporate the stress-strain data into an elastic-plastic finite element model of indentation, Abudaia *et al.* fitted the data to the Ramberg-Osgood (1943) relation of the form:

$$\varepsilon = \frac{\sigma}{E} + \left(\frac{\sigma}{\sigma_1}\right)^N$$

where the constants were found to be σ_1 = 4060 MPa, N = 10.7 and E = 190 GPa in order to produce the fitted curve shown in Figure 7.20.

This relation was programmed into the ABAQUS finite element model, and a range of loading and unloading cycles at various maximum loads and contact widths were repeated with the revised material model. Contact widths (a) of 0.3mm, 0.4mm, 0.5mm and 0.6mm were investigated, with maximum values of p_0 from 3.6 GPa to 8.8 GPa (which represents p_0/Y ratios between 1.8 and 4.4) allowing for direct comparison with the results shown in section 7.4.5 for the constant-rate strain hardening material model.

The average non-dimensional shape of the residual deformation following loading is shown in Figure 7.21, compared to that previously calculated using the linear strain-hardening material model as described in section 7.4.5

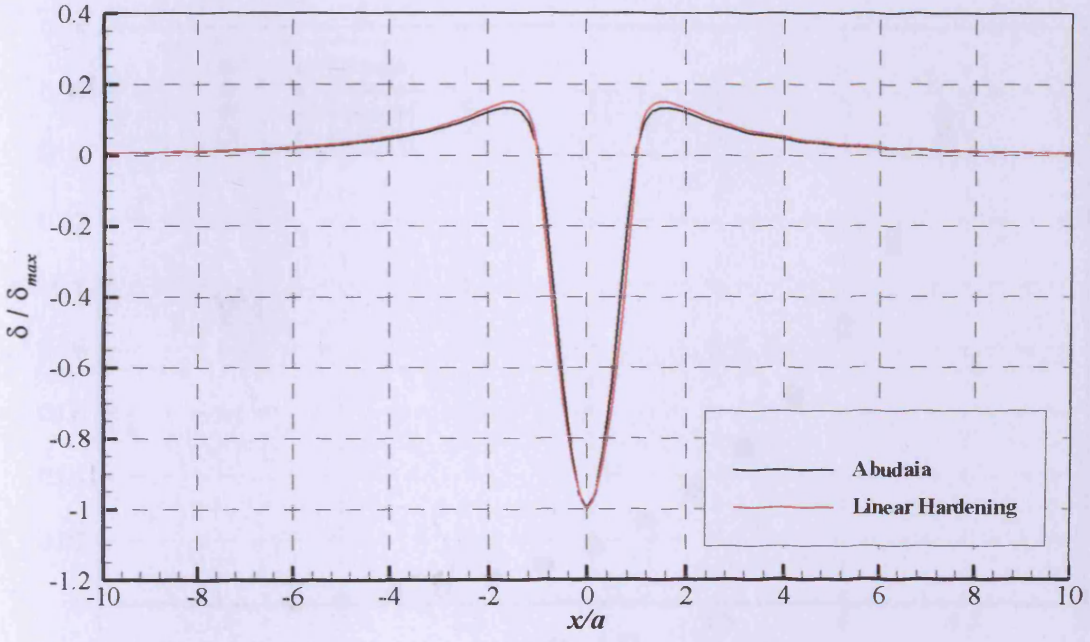

Figure 7.21: Comparison of residual deformation using Abudaia and Linear Hardening material models

Figure 7.21 shows that the analysis performed using the material data of Abudaia shows little difference in the deformed profile when compared to the previous work using a linear hardening model. When using the Abudaia model, there is a slight narrowing of the deformed shape in the region within the contact zone, i.e. $-1 < x/a < 1$, and a consequent reduction in the height of the "piled up" region immediately outside the contact zone. The maximum magnitude of the "piling up" decreases from $\delta / \delta_{max} = 0.151$ for the linear hardening model to $\delta / \delta_{max} = 0.134$ for the Abudaia model.

Figure 7.22 shows the non-dimensional maximum deflection, δ_{max} / a, obtained for four different contact dimensions using the Abudaia material model. The non-dimensionalisation method used for the results obtained using the linear hardening model also brings these results onto one single trend line.

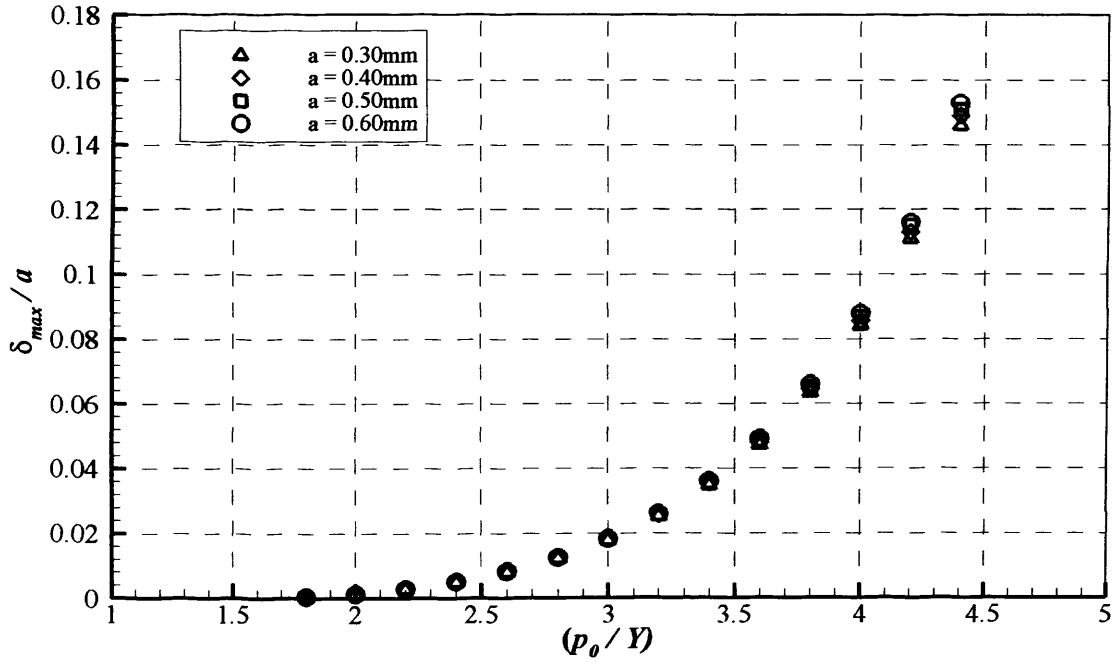

Figure 7.22: Non-dimensional maximum deflection using Abudaia material model

It is also interesting to compare the maximum deflection curve shown in Figure 7.22 with that shown in Figure 7.18, obtained using the linear hardening model with Y = 2000 MPa. These data are shown in Figure 7.23.

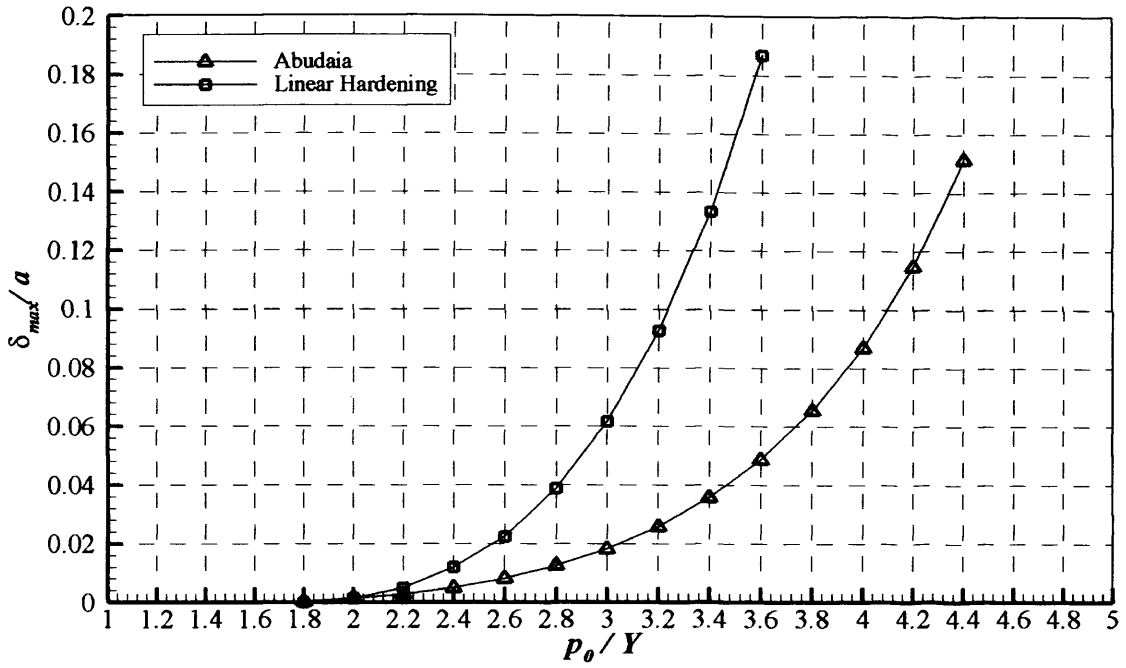

Figure 7.23: Comparison of non-dimensional deflection results from Linear Hardening model and Abudaia model

Figure 7.23 clearly shows that the results using the Abudaia material model predict lower residual deflections than those obtained using the linear hardening model. This is due to the higher levels of strain-hardening inherent in the Abudaia model than the linear hardening model. The linear hardening model represents an arbitrary material model with the same nominal yield strength as the Abudaia model, which more closely represents the typical surface material properties of engineered components such as the disk machine test disks.

7.5 Towards an EPHL model for real rough surfaces

It is envisaged that the relations between load and maximum deflection (represented by Figure 7.22 for the Abudaia material model) and the shape of the residual plastic deformation (represented by Figure 7.21 for the Abudaia material model) could be incorporated into an EHL solution in a similar manner to that of Xu *et al.* (1996), as described in Section 7.2.3. The use of the data shown in Figures 7.21 and 7.22 would replace the finite element analyses performed during the convergence procedure in Xu's model.

In order to incorporate the work presented here, it would be necessary within each time-step to identify asperities which experience pressures sufficient to cause yielding. Once each asperity has been identified, the micro-contact width (a) and pressure (p_0) may be estimated, and then used with the data in Figures 7.21 and 7.22 to estimate the magnitude and shape of the plastic deformation caused by this load. These data could then be used to modify the surface geometry, via the use of a suitable relaxation scheme. The time-step could then be re-converged with the modified geometry, and this process repeated iteratively until there was no change in the calculated plastic deformation.

Whilst the use of this proposed method does have inherent simplifications (such as an assumed Hertzian distribution of pressure at each asperity micro-contact), it is anticipated that it offers significant advantages in terms of speed of computation when compared to methods which perform finite element simulations during the convergence of each time step.

Conclusions and Future Work

8.1 Summary of Work

This thesis has been concerned with the investigation of the thermal behaviour of heavily loaded EHL contacts. Following an initial investigation using previously acquired experimental data a test rig was extensively modified and developed into a comprehensively instrumented tool for investigating the fundamental question of how the frictional heat generated at an EHL contact is divided between the two contacting surfaces. Using this rig, a test programme has been carried out which investigated a range of sliding speeds and loads using a synthetic gas turbine engine oil, Mobil Jet II. In parallel with the test programme a numerical model of heat conduction within the test disks was developed which uses experimental data as temperature boundary conditions in order to analyse the experimental results. This software was used to analyse the experimental results in order to calculate the division of heat between the disks.

However, during the experimental work the fast disk results were found to be inconsistent. This was reinforced upon numerical analysis of the fast disk results. There remains significant work to be carried out to eliminate these inconsistencies and further develop the method, and this is discussed in Section 8.2. Whilst the repeatable slow disk measurements have been analysed in this thesis and found to give consistent estimates of the heat partition, the availability of reliable fast disk data would allow an independent calculation of the heat partition to be carried out in order to validate the predictions reported here.

The findings of this work have been discussed throughout this thesis and published in three journal papers (Clarke *et al.*, 2006, 2007 and Evans *et al.*, 2009) and so, in the interests of brevity, these discussions will not be repeated here. This chapter therefore contains a discussion of proposed future work, together with a summary of the main conclusions.

8.2 Future Work – Heat Partition

As explained in Chapter 5, the fast disk temperatures proved to be unreliable. Tests were carried out during the experimental programme in an attempt to identify the source of this error. A number of repeat tests were carried out, including some in which the instrumentation connections were swapped such that the fast disk temperatures were being amplified and passed into the computer using the slow disk instrumentation and cabling, and *vice versa*. The results of these tests, in which the slow disk results remained consistent throughout, shows that the cause of the error is not the instrumentation or computer hardware, but has its origins in the slip rings or thermocouples and wiring within the test disk and shaft.

Due to the low level of thermocouple signals (in the mV range) they are very susceptible to electrical noise and spurious voltages distorting the signal. The thermocouple signals have to pass through the slip rings before they reach the amplifiers, and it would be logical to initially focus any investigation into the fast disk signal anomalies on the slip rings. Any noise and stray voltages being generated by the slip rings is likely to be proportional to their speed of rotation. Thus it may be

expected that the effect would be more significant on the fast shaft signals since the fast shaft rotates (for the slide/roll ratio used in this work) at over four times the slow shaft speed. In order to test the effect of the slip rings on the signal a test is proposed whereby a thermocouple (or thermocouples) is placed in a temperature-controlled water bath (or preferably a thermo-well if one could be obtained). The signal from the thermocouple would be wired to the stator brushes of one pair of slip ring channels. On the rotor connections (usually made to the disk thermocouple wires) a jumper connection would be made between two pairs of channels. The stator brushes of the second pair of channels would then be connected to the instrumentation system. A second thermocouple would be directly connected to the instrumentation system. This set-up could therefore be used with the test rig operating at various speeds to investigate the speed-related errors being introduced into the signal by the slip rings. As an alternative to the thermocouples, a precision voltage source could be used with a magnitude similar to the voltages produced by the thermocouples. Should problems be identified with the thermocouples, it would be necessary to consult the manufacturers in order to determine the likely cause and to identify potential solutions.

In the event that the slip rings are shown to be reliable, then the test disks should be replaced with a new pair with replacement thermocouples. Repeat runs of tests will quickly establish whether the new disks and thermocouples are producing reliable and repeatable fast disk results.

If the errors are found to be caused by the slip rings, it would be advisable to either eliminate the slip rings or increase the signal level such that the errors are no longer

significant. This could be achieved by mounting thermocouple amplifiers on the shafts so that high level (e.g. 0 – 5 V DC) signals are transmitted via the slip rings as opposed to the current low level (mV DC) signals. A number of miniature thermocouple amplifiers are now available, some of which are specifically designed to be mounted on rotating devices. For example, the AMP-TC thermocouple amplifier introduced in 2007 by Michigan Scientific (Michigan Scientific, 2007) is shown in Figure 8.1.

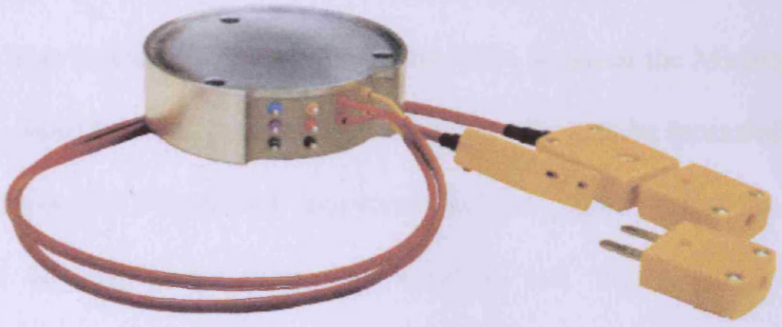

Figure 8.1: On shaft thermocouple amplifier (Michigan Scientific, 2007)

The unit is available with up to three thermocouple channels in the package shown in Figure 8.1, which is approximately 54 mm in diameter and 17mm in depth. It would be relatively straightforward to modify the existing rig to accommodate two such amplifiers on each shaft. The amplifiers also feature cold-junction compensation circuitry. They do not linearise the output (as the current 5B series amplifiers do) but this is easily achievable within the LabVIEW software. The manufacturers claim the units to be suitable for use with either grounded or isolated thermocouples (as currently installed in the test disks) and as such should not be susceptible to the grounding problems which occurred with the original thermocouple amplifiers used on the test rig. However, were these units to be used, careful discussions as to their suitability would be necessary with the manufacturers to avoid such issues. If

necessary, a separate amplifier could be used for each channel, each fed via the slip rings with a galvanically isolated power supply. This would necessitate the use of at least a 19-way slip ring to carry 6 separate DC feeds (12 channels as each 0V line is separate in such a system) plus 1 signal common and 6 signal channels. However, according to the data currently available in the manufacturer's documentation on the unit such a set-up is unlikely to be necessary and thus the power supply and signal wires could be accommodated easily on the existing 12 way slip ring unit (2 channels for power supply, plus 1 signal common and six signal channels). Other miniature amplifiers are also available, such as the Texys THA series or the Michigan Scientific AMP-TC-M1, which are sufficiently small to enable them to be mounted on the shaft, but the unit shown in Figure 8.1 represents in the author's view the neatest and simplest unit to incorporate into the existing test rig design. Preliminary investigations suggest that the two amplifier modules necessary to handle the six thermocouples on each shaft could be incorporated into the existing rig without the need for significant modifications.

A more complex, but potentially noise-immune system is that proposed by Azizi and Jalilian (2004), who developed a system mounted on rotating parts of large electric motors which converted signals from thermocouples mounted on the rotating components and transmitted them via a non-contact optical transmitter to a data acquisition system. However, it is suspected that the development of such a system could easily become the focus of a research project in itself! Alternatively, low-cost wireless thermocouples amplifiers are available which transmit the data via a Bluetooth link similar to that used in some mobile telephony to transmit data over short distances. The wireless amplifiers have a sufficiently low current draw to

enable them to be battery powered and it may be possible to mount such units on the rotating shafts of the test rig in order to completely eliminate the slip ring units.

However, the current rig design is somewhat limited in that the temperature gradients being measured are inherently rather small due to the close proximity of the two radial layers of thermocouples. The thermocouples were placed as far apart as was possible but this was limited by the desire to incorporate them into the standard design of test disk used on current scuffing test rigs at Cardiff. In addition, the disks feature a groove on one side (designed to allow disks to be engraved with a serial number). The disks are mounted against a deep shoulder and this, together with the retaining nut which clamps the disk against the shoulder, means that the insulating washers are only able to extend radially inwards beyond the inner layer of thermocouples by approximately 2mm. These conditions may be the cause of the asymmetry noted in the experimental results. A number of modifications are therefore proposed to the shafts to enable the fitting of much larger insulating washers and to increase the distance between the two layers of thermocouples. The disks are mounted on the shafts with a heavy press fit and, as such, the retaining nuts are only present as a backup. It is therefore proposed to re-design the shafts to include a much reduced shoulder height, together with a pressed on tubular spacer which fits between the disk and the drive-side shaft bearing to replace the retaining nut. The disks would also be re-designed to remove the groove. It would then be possible to fit full-height insulating washers to the disk faces and there would also be scope to move the inner layer of thermocouples radially towards the shaft centre-line, thereby increasing the difference between the measured temperatures. The proposed re-design of the shafts is shown in outline in Figure 8.2.

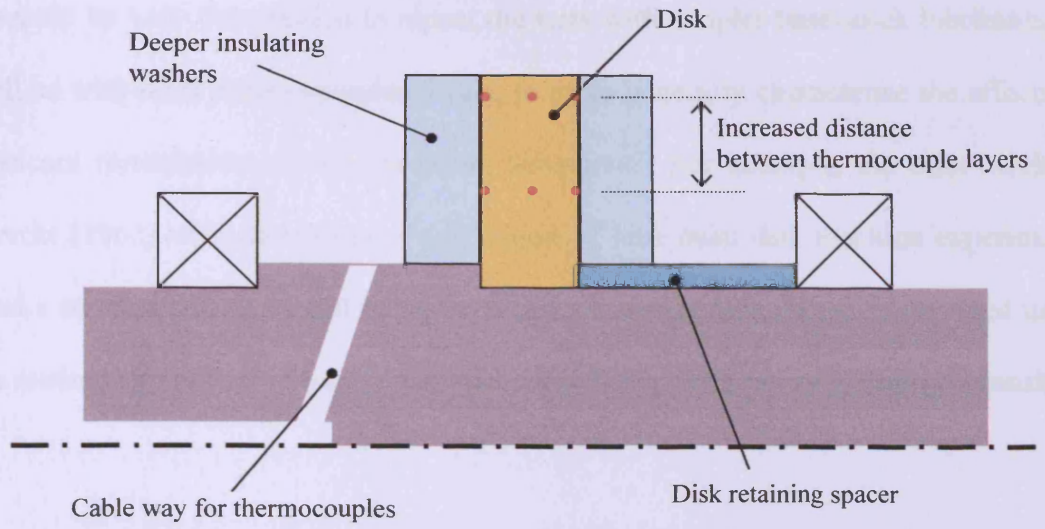

Figure 8.2: Proposed re-designed shaft and disk arrangements

Once the problems identified with the current test rig have been solved, the aim of a future work programme must be to:

1) Validate the current heat partition results with reliable independent slow and fast disk measurements.
2) Carry out tests over a wider range of slide-roll ratios with the current lubricating oil to establish whether the current observations as to β values are generally true or restricted to the particular operating conditions adopted.
3) Investigate other lubricants.

Point (3) of the proposed test programme is particularly interesting. The EHL analysis in Chapter 2 suggests that slipping of the lubricant at or near the fast surface is responsible for heat partition behaviour which favours the faster surface. However,

the lubricant used in these tests is a fully-formulated synthetic gas turbine engine oil. It would be very informative to repeat the tests with simpler base-stock lubricants, as well as with other fully-formulated oils, to more generally characterise the effects of lubricant formulation on heat partition behaviour. For example, the early work of Merritt (1962) who determined the partition of heat from disk machine experiments used a mineral oil. It would be interesting to compare measurements obtained using the methods presented in this thesis, with a similar mineral oil, with Merritt's results.

8.3 Future Work – Plastic Deformation

Chapter 7 presents an attempt to develop a simple characterisation of plastic deformation of a semi-infinite solid, in order to facilitate the development of an Elasto-Plastic Hydrodynamic Lubrication (EPHL) solver. Whilst the basic development of simple expressions for the residual deformation following loading beyond the yield point has been completed, much work remains to be done. Firstly, the effect of multiple cycles of loading needs to be quantified, as individual asperities within a surface will experience multiple loading cycles as they pass through the contact. The plastic deformation results then need to be incorporated into an existing EHL solver to allow EPHL analyses to be carried out. Suitable line and point contact solvers already exist within the Cardiff Tribology Group.

Once the solver has been developed, it would be useful to attempt to correlate the results with measurements such as those of Davies (2005) who took repeated measurements of surface profiles at various stages during the running in of ground

steel disks and was able to detect the flattening of asperity tips thought to be due to plastic deformation.

8.4 Summary of conclusions

- Heat partition is a more discerning measure of lubricant rheology within EHL films than friction.
- Extensive EHL modelling (Chapter 2) using currently available rheological and viscosity models has shown significant contradictions with heat partition behaviour deduced from experiments.
- In order to reproduce similar heat partition to that determined by the author's previous analysis of experimental data (Clarke *et.al.,* 2007), it is necessary to use a limiting shear stress rheological model together with the higher Barus viscosity. This rheological combination leads to slip within the film, which is taken to occur at the peak temperature position which is at or near the faster surface. Therefore, the distribution of shear heating across the film is not even, with high shear concentrated close to the faster surface. Such a shear distribution has been found to be necessary to reproduce the heat partition deduced from analysis of the experimental data
- A test rig has been developed (Chapter 3) to enable more detailed measurements to be made of the temperature distributions within test disks. This rig allows the measurement of six temperatures (at two different radial positions) within each test disk

- A series of tests (Chapter 5) has been carried out using a synthetic gas turbine engine oil over a range of sliding speeds between 10 and 20 m/s and at loads corresponding to a maximum Hertzian contact pressure of 1.6 GPa.
- The data obtained from the slow disk thermocouples have been shown to be repeatable and reliable, whereas there are some concerns over the accuracy of the measurements recorded from the fast disk thermocouples.
- A conduction analysis (chapters 4 and 6) of the results of these tests has been carried out, where the partition of heat between the disks and the level of convective cooling from the disk surface were adjusted to give an optimal agreement between model results and the experimental data.
- The analysis of the fast disk data gave inconsistent results, emphasizing the errors in the fast disk measurements.
- The conduction analysis of the slow disk data found that on average 40% of the total frictional heat dissipated at the contact has to pass into the slow disk in order to match most accurately the experimentally measured temperatures. By implication an average 60% of the frictional heating passes into the fast disk (although unfortunately the fast disk results are insufficiently reliable to provide independent corroboration of this).
- This finding is in agreement with both the author's previous findings (Clarke *et al.*, 2006) that approximately 60 to 70% of the frictional heat passes into the fast disk, and the early work of Merritt (1962).
- Provided that the problems with the fast disk measurements can be overcome, the combination of the thermal EHL modelling, a suitably instrumented disc machine and detailed heat partition analysis offers considerable promise as a means of studying the rheological and traction behaviour of lubricants in an

EHL contact. This approach has the potential to become a much more discerning experimental technique for comparing EHL rheological models than the conventional approach of simple friction measurement in EHL rolling/sliding contacts.

References

Abukhshim, N.A., Mativenga, P.T., Sheikh, M.A., 2005, "Investigation of heat partition in high speed turning of high strength alloy steel", *International Journal of Machine Tools and Manufacture*, v.45, pp. 1687-1695.

Abbott, E.J. and Firestone, F.A., 1933, "Specifying surface quality – a method based on accurate measurement and comparison", *Mech. Engr.*, v. 55, pp. 569.

Abudaia, F.B., Evans, J.T. & Shaw, B.A., 2005, "Spherical indentation fatigue cracking", *Materials Science and Engineering A*, v. 391, no. 1-2, pp. 181-187.

Archard, J.F., 1959, "The temperature of rubbing surfaces", *Wear*, v.2 part 6, pp. 438-455.

Azizi, H. & Jalilian, A., 2004, "Thermal monitoring of cage induction motor rotating parts", *Proceedings of 4th IEEE-GCC Conference*, pp. 308-311.

Bair, S., 2001, "The variation of viscosity with temperature and pressure for various real lubricants", *Trans. ASME Journal of Tribology*, v.123, pp. 433-436.

Bair, S., 2004, "Roelands' missing data", *Proc. IMechE: Part J Journal of Engineering Tribology*, v.218, pp. 57-60.

Bair, S. & Winer, W.O., 1979a, "A rheological model for elastohydrodynamic contacts based on primary laboratory data", *Trans. ASME Journal of Tribology*, v.101, pp. 258-265.

Bair, S. & Winer, W.O., 1979b, "Shear strength measurements of lubricants at high pressure", *Trans. ASME Journal of Lubrication Technology*, v.101, pp. 251-257.

Barber, J.R., 1967, "Distribution of heat between sliding surfaces", *Journal of Mechanical Engineering Science*, v.9, no.5, pp. 351-354.

Beghini, E., Dwyer-Joyce, R.S., Ioannides, E., Jacobson, B., Lubrecht, A.A. & Tripp, J.H., 1992, "Elastic/plastic contact and endurance life prediction", *J. Phys. D: Appl. Phys.*, v. 25, pp. 379-383.

Blok, H., 1937, "Theoretical study of temperature rises at surfaces of actual contact under oiliness conditions", *Proceedings of the IMechE – General discussion on lubrication 2*, pp. 222-235.

Blok, H., 1969, "Recent developments in gear tribology", *Proceedings of the IMechE*, v.184, pp. 21-29.

Bos, J. & Moes, H., 1995, "Frictional heating of tribological contacts", *Trans. ASME Journal of Tribology*, v.117, pp171-177.

Carslaw, H.S., & Jaeger, J.C., 1959, "Conduction of heat in solids", Oxford Press, Second Edition.

Challen, J.M.& Downson, D., 1978, "The calculation of interfacial temperatures in a pin-on-disc machine", *Proceedings of the 1978 Leeds-Lyon Conference*, IMechE, London, pp. 87-93.

Chang, L., 1992, "Traction in thermal elastohydrodynamic lubrication of rough surfaces", *Trans. ASME Journal of Tribology*, v.114, pp. 186-191.

Chang, W.R., Etsion, L., and Bogy, D.B., 1987, "An elastic-plastic model for the contact of rough surfaces", *Trans. ASME Journal of Tribology*, v. 109, pp. 263.

Cheng, H.S., 1965, "A refined solution to the thermal elastohydrodynamic lubrication of rolling and sliding cylinders", *Transactions of the ASLE*, v.8, pp. 397-410.

Clarke, A., Sharif, K.J., Evans, H.P., & Snidle, R.W., 2006, "Heat partition in rolling/sliding elastohydrodynamic contacts", *Trans. ASME Journal of Tribology*, v.128, pp. 67-78.

Clarke, A,. Sharif, K.J., Evans, H.P. Snidle, R.W., 2007, "Elastohydrodynamic modelling of heat partition in rolling-sliding point contacts", *Proc. Instn. Mech. Engrs Part J, Jn of Engng Tribology*, v. 221, pp. 223-235.

Corning Inc., MACOR Machinable Ceramic Datasheet, New York, no date.

Croft, D.R. and Stone, J.A.R., 1977, "Heat transfer calculations using finite difference equations", Sheffield Hallam University Press, Sheffield.

Davies, C.N., 2005, Effects of non-Newtonian rheology on the line contact elastohydrodynamic lubrication problem, PhD Thesis, Cardiff University.

Deolalikar, N., Sadeghi, F., & Marble, S., 2008, "Numerical modelling of mixed lubrication and flash temperature in EHL elliptical contacts", *Trans. ASME Journal of Tribology*, v.130.

Department of Education and Science, 1966, "Lubrication (Tribology) Education and Research. A Report on the Present Position and Industries' Needs", HMSO, London.

Dhulipalla, A.J., 2006, "Effect of surface finish and hard coatings on scuffing of steel disks", PhD Thesis, Cardiff University.

Dowson, D. and Higginson, G.R., 1959, "A numerical solution to the elastohydrodynamic problem", *Proceedings of the IMechE: Journal of Mechanical Engineering Science*, v.1, pp. 6-15.

Dowson, D., Higginson, G.R., & Whitaker, A.V., 1962, "Elastohydrodynamic lubrication: a survey of isothermal solutions", *Journal of Mechanical Engineering Science*, v.4, pp121 onwards.

Dowson, D. & Higginson, G.R., 1966, "Elastohydrodynamic lubrication", Pergammon Press.

Dowson, D., 1979, "History of Tribology", Longman Ltd.

Evans, H.P. & Hughes, T.G., 2000, "Evaluation of deflection in semi-infinite bodies by a differential deflection method", *Proc. IMechE : Part C Journal of Mechanical Engineering Science*, v.214, pp. 563-584.

Evans, H.P., Clarke, A., Sharif, K.J. & Snidle, R.W., 2009, "The role of heat partition in elastohydrodynamic lubrication", *Tribology Transactions*, in press.

Faulkner, A., & Arnell, R.D., 2000, "The development of a finite element model to simulate the sliding interaction between two, three-dimensional, elastoplastic, hemispherical asperities", *Wear*, v.242, pp. 114-122.

Freeth, T., *et.al.*, "Decoding the ancient Greek astronomical calculator known as the Antikythera Mechanism", *Nature*, v.444, pp. 587-591.

Gao, J., Lee, S.C., Ai, X., Nixon, H., 2000, "An FFT-based transient flash temperature model for general three-dimensional rough surface contacts", *Trans. ASME Journal of Tribology*, v.122, pp. 519-523.

Gohar, R., 2001, "Elastohydrodynamics", 2nd Edition, Imperial College Press.

Greenwood, J.A. and Williamson, J.B.P., 1966, "Contact of nominally flat surface", *Proc. Roy. Soc.,* London, Series A295, pp. 300-319.

Greenwood, J.A., 1991, "An interpolation formula for flash temperatures", *Wear*, v.150, pp. 153-158.

Grubin, A.N., 1949, "Investigation of the contact of machine components", Central Scientific Research Institute for Technology and Mechanical Engineering, Book No. 30, Moscow, DSIR Translation No 337.

Harpavat, G., 1974, "Frictional heating of a uniform finite thickness material rubbing against an elastomer", *Polymer Science and Technology*, pp. 205-221.

He, L., & Ovaert, T.C., 2008, "Heat partitioning coefficient calculations for sliding contacts with friction", *Tribology Transactions*, v.51:1, pp. 12-18.

Hertz, H., 1881, "On the contact of elastic solids", *J. reine und angew. Math.*, v.92, pp. 156-171.

Holmes, M.J.A., Evans, H.P., Hughes, T.G., Snidle, R.W., 2003, "Transient elastohydrodynamic point contact analysis using a new coupled differential deflection method: Parts 1 and 2", *Proc. IMechE: Part J Journal of Engineering Tribology*, v.217, pp. 289-321.

Horng, J.H., 1998, "An elliptic elastic-plastic asperity microcontact model for rough surfaces", *Trans. ASME Journal of Tribology*, v. 120, pp. 82-88.

Jackson, R.L. & Green, I., 2003, "A finite element study of elasto-plastic hemispherical contact", *Proceedings of 2003 STLE/ASME Joint International Tribology Conference.*

Jackson, R.L. & Green, I., 2003, "A statistical model of elasto-plastic asperity contact of rough surfaces", *Proceedings of 2003 STLE/ASME Joint International Tribology Conference.*

Jaeger, J.C., 1942, "Moving sources of heat and the temperature of sliding contacts", *Proceedings of the Royal Society of New South Wales*, v.76, pp. 203-224.

Jeng, Y.-R. & Wang, P.-Y., "An elliptical microcontact model considering elastic, elastoplastic, and plastic deformation", *Trans. ASME Journal of Tribology*, v. 125, pp. 232-240.

Johnson, K.L. & Tevaarwerk, J.L., 1977, "Shear behaviour of elastohydrodynamic oil films", *Proc. R. Soc. Lond. A.*, v.356, pp. 215-236.

Johnson, K.L., 1985, "Contact Mechanics", Cambridge University Press, Cambridge.

Kennedy, F.E., 1981, "Surface temperatures in sliding systems – a finite element analysis", *Trans. ASME Journal of Lubrication Technology*, v.103, pp. 90-96.

Kennedy, T.C., Plengsaard, C., & Harder, R.F., 2006, "Transient heat partition factor for a sliding railcar wheel", *Wear*, v.261, pp. 932-936.

Kim, K.H. and Sadeghi, F., 1991, "Non-Newtonian elastohydrodynamic lubrication of a pointcontact" *Trans ASME Jn of Tribology*, v.112, pp. 703-711.

Knoethe, K. & Liebelt, S., 1995, "Determination of temperatures for sliding contact with applications for wheel-rail systems", *Wear,* v.189, pp. 91-99.

Kogut, L. & Etsion, I., 2002, "Elastic-plastic contact analysis of a sphere and a rigid flat", *Trans. ASME Journal of Applied Mechanics*, v. 69, pp. 657-662.

Kogut, L., & Etsion, I., 2003, "A finite element based elastic-plastic model for the contact of rough surfaces", *Tribology Transactions*, v. 46, no.3, pp.383-390.

Kogut, L. & Etsion, I., 2004, "A static friction model for elastic-plastic contacting rough surfaces", *Trans. ASME Journal of Tribology*, v. 126, pp. 34-40.

Komvopoulos, K. & Ye, N., 2002, "Elastic-plastic finite element analysis for the head-disk interface with fractal topography description", *Trans. ASME Journal of Tribology*, v. 124, pp. 775-784.

Komanduri, R. & Hou, Z.B., 2001, "Analysis of heat partition and temperature distribution in sliding systems", *Wear*, v.251, pp. 925-938.

Krall, E.R., Komvopoulos, K. & Bogy, D.B., 1993, "Elastic-plastic finite element analysis of repeated indentation of a half-space by a rigid sphere", *Trans. ASME Journal of Applied Mechanics*, v. 60, pp. 829-841.

Krall, E.R., Komvopoulos, K. & Bogy, D.B., 1995a, "Finite element analysis of repeated indentation of an elastic-plastic layered medium by a rigid sphere, part 1: surface results", *Trans. ASME Journal of Applied Mechanics*, v. 62, pp. 20-28.

Krall, E.R., Komvopoulos, K. & Bogy, D.B., 1995b, "Finite element analysis of repeated indentation of an elastic-plastic layered medium by a rigid sphere, part 2: subsurface results", *Trans. ASME Journal of Applied Mechanics*, v. 62, pp. 29-42.

Kucharski, S., Klimczak, T., Polijaniuk, A. & Kaczmarek, J., 1994, "Finite-elements model for the contact of rough surfaces", *Wear*, v. 177, pp. 1-13.

Kuhlmann-Wilsdorf, D., 1987a, "Demistifying flash temperatures – 1. Analytical expressions based on a simple model", *Materials Science and Engineering*, v.93, pp. 107-117.

Kuhlmann-Wilsdorf, D., 1987b, "Temperatures at contact spots: dependence on velocity and on role reversal of two materials in sliding contact", *Trans. ASME Journal of Tribology*, v.109, pp. 321-329.

Labfacility Ltd, 2006, "The Temperature Handbook – a practical guide to temperature measurement", Middlesex.

Larsson, R., Larsson, P.O., Eriksson, E., Sjöberg, M. & Höglund, E., 2000, "Lubricant properties for input to hydrodynamic and elastohydrodynamic lubrication analyses", *Proc. IMechE: Part J Journal of Engineering Tribology*, v.214, pp. 17-27.

Larsson, R. & Andersson, O., 2000, "Lubricant thermal conductivity and heat capacity under high pressure", *Proc. IMechE: Part J Journal of Engineering Tribology*, v.214, pp. 337-342.

Lestyan, Z., Varadi, K., Albers, A., 2007, "Contact and thermal analysis of an alumina-steel dry sliding friction pair considering the surface roughness", *Tribology International*, v.40, pp. 982-994.

Liu, G., Zhu, J., Yu, L. and Wang, Q.J., 2001, "Elasto-plastic contact of rough surfaces", *Tribology Transactions*, v. 44, no. 3, pp. 437-443.

Liu, G., Liu, T. & Wang, Q.J., 2006, "An element-free Galerkin-finite element coupling method for elasto-plastic contact problems", *Trans. ASME Journal of Tribology*, v. 128, pp. 1-9.

Liu, Z., Neville, A. & Reuben, R.L., 2001, "Analyzing elastic-plastic real rough surface contact in running-in", *Tribology Transactions*, v. 44, no. 3, pp. 428-436.

Linck, V., Saulot, A., & Baillet, L., 2006, "Consequence of contact local kinematics of sliding bodies on the surface temperatures generated", *Tribology International*, v.39, pp. 1664-1673.

Lingard, S., 1984, "Estimation of flash temperatures in dry sliding", *Proceedings of the IMechE – Part C: Journal of Mechanical Engineering Science*, v.198, pp. 91-97.

Manton, S.M., O'Donoghue, J.P., & Cameron, A., 1967, "Temperatures at lubricated rolling/sliding contacts", *Proceedings of the Institution of Mechanical Engineers*, v.182, part 1, pp. 813-823.

Martin, H.M., 1916, "The lubrication of gear teeth", *Engineering*, v.102, pp. 199-204.

Mayeur, C., Sainsot, P. & Flamand, L., 1995, "A numerical elastoplastic model for rough contact", *Trans. ASME Journal of Tribology*, v. 117, pp. 422-429.

Merritt, H.E., 1962, "Gear tooth contact phenomena", *Proceedings of the Institution of Mechanical Engineers*, v.176, no.7, pp. 141-163.

Michigan Scientific, 2007, Product Brochure – "AMP-TC Thermocouple Rotating Amplifier".

Michigan Scientific, 2008, Technical Note 102B, "Thermocouples and thermocouple slip ring circuits".

Mobil Oil Corporation, 1979, "Mobil EHL Guide Book", Products Department, 150 East 42nd Street, New York.

Olver, A.V., 1991, "Testing transmission lubricants: the importance of thermal response", *Proceedings of the IMechE – Part G: Journal of Aerospace Engineering*, v.205, pp. 35-44.

Olver, A.V., 1994, "Thermal matching of tribological systems", in *Proceedings of the Twentieth Leeds-Lyon Symposium on Tribology* - "Dissipative processes in tribology", Elsevier, Amsterdam.

Olver, A.V. & Spikes, H.A., "Prediction of traction in elastohydrodynamic lubrication", *Proceedings of the IMechE: Part J – Journal of Engineering Tribology*, v.212, pp. 321-332.

Patching, M.J., 1994, "The effect of surface roughness on the micro-elastohydrodynamic lubrication and scuffing performance of aerospace gear tooth contacts", PhD thesis, University of Wales College of Cardiff.

Patching, M.J., Kweh, C.C., Evans, H.P., & Snidle, R.W., 1995, "Conditions for scuffing failure of ground and superfinished steel disks at high sliding speeds using a gas turbine engine oil", *Trans. ASME Journal of Tribology*, v.117, pp. 482-489.

Permabond Engineering Adhesives, ES550 Technical Information Sheet, no date.

Petrusevich, A.I., 1951, "Fundamental conclusions from the contact-hydrodynamic theory of lubrication", *Izv. Akad. Nauk. SSSR* (OTN). v.2, pp. 1-11 (MOD translation 293).

Powierza, Z.H., Klimczak, T., and Polijanniuk, A., 1992, "On the experimental verification of the Greenwood-Wiliamson model for the contact of rough surfaces", *Wear*, v. 154, pp. 115-124.

Prodan, D. & Diaconescu, E., 2003, "Theoretical and experimental investigations of an elasto-plastic circular contact bounded by real rough surfaces", *Proceedings of 2003 STLE/ASME Joint International Tribology Conference.*

Qiao, H, 2005, Prediction of contact fatigue for the rough surface elastohydrodynamic lubrication line contact problem under rolling and sliding conditions, PhD Thesis, Cardiff University.

Ramberg, W. & Osgood, W.R., 1943, "Description of stress-strain curves by three parameters", *Technical note no. 902*, National Advisory Committee for Aeronautics, Washington DC.

Reynolds, O., 1886, "On the theory of lubrication and its application to Mr Beauchamp Tower's experiments, including an experimental determination of the viscosity of olive oil", *Phil. Trans. R. Soc.*, v.177, pp. 157-234.

Roelands, C.J.A., 1966, "Correlation aspects of the viscosity-temperature-pressure relationship of lubricating oils", PhD Thesis, Technical University Delft, The Netherlands, published by V.R.B. Gronigen, The Netherlands.

Sadeghi, F. & Dow, T.A., 1987, "Thermal effects in rolling/sliding contacts: Part 2 – Analysis of thermal effects in fluid film", *Trans. ASME Journal of Tribology*, v.109, pp. 512-517.

Sadeghi, F. & Sui, P.C., 1990, "Thermal elastohydrodynamic lubrication of rolling/sliding contacts", *Trans. ASME Journal of Tribology*, v.112, pp. 189-195.

Salti, B. & Laraqi, N., 1999, "3-D numerical modelling of heat transfer between two sliding bodies: temperature and thermal contact resistance", *International Journal of Heat and Mass Transfer*, v.42, pp. 2363-2374.

Schofield, R.E. & Thornley, R.H., 1977, "The elastic and plastic components of deflection of model asperities in the shape of parabolic cusps", *Bulletin of the JSME*, v. 20, no. 146, pp. 1042-1050.

Sharif, K.J., Kong, S., Evans, H.P., & Snidle, R.W., 2001, "Contact and elastohydrodynamic analysis of worm gears – Part 1: Theoretical formulation", *Proceedings of the IMechE: Part C – Journal of Mechanical Engineering Science*, v.215, pp. 817-830.

Sharif, K.J., Morris, S.J., Evans, H.P. and Snidle, R.W., 2001, "Comparison of non-Newtonian EHL models in high sliding applications". *Proc. 27th Leeds-Lyon Symp. on Tribology, Lyon (2000)*, pp 787-796, Elsevier, Amsterdam.

Sharif, K.J., Evans, H.P., Snidle, R.W., Newall, J.P., 2004, "Modelling of film thickness and traction in a variable ratio traction drive rig", *Trans. ASME Journal of Tribology*, v.126, pp. 92-104.

Sharif, K.J., 2008, *Private Communication.*

Ståhl, J. & Jacobson, B.O., 2003, "A lubricant model considering wall-slip in EHL line contacts", *Trans. ASME Journal of Tribology*, v.125, pp. 523-532.

Snidle, R.W. and Evans, H.P., 1990, "Thermal distress-related failure of high speed gearing", University of Wales College of Cardiff, Division of Mechanical Engineering and Energy Studies, Report No. 1621.

Sui, P.C. & Sadeghi, F., 1991, "Non-Newtonian thermal elastohydrodynamic lubrication", *Trans. ASME Journal of Tribology*, v.113, pp. 390-397.

Tabor, D., 1951, "The Hardness of Metals", Oxford University Press, Oxford.

Tao, Q., Lee, H.P. & Lim, S.P., 2001, "Contact mechanics of surfaces with various models of roughness descriptions", *Wear*, v. 249, pp. 539-545.

Tian, X. & Kennedy, F.E., 1993, "Contact surface temperature models for finite bodies in dry and boundary lubricated sliding", *Trans. ASME Journal of Tribology*, v.115, pp. 411-418.

Tian, X. & Kennedy, F.E., 1994, "Maximum and average flash temperatures in sliding contacts", *Trans. ASME Journal of Tribology*, v.116, pp. 167-174.

Tower, B., 1883, "First report on friction experiments (friction of lubricated bearings)", *Proceedings of the IMechE*, November 1883, pp. 632-659.

Tower, B., 1885, "Second report on friction experiments (experiments on the oil pressure in a bearing)", *Proceedings of the IMechE*, January 1885, pp. 58-70.

Tudor, A., & Khonsari, M.M., 2006, "Analysis of heat partitioning in wheel/rail and wheel/brake shoe friction contact: an analytical approach", *Tribology Transactions*, v.49, pp. 635-642.

Varadi, K., Neder, Z., Friedrich, K., Flock, J., 1998, "Numerical and finite element contact temperature analysis of real composite-steel surfaces in sliding contact", *Tribology International*, v.31, no.11, pp. 669-686.

Venner, C. H. and Lubrecht, A. A., 1994, "Numerical simulation of a transverse ridge in a circular EHL contact under rolling/sliding". *Trans. ASME, J. Tribology*, v. 116, pp. 751-761.

Vick, B. & Furey, M.J., 2001, "A basic theoretical study of the temperature rise in sliding contact with multiple contacts", *Tribology International*, v.34, pp. 823-829.

Wang, S.H. & Zhang, H.H., 1987, "Combined effects of thermal and non-Newtonian character of lubricant on pressure, film profile, temperature rise, and shear stress in EHL", *Trans. ASME Journal of Tribology*, v.109, pp. 667-670.

Wolff, R., Nonaka, T., Kubo, A., & Matsuo, K., 1992, "Thermal elastohydrodynamic lubrication of rolling/sliding line contacts", *Trans. ASME Journal of Tribology*, v.114, pp. 706-713.

Xu, G., Nickel, D.A., Sadeghi, F. & Ai, X., 1996, "Elastoplastohydrodynamic lubrication with dent effects", *Proc. IMechE Part J: Journal of Engineering Tribology*, v. 210, pp. 233-245.

Xuesheng, C., Qin, Y. & Balendra, R., 2004, "Development of a statistical parameter-based surface model for the simulation of variation of surface roughness with contact pressure", *Journal of Materials Processing Technology*, v. 145, pp. 247-255.

Yasutomi, S., Bair, S., & Winer, W.O., 1984, "An application of a free volume model to lubricant rheology", *Trans. ASME Journal of Tribology*, v.106, no.2, pp. 291-303.

Yevtushenko, A., Ukhanska, O., Chapovska, R., 1996, "Friction heat distribution between a stationary pin and a rotating disc", *Wear*, v.196, pp. 219-225.

Zhang, H., Chang, L., Webster, M.N. & Jackson, A., 2003, "Effects of friction on the contact and deformation behaviour in sliding asperity contacts", *Tribology Transactions*, v. 46, no.4, pp. 514-521.

Zhao, Y., Maietta, D.M. & Chang, L., "An asperity microcontact model incorporating the transition from elastic deformation to fully plastic flow", *Trans. ASME Journal of Tribology*, v. 122, pp. 86-93.

Zhu, D., & Hu, Y., 2001, "A computer program package for the prediction of EHL and mixed lubrication characteristics, friction, subsurface stresses and flash temperatures based on measured 3-D surface roughness", *Tribology Transactions*, v.44, pp. 383-390.

Appendix A

Corning Inc. Brochure

Macor Machinable Ceramic

Corning Incorporated
Lighting & Materials
Houghton Park CB-08
Corning, New York 14831
tel: 607-974-4331
fax: 607-974-7618

www.corning.com
e-mail: lmacor@corning.com

MACOR 01

Printed in the U.S.A.

MACOR®

CORNING
Discovering Beyond Imagination

Lighting &
Materials

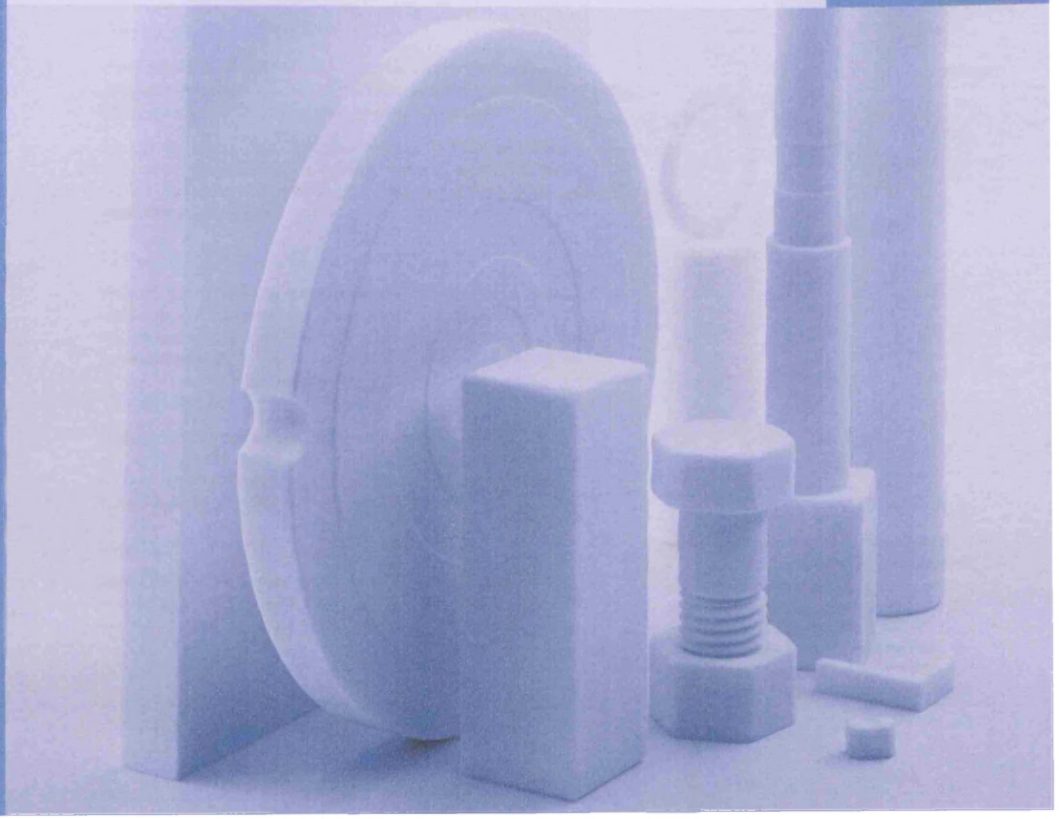

MACOR®
Machinable Glass Ceramic

- is MACHINABLE with ordinary metal working tools
- allows FAST TURNAROUND, no post firing required
- holds TIGHT TOLERANCES, up to .0005"
- withstands HIGH TEMPERATURE, up to 1000°C (no load)
- is CLEAN, no outgasing and zero porosity

With MACOR® Machinable Glass Ceramic (MGC), fabrication is fast because it can be machined into complicated shapes and precision parts with ordinary metal working tools, quickly and inexpensively, and it requires no post firing after machining. That means no frustrating delays, no expensive hardware, no post fabrication shrinkage, and no costly diamond tools to meet specifications.

Properties

MACOR® Machinable Glass Ceramic has a continuous use temperature of 800°C and a peak temperature of 1000°C. Its coefficient of thermal expansion readily matches most metals and sealing glasses. It is nonwetting, exhibits zero porosity, and unlike ductile materials, won't deform. It is an excellent insulator at high voltages, various frequencies, and high temperatures. When properly baked out, it won't outgas in vacuum environments.

Machining

Machining tolerances are surprisingly tight, up to .0005". It can be machined to a surface finish of less than 20µin. and polished to a smoothness of 0.5µin.-AA. Configurations are limited only by available equipment and the experience of the machinist.

Sealing, Joining and Metalizing

MACOR MGC can also be joined or sealed - both to itself and to other materials - in a number of ways: metalized parts can be soldered together and brazing has proven an effective method of joining the material to various metals; epoxy produces a strong joint, and sealing glass creates a vacuum tight seal. Even a straight-forward mechanical joint is possible.

It can be thick film metalized using metal inks, or thin film metalized by sputtering.

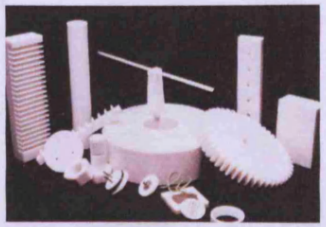

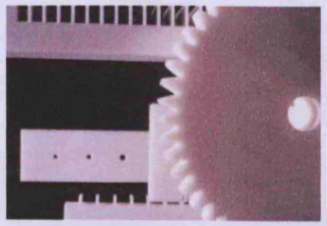

Applications

Ultra-High Vacuum Environments

MACOR® Machinable Glass Ceramic is used as an insulator or coil support and for vacuum feed-throughs. In these applications, the conductive materials are supported by the MACOR MGC part and a compatible sealing glass is used to produce a vacuum-tight, hermetic seal.

Constant Vacuum Applications

MACOR MGC parts are found in spacers, headers and windows for microwave tube devices and as sample holders in field ion microscopes.

Aerospace Industry

Over 200 distinctly shaped MACOR MGC parts can be found on America's reusable Space Shuttle Orbiter. Retaining rings of MACOR MGC are used at all hinge points, windows and doors.

Also, large pieces of MACOR glass ceramic are used in a NASA spaceborne gamma radiation detector. For this application, frame corners are joined by a combination of machined (butt-lap) mechanical joints and a sealing glass.

Nuclear-Related Experiments

Since MACOR MGC is not dimensionally affected by irradiation, small cubes of the material are machined to a tolerance of one micron and used as a reference piece to measure dimensional change in other materials.

Welding Nozzles

Welding equipment manufacturers are using MACOR MGC as a nozzle on the tips of oxyacetylene torches. The material's nonwetting characteristic means molten particles won't adhere to and decrease the effectiveness of the nozzle.

Fixtures

MACOR MGC is used as an electrode support and burner block in several industrial high heat, electrical cutting operations due to its low thermal conductivity and excellent electrical properties.

Medical Equipment

Producers of medical components are intrigued by MACOR MGC's inertness, precise machinability and dimensional stability.

The Point is this:

When you need the performance of a technical ceramic (high use temperature, electrical resistivity, zero porosity) and your application demands the ready fabrication of a complicated shape (quickly, precisely, privately), look at MACOR MGC. It will lower costs and substantially reduce the time between design and actual use.

Properties

I. Thermal

	SI/Metric	English
Coefficient of Expansion		
-200 - 25°C	$74x10^{-7}$/°C	$41x10^{-7}$/°F
25 - 300°C	$93x10^{-7}$/°C	$52x10^{-7}$/°F
25 - 600°C	$114x10^{-7}$/°C	$63x10^{-7}$/°F
25 - 800°C	$126x10^{-7}$/°C	$70x10^{-7}$/°F
Specific Heat, 25°C	.79 KJ/kg°C	0.19 Btu/lb°F
Thermal Conductivity, 25°C	1.46 W/m°C	10.16 $\frac{\text{Btu in}}{\text{hr ft}^2\text{°F}}$
Thermal Diffusivity, 25°C	$7.3x10^{-7}m^2/s$	0.028 ft^2/hr
Continuous Operating Temperature	800°C	1472°F
Maximum No Load Temperature	1000°C	1832°F

II. Mechanical

	SI/Metric	English
Density	2.52 g/cm^3	157 lbs/ft^3
Porosity	0%	0%
Young's Modulus, 25°C (Modulus of Elasticity)	66.9 GPa	$9.7x10^6$psi
Poisson's Ratio	0.29	0.29
Shear Modulus, 25°C	25.5GPa	$3.7x10^6$psi
Hardness, Knopp, 100g	250	250
Rockwell A	48	48
Modulus of Rupture, 25°C (Flexural Strength)	94 MPa (minimum specified average value)	13,600 psi
Compressive strength	345 MPa	50,000 psi
Fracture Toughness	1.53 MPa $m^{0.5}$	1,390 psi $in^{0.5}$

III. Electrical

	SI/Metric	English
Dielectric Constant, 25°C		
1 KHz	6.03	6.03
8.5 GHz	5.67	5.67
Loss Tangent, 25°C		
1 KHz	$4.7x10^{-3}$	$4.7x10^{-3}$
8.5 GHz	$7.1x10^{-3}$	$7.1x10^{-3}$
Dielectric Strength (AC) avg. (at 12 mil thickness and 25°C)	9.4 KV/mm	785 V/mil
Dielectric Strength (DC) avg. (at 12 mil thickness and 25°C)	62.4 KV/mm	5206 V/mil
DC Volume Resistivity, 25°C	$>10^{16}$ ohm-cm	$>10^{16}$ ohm-cm

IV. Chemical

	Tests			Results
				Weight Loss (mg/cm^2)
Solution	pH	Time	Temp.	Gravimetric
5% HCL (Hydrochloric Acid)	0.1	24 hrs.	95°C	~ 100
0.002 N HNO_3 (Nitric Acid)	2.8	24 hrs.	95°C	~ 0.6
0.1 N $NaHCO_3$ (Sodium Bicarbonate)	8.4	24 hrs.	95°C	~ 0.3
0.02 N Na_2CO_3 (Sodium Carbonate)	10.9	6 hrs.	95°C	~ 0.1
5% NaOH (Sodium Hydroxide)	13.2	6 hrs.	95°C	~ 10
Resistance to water over time				
H_2O	7.6	1 day*	95°C	0.01
		3 days*	95°C	0.07
		7 days*	95°C	9.4
		3 days**	95°C	0.06
		6 days**	95°C	0.11

*Water not freshened daily
**Water freshened daily

Technical Data

The general characteristics of this material described below were derived from laboratory tests performed by Corning from time to time on sample quantities. Actual characteristics of production lots may vary.

Modulus of Rupture

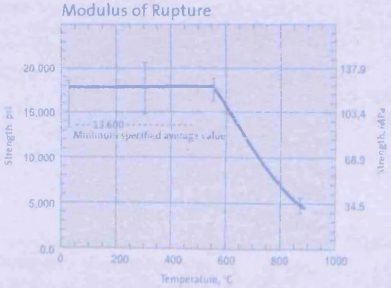

Thermal Expansion

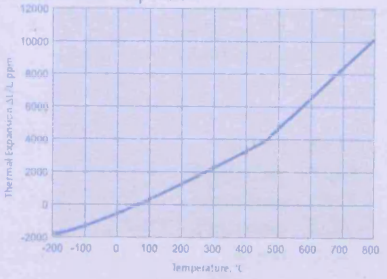

DC Volume Resistivity

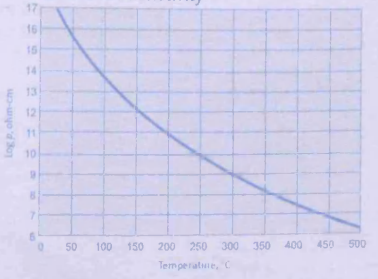

Thermal Conductivity

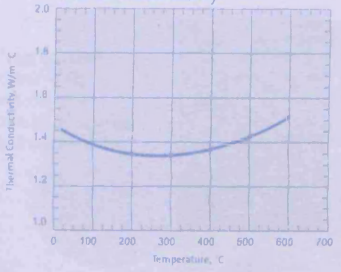

Dielectric Constant

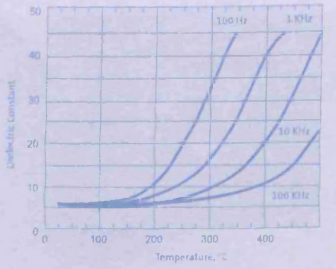

Young's Modulus

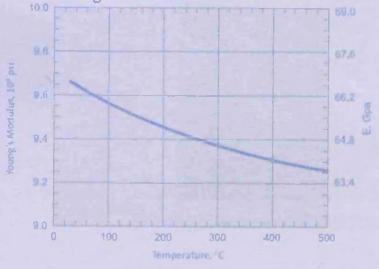

Loss Tangent

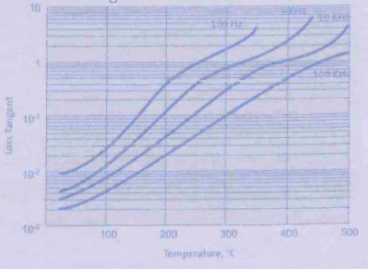

Machining

Key factors for successful machining are proper machining speeds and coolant.

MACOR Machinable Glass Ceramic can be machined with high speed steel tools, but carbide tools are recommended for longer wear.

Achieve the best results by using a water-soluble coolant, such as Cimstar 40 - Pink, especially formulated for cutting and grinding glass or ceramics.

No post firing is required after machining.

Grinding

Diamond, silicon-carbide or aluminum-oxide grinding wheels can be used.

Polishing

Start with loose 400-grit silicon carbide on a steel wheel. For the final polish, use cerium oxide or alumina on a polishing pad for glass or ceramics. A 0.5µin.-AA finish can be achieved.

Sawing

Use a carbide grit blade at a band speed of 100 fpm. An alternative is a silicon carbide or diamond cut-off wheel.

Turning

Cutting speed	30-50 sfm
Feed rate	.002-.005 ipr
Depth of cut	.150-.250 in.

Milling

Cutting speed	20-35 sfm
Chip load	.002 ipt
Depth of cut	.150-.200 in.

Drilling

Drill size	Spindle Speed	Feed Rate
1/4 in.	300 rpm	.005 ipr
1/2	250	.007
3/4	200	.010
1	100	.012
2	50	.015

Allow at least .050" of extra material on the back side for breakout. This excess can be removed after drilling.

Tapping

Make clearance holes one size larger than those recommended for metals. Chamfer both ends of the hole to reduce chipping. Run the tap in one direction only. (Turning the tap back and forth can cause chipping.) Continuously flush with water or coolant to clear chips and dust from the tap.

Composition

MACOR Machinable Glass Ceramic is a white, odorless, porcelain-like (in appearance) material composed of approximately 55% fluorophlogopite mica and 45% borosilicate glass. It has no known toxic effects; however, the dust created in machining can be an irritant. This irritation can be avoided by good housekeeping and appropriate machining techniques. The material contains the following compounds:

	Approximate Weight %
Silicon - SiO_2	46%
Magnesium - MgO	17%
Aluminum - Al_2O_3	16%
Potassium - K_2O	10%
Boron - B_2O_3	7%
Fluorine - F	4%

Randomly oriented mica flakes in the microstructure of MACOR MGC are the key to its machinability.

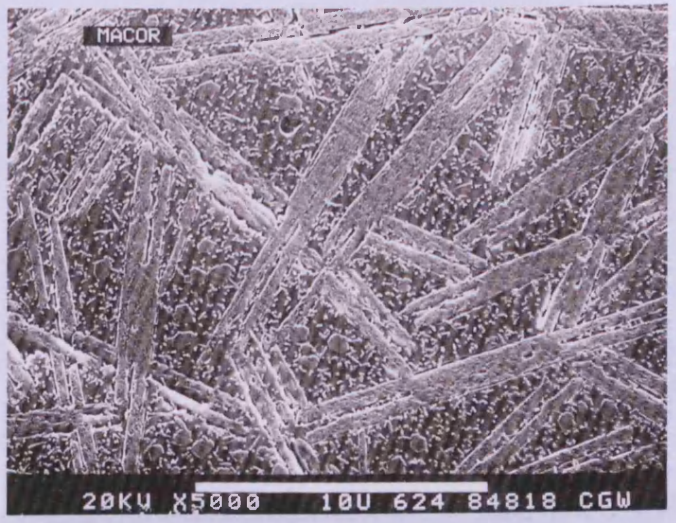

Microstructure of MACOR MGC 5000X magnification.

Appendix B

Michigan Scientific Technical Note 102-B

Thermocouples and thermocouple slip ring circuits

Technical Note No. 102-B

THERMOCOUPLES AND THERMOCOUPLE SLIP RING CIRCUITS

A simple thermocouple circuit is shown in Figure 1.

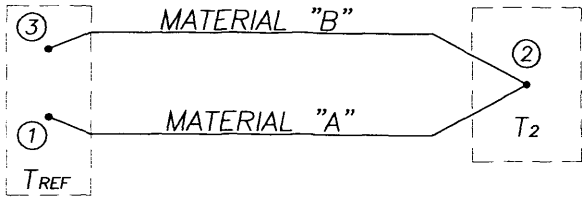

Figure 1. Simple thermocouple circuit.

Let points **1** and **3** be thermally integrated i.e. the temperature at point **1** always equals the temperature at point **3** and let this temperature equal T_{ref}. If the temperature at point **2** does not equal the reference temperature ($T_2 \neq T_{ref}$), there is an end-to-end voltage or electromotive force (EMF) generated along the length of material "A" wire and another end-to-end EMF generated along the length of material "B" wire. The magnitude of the end-to-end EMF generated is a function of the temperature difference between the ends of the wire, or stated another way, is a function of the integrated temperature gradient along the entire length of wire. EMFs are not generated at wire junctions; they are generated along the lengths of the wires.

By algebraically summing voltages, the EMF between **1** and **3** is equal to the EMF from **1** to **2** plus the EMF from **2** to **3**. Therefore the magnitude of the EMF developed between points **1** and **3** is a function of the temperature at point **2**. Hence, the connection or junction of the two thermocouple wires at point **2** defines a location of where temperature can be sensed as well as serving to complete the electrical circuit.

Figure 2 shows the EMF versus temperature behavior of several common thermocouple materials with reference to platinum. Note that the two materials used to make a thermocouple type (e.g. K-type, J-type, etc.) are those that exhibit a "large" mutual divergence.

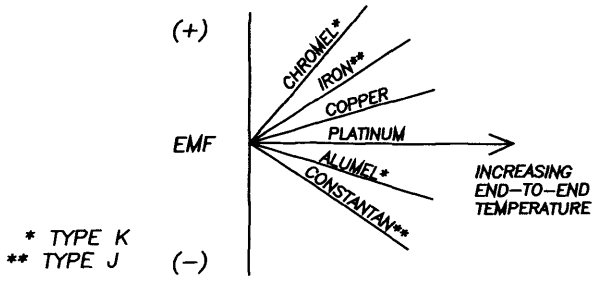

Figure 2. EMF vs. temperature for various materials.

8500 Ance Road
Charlevoix, MI 49720
Tel: 231-547-5511
Fax: 231-547-7070

MICHIGAN SCIENTIFIC corporation

http://www.michsci.com
E-mail: mscinfo@michsci.com

321 East Huron Street
Milford, MI 48381
Tel: 248-685-3939
Fax: 248-684-5406

Technical Note No. 102-B

The EMF versus temperature plot of the circuit depicted in Figure 1 for a K-type thermocouple is shown in Figure 3.

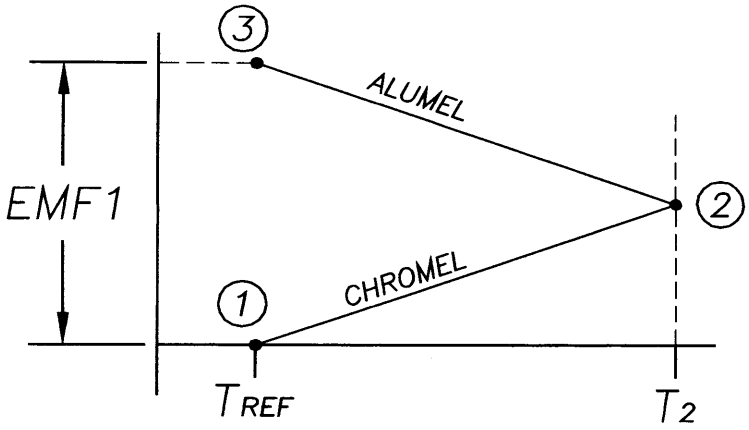

Figure 3. EMF vs. temperature for K-type T/C circuit of Figure 1.

As we have seen, the EMFs generated are dependent upon the *differences* of temperature, so we need to know the temperature of points **1** and **3** in order to measure the temperature at point **2**. Furthermore, we need a means of connecting points **1** and **3** to a readout device (e.g. a voltmeter) and the leadwires to this device will introduce another material (e.g. copper) that is subject to thermal EMF generation.

Figure 4 shows the circuit of Figure 1 using K-type thermocouple materials but now includes a readout device with copper leadwires and a reference temperature zone held at T_{ref}. The EMF versus temperature plot for this arrangement is shown in figure 5.

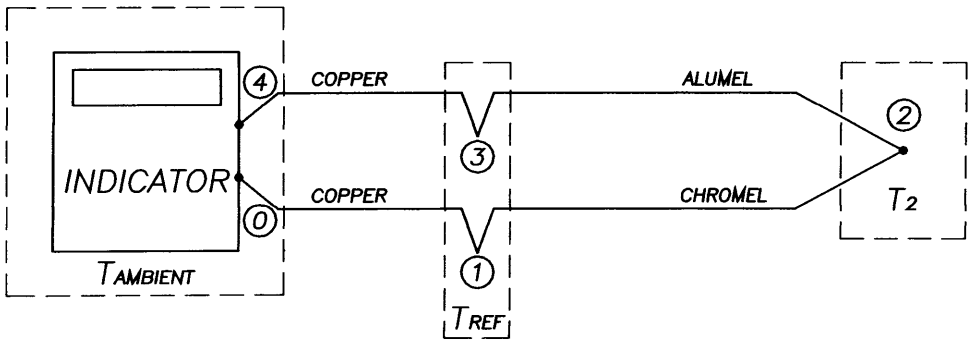

Figure 4. Simple K-type thermocouple circuit with indicator and temperature reference.

8500 Ance Road
Charlevoix, MI 49720
Tel: 231-547-5511
Fax: 231-547-7070

MICHIGAN SCIENTIFIC corporation

http://www.michsci.com
E-mail: mscinfo@michsci.com

321 East Huron Street
Milford, MI 48381
Tel: 248-685-3939
Fax: 248-684-5406

Technical Note No. 102-B

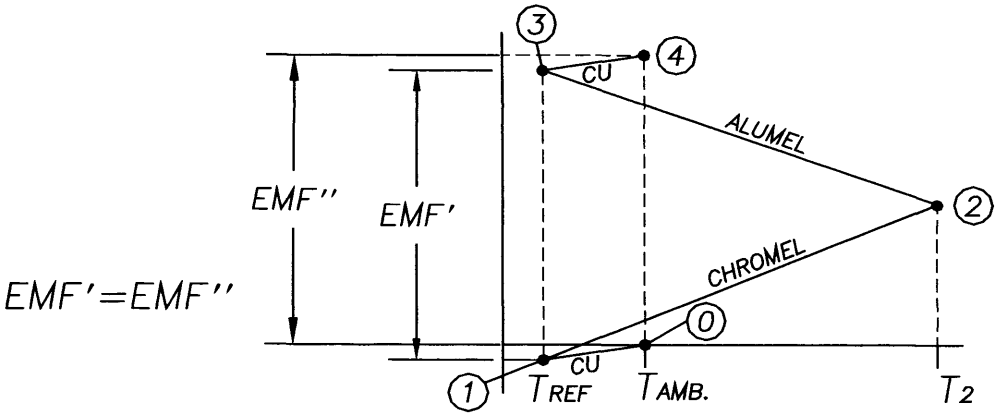

Figure 5. EMF vs temperature plot of circuit shown in figure 4.

Examination of figure 5 reveals that the introduction of the copper leadwires has no effect upon the output EMF as long as points **0** and **4** are at the same temperature.

We still however need a means of holding both points **1** and **3** at some *known* temperature, T_{ref}. Historically, this has been achieved through the use of an ice water bath. (Consequently, published thermocouple tables provide output voltage with respect to a reference junction temperature of 0° C.)

Since ice baths are not usually practical to implement, other methods to obtain or emulate a reference junction have been developed. One method utilizes an electrical resistance bridge circuit that contains a temperature sensitive resistor element. This bridge circuit is placed in series with the thermocouple circuit and is thermally integrated with the reference junction (points **1** and **3**). With the reference junction at 0° C, the bridge does not introduce any voltage. However, when the reference junction deviates from 0° C (say for example to the ambient temperature of the indicator), the bridge will automatically introduce a voltage equal and opposite to the thermocouple-EMF change that also results from this reference junction temperature deviation. Thus an equivalent 0° C reference junction temperature is effectively maintained.

CONSEQUENCE OF INTRODUCING A SLIP RING (OR CONNECTOR) BETWEEN THE INDICATOR AND THE MEASUREMENT POINT.

Figure 6 shows the circuit of Figure 4 with a slip ring placed between the indicator and measurement point **2**, where **S1** and **S2** are slip ring stator terminals and **R1** and **R2** are the corresponding slip ring rotor terminals respectively. Note that the reference junction discussed above is physically located within the "INDICATOR".

8500 Ance Road
Charlevoix, MI 49720
Tel: 231-547-5511
Fax: 231-547-7070

MICHIGAN SCIENTIFIC corporation

http://www.michsci.com
E-mail: mscinfo@michsci.com

321 East Huron Street
Milford, MI 48381
Tel: 248-685-3939
Fax: 248-684-5406

Technical Note No. 102-B

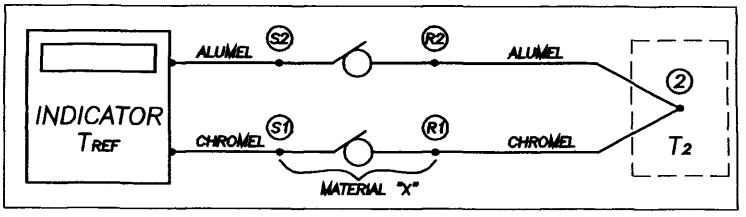

Figure 6. Thermocouple circuit with slip ring.

If there is no temperature difference between the stator and the rotor terminals, the temperature at **S1** equals the temperature at **R1** and the temperature at **S2** equals the temperature at **R2**. The EMF vs. temperature graph for this case is shown in Figure 7.

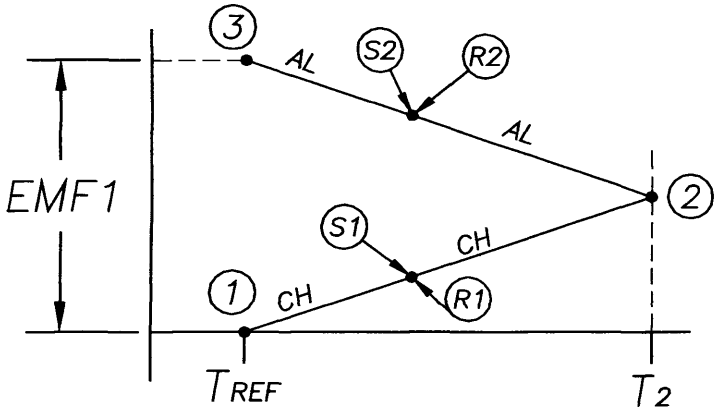

Figure 7. EMF vs. temperature for T/C with slip ring – NO temperature difference across slip ring terminals.

Since there is no temperature difference, $\Delta T=0$ across the slip ring so the stator and rotor connection points overlay each other as shown on the graph. In this case there will be no error in measurement. However, if a temperature difference does exist across the slip ring, the EMF versus temperature graph will look like that shown in Figure 8 where "X" represents the conductive path through the slip ring.

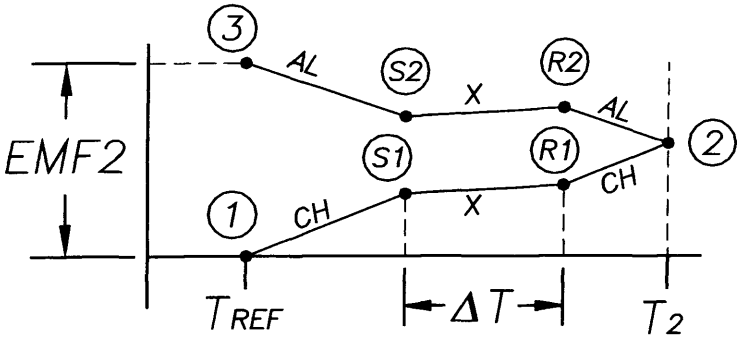

Figure 8. EMF vs. temperature for T/C with slip ring – with temperature difference ΔT across slip ring.

8500 Ance Road
Charlevoix, MI 49720
Tel: 231-547-5511
Fax: 231-547-7070

MICHIGAN SCIENTIFIC corporation
http://www.michsci.com
E-mail: mscinfo@michsci.com

321 East Huron Street
Milford, MI 48381
Tel: 248-685-3939
Fax: 248-684-5406

Technical Note No. 102-B

In this case EMF2 < EMF1 signifying that the actual temperature of the test part at point **2** is higher than measured. Examining Figures 7 and 8 we see that the difference between EMF2 and EMF1 corresponds to ΔT. Therefore, the actual temperature at point **2** is higher than measured by an amount equal to ΔT.

In the previous example the temperature of the rotor was taken to be greater than the stator. If the stator temperature is greater than the rotor temperature the EMF vs. temperature diagram will look as shown in Figure 9.

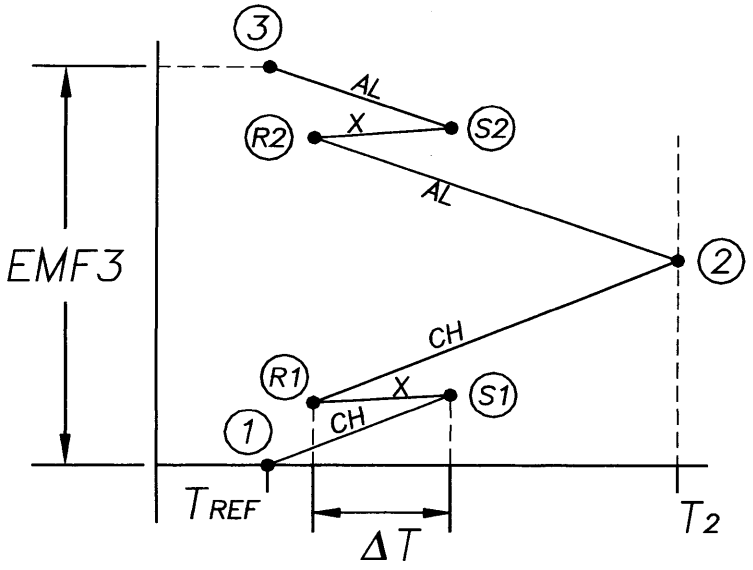

Figure 9. EMF vs. temperature for T/C with slip ring – with temperature difference ΔT across slip ring, stator terminal temperature greater than rotor terminal temperature.

Note that EMF3 > EMF1 signifying that the actual temperature of the test part at point **2** is lower than measured. As before, the magnitude of the error is equal to ΔT.

This discussion has been somewhat simplified in that actual slip ring assemblies can contain several connections of various materials between the stator and rotor terminals proper (i.e. conductive path "X"). All of these connected materials are subject to the kind of temperature gradient errors discussed and combine to produce a net error.

Temperature gradient errors associated with slip rings can be eliminated by placing a thermocouple amplifier (with built-in "cold junction" reference) on the spinning side of the slip ring as shown in Figure 10. Compare this figure to Figure 6. In this arrangement the slip ring is no longer in series with the thermocouple wire and therefore temperature differences across the slip ring will not manifest themselves as measurement error.

8500 Ance Road
Charlevoix, MI 49720
Tel: 231-547-5511
Fax: 231-547-7070

MICHIGAN SCIENTIFIC corporation
http://www.michsci.com
E-mail: mscinfo@michsci.com

321 East Huron Street
Milford, MI 48381
Tel: 248-685-3939
Fax: 248-684-5406

Technical Note No. 102-B

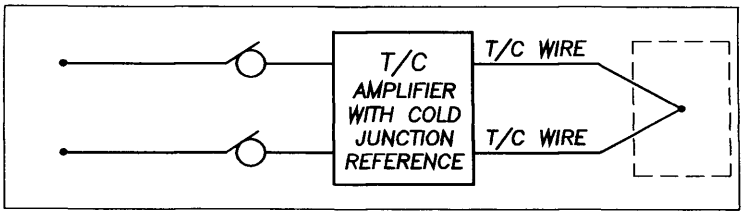

Figure 10. Slip ring with thermocouple spinning amplifier.

Michigan Scientific makes Spinning Thermocouple Amplifiers for end of shaft and tubular type slip rings. These amplifiers contain a cold junction reference and provide gain to improve the signal to noise ratio.

The temperature gradient and graphical analysis approach used to describe thermocouple behavior in this tech note is patterned after that presented by Dr. Robert J. Moffat in an article reprinted in *Applied Measurement Engineering* by Charles P. Wright, Prentice Hall, 1995. This article is suggested reading for further information about thermocouple theory and practice.

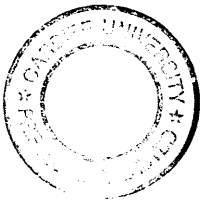

8500 Ance Road
Charlevoix, MI 49720
Tel: 231-547-5511
Fax: 231-547-7070

MICHIGAN SCIENTIFIC corporation

http://www.michsci.com
E-mail: mscinfo@michsci.com

321 East Huron Street
Milford, MI 48381
Tel: 248-685-3939
Fax: 248-684-5406